



# Optimizing the Efficacy of Adoptive T Cell Transfers and CAR-T Therapies

## Citation

Liu, Yutong. 2023. Optimizing the Efficacy of Adoptive T Cell Transfers and CAR-T Therapies. Doctoral dissertation, Harvard University Graduate School of Arts and Sciences.

## Permanent link

<https://nrs.harvard.edu/URN-3:HUL.INSTREPOS:37375491>

## Terms of Use

This article was downloaded from Harvard University's DASH repository, and is made available under the terms and conditions applicable to Other Posted Material, as set forth at <http://nrs.harvard.edu/urn-3:HUL.InstRepos:dash.current.terms-of-use#LAA>

## Share Your Story

The Harvard community has made this article openly available.  
Please share how this access benefits you. [Submit a story](#).

[Accessibility](#)

HARVARD UNIVERSITY  
Graduate School of Arts and Sciences



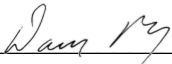
DISSERTATION ACCEPTANCE CERTIFICATE

The undersigned, appointed by the


Harvard John A. Paulson School of Engineering and Applied Sciences  
have examined a dissertation entitled:

“Optimizing the Efficacy of Adoptive T Cell Transfers and CAR-T Therapies”

presented by: Yutong Liu

Signature   
*Typed name:* Professor D. Mooney

Signature \_\_\_\_\_  
*Typed name:* Professor K. Wucherpennig

Signature   
*Typed name:* Professor D. Ingber

April 5, 2023

**Optimizing the Efficacy of  
Adoptive T Cell Transfers and CAR-T Therapies**

A dissertation presented by

**Yutong Liu**

to

The John A. Paulson School of Engineering and Applied Sciences

in partial fulfillment of the requirements

for a degree of

Doctor of Philosophy

in the subject of

Engineering Sciences

Harvard University

Cambridge, Massachusetts

April 2023

© 2023 Yutong Liu

All rights reserved

## **Optimizing the Efficacy of Adoptive T Cell Transfers and CAR-T Therapies**

### **Abstract**

Adoptive T cell therapy (ACT), including chimeric antigen receptor (CAR) T cell therapy, is a type of immunotherapy that typically uses a patient's own T cells to treat tumors. While ACT has demonstrated tremendous success in hematological malignancies, its efficacy in solid tumors remains limited. Current approaches to improving ACT efficacy focus on developing new CAR vectors that give T cells more advanced properties. However, research and clinical trial data have revealed that the phenotype of the T cell product could also significantly affect its efficacy. This thesis explores two ways to control the phenotypes of T cells to achieve better efficacy against tumors.

In the first part, T cells were metabolically labeled with unnatural sugar nanoparticles. Subsequent cytokine conjugation onto T cells allowed them to preferentially differentiate into a type 1 immune response. This method also addressed the obstacle of antigen escape in ACT treatment by activating host immunity and inducing antigen spreading, resulting in a significantly prolonged lifespan in solid tumor models and complete response with only half of the usual curative dose in liquid tumor models.

In the second part, the effects of mechanical properties of the extracellular matrix (ECM) on T cells were studied, and its potential applications in ACT product manufacturing were explored. A model ECM based on collagen type I was developed to allow for independent control of matrix

stiffness and viscoelasticity, and was subsequently used to generate phenotypically and functionally distinct T cells. T cells harvested from more elastic matrices demonstrated a more effector-like phenotype and better efficacy against tumors in vivo.

These two approaches shed light on methods to improve and optimize T cell product manufacturing by controlling the phenotype of the final T cell product.

# Table of Contents

<b>Title Page</b> .....	<b>i</b>
<b>Copyright</b> .....	<b>ii</b>
<b>Abstract</b> .....	<b>iii</b>
<b>Table of Contents</b> .....	<b>v</b>
<b>Dedication</b> .....	<b>x</b>
<b>Acknowledgement</b> .....	<b>xi</b>
<b>Chapter 1: Introduction</b> .....	<b>1</b>
<i>1.1 – Motivation of thesis</i> .....	<i>1</i>
<i>1.2 – Aims and significance</i> .....	<i>2</i>
<i>1.3 – Thesis overview</i> .....	<i>3</i>
<b>Chapter 2: Current progress on the optimization of CAR-T manufacturing</b> .....	<b>4</b>
<i>2.1 – Outline</i> .....	<i>4</i>
<i>2.2 – Introduction</i> .....	<i>4</i>
<i>2.3 – Parameters that affect CAR-T efficacy</i> .....	<i>6</i>
2.3.1 – Memory composition.....	7
2.3.2 – CD4:CD8 ratio.....	11
2.3.3 – CAR-T and the tumor microenvironment.....	15
2.3.4 – Preconditioning and lymphodepletion.....	17
<i>2.4 – Controlling T cell phenotypes</i> .....	<i>19</i>
2.4.1 – Optimizing Signals 1-2.....	19
2.4.2 – Optimizing Signal 3.....	21
2.4.3 – Fine-tuning downstream signaling .....	24
2.4.4 – Modulating ACT in vivo .....	27
2.4.5 – Rapid manufacturing and in vivo expansion .....	29
<i>2.5 - Future Directions</i> .....	<i>31</i>

<b>Chapter 3: Cytokine conjugation to enhance T cell therapy .....</b>	<b>36</b>
3.1 – <i>Outline</i> .....	36
3.2 – <i>Abstract</i> .....	36
3.3 – <i>Introduction</i> .....	37
3.4 – <i>Results</i> .....	38
3.4.1 – Nanoparticle-mediated metabolic labeling is efficient and durable, and doesn't affect T cell function or phenotype.....	38
3.4.2 – Cytokines can be conjugated onto azido-labeled T cells and alter T cell function .....	41
3.4.3 – Cytokine conjugation promotes T cell persistence and effector differentiation in vivo.....	47
3.4.4 – IL-12 conjugation enhances T cell solid tumor penetration and endogenous Th1 response.....	50
3.4.5 – IL-12 conjugation to T cells activated endogenous dendritic cells and led to antigen spread .....	53
3.4.6 – Co-conjugation of cytokines enhances ACT, and IL-12 conjugation improves sub-curative CAR-T therapy .....	55
3.5 – <i>Discussion</i> .....	58
3.6 – <i>Methods</i> .....	62
3.6.1 – Study Design.....	62
3.6.2 – Animal Handling .....	62
3.6.3 – Preparation of G400 NP.....	62
3.6.4 – T cell isolation, activation, culturing, and azido-labeling .....	63
3.6.5 – Flow cytometry analysis of azido-labeled T cells .....	64
3.6.6 – Imaging and Azido-signaling analysis of azido-labeled T cells with confocal imaging.....	64
3.6.7 – DBCO-modification of cytokines and verification.....	64
3.6.8 – Conjugating DBCO-modified cytokines onto T cells .....	64
3.6.9 – Flow cytometry for in vitro and in vivo cell analysis.....	65
3.6.10 – Cytolysis Assay .....	66
3.6.11 – CAR-T Generation.....	66
3.6.12 – B16-F10 melanoma model .....	67
3.6.13 – Xenograft lymphoma model.....	68
3.6.14 – Cell isolation from tumor and lymph node.....	68



3.6.15 – T cell activation assay and intracellular cytokine staining .....	69
3.6.16 – Tetramer staining .....	69
3.6.17 – Statistical Analysis.....	70
<b>Chapter 4: Matrix viscoelasticity regulates T cell phenotype .....</b>	<b>71</b>
4.1 – <i>Outline</i> .....	71
4.2 – <i>Abstract</i> .....	71
4.3 – <i>Introduction</i> .....	72
4.4 – <i>Results</i> .....	74
4.4.1 – T cell phenotype varies in mechanically distinct tissues in vivo.....	74
4.4.2 – Synthesizing collagen-based ECM mimetic with tunable mechanical properties.....	76
4.4.3 – Collagen modification and crosslinker have minimal effects on T cell adhesion and phenotype.....	80
4.4.4 – ECM viscoelasticity modulates T cell phenotype in complex ECM.....	81
4.4.5 – Extracellular matrix viscoelasticity modulates T cell transcriptomic profile .....	82
4.4.6 – AP-1 Pathway is enhanced in T cells cultured in slow relaxing ECM in vitro, and in tumors and fibrotic tissues in vivo.....	86
4.4.7 – Matrix viscoelasticity impacts pattern of AP-1 protein expression.....	89
4.4.8 – ECM viscoelasticity does not select for specific T cell clones.....	91
4.4.9 – ECM viscoelasticity imprints long-term T cell phenotype .....	95
4.4.10 – ECM viscoelasticity modulates the phenotypes of T cells subjected to different modes of prior activation.....	99
4.4.11 – Tuning matrix viscoelasticity leads to functionally distinct T cells. ....	101
4.4.12 – ECM viscoelasticity modulates the phenotype and function of T cells undergoing chronic stimulation .....	105
4.5 – <i>Discussion</i> .....	107
4.6 – <i>Methods</i> .....	111
4.6.1. – Material Synthesis .....	111
4.6.2 – Col-Nb crosslinking and T cell encapsulation in Col-Nb.....	111
4.6.3 – Col-Nb-Matrigel IPN crosslinking and subsequent T cell encapsulation .....	112
4.6.4 – Shear rheological characterization.....	112

4.6.5 – Nanoindentation.....	113
4.6.6 – SHG and Cryo-SEM imaging.....	113
4.6.8 – Tumor cell culturing.....	115
4.6.9 – T Cell Isolation from Collagen Matrices.....	115
4.6.10 – Flow cytometry.....	116
4.6.11 – Flow Cytometry Analyses.....	116
4.6.12 – CAR T cell Generation.....	118
4.6.13 – Xenograft lymphoma model.....	118
4.6.14 – T cell cytotoxicity assay and Intracellular Cytokine Staining (ICS).....	119
4.6.15 – cJun Immunoprecipitation.....	120
4.6.16 – Western Blotting.....	120
4.6.17 – cJun Inhibitor studies.....	121
4.6.18 – Single Cell RNA Sequencing and Analysis.....	121
4.6.19 – Single cell RNA and TCR Sequencing and Analysis.....	123
4.6.20 – Analysis of Published Single Cell and Bulk RNA Sequencing Datasets.....	124
4.6.21 – Correlation Coefficient Analysis.....	126
4.6.22 – Statistical Analysis.....	128
<b>Chapter 5: Thesis summary and future directions.....</b>	<b>129</b>
5.1 – Thesis Summary.....	129
5.2 – Limitation of the thesis and future directions.....	131
5.2.1 – Limitations for Aim 1:.....	131
5.2.2 – Limitations for Aim 2:.....	133
5.2.3 - Limitations for Aim 1 and 2.....	134
<b>Chapter 6: References.....</b>	<b>136</b>
<b>Appendices.....</b>	<b>158</b>
<b>Appendix 1: Tables for Chapter 4.....</b>	<b>158</b>
A1.1 – Donor information.....	158
A1.2 – Tumor cell gene signature.....	158

<i>A1.3 – Differential gene expression for slow relaxing gels</i> .....	173
<i>A1.4 – Differential gene expression for fast relaxing gels</i> .....	199
<i>A1.5 – Top genes in in vitro gels from cNMF analysis</i> .....	212
<i>A1.6 – Top genes in liver fibrosis from cNMF analysis</i> .....	216
<i>A1.7 – Top genes in idiopathic pulmonary fibrosis from cNMF analysis (dataset 1)</i> .....	222
<i>A1.8 – Top genes in idiopathic pulmonary fibrosis from cNMF analysis (dataset 2)</i> .....	226
<i>A1.9 – List of antibodies</i> .....	231
<b>Appendix 2 – Detailed protocols</b> .....	<b>234</b>
<i>A2.1 – Synthesis of G400 sugar polymer</i> .....	234
<i>A2.2 – Preparation of G400 sugar nanoparticles and metabolic labelling of T cells</i> .....	237
<i>A2.3 – Synthesis of DBCO-cytokine and cytokine conjugation onto T cells</i> .....	237
<i>A2.4 – Manufacturing of CAR viruses and CAR-T cells</i> .....	238
<i>A2.5 – Collagen modification, crosslinking, cell embedding, and fabrication of Matrigel-Collagen-Nb interpenetrating networks</i> .....	240
<i>A2.6 – Rheology on Col-Nb gels</i> .....	240
<b>Appendix 3 – Manufacture and expansion of CIML NK cells with mesoporous silica rod system</b> .....	<b>243</b>
<i>A3.1 – Introduction</i> .....	243
<i>A3.2 – Methods</i> .....	244
A3.2.1 – Manufacture of MSR scaffold with membrane bound IL-21 and 4-1BB.....	244
A3.2.2 – Manufacture of MSR with loaded IL-18 and IL-21 for sustained release.....	247
<b>Appendix 4 – Effects of ECM mechanical properties on NK cells</b> .....	<b>249</b>
<i>A4.1 – Introduction</i> .....	249
<i>A4.2 – Methods for embedding NK cells into Col-NB gels</i> .....	250

## **Dedication**

To my mom and dad, who constantly supported my choices and encouraged me from the other side of the ocean.

To my grandma and grandpa, who raised me up during the first years of my life and continuously supported me with love.

To all the girls who wish to pursue math, science, and engineering.

## Acknowledgement

I would like to begin by expressing my deepest gratitude to my PhD advisor, Dr. David Mooney, for his unwavering support throughout my journey. From the moment he admitted me into his lab, he has provided me with all the resources, guidance, and mentorship that I needed to thrive, even during the toughest times. Despite his busy schedule, he always made time for me, showing genuine interest in my research and personal growth, and going above and beyond to support me. I am continually impressed by his dedication to his students, his rigorous pursuit of scientific knowledge, and his humility despite his many achievements. He has been a true role model, and it has been an honor to learn from him.

I would also like to extend my gratitude to my thesis committee members, Dr. Donald Ingber and Dr. Kai Wucherpfennig. Their extensive knowledge in the fields of biomechanics and cancer immunology has been invaluable to my research, and their insightful feedback and probing questions have helped me to refine my work. I am very grateful for their discussions and the feedback they have provided. Additionally, I am grateful for the collaborations they have helped set up with their labs, which brought interesting scientific questions and opened doors to new fields.

I owe a debt of gratitude to my first research mentors, Dr. Irina Conboy and Dr. Mike Conboy, who welcomed me into their lab at UC Berkeley when I couldn't find another position. Over the course of three years, they personally mentored me and trusted me, a mere undergraduate, with independent research projects. They also introduced me to lab alumni who had gone through the same process and supported my application as an international student. It was their guidance and support that fostered my passion for research and paved the way for my pursuit of a PhD.

I am also grateful to my colleagues and collaborators who provided invaluable input and mentorship for my thesis. Dr. Kwasi Adu-Berchie and I worked closely together on one of the projects in this thesis since my first day in the lab. He is one of the most careful persons when it comes to experiments, and I really appreciate this despite always asking him to do experiments faster. Thank you for all your intellectual input and guidance. I would like to thank Dr. Hua Wang, Dr. David Zhang, and Dr. Kyle Vining for helping me shape my thesis, providing input and feedback for my work, and teaching me key experimental techniques. I would also like to thank Dr. Joshua Brockman, for the liveliness you brought to lab and hosting parties at your place, and for the three adorable cats you have. Additionally, I would like to thank Matt Pezone, Joan Cassidy, Molly Carlson, and Eileen Barrette, for dealing with all the logistics and keeping the lab running smoothly for so many years. Last not but least, I'd like to thank rest of the Mooney lab members who have all made this place fun, safe, and rewarding.

I would also like to express my gratitude to the exceptional researchers I had the pleasure of collaborating with from other institutions, including Dr. Jason Pyrdol, Jingyi Zhou, Dr. Adam Sperling, Dr. Eric Smith, Dr. Mubin Tarannum, Dr. Yuncheng Man, and Dr. Yunhao Zhai. Working with each of you has been an enriching experience, and I have learned so much from your expertise and passion for research. I also owe deep gratitude to all the supporting members from the Wyss Institute, including Michael Carr, Maurice Perez, Eric Zigon, and Thomas Ferrante. Each of them provided tremendous help maintaining the smooth, day-to-day functions of the lab, and taught me valuable experimental skills that were vital to my thesis project.

I would like to thank all the friends that have supported my journey at Harvard. My roommates, Yijun Wang and Wenqing Xu, who are both scientists themselves, were invaluable confidantes,

sharing in the joys and frustrations of scientific research and life in general. I would like to thank the close friends that I had met during my PhD, Grace Zhu, Esq., Ziqi Lu, Dr. Jinlin Li, Yan Zhao, Dr. Chun Hu, Dr. Jiachen Lin, Dr. Xizhi Chen, Dr. Ruo Chen Zhang, Dr. Ruiqiong Guo, Dr. Liang Chang, and Dr. Yifang Shui, as well as my close friends that I met previously who are now across continents and oceans, Fanding Gao, Tianqi Xin, Mengyao Zhou, Maggie Sheng, Dr. Lizhen Ma. Thank you for keeping me away from depression, which is not uncommon among PhDs, and instilling non-stop laughter into my life. I appreciate the unwavering support and intellectual curiosity you have provided, and I enjoyed the times we spent in mountains, restaurants, beaches, Airbnbs in decadent towns, or just across the screens in our hands.

I would like to express my heartfelt gratitude to my family for their unwavering support throughout my academic journey. My parents, Jinzhu Liu and Xiuying Gai, both accomplished engineers, have instilled in me an open-minded approach and encouraged me to pursue my academic interests. My grandparents, Suqin Li and Yunwen Gai, played an instrumental role in my upbringing and showered me with love and care. I am also grateful for the companionship of my beloved cat, Meiyou (Null), who brought joy and warmth to my life during the past year, even though cleaning up after his antics was not always a breeze, and he still owes me my favorite fridge magnet. He knocked over another bottle while I am writing this paragraph.

Finally, I'd like to acknowledge the funding sources that supported this work: the Food and Drug Administration (R01FD006589), National Cancer Institute (U54 CA244726, R01 CA276459), and the Wyss Institute Director's Fund and Validation Project.

## **Chapter 1: Introduction**

This chapter first provides a motivation for the thesis, presents the hypothesis and specific aims of the thesis, and discusses the significance of the work.

### **1.1 – Motivation of thesis**

T cells play a critical role in eliciting immune responses against tumors, and one way to harness their anti-tumor potential is through adoptive cell transfer (ACT). In ACT, T cells or other types of immune cells are harvested from a patient, manipulated *ex vivo*, and reinfused back into the patient<sup>1-3</sup>. Currently, ACT has been explored for non-genetically modified T cells in melanoma, as well as genetically modified T cells that express antigen-specific T cell receptors (TCR) or chimeric antigen receptors (CAR), depending on whether the antigen is recognized with the presence of major histocompatibility complexes (MHCs)<sup>4,5</sup>. However, while ACT has demonstrated great potential in hematological tumors, its efficacy in solid tumors remains limited, and very little success has been observed.

There are two major obstacles for adoptive T cell transfer to be effective in solid tumors. First, the efficacy of CAR-T cells is not fully harnessed. Recent research has demonstrated that not all T cell populations have the same anti-tumor efficacy when reinfused back into the body.

However, current CAR-T therapies rarely select for specific populations that have proven to be more effective. Therefore, one potential way to boost the efficacy of ACT in solid tumors is to generate or polarize T cells into desired phenotypes before infusion. This has been achieved mainly by either designing CAR vectors with new functions or preselecting for T cell populations before infusion<sup>6,7</sup>. However, designing new CAR vectors involves complicated testing and is often limited by the length of vectors and gene expression silencing. Second, T cell



activity and function are further suppressed or deprived post-infusion. T cells are blocked from entering the tumor by the dense and crosslinked tumor extracellular matrices (ECM), their immune activities are suppressed by the tumor microenvironment, and their tumor-specificity is lost over time as a result of tumor antigen escape<sup>8-11</sup>. Given these challenges, it is of great interest to explore ways to increase CAR-T efficacy to overcome these obstacles.

## **1.2 – Aims and significance**

The central hypothesis of the thesis is that **the efficacy of adoptive T cell transfer products could be enhanced by fine tuning the T cell phenotype within the product**. This hypothesis is further addressed with the following specific aims:

Aim 1 (Chapter 3): **Direct T cell differentiation and phenotype to enhance the efficacy of adoptive T cell therapies by metabolically labeling T cells with unnatural, azide-containing sugar, and conjugating anti-tumor cytokines onto T cells**. It is hypothesized that conjugating cytokines onto T cells via metabolic labeling could allow for local, concentrated presentation of otherwise toxic anti-tumor cytokines and guide the differentiation of T cells into anti-tumor phenotypes. This method significantly boosts T cells' effector functions and enhances their ability to infiltrate solid tumors, allowing subcurative doses of CAR-T cells to achieve a curative response. Additionally, with increased tumor killing, this method activates the host immune system, encourages antigen spreading, and partially addresses the problem of antigen heterogeneity in solid tumors. This method is a simple and straightforward way to boost the efficacy of CAR-T cells and could be easily integrated into the current CAR-T manufacturing pipeline.

**Aim 2 (Chapter 4): Develop and characterize a collagen type 1-based model extracellular matrix (ECM) where the stiffness and the viscoelasticity of the ECM could be independently tuned to generate phenotypically and functionally distinct T cell populations for adoptive T cell therapy.** The role of mechanical properties on cells has been demonstrated in a variety of cell types, including tumor cells, fibroblasts, and monocytes. However, little research has been done on how the mechanical properties of the ECM affect T cells and whether these findings can be utilized to manufacture more effective T cell products. By developing and characterizing a model ECM where the stiffness and viscoelasticity could be independently tuned, the system allows for a detailed understanding of the phenotype and functional changes from changes in each individual parameter and provides a basis for the detailed characterization of underlying signaling pathways that govern these changes. The findings could serve as guidance for new CAR-T cell manufacturing strategies, in addition to providing more insight into pathologies with altered ECM, such as solid tumors and fibrosis.

### **1.3 – Thesis overview**

This thesis is organized as follows. Chapter 2 provides an overview of the current understanding of how different T cell phenotypes dictate the final efficacy of adoptive T cell products and the methods that people have explored to control T cell phenotype. Chapter 3 presents research on the metabolic labeling and cytokine conjugation of T cells. In Chapter 4, a collagen type 1-based model ECM is introduced, and its ability to generate phenotypically and functionally distinct T cells for adoptive T cell transfers is discussed. Chapter 5 summarizes the findings of the thesis, and discuss the limitations and future directions of the work.

## **Chapter 2: Current progress on the optimization of CAR-T manufacturing**

This chapter was previously published as a review article in Liu, Y., Sperling, A. S., Smith, E. L. & Mooney, D. J. Optimizing the manufacturing and antitumour response of CAR T therapy. *Nature Reviews Bioengineering* 2023 1–15 (2023) doi:10.1038/S44222-023-00031-X.

### **2.1 – Outline**

The phenotype of the final T cell product substantially affects in vivo anti-tumor efficacy and various strategies have been developed to manipulate T cell phenotype during chimeric antigen receptor (CAR)-T manufacturing to improve in vivo responses after T cell infusion. This chapter provide an overview of specific T cell attributes that influence the performance of adoptive T cell transfers (ACT), as well as how different T cell subsets interact with the immunosuppressive tumor microenvironment, including the role of preconditioning in CAR-T therapies (2.3). The chapter then discusses strategies to control T cell phenotype and anti-tumor performance after infusion through manipulation of the 3 signals for T cell activation and downstream signaling pathways during manufacturing (2.4.1 – 2.4.4). Finally, the chapter ends by discussing developments in rapid manufacturing of CAR-T cell products (2.4.5).

### **2.2 – Introduction**

Infusion of T cells with specificity to tumor antigens has demonstrated the ability to control or even eliminate tumor malignancies. This process, termed adoptive T cell transfer (ACT), typically involves isolation of T cells from patients, their expansion and activation ex vivo, followed by re-infusion of the activated T cells back into patients to direct anti-tumor responses. ACT using tumor-infiltrating lymphocytes (TILs) and systemic administration of interleukin

(IL)-2 induce substantial, and in some cases, complete response, in patients with metastatic melanoma<sup>1-3</sup>. Since then, multiple strategies have been explored to direct tumor-specific T cell responses. T cells have been genetically modified to bear tumor-antigen-specific T-cell receptors (TCRs) and chimeric antigen receptors (CARs) to induce more potent and specific anti-tumor responses<sup>15,16</sup>.

CAR-T has gained particular attention given its success against hematological malignancies and has been approved for the treatment of acute lymphoblastic leukemia (ALL), large B-cell lymphoma and multiple myeloma<sup>17-19</sup>. CARs are synthetic receptors used to redirect T cell activity to target cells with a specific cognate antigen, regardless of the T cell's original specificity. The CAR construct consists of an extracellular domain for antigen recognition (usually a scFv antibody) and an intracellular domain for T cell signaling (usually CD3 $\zeta$ ) and activation (usually CD28 and/or 4-1BB)<sup>20</sup>. Currently, three generations of CARs have been designed which differ in their intracellular domain construct: first generation CARs contain only CD3 $\zeta$ , second generation CARs possess an additional co-stimulatory domain fused to CD3 $\zeta$  and third generation CARs contain two co-stimulatory domains, CD28 and 4-1BB, fused to CD3 $\zeta$ <sup>21</sup>. Future generations of CARs bearing more complicated functions are being explored pre-clinically, including the recognition of multiple antigens, simultaneous expression of adjuvant molecules or circuits to terminate CAR function through apoptosis<sup>22</sup>.

However, although CAR-T therapy has achieved phenomenal success in hematological malignancies, it has faced considerable challenges in solid tumors<sup>17,18</sup>. Clinical trial results of CAR-T therapy targeting cell-surface tumor-specific antigens in solid tumors have been largely discouraging, with more than half of patients receiving the therapy having a stable or even

progressive tumor, and only 13% patients having any therapeutic response<sup>23,24</sup>. This poor efficacy against solid tumors likely has many causes, including the limited number of known tumor specific antigens, limited T cell persistence and fitness before reaching the tumor site, poor solid tumor penetration and the immunosuppressive tumor microenvironment (TME)<sup>18,25,26</sup>.

Efforts are ongoing to solve these issues. Aside from various CAR designs and CAR-T functionalization through genetic engineering methods, the phenotypes of the final CAR-T product substantially impact the final therapeutic efficacy<sup>27-29</sup>. In this review, we will discuss how phenotypes of CAR-T products affect CAR-T fitness, survival, solid tumor penetration and interactions with the patient's tumor and immune system. Moreover, we will explore emerging strategies that could be used to control and optimize phenotypes of CAR-T cells in the absence of genetic manipulation. Specifically, we first discuss important parameters in CAR-T clinical efficacy and factors from the TME and preconditioning that influence CAR-T response. We then look into methods that can be used to tune the specific phenotypes of CAR-T cells during their manufacture, by manipulating the 3 signals for T cell activation and downstream signaling pathways, as well as recent developments in rapid manufacturing. We envision these strategies to be readily integrated into the current T cell manufacturing process to direct and optimize CAR-T phenotypes for improved therapeutic responses. We do not focus on the design of CAR vectors nor other genetic manipulations, as those have recently been reviewed elsewhere<sup>21,30</sup>.

### **2.3 – Parameters that affect CAR-T efficacy**

Early research and clinical trials for CAR-T and other ACT therapies largely focused on the cell dose, without delineating the specific phenotypes of T cells. However, T cell therapies are typically comprised of heterogeneous mixtures of cells that differ in many parameters, such as

memory differentiation profiles, activation and exhaustion states and cytokine release profiles. Each of these variables influence numerous functions of T cells, including their ability to migrate and localize to a tumor, their cytolytic activity, cytokine release and metabolism, all of which are essential for T cells to mediate tumor regression following ACT. It is now clear that T cells with different memory potential, the presence of CD4 T cells and specific subsets of CD4 T cells can alter clinical outcome.

### *2.3.1 – Memory composition*

A key parameter for therapeutic efficacy is the memory potential of transferred T cells (Figure 1.1). Upon antigen challenge, naïve T cells ( $T_N$ ) rapidly (up to 50,000-fold in the course of a week) divide into memory T cells and effector T cells ( $T_{Eff}$ ) that clear cells displaying the antigen (for example, infected cells)<sup>31</sup>. Once these cells are removed, most of the expanded T cells die, but a small pool of memory T cells remain in the body to provide long-term protection (for up to 75 years)<sup>32</sup>. Upon re-exposure to the same antigen, these memory T cells are able to expand quickly and elicit a strong immune response<sup>33</sup>. Memory T cells include several subtypes: stem cell memory ( $T_{SCM}$ ), central memory ( $T_{CM}$ ) and effector memory ( $T_{EM}$ ), which represent increasingly differentiated cells. As T cells differentiate from naïve cells through the memory hierarchy, their proliferation potential decreases while their cytolytic activities increase<sup>33,34</sup>.

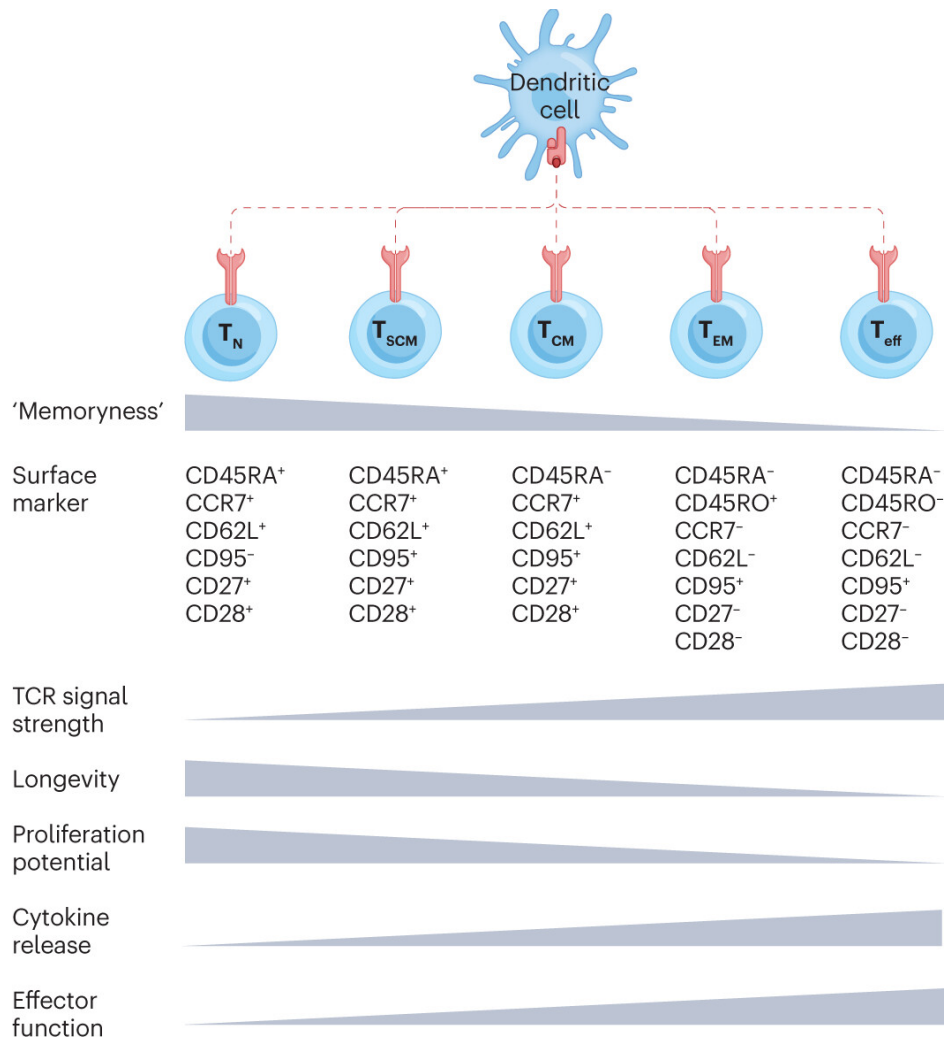


**Figure 2.1, T cell memory phenotypes affect anti-tumor capability.** T cells differentiate to varying phenotypic states following antigen stimulation. Depending on the strength and duration of T cell receptor (TCR) signalling, T cells will adopt different memory phenotypes. As T cells further differentiate, they lose proliferation potential, but adopt more anti-tumor effector functions. For adoptive transfer, T cell products with less differentiated T cells have better overall therapeutic efficacy given their strong proliferation and expansion potential.  $T_N$ , naïve T cells;  $T_{SCM}$ , stem cell memory T cells;  $T_{CM}$ , central memory T cells;  $T_{EM}$ , effector memory T cells;  $T_{Eff}$ , effector T cells.

Preclinical studies show that higher ratios of  $T_N$  and  $T_{CM}$  in T cell populations genetically engineered to express tumor-specific T cell receptors (TCRs) confer superior anti-tumor efficacy upon adoptive transfers<sup>35-38</sup>. The same trend is observed in CAR-T therapies as well, where higher frequencies of  $T_N$ ,  $T_{SCM}$  and  $T_{CM}$  improve anti-tumor efficacy in animal models, patient-

derived samples and clinical trials (CHP-12-009915, NCT01865617, DDHK97-29/P00.0040C)<sup>39-45</sup>. These findings might relate to the higher proliferation potential of these cells compared to  $T_{\text{Eff}}$ , leading to better persistence and higher cell numbers at peak response<sup>40</sup>. These cell populations also release higher levels of anti-tumor cytokines, such as IL-2, upon antigen stimulation, whereas the cytolytic activity of their daughter cells is similar to that of more terminally-differentiated T cells<sup>40</sup>. Compared with  $T_{\text{Eff}}$ , these T cell populations have higher expression of activation markers such as CD28 and lower expression of exhaustion markers such as T cell immunoglobulin and ITIM domain (TIGIT), lymphocyte-activation gene (LAG3) and programmed cell death protein 1 (PD1), and are thereby more likely to resist exhaustion and loss of cytolytic activities<sup>37,39,40</sup>.

$T_{\text{SCM}}$ , in particular, have received increasing attention. Given their extreme longevity, robust proliferation potential and the ability to reconstitute the  $T_{\text{CM}}$  and  $T_{\text{EM}}$  compartments, minimally differentiated  $T_{\text{SCM}}$  cells display more potent anti-tumor responses than  $T_{\text{CM}}$  and  $T_{\text{EM}}$  cells in murine melanoma models<sup>28,46,47</sup>. Notably, the ratio of  $T_{\text{SCM}}$  is positively correlated with the extent of expansion after adoptive transfer and the number of long-term circulating memory T cells<sup>48</sup>. Moreover, in pre-clinical studies, mouse and human effectors derived from  $T_{\text{N}}$  and  $T_{\text{SCM}}$  demonstrate greater proliferative burst and higher cytokine secretion, leading to a more potent antitumor activity compared to those derived from  $T_{\text{CM}}$ <sup>35,37</sup>. They also display minimal levels of terminal differentiation markers such as KLRG1 and CD57 and longer telomere lengths<sup>35,37</sup>.

Given that memory differentiation of T cells is largely linear and unidirectional, arresting T cells in an early differentiation stage before transfer could be desirable to induce a more potent and long-lasting anti-tumor response<sup>49</sup>. Currently, cell surface markers are used to select and isolate



specific T cell populations. Human T cells at different memory stages can be differentiated based on surface markers including CD62L, CD45RA, CD45RO, and sorted with biotinylated or magnetic beads, or fluorescence-activated cell sorting (FACS)<sup>35,40,47,50</sup>. Alternatively, T cells can be manufactured to favor certain memory populations based on the cytokines present in the culture or other factors<sup>51-53</sup>. The resulting population is less pure compared with sorting, but might be preferred because their production requires less time and resources, and can be easily integrated into the current CAR-T manufacturing protocol. A strategy to achieve a similar outcome is the inclusion of phosphoinositide 3-kinases (PI3K) inhibitors in the culture media<sup>54,55</sup>, which is one of the most clinically advanced approaches. The B-cell maturation antigen (BCMA)-targeted CAR T cell therapy bb21217, differs from the U.S. Food and Drug Administration (FDA) approved Idecabtagene Vicleucel (Ide-cel, formerly bb2121) through the inclusion of a PI3K inhibitor during manufacturing (CRB-402 trial; NCT03274219). These Phase I results look promising, with a highly naïve T cell phenotype generated at the end of the manufacturing process and outstanding clinical responses (objective response rate of 69%)<sup>56</sup>. However, given the high overall response rates with BCMA-targeted CAR T cell therapies for myeloma without the PI3K inhibitor, it is challenging to demonstrate clinical improvement in a single arm study. 2seventy bio and Bristol-Myers Squibb have jointly announced that they will not pursue further clinical development of this approach, highlighting the challenges of translating preclinical findings to convincing clinical outcome improvements in the manufacturing space.

Other approaches have focused on maintaining a less differentiated T cell product, including developing rapid manufacturing procedures and potentially collecting T cells earlier in the disease course or using ‘off-the-shelf’ T cell products from healthy donors to avoid the

deleterious impact of multiple lines of therapy on the patients T cells<sup>57-60</sup>. The influence of previous treatments on T cell subsets and phenotypes can hamper the goal of manufacturing CAR T cells for in vivo expansion<sup>58-60</sup>. For example, after first-line (induction) therapy, T cells from patients with multiple myeloma have a higher CD4:CD8 ratio and a higher %CD8+CD45RO-CD27+ (T<sub>N</sub>, T<sub>SCM</sub>) population compared to T cells from more heavily pre-treated relapsed and refractory patients. Similarly, T cells from post-induction patients increase population doublings during a fixed manufacturing period compared to T cells from relapsed and refractory patients. Interestingly, the same T cell immunophenotype patterns (greater CD4:CD8 ratio; greater %CD8+CD45RO-CD27+) detected in less heavily pre-treated patients were also observed when comparing responding (partial response or better) patients to non-responding. These observations provide further evidence that the starting T cell phenotype influence the post-manufacturing CAR T cell product.

### *2.3.2 – CD4:CD8 ratio*

The CD4:CD8 ratio of the final T cell product is also believed to be a key aspect of therapeutic impact. CD4+ T cells are important for the maintenance and full activation of cytotoxic T cells and the induction of an effective memory response<sup>61-63</sup>. However, most current CAR-T products do not use population selection. Given that T cells derived directly from patients greatly diverge in CD4:CD8 ratio, the final clinical outcome of CAR-T cell products is also affected. Moreover, the CD4:CD8 ratio generally decreases throughout the CAR-T manufacturing process, because CD8+ T cells are significantly more proliferative than CD4+ T cells<sup>64</sup>.

The synergistic activity between CD4 and CD8 was first shown in mouse CAR-T models, and then in human studies. In murine models of pulmonary metastasis and lymphoma, CAR-T cell

products with balanced CD4:CD8 ratio translate into higher cell frequencies at peak response, leading to an increased co-localization of CD4<sup>+</sup> and CD8<sup>+</sup> CAR-T cells at the tumor site and improvement of overall anti-tumor response<sup>40,65,66</sup>. This synergistic effect is likely to be caused by the secretion of T helper type 1 (Th1) cytokines by CD4<sup>+</sup> T cells at the tumor site, because these phenotypes have anti-tumor activity themselves while also boosting CD8<sup>+</sup> cytotoxicity<sup>40,65,66</sup>. Pre-selection of CD4 and CD8 cells followed by separate transduction generates a balanced CAR-T product irrespective of patient-to-patient differences in apheresis products<sup>67,68</sup>. In patients, a balanced CD4:CD8 ratio improves CAR-T cell products efficiency regardless of the initial memory composition of the CD8 T cells, as demonstrated by an increase of complete response rate and reduction in cell dose by 5- to 100- fold compared to those used in previous clinical trials (NCT01865617, NCT02028455)<sup>45,69,70</sup>. Moreover, the absence, or minimal numbers, of either CD4 or CD8 significantly reduce the potency of the final CAR-T product<sup>71</sup>. These clinical trials demonstrate that it is possible to preselect and adjust the CD4:CD8 ratio even in heavily-pretreated patients with highly variable T cell subsets. One example is lisocabtagene maraleucel (liso-cel, formerly JCAR017), which is manufactured with a fixed CD4:CD8 ratio and is FDA-approved for the treatment of patients with relapsed non-Hodgkin lymphoma (NCT02631044)<sup>72</sup>. This product has comparable response rates to other anti-CD19 CAR-T cell products with cross-trial comparison suggesting improved toxicity profile and lower levels of cytokine release syndrome. Direct head-to-head comparisons will be needed to confirm the clinical superiority of this fixed CD4:CD8 approach.

Specific subtypes of CD4<sup>+</sup> T cells could also affect the final efficacy of CAR T products (Figure 1.2a). In murine lymphoma models, Th1 CD4<sup>+</sup> T cells demonstrate strong anti-tumor effects, primarily by activating and regulating cytotoxic T lymphocytes (CTL) and providing local

presentation of anti-tumor IL-12 and interferon gamma (IFN- $\gamma$ )<sup>73,74</sup>. The role of Th2 CD4+ T cells is more controversial. In some cases, Th2 cells induce tumor necrosis, and adoptive transfer of Th2 cells results in the eradication of solid tumors in murine lymphoma and melanoma models<sup>73-75</sup>. In other cases, Th2 cytokines such as IL-4 and IL-13 induce pro-tumor activities of myeloid cells and increase the invasiveness and proliferation of malignant cells<sup>76-79</sup>. There is currently no consensus as to the cause for these disparate findings. Pro-tumor activities of Th17 are often observed under chronic inflammatory environments and are considered to be caused by chronic exposure to Th17 CD4+ T cells and their cytokines (such as IL-17)<sup>80-82</sup>. However, adoptive transfer of tumor-specific Th17 T cells and IL-23 expressing CAR-Ts leads to superior anti-tumor activity compared with regular T cells and CAR-Ts, while encouraging the recruitment of dendritic cells and activation of tumor-specific CD8+ T cell in solid tumor models<sup>83-85</sup>. T follicular helper cells (Tfh) CD4+ T cells generate tertiary lymphoid structures (TLS) at the tumor site which can promote immune cell infiltration into tumors and orchestrate anti-tumor immunity across cellular and humoral immunity in animal models<sup>86-88</sup>. Altogether, these data suggest that appropriate polarization of CD4+ T cells should be considered in manufacturing the final product for CAR-T therapies.

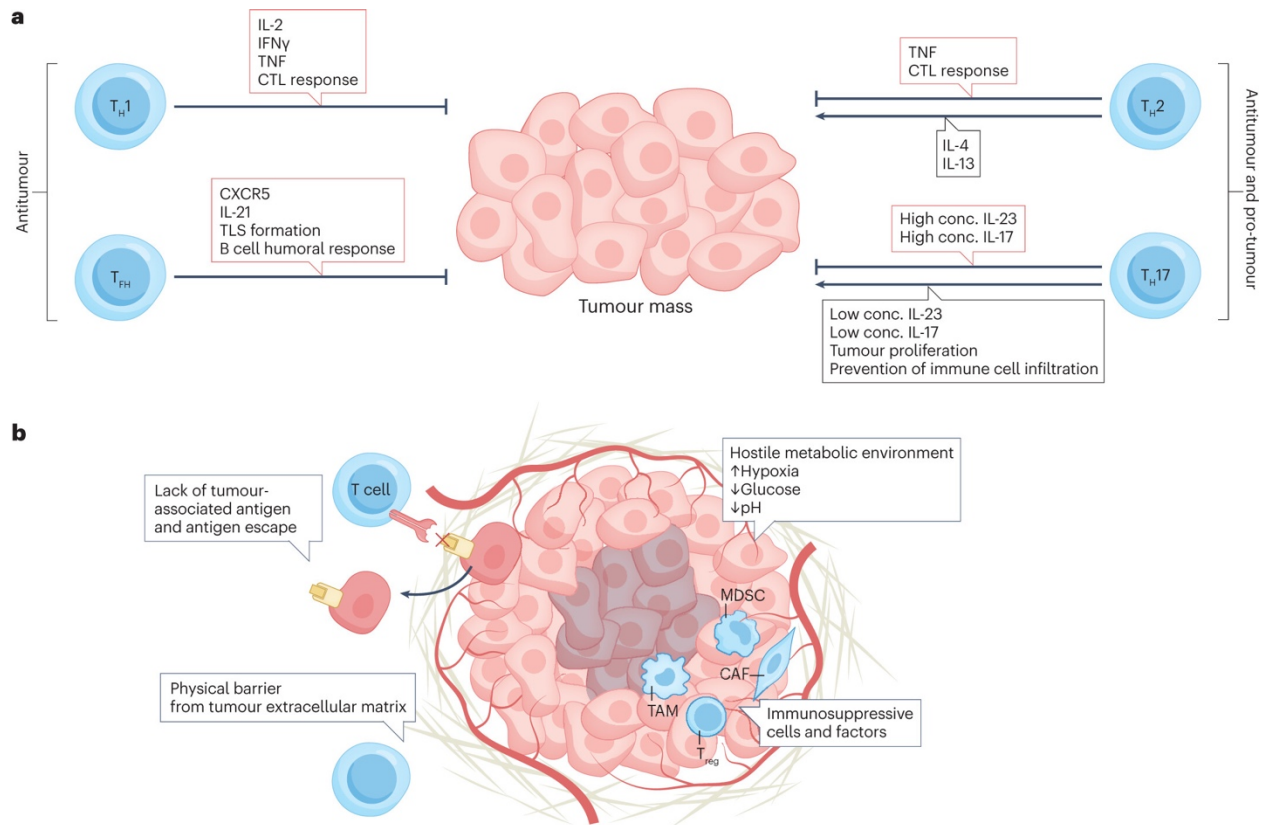


**Figure 2.2, CD4<sup>+</sup> subset composition and the tumor microenvironment affect the outcome of ACT treatment. a,** Different CD4<sup>+</sup> T cell subsets contribute differently to anti-tumor immunity. T helper cells 1 (Th1) and T follicular helper cells (Tfh) are largely anti-tumor. Th1 activate cytotoxic T lymphocytes (CTL) and secrete anti-tumor cytokines locally while Tfh generate tertiary lymphoid structures (TLS) to promote immune cell infiltration into tumors. However, Th2 and Th17 provide both anti-tumor and pro-tumor activities. While Th2 can secrete anti-tumor cytokines, they also secrete interleukin-4 (IL-4) and IL-13 and induce pro-tumor activities in myeloid cells. Local, high-level secretion of Th17 cytokines by adoptively transferred Th17 T cells can be anti-tumor, whereas chronic exposure to Th17 cytokines accelerate tumor growth. **b,** The tumor microenvironment (TME) presents multiple obstacles for efficient adoptive T cell transfers (ACT) treatment against solid tumors. These barriers include inefficient T cell recruitment to tumor sites owing to chemokine receptor mismatches, the physical barrier that impedes T cell infiltration, lack of tumor-associated antigen for chimeric antigen receptor T cells (CAR-T) targeting and the potential of antigen escape, a hostile metabolic environment that suppresses T cell functions and immunosuppressive cells and factors that suppress T cell effector function and induce T cell exhaustion. TNF, tumor necrosis factor; IFN, interferon; ECM, extracellular matrix; TAM: tumor associated macrophages; MDSC, myeloid-derived suppressor cells; Treg: regulatory T cells; CAF, cancer associated fibroblasts.

### 2.3.3 – CAR-T and the tumor microenvironment

The efficacy of adoptively transferred T cells in the treatment of solid tumors is hindered by several challenges that are distinct from hematologic cancers. These limitations include T cell localization and infiltration into the solid tumor, the absence of tumor antigens that are highly and uniformly expressed across cancerous cells and the TME, which is characterized by hypoxia, oxidative stress and immunosuppressive inhibitory molecules, cells and cytokines (Figure 1.2b).

Recruitment of T cells into tumors is guided by the expression of chemokine receptors that correspond to chemokines produced in the TME. Altered signalling pathways in tumor cells, such as inactivation of STAT3 and p53, could downregulate the production of T-cell attracting chemokines. Moreover, T cells might also lack the expression of chemokine receptors that match the chemokine profile within the TME. These mismatches reduce the recruitment of T cells and other immune cells to the tumor site in murine melanoma and liver carcinoma models<sup>89-91</sup>.

Furthermore, CAR-T cells that reach the tumor site still face various impediments to infiltrate and eradicate the tumor. First, is the presence of a physical barrier owing to extensive deposition and crosslinking of extracellular matrix molecules such as collagen and hyaluronan, which physically limit T cell access to tumors<sup>8,9</sup>. Additionally, cells in the TME can upregulate immunosuppressive chemokines such as CXCL12 and CXCL15, further excluding the infiltration of T cells<sup>92-94</sup>.

Unlike hematological malignancies, where there is one or multiple uniformly and highly expressed antigens on all malignant cells, the heterogeneity of solid tumors limits the identification of antigens that can be effectively targeted by CAR-T cells. Moreover, many tumor-associated antigens whose expression is elevated in cancerous cells are also expressed in

healthy cells at low levels, which substantially increases the off-target toxicity for CAR-T cells. For example, CAR-T targeting erb-b2 receptor tyrosine kinase 2 (ErbB2, also known as Her-2) for colon cancer metastasis and CAR-T targeting GD2 for neuroblastoma led to fatal cytokine release syndrome and severe neurotoxicity<sup>95,96</sup>. Additionally, greater antigen heterogeneity in solid tumors increases the likelihood for antigen escape during ACT treatment as the expression of the original target antigen is downregulated, allowing cancerous cells to escape CAR-T targeting. One potential solution is to exploit crosstalk between CAR-T and the TME, because CAR-T cells can modify the TME post infusion<sup>97,98</sup>. Specifically, CD4<sup>+</sup> CAR-T cells activate host immune responses and boost antigen presentation, whereas CAR-T-derived IFN- $\gamma$  supports the anti-tumor activity of endogenous T and natural killer cells<sup>98</sup>. Exploiting the molecular and cellular crosstalks between CAR-T and the TME provides opportunities to achieve effective and durable responses against solid tumors by boosting host immunity.

The TME can also present a hostile metabolic environment to T cells. The abnormal vasculature of tumors not only prevents T cells from effectively accessing the cancerous cells, but also creates a hypoxic environment that metabolically suppresses oxidative phosphorylation. In murine neuroblastoma models and proteomics analysis from melanoma patients, this effect considerably impairs the proliferation and survival of T<sub>N</sub> and T<sub>CM</sub>, memory T cell populations that have proven important in controlling tumor growth and is also negatively correlated with antigen presentation and TIL responsiveness<sup>99-101</sup>. Furthermore, solid tumors display depleted glucose in the TME owing to competition from fast-growing cancerous cells<sup>102-104</sup>. Given aerobic glycolysis is essential for T cells to develop effector functions, this condition can dampen the responsiveness of TILs against tumor antigens and result in irreversible T cell dysfunction over the long term<sup>105,106</sup>. These changes can be partially compensated by

upregulating other metabolic pathways. For example, hypoxia and glucose depletion enhance fatty acid catabolism in CD8<sup>+</sup> TILs, allowing them to partially preserve effector functions and slow tumor progression<sup>107</sup>. Ketone bodies could also serve as alternative energy source<sup>107</sup>.

Finally, the TME hosts various immunosuppressive cells and factors that further impair the functions of TILs and infiltrated CAR-Ts. Cancer associated fibroblasts (CAFs) and immune cells such as myeloid-derived suppressor cells (MDSCs), tumor associated macrophages (TAMs), tumor associated neutrophils (TANs) and regulatory T cells (Tregs) support the secretion of immunosuppressive factors such as transforming growth factor beta (TGF- $\beta$ ) and indoleamine 2,3-dioxygenase (IDO), as well as agents such as vascular endothelial growth factor (VEGF) that drive the development of abnormal vasculature<sup>108</sup>. Tregs also impair T cell function by consuming local IL-2 required for T cell survival and expansion<sup>10</sup>. Chronic tumor antigen exposure also results in long-lasting activation of T cells. Furthermore, the expression of checkpoint inhibitory molecules such as PD-L1 and CEACAM1 on tumor cells and plasmacytoid dendritic cells also induces T cell exhaustion<sup>109–111</sup>. Together, these components modulate the TME and suppress activities of infiltrating antigen-presenting cells (APCs) and cytotoxic T cells, thus limiting the efficacy of ACT in solid tumors.

#### *2.3.4 – Preconditioning and lymphodepletion*

Preconditioning with lymphocyte targeting agents such as cyclophosphamide (Cy), fludarabine (Flu), anti-CD52 antibodies or bendamustine prior to T cell infusion is integral to ACT proliferation and engraftment<sup>112</sup>. This improvement is often attributed to the elimination of immunosuppressive cells such as Tregs and the reduction of cells competing for cytokines to ‘make space’ for infused T cells<sup>113</sup>. The current preconditioning standard is the combination of



Flu and Cy, starting about 5 days prior to ACT infusion<sup>72,114–116</sup>. Whether differences in the dosing of these drugs, or the use of alternative agents, improves the activity and toxicity CAR-T cell products remains unknown. In a retrospective analysis, the use of bendamustine was associated with equivalent activity but an improved toxicity profile when compared to Flu and Cy in patients receiving tisagenlecleucel, an FDA-approved anti-CD19 CAR-T cell product<sup>117</sup>. The availability of effective alternative lymphodepleting regimens has been recently highlighted, because manufacturing problems have led to international shortages of fludarabine.<sup>118</sup>

Preconditioning also has other beneficial effects beyond depletion of host T cells, including a direct impact on the TME during ACT. Chemotherapy induces immunogenic cell death (ICD) and helps establish an environment prone to immune infiltration<sup>119</sup>. Preconditioning with Cy alone or in combination with oxaliplatin (Ox) results in TME remodelling by repolarizing local myeloid cells and increasing the expression of multiple T-cell-recruiting chemokines by cells residing in the TME, thereby increasing CAR-T cell recruitment in murine lung tumor and prostate carcinoma models<sup>120,121</sup>. These benefits are furthered when immune checkpoint blockade (ICB) is used in combination with Ox and Cy, leading to significantly higher CAR-T accumulation at the tumor site and prolonged mouse survival<sup>121</sup>. Similarly, local, low-dose radiotherapy (0.5-6 Gy) also promotes ICD, increases the cross-presentation of tumor-associated antigens and T cell infiltration and provides synergistic effects with ICB in murine mammary carcinoma models<sup>122–125</sup>. These studies raise the possibility that chemo and radiotherapies might act in synergy with ACT by remodeling the TME for better T cell infiltration and stronger anti-tumor response.

## 2.4 – Controlling T cell phenotypes

Current ACT manufacturing protocols rely on ex vivo activation and expansion of patient-isolated T cells. Different strategies have been explored to optimize T cell activation to improve clinical performance. Primary T cell activation requires three signals, T cell receptor binding (Signal 1), binding to costimulatory molecules (Signal 2) and cytokines that direct and amplify T cell differentiation and expansion (Signal 3)<sup>126</sup>. Each of these three signals has a vital role in controlling the resulting phenotypes and function of the T cells. Strategies to optimize ACT include manipulation of these three key signals, direct modulation of downstream signalling pathways and co-delivery of immunomodulatory agents with T cells.

### 2.4.1 – Optimizing Signals 1-2

Various approaches to manipulate TCR signalling and relevant T cell co-stimulatory pathways have been explored to obtain enough CAR-T cells with favourable phenotype profiles, including the use of soluble agonistic antibodies and artificial antigen presenting cells (aAPCs) (Figure 1.3). The most extensively studied combination is two antibodies targeting CD3 and CD28. Early reports found that anti-CD3 and anti-CD28 immobilized onto beads induced higher TCR expression and increased cytotoxicity against tumor cells compared with soluble agonistic anti-CD3/CD28 antibodies<sup>127</sup>. The material from which aAPCs are constructed affects the final memory profile of T cells, with certain materials preferably generating T<sub>CM</sub>-concentrated populations<sup>127,128</sup>. The size and shape of the aAPC have also been demonstrated to affect CAR T cell generation. For example, a large, continuous surface area on the  $\mu\text{m}$ -scale yields sufficient receptor engagement to form cell interactions that support proliferation<sup>129</sup>. Moreover, materials

with high aspect ratios, such as carbon nanotubes and mesoporous silica rods, promote expansion by increasing cell interactions on the longer-axis of the geometry<sup>130–133</sup>.

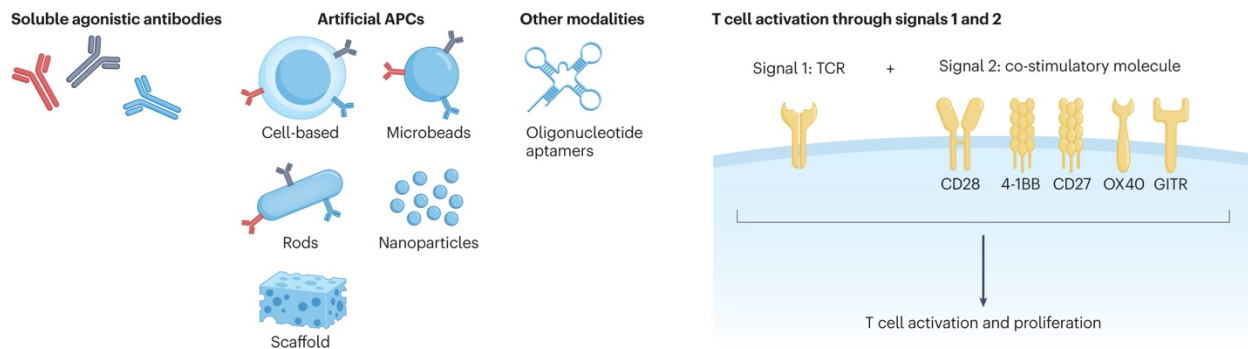


**Figure 2.3, Controlling CAR-T phenotype by modulating the 3 signals for T cell activation.** Soluble agonistic antibodies and artificial antigen-presenting cells (aAPCs) are commonly used to provide Signals 1&2. aAPCs include non-APC cells with enforced expression of stimulatory molecules, microbeads, rods, nanoparticles or scaffolds conjugated with stimulatory antibodies. Other modalities, such as oligonucleotide aptamers, have also been used to provide Signals 1&2 to T cells. TCR, T cell receptor.

The duration of CD3/CD28 co-stimulation also affects the final memory profile of T cells, with short stimulations (< 48 hrs) resulting in a preferable T<sub>SCM</sub> phenotype<sup>134</sup>. Similarly, shortening TCR stimulation later in the response (for example, after 7 days) favours memory T cell generation<sup>135–137</sup>. Receptor clustering, which allows the formation of immune synapses, is supported either with the use of flexible polymers and lipid bilayers to facilitate surface ligand mobility, or with micro-patterning methods to mimic ligand positioning in natural APCs<sup>130,138–140</sup>. These factors could also be relevant for other co-stimulatory pathways besides CD28.

A variety of other agents, beyond CD28, have been explored as co-stimulatory molecules. For example, 4-1BB stimulation preferentially expands antigen-reactive memory cells, induces more

cytolytic activity, prolongs T cell persistence and supports function upon re-exposure to antigen<sup>141–143</sup>. Interestingly, 4-1BB co-stimulation also prolongs CD27 and CD28 expression and increases T cells' responsiveness to re-stimulation<sup>144,145</sup>. When used in conjunction with CD3/CD28 co-stimulation, 4-1BB co-stimulation retains central memory and effector memory populations that are crucial for successful adoptive cell transfers<sup>146</sup>. In addition to using aAPCs and adding soluble agonistic antibodies into culture medium, oligonucleotide-based aptamers that bind to 4-1BB have been developed and proven to be effective in activating T cells through 4-1BB<sup>147</sup>. These aptamers provide a potentially cheaper and easier-to-manufacture alternative to antibodies and could be developed to target other co-stimulatory signalling pathways.

The use of agonistic antibodies of other costimulatory molecules have been explored, including CD27, OX40 and GITR, although they have yet to be tested with aAPC systems. For example, CD27 co-stimulation shows comparable T cell expansion with 4-1BB co-stimulation, but activates memory populations with a bias towards CD8+ T cells<sup>148</sup>. OX40 co-stimulation prolongs survival and exhibit synergistic effects with 4-1BB<sup>149,150</sup>. One way to further improve ex vivo activation protocols could be to target multiple co-stimulatory pathways; however, an important caveat is that a balanced T<sub>SCM</sub> and T<sub>CM</sub> population is desirable, because products consisting solely of terminally differentiated T cells are likely to yield poorer clinical outcomes.

#### *2.4.2 – Optimizing Signal 3*

T cell expansion and differentiation can also be mediated by presenting various cytokines (Table 1). For example, IL-2, the first explored and most used cytokine in clinical and research settings, enhances T cell proliferation and clonal expansion in vitro and in vivo<sup>136,137</sup>. However, it can impair the antitumor function of adoptively transferred T cells by differentiating them to the

terminal T<sub>Eff</sub> state<sup>151,152</sup>. One family of cytokines that has drawn attention is  $\gamma_C$  cytokines, which signal through receptors that contain the common  $\gamma$  ( $\gamma_C$ ) chain subunit.  $\gamma_C$  cytokines, including IL-15, IL-7 and IL-21 generate and maintain CD8<sup>+</sup> memory T cells. IL-15 maintains T<sub>SCM</sub> populations while supporting proliferation, whereas IL-7 is indispensable to the survival and maintenance of naïve and memory T cells<sup>51,52</sup>. IL-21 arrests T cells at the T<sub>CM</sub> stage, stimulates anti-tumor responses and limits exhaustion<sup>53,153</sup>. Moreover, an IL-15 superagonist, a fusion protein of IL-15 and its high affinity receptor IL-15R $\alpha$ , has been a popular target in pre-clinical and clinical studies owing to its stronger T cell stimulation and longer half-life than regular IL-15<sup>154</sup>.

**Table 1. Modulating Signal 3 controls T cell phenotype**

	Cytokines	Function as Signal 3	References
$\gamma_C$ cytokines	IL-2	Potently enhances T cell proliferation and induces terminal differentiation of T cells into T <sub>Eff</sub>	144,151
	IL-7	Modulates survival of naïve and memory T cells	51,155
	IL-15	Supports T cell survival and maintains CD8 <sup>+</sup> T cell memory	51
	IL-15/IL-15R $\alpha$	Potently enhances proliferation of memory T cells, supports T cell survival and enhances secretion of anti-tumor cytokines	154

	IL-21	Arrests T cells at T <sub>CM</sub> and limits T cell exhaustion	53,153
Non $\gamma_C$ cytokines	IL-12	Promotes Th1 differentiation and enhances secretion of anti-tumor cytokines	156
	IFN- $\alpha$	Promotes Th1 differentiation and supports the generation and survival of CTLs and memory T cells	156
	IL-23	Supports proliferation of memory Th17 cells, improves T cell proliferation and limits exhaustion	85

Abbreviations: IL: interleukin, T<sub>EF</sub>: effector T cell, T<sub>CM</sub>: central memory T cells Th1: T helper 1 cell, Th17: T helper 17, CTL: cytotoxic T lymphocyte

Non  $\gamma_C$  cytokines, including IL-12, IFN- $\alpha$  and IL-23 have also been shown to affect CAR-T efficacy. For example, IL-12 supports Th1 differentiation and simulates the production of anti-tumor cytokines<sup>156</sup>. Similarly, IFN- $\alpha$  supports Th1 differentiation and promotes the survival of cytotoxic T lymphocytes and memory CD8<sup>+</sup> T cells while promoting CD8<sup>+</sup> T cell priming<sup>157</sup>. IL-23 supports the proliferation of memory T cells, especially Th17 cells, which induce strong anti-tumor activities<sup>85</sup>. Cytokine combinations have also shown synergistic effects. For example, IL-15, IL-21 and IL-7 used in different combinations to promote T<sub>N</sub> and T<sub>SCM</sub> populations with or without the presence of IL-2, and even selectively enrich memory T cells in late-stage

effector-dominated populations<sup>43,127,158–160</sup>. IL-12 has also been used with  $\gamma_C$  cytokines to induce highly activated memory T cells with potential for long-term survival<sup>160</sup>.

Despite their key functions, cytokine stimulation has limitations. For example, IL-12 generates potent anti-tumor response at the expense of favoring the production of fully differentiated T<sub>Eff</sub> cells<sup>161</sup>. Cytokines such as IL-17 and IL-23 can be anti-tumor in certain scenarios and pro-tumor in others. Moreover, many of these cytokines exhibit strong toxicity in cell cultures, especially at high concentrations. These effects can be attenuated by appropriately presenting cytokines in the context of Signal 1 and 2 in an aAPC system<sup>130,132,134,140</sup>. For example, these systems can be designed to provide local, sustained cytokine signaling with lower doses of cytokine compared to traditional one-time exposure to large amounts and are being used to define optimal timing of Signals 1, 2 and 3. However, irrespective of the approach, protocols need to be optimized in relation to the amount, timing and combination of cytokines for ex vivo T cell manufacturing.

#### *2.4.3 – Fine-tuning downstream signaling*

T cell phenotype can also be directly modulated by controlling signaling pathways downstream of T cell activation signals (Figure 1.4a). This strategy targets major pathways such as PI3K-AKT-mTOR, Notch, Wnt/ $\beta$ -catenin, MAPK/ERK and elements of overall T cell metabolism. Directly downstream of TCR signaling, the PI3K-AKT-mTOR pathway modulates T cell memory differentiation and metabolism and has been a commonly pursued target in adoptive T cell therapies. Blocking PI3Ks, Akt1/2 and mTOR, as well as the PIM kinase that regulates mTORC1, have all been shown to generate tumor-reactive T cells with T<sub>SCM</sub> and T<sub>CM</sub> properties, enhanced anti-tumor toxicity, elevated Th1 cytokine secretion and improved in vivo persistence in animal models and patient-derived samples<sup>162–171</sup>. Moreover, blocking PI3K $\delta$  and

Akt1/2 can rescue proliferation of exhausted T cells obtained from heavily pre-treated patients<sup>162,167</sup>. Interestingly, despite being directly downstream of TCR signaling, inhibitors of the PI3K-Akt-mTOR pathway have little effect on T cell proliferation and viral transduction, and their use is compatible with CAR-T manufacturing<sup>54,165-167</sup>. One potential caveat is that premature inhibition of TCR signaling pathways could also generate immunosuppressive regulatory CD4+ T cells<sup>172</sup>.

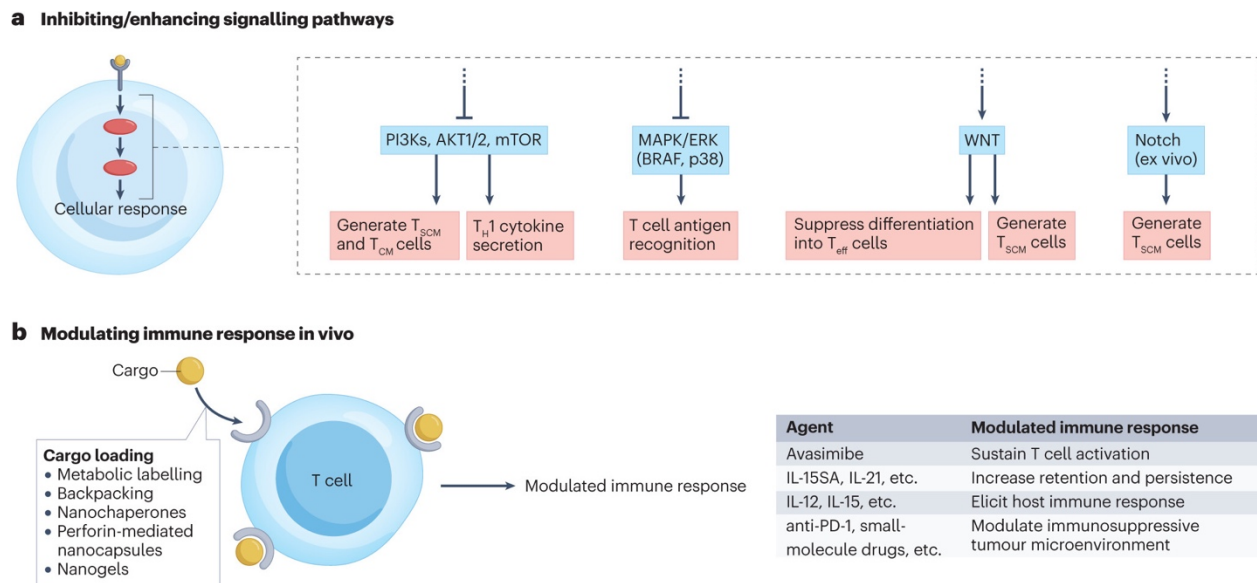


**Figure 2.4, Additional strategies to modulate CAR-T phenotype. a,** Inhibiting or enhancing intracellular signaling pathways can modulate T cell phenotype. Blocking the PI3K-AKT-mTOR pathway and other kinases that regulate the mammalian target of rapamycin (mTOR) (for example PIM) could generate T<sub>SCM</sub> and T<sub>CM</sub> cells with enhanced cytotoxicity, elevated cytokine secretion and improved in vivo persistence. Limiting glycolysis and modulating T cells towards oxidative phosphorylation (OXPHOS) improve T cell anti-tumor response. Notch activation induces T<sub>SCM</sub>-like cells but needs to be tightly regulated owing to Notch's role in cancer initiation and progression. Reinforcing Wnt signaling can generate T<sub>SCM</sub> cells. Inhibiting specific elements of MAPK/ERK can improve anti-tumor efficacy of T cells. T<sub>SCM</sub>, stem cell memory; T<sub>CM</sub>, central memory. **b,** Adoptively transferred cells can be modified to carry cargos that modulate their interaction with the host immune system by increasing retention, activating the host innate and adaptive immune system and diminishing exhaustion and immunosuppression. IL, interleukin; PD-1, programmed cell death protein 1.



These inhibitors function in part by reducing glycolysis, guiding T cells toward oxidative metabolism and maintaining T cells in a less differentiated state that is less prone to exhaustion<sup>54,162,166,171</sup>. Despite inhibiting T cells from gaining effector functions, blocking aerobic glycolysis does not abrogate T cell proliferation or survival<sup>105</sup>. In general, limiting glycolysis and modulating T cells towards oxidative phosphorylation (OXPHOS) and fatty acid metabolism during ex vivo expansion can improve anti-tumor responses in vivo<sup>173–175</sup>. The media used for ex vivo T cell culturing typically has non-physiological levels of metabolites, and media manipulation could also re-program T cell metabolism<sup>174,176</sup>. For example, supplementing L-arginine enhances T cell survival and anti-tumor activity, whereas adding acetate augments acetylation and enhances effector functions when T cells are under stress<sup>177,178</sup>. The impact of other metabolites and their optimal dosage are yet to be explored.

Other pathways explored to modulate T cell phenotype include Notch, Wnt/ $\beta$ -catenin and MAPK/ERK. Notch activation induces potent anti-tumor responses in murine fibrosarcoma and lung carcinoma models<sup>179,180</sup>. Co-culturing T cells with Notch ligand-expressing stromal cells or with a Notch-ligand containing agent induces T<sub>SCM</sub>-like cells with high proliferative potential and anti-tumor activities in murine leukaemia and lymphoma models<sup>181,182</sup>. However, Notch has also been shown to be involved in cancer initiation and progression, and inhibitors and antibodies against Notch have been widely explored as anti-tumor treatments<sup>183</sup>. Therefore, using Notch to modulate T cell phenotype can only be applicable during ex vivo expansion, and the signalling needs to be tightly modulated to avoid pro-tumor activities after adoptive transfer. Wnt regulates CD8<sup>+</sup> stemness by suppressing differentiation into T<sub>Eff</sub> cells, and T<sub>SCM</sub> are generated by reinforcing Wnt signaling through inhibition of serine-threonine kinase glycogen synthase kinase-3 $\beta$  (Gsk-3 $\beta$ ) or Wnt3a<sup>46,184</sup>. Additionally, Wnt/ $\beta$ -catenin modulates the anti-tumor

activities of Th17 CD4+ T cells<sup>185</sup>. Finally, despite the risk of broad MAPK or ERK inhibition having detrimental effects on T cell proliferation and function, inhibiting specific elements of the signaling pathway, such as BRAF and p38, could enhance T cell antigen recognition and improve anti-tumor efficacy<sup>186-188</sup>.

Overall, these studies demonstrate that T cell phenotype can be tuned by directly modulating signaling pathways downstream of T cell activation. However, given that each of these pathways control multiple cellular functions, and could play drastically different roles at different time points or in different cell types, caution needs to be taken when modulating T cell phenotypes through direct manipulation of these pathways.

#### *2.4.4 – Modulating ACT in vivo*

Different strategies are also being explored to directly influence CAR-T in vivo retention, increase engagement with the host immune system or overcome the immunosuppressive TME (Figure 1.4b). For example, metabolism-modulating drugs such as Avasimibe inserted into T cell membranes prior to adoptive transfer induce sustained T cell activation upon recognition of tumor antigens in murine melanoma models<sup>189</sup>. Conjugating IL-12 onto T cells via metabolic labelling activates host immune response, induces antigen spreading, and significantly reduces the number of T cells needed to achieve a complete response in murine melanoma and xenograft lymphoma models<sup>190</sup>. Furthermore, local delivery of IL-12 and IL-15 in conjunction with CAR-T cells activates host dendritic cells, encourages presentation of tumor antigens, re-programs immune-suppressive cells in the TME and increases anti-tumor efficacy in murine models of ovarian peritoneal carcinomatosis and transfectoma<sup>191-193</sup>. In addition to genetically modifying CAR T cells to secrete cytokines, these findings support the concept of loading cytokines onto T

cells during manufacturing through metabolic labelling, backpacking, nanochaperones, perforin-mediated nanocapsules and other methods that have proven effective in T cells or other immune cells<sup>194–197</sup>. In support of this concept, loading T cells during manufacturing with magnetic nanoparticles or nanogels containing IL-15 and IL-21 increases retention and persistence of T cells *in vivo*<sup>198,199</sup>. Moreover, backpacking large amounts of the IL-15 superagonist onto T cells (up to 8 µg per 10<sup>6</sup> cells) boosts proliferation of adoptively transferred cells, thereby increasing anti-tumor efficacy by expanding T cell number at peak response<sup>194</sup>. Similarly, inactivating PD-1 or TGFBR in transduced T cells or delivering small-molecule drugs or biologics (such as anti-PD-1) as T cells enter tumors helps adoptively transferred T cells and T cells residing in tumors to overcome immunosuppression and exhaustion<sup>200–204</sup>. Delivery of demethylation agents can counter the increased methylation associated with CAR-T cells post infusion while maintaining memory, recall potential and prevent exhaustion over time<sup>205,206</sup>.

Strategies that do not require CAR-T cells to be genetically modified could be readily integrated into the current CAR-T manufacturing process. Importantly, the therapeutic window is essential to the success of these approaches. In two separate studies, genetic expression of IL-12 (in TILs with nuclear factor of activated T-cells (NFAT)-controlled inducible design) or expression of a dominant negative TGFBR in conjunction with a prostate-specific membrane antigen (PSMA)-targeted CAR, potentially efficacious clinical outcomes were compromised by toxicity<sup>203,207</sup>. We look forward to seeing clinical data from additional approaches modulating ACT that enhance T cell function and/or overcome a suppressive TME without increased risk of toxicity.

#### 2.4.5 – Rapid manufacturing and in vivo expansion

Recent efforts have focused on eliminating or decreasing the ex vivo activation and manufacturing time, and in vivo cell expansion to produce more active products (Box 1)<sup>208</sup>. These approaches benefit from a shorter ‘vein-to-vein’ time required to administer therapy to patients who often have aggressive cancers<sup>50</sup>. For example, aAPCs based on mesoporous silica rods promote up to 10-fold greater expansion than beads currently used in the clinics, thus reducing the time needed to obtain sufficient cells for infusion<sup>130</sup>. Lentiviral transduction efficiency is lower in non-activated T cells compared to activated ones, however, this limitation can be partially overcome by combining changes to the culture media (for example, 3-6 hr serum starvation) and the surface area to volume ratio of the cell containers (for example increasing the culturing surface area to up to 4-fold while maintaining the culturing volume). Twenty-four-hour transduction of T cells using these approaches led to improved anti-tumor activity in a mouse model of leukemia<sup>57</sup>. Similarly, 24-hour transduction of T-cells in combination with T-cell activation generate anti-CD19 (YTB323) and anti-BCMA (PHE885) CAR-T cells in two ongoing Phase 1 clinical trials (NCT03960840 and NCT05172596)<sup>209,210</sup>. Manufacturing was completed in under two days, and fixed cell doses ranging from 2.5 to 30 million transduced cells were tested. In vivo expansion, preservation of a T<sub>N</sub> and T<sub>SCM</sub> phenotype and complete response were observed at all dose levels tested, but whether this will lead to improved persistence and long-term efficacy remains to be seen.

The possibility of directly transducing CAR-T cells in vivo has also been explored in animal models. For example, host T cells can be transduced with CAR vectors either by directly injecting CAR-vector-bearing viruses into the animal using CAR-encoding mRNAs carried in

polymer or lipid nanoparticles, or by activating and transducing T cells in virus-bearing scaffolds<sup>211-215</sup>. These methods produce potent CAR-T cells with equal antitumor efficiency as those manufactured *ex vivo* while benefiting from only one viral delivery. *In vivo* production of CAR-T cells reduces the time, cost and labor associated with traditional CAR-T manufacturing by eliminating the steps for T cell isolation, modification and expansion. However, challenges remain in controlling the specific cell types modified by viruses *in vivo*. Moreover, most CAR-T cells produced *in vivo* are tested in hematologic tumor models. Their potency against solid tumors remains to be tested, but they are likely to face similar challenges as *ex vivo* approaches. Given the small numbers of cells infused, these rapid manufacturing approaches allow repeated dosing, which could help overcome issues with CAR-T cell persistence and exhaustion.

### **Box 1: Technology transfer considerations**

The translation of technologies associated with the chimeric antigen receptor T cells (CAR-T) manufacturing processes, specifically with relation to activation and expansion, are still in the early development phase. Scaling up CAR-T production with automation is an urgent need. Automated platforms promise greater cell viability, higher transduction efficiency, lower variation in cell subsets and have been successfully used in clinical trials<sup>276</sup>. In addition to increasing CAR-T product consistency, automated systems could also reduce dependency on technicians and scientists, facilitating broader commercialization and patient accessibility while reducing the manufacturing time by 30-40%.

Furthermore, developing end-to-end production systems could facilitate the establishment of decentralized CAR-T manufacturing. Current CAR-T therapies use a centralized manufacturing model, where one manufacturing site that meets good manufacturing practice (GMP) requirements serves multiple clinical centers<sup>277</sup>. Each manufacturing site generally provides only one step, but rarely all of the steps of the entire CAR-T manufacturing process. Although this centralized system might streamline production of parallel products from multiple patients, it also considerably increases logistical and distribution challenges. Modularization, miniaturization and integration of steps including, but not limited to, viral production, ex vivo T cell transduction, activation and expansion and quality control in the CAR-T manufacturing process allow an automated, end-to-end solution for manufacturing CAR-T at the treatment site. This decentralization could increase total CAR-T production capacity and reduce the time and cost associated with CAR-T production while permitting more precise and personalized treatments. Furthermore, allowing healthcare sites to produce CAR-T products could also promote competition in the CAR-T therapy market, thereby reducing manufacturing cost.

## **2.5 - Future Directions**

ACT and CAR-T therapies have demonstrated utility for hematological cancers, but face limitations in the treatment of solid tumors. Emerging data from pre-clinical research and clinical trials have improved our understanding of the correlation between T cell phenotype and the final clinical outcome. As a result, various strategies to control T cell phenotype and composition in CAR-T products are being explored.

Although the impact of specific signaling pathways on T cell phenotype have been studied, T cell mechanosensitivity remains largely unexplored. Beyond the catch-bond status of the TCR, physical cues from the microenvironment are also believed to regulate T cell phenotype and function. The lymph nodes in which T cells are primed exhibit distinct mechanical properties during disease and vaccination, and T cells subsequently traffic through blood and tissues of varying stiffness. For example, adhesion on stiff substrates enhances T cell proliferation, formation of the immune synapse and T cell activation<sup>216–218</sup>. These substrates also promote the generation of Th1 CD4<sup>+</sup> T cells and production of anti-tumor cytokines<sup>217,218</sup>. Similarly, culture of T cells in three-dimensional (3D) compared to 2D substrates with matching stiffness increases proliferation and enhances activation and cytokine secretion<sup>218</sup>. Other physical parameters of the extracellular matrix, including porosity and viscoelasticity (which describes a material's time-dependent mechanical response to applied stresses and strains), could influence T cell proliferation and activation. However, little effort has been made to investigate these variables in the context of T cell manufacturing.

As a highly personalized therapy, CAR-T cells exhibit patient-to-patient variability in genetics, disease entity, tumor burden and treatment history (Box 2). As a result, individual patients might benefit from different CAR-T products with diverse phenotypic profiles and ex vivo culturing protocols<sup>219</sup>. Models that predict patient prognosis could therefore be useful<sup>220</sup>. More importantly, models and algorithms that predict and guide the production of CAR-T products to achieve the optimal T cell phenotype based on treatment history and patient T cell composition, could be essential to further optimizing the production and efficacy of CAR-T cells.

## **Box 2: Translational considerations**

A number of challenges currently limit the translation of adoptive T cell transfers (ACT), and chimeric antigen receptor T cells (CAR-T) in particular. CAR-T can induce substantial side effects, including cytokine release syndrome (CRS) and immune effector cell-associated neurotoxicity syndrome (ICANS) after infusion into the patient<sup>278</sup>. Currently, treatment of CRS mainly involves Tocilizumab (interleukin (IL)-6R antagonist) and steroids<sup>279</sup>. Other treatments, such as Siltuximab (anti-IL-6 mAb) and Anakinra (IL-1 antagonist) are also being explored, but their clinical efficacy remains uncertain<sup>279</sup>. Models and prediction algorithms are being built to identify biomarkers that predict the severity of post-treatment CRS and ICANS<sup>280,281</sup>.

One challenge with scaling up CAR-T production is the transition of patient materials across many collection, manufacturing and treatment sites, sometimes even across continents<sup>50</sup>. Hospitals often use product identifiers different from those of manufacturers, and patient and product information might be lost throughout the process<sup>282</sup>. Establishing a digital supply chain in which all stakeholders contribute and keep track of the product and its performance could reduce lead time and ensure accurate delivery of CAR-T products<sup>283</sup>.

Translation of CAR-T products also faces regulatory burdens. Regulatory guidelines for cell and gene therapies are not synchronized across countries and regions<sup>284</sup>. The more countries are involved in a clinical trial, the more robust the manufacturing process needs to be to meet all requirements, resulting in a longer and more expensive process. Regulations on manufacturing and clinical trials within each country are also becoming stricter, resulting in prolonged approval times and contributing to the high cost of CAR-T therapy<sup>285</sup>. This increase in administrative work could also prevent dying patients from gaining access to newer treatments<sup>285,286</sup>. Therefore, strategically and responsibly reducing requirements, time and paperwork associated with regulatory approval could potentially produce a net positive effect on cancer patients<sup>285</sup>.

There is also potential to use ACT and CAR-T therapies in conjunction with other modalities of cancer treatment. For example, chemotherapy enhances CAR-T recruitment to solid tumors, whereas low-dose radiation therapy sensitizes solid tumors to CAR-T cells, promotes T cell infiltration and increases T cell effector function<sup>121,221</sup>. Within the immunotherapy space, a combination of CAR-T and immune checkpoint inhibitors (ICI) can provide synergistic effects;



CAR-T therapy induces the tumor immune infiltrate needed for response to ICI, whereas ICI reduces CAR-T exhaustion and promote proliferation and functional capabilities<sup>222,223</sup>. ACT and CAR-T have also been explored in combination with oncolytic virotherapy (OV), which employs genetically engineered viruses with preferred replication in tumor cells. OVs support ACT by converting cold tumors into hot ones, attracting T cells to localize to and infiltrate the tumor, and activating the patient's innate immune response<sup>224,225</sup>. Overall, combinations with other cancer treatments are promising, but the details, such as timing, dosage, applicability to specific patients and tumor types, still needs to be established through extensive pre-clinical studies and clinical trials.

ACT and CAR-T therapies have led to long-term, durable immunity against hematological malignancies. It is expected that the growing knowledge on ACT and CAR-T will allow manufacturing processes to equip these cells to combat the multiple obstacles they face against solid tumors, thereby expanding their clinical utility (Box 3).

### **Box 3: Low-resource considerations**

CAR-T therapy is currently complex and requires dedicated facilities and expertise, making it difficult to implement in developing countries/regions and limiting its availability in low-income populations. One key challenge is access to qualified healthcare facilities. There is a substantial disparity in using CAR-T therapy across socioeconomic statuses. In the US, only 7.3% of CAR-T patients are from low-income neighborhoods<sup>287</sup>. Outside of the US, only a handful of patients are from middle- and low-income countries/regions, and CAR-T trials are absent in Africa, South America and India<sup>288</sup>. Measures are being taken to address these disparities. Digital healthcare solutions which allow patients to attend follow-up care online and coordinate with off-site centres closer to patient homes could reduce the travel burden experienced by low-income patients residing in regions where the therapy is not available. In India, startups are developing their own CAR-T therapies and using local bone marrow transplantation centres and local and cheaper labour to reduce the total treatment price<sup>288</sup>.

Furthermore, sophisticated infrastructures are required for good manufacturing practice (GMP) facilities, as well as for proper storage and distribution conditions. Unlike most vaccines, distribution of viral vectors and patient cells requires temperatures lower than -150°C. Cryopreservation is still considered a necessity for long-term storage, and the lack of reliable ultra-cold-chains (UCC) in mid- and low- income countries/regions pose considerable challenges to the transportation of live cell products. Expanding UCC networks in these locations requires funding, equipment and the expertise required to install and operate them after procurement<sup>289</sup>. One potential alternative is to use dry ice, which faces similar challenges to ultra-cold freezers and would not provide the same performance over the long run. Another solution is to develop biopreservation and cryopreservation media, which could help mitigate the risks associated with transportation or storage under suboptimal conditions and reduce cellular stress caused by repeated freeze-thaw cycles.<sup>290,291</sup>

### **Chapter 3: Cytokine conjugation to enhance T cell therapy**

This chapter was previously published as a research article in Liu, Y. *et al.* Cytokine conjugation to enhance T cell therapy. *Proc Natl Acad Sci U S A* **120**, e2213222120 (2023).

#### **3.1 – Outline**

This chapter presents an easily-integratable approach to enhance the efficacy of adoptive T cells and CAR-T cells by metabolically labeling T cells with unnatural sugar and conjugating anti-tumor cytokines onto T cells. Detailed protocols are in Appendix 2.1-2.4.

#### **3.2 – Abstract**

Adoptive T cell transfer (ACT) therapies suffer from a number of limitations (e.g., poor control of solid tumors), and while combining ACT with cytokine therapy can enhance effectiveness, this results in significant side-effects. Here, we describe a nanotechnology approach to improve the efficacy of ACT therapies by metabolically labeling T cells with unnatural sugar nanoparticles, allowing direct conjugation of anti-tumor cytokines onto the T cell surface during the manufacturing process. This allows local, concentrated activity of otherwise toxic cytokines. This approach increases T cell infiltration into solid tumors, activates the host immune system towards a Type 1 response, encourages antigen spreading, and improves control of aggressive solid tumors and complete blood cancer regression with otherwise non-curative doses of CAR-T cells. Overall, this method provides an effective and easily-integrated approach to the current ACT manufacturing processes to increase efficacy in various settings.

### 3.3 – Introduction

Adoptive cell transfer (ACT) of tumor-specific T cells has been shown to elicit tumor regression in patients in a variety of settings, but suffers from a number of limitations<sup>1-3,16</sup>. In these therapies, a patient's own T cells are typically isolated, activated and expanded *ex vivo*, and reinfused back into the patient. The therapeutic potential of ACT has been highlighted with the development of chimeric antigen receptor (CAR) T cell therapies, where T cells isolated from patients are genetically engineered to redirect their specificity against a tumor-specific cognate antigen<sup>20,21</sup>. However, while CAR-T therapies have been successful with certain hematological malignancies<sup>17,18</sup>, variable outcomes can result, and little success has been achieved to date with solid tumors due to poor T cell persistence and fitness, poor solid tumor penetration, and immunosuppression from the tumor microenvironment<sup>18,20,26,226</sup>.

A range of strategies have been explored to enhance adoptive T cell efficacy, including the design of CAR-T with a transgenic payload (TRUCKs), delivery vehicles for the ACT, and systemic delivery of anti-tumor cytokines and factors that modulate the immunosuppressive tumor-microenvironment. Although TRUCK CAR-Ts were effective at inducing response at lower dosages, the expression of the transgenic payload was not limited to the tumor, resulting in substantial systemic toxicity observable in all major tissues<sup>7,207,227,228</sup>. Various cytokines, including IL-2, IL-12, IL-21, IL-15 have been systemically administered in animal models and clinically to improve efficacy of ACT and CAR-T therapies<sup>1,3,229-233</sup>. However, systemic delivery leads to toxicity and the rapid development of lethal inflammatory syndromes<sup>229-231,234</sup>.

Additionally, the fast clearance rate of these agents and their untargeted distribution also resulted in minimal therapeutic activity in many clinical trials<sup>235</sup>. Local delivery of these agents has been

explored by backpacking cytokine onto T cells and other immune cells. However, these approaches required complicated processes to manufacture the backpacks and load the agents onto cells for delivery, resulting in prolonged manufacturing time in clinical use<sup>194,236,237</sup>. Additionally, backpacking strategies may impair physiological functions of T cells due to long-term occupation of functional molecules on T cell surfaces<sup>194</sup>.

Here, we demonstrate a simple and flexible approach to improve the efficacy of ACT therapies against solid tumors by conjugating anti-tumor cytokines directly onto T cells before adoptive transfers. T cells were metabolically labeled simply by adding nanoparticles comprised of unnatural azido sugars directly to the culture medium during cell expansion. This leads to labeling of the cellular glyocalyx with desired functional groups<sup>238–240</sup>. Anti-tumor cytokines were then directly added to washed T cells for conjugation via click chemistry onto cell surfaces. We demonstrate that this simple and easily scalable method increases T cell effector function *in vivo* after adoptive transfer, and can activate the endogenous immune system to encourage antigen spreading, allowing the recognition of additional tumor-specific antigens to enhance therapeutic efficacy.

### **3.4 – Results**

#### *3.4.1 – Nanoparticle-mediated metabolic labeling is efficient and durable, and doesn't affect T cell function or phenotype*

To conjugate cytokines onto T cells, T cells were first metabolically labeled with unnatural azido-sugar nanoparticles. G400 nanoparticles (G400 NP), a polymer of azido-sugar (n=400) derived from Ac<sub>4</sub>ManAz<sup>241</sup>, was directly added to T cell cultures (Figure 3.1a). After cellular uptake, G400 NP yields monomeric sugar-azide which is utilized in cellular metabolism, and is

integrated into membrane glycoproteins to provide azide groups on the T cell surface. DBCO-labeled cytokines were then added to washed T cells to conjugate cytokines onto T cell surfaces for downstream *in vitro* and *in vivo* use (Figure 3.1a). The ability of unnatural azido-sugars to metabolically label the glycocalyx of T cells was first explored. 72 hours after G400 NPs were added to T cell cultures, and T cells were found to be effectively metabolically labeled, as reflected by the increase in azide signaling. Furthermore, metabolic labeling was dose dependent, as reflected by cell-surface azide intensity quantification; saturation of the cell surface was reached at 200  $\mu\text{M}$  of G400 NPs (Figure 3.1b). Labeling was durable and efficient, as all T cells exhibited positive azide signal after 3 days, and more than 50% maintained a positive azide signal at least 9 days after initial labeling and G400 washout (Figure 3.1c-d). Importantly, exposure to high concentrations of G400 NP treatment didn't significantly alter T cell proliferation, survival nor phenotype (Figure 3.2). 200  $\mu\text{M}$  G400 NPs was used in all subsequent studies, as it provided maximum azido-labeling.

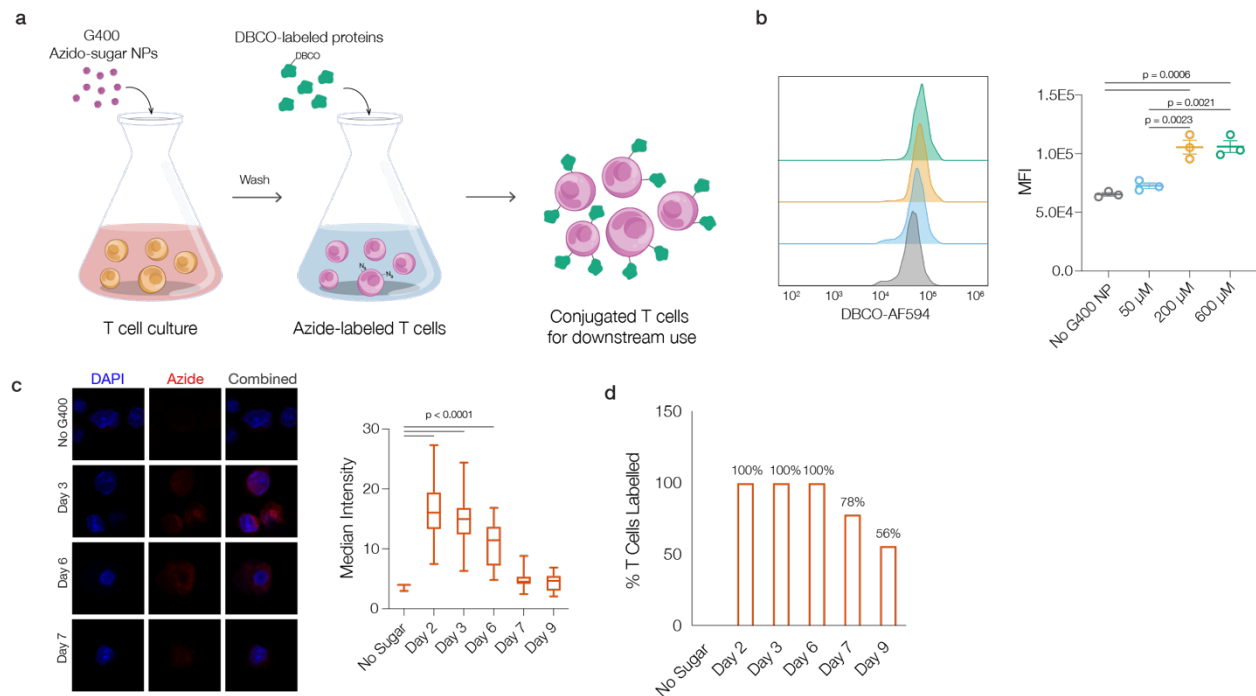


**Figure 3.1, Azido-sugar nanoparticles metabolically label T cells with cell-surface azide groups. a,** Schematic of metabolic labeling and cytokine conjugation of T cells with azido-sugar G400 NPs. Azido-sugar nanoparticles are directly added to T cell culture, enter T cells via endocytosis, and lead to presentation of azide group on T cell surfaces. After T cells are metabolically labeled, T cells are washed, and DBCO-labeled proteins (e.g. cytokines) directly added to produce conjugated T cells for downstream use. **b,** Median fluorescence intensity (MFI) of T cell surface azide signals after T cells are treated with G400 NPs at various concentrations for 3 days ( $n=3$ , one-way ANOVA and Tukey's test). **c,** Representative fluorescent imaging and quantification of maintenance of azide signal from T cells, and **(d)** percentage of T cells with positive azide signal over time. T cells were treated with 200  $\mu$ M G400 NP for 3 days, after which G400 NP in the medium was removed (Day 0) and T cells were subsequently cultured free of G400 NP (one-way ANOVA and Tukey's test).

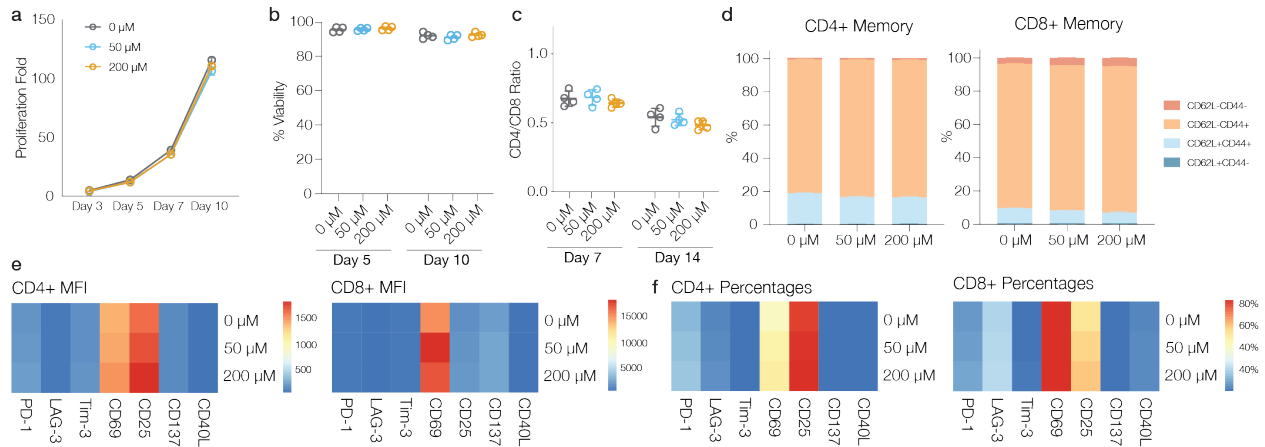


**Figure 3.2, Azido-sugar nanoparticles label T cells without affecting T cell function and phenotype.** **a**, Cell count, **(b)** viability, and **(c)** CD4/CD8 ratios in T cells incubated in various concentrations of G400 NP over time. **d**, Percentages of T cell populations expressing markers indicative of different memory phenotypes on day 10. **e**, MFI of and **(f)** percentage of positive cells for various activation and exhaustion markers T cells incubated in various concentrations of G400 NP on day 10 of culture. (n=3)

### 3.4.2 – Cytokines can be conjugated onto azido-labeled T cells and alter T cell function

The ability of azido-labeling to mediate targeted conjugation of DBCO-modified cytokines to T cells, and the impact of cytokine conjugation on the cells were next examined. A number of anti-tumor cytokines, including IL-12, IL-21, and TNF- $\alpha$ , were first modified with DBCO-sulfo-NHS, and the modification confirmed via MALDI-TOF (Figure 3.3). DBCO-modified cytokines maintained the majority of their activity (Figure 3.4). Bioactivity was inversely correlated with the degree of modification, and 2-3 DBCO molecules per cytokine were used in all further studies to maintain activity while allowing for efficient conjugation to T cells. DBCO-modified cytokines were simply added to the medium of azido-labeled T cells to allow conjugation via click reaction (30 minutes at 4°C), and T cells subsequently washed to remove non-conjugated cytokine. As expected, cytokine conjugation via click chemistry was dose-dependent, with higher concentrations of DBCO-cytokines resulting in higher percentage of cell-surface cytokine



(Figure 3.5). The amount of DBCO-IL-12 loaded onto T cells was then quantified with ELISA, and was positively correlated with the concentration of cytokines added to the cells (Figure 3.6a). With exposure to 200 ng/ml of IL-12, ~210 ng of IL-12 was conjugated per 1 million T cells (Figure 3.6a).

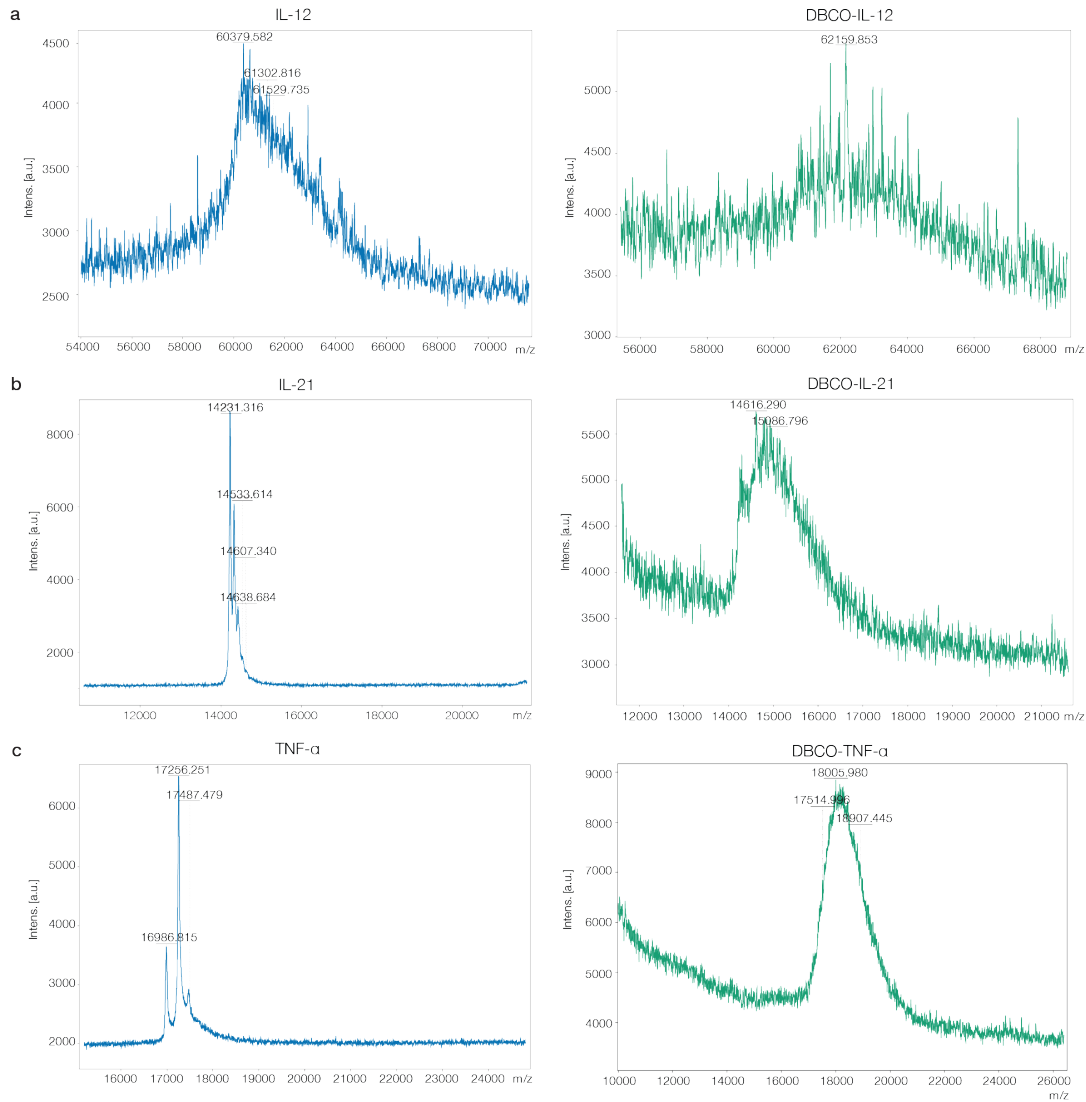


**Figure 3.3, MALDI-TOF spectrum for unmodified and DBCO-modified cytokines. a, IL-12, (b) IL-21, and (c) TNF- $\alpha$ .** Each cytokine molecule has an average of 2-3 conjugated DBCO groups.



**Figure 3.4, DBCO-modified cytokines exhibit slightly lower bioreactivity compared with unmodified counterparts.** Representative phenotyping data of showing CD4/CD8 ratio, and percentages of positive cells for various activation and exhaustion markers for T cells treated with various concentrations of soluble (a) DBCO- and unmodified- IL-12, (b) DBCO- and unmodified- IL-21, (c) DBCO- and unmodified- TNF- $\alpha$ . (n=3, two-way ANOVA test)

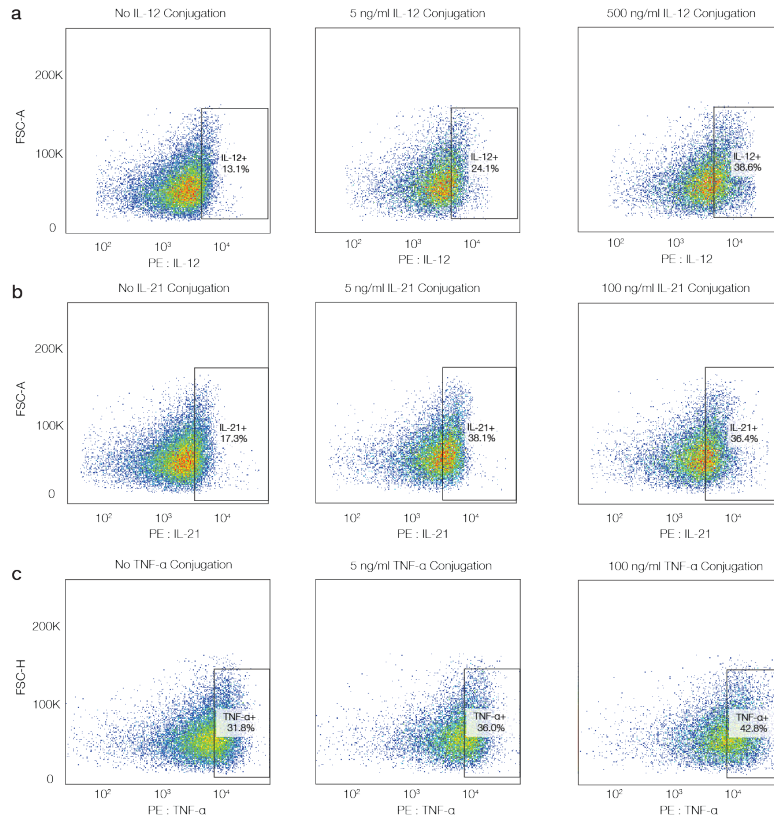


**Figure 3.5, DBCO-cytokine could be conjugated onto G400 NP treated T cells.** Flow cytometry data showing percentage of T cells with positive staining for (a) IL-12, (b) IL-21, and (c) TNF- $\alpha$  when conjugated with various concentrations of cytokines. Representative groups are T cells conjugated with DBCO-cytokine (“NP + Conjugated cytokine”; green), treated with continuously soluble cytokine (“NP + Continuous cytokine”; blue), or temporarily exposed to cytokine for duration of reaction time (“NP + Transient cytokine”; purple).

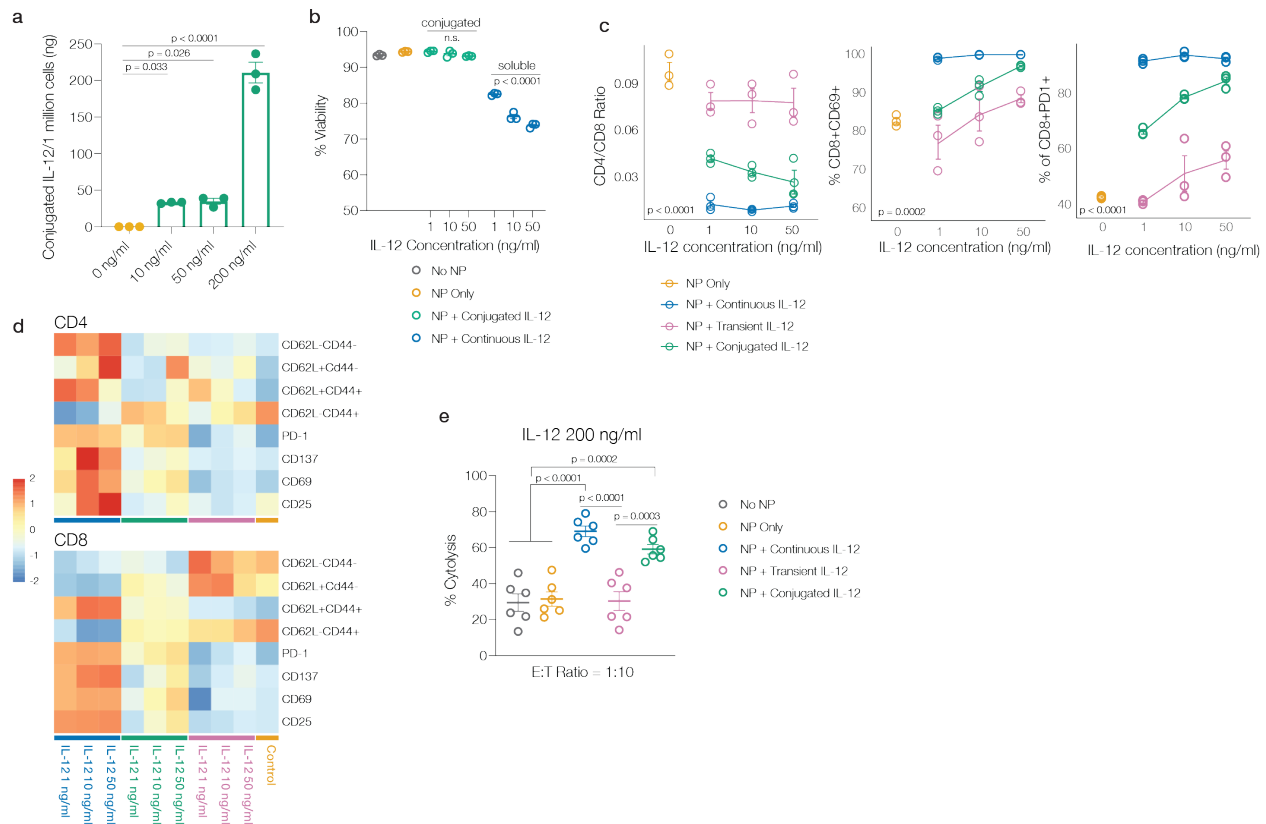


**Figure 3.6, Azido labeling of T cells allows conjugation of DBCO-cytokines to generate potent cytokine-dependent inflammatory phenotypes. a,** ELISA quantification of the amount of DBCO-IL-12 conjugated onto 1 million T cells at various DBCO-IL-12 concentrations (n=3, one-way ANOVA and Tukey’s test). **b,** Viability data for T cells receiving no IL-12, conjugated with DBCO IL-12, and presented with soluble IL-12 (no DBCO label) in media in *in vitro* culture for 7 days (n=3). **c,** Representative phenotyping data and **(d)** heatmap data showing memory phenotype markers and activation and exhaustion markers, for T cells conjugated with DBCO-IL-12 (“NP + Conjugated IL-12”; green), treated with continuously soluble IL-12 (“NP + Continuous IL-12”; blue), or temporarily exposed to IL-12 for duration of reaction time (“NP + Transient IL-12”, purple) at different cytokine concentrations cultured *in vitro* for 7 days (n=3, two-way ANOVA). **e,** Anti-B16-F10 tumor cell cytolytic activities of Pmel-1 T cells conjugated with DBCO-IL-12 (“NP + Conjugated IL-12”; green), treated with soluble IL-12 (“NP + Continuous IL-12”; blue), or temporarily exposed to IL-12 (“NP + Transient IL-12”, purple) (n=6, one-way ANOVA and Tukey’s test).

The impact of conjugated cytokines was next assessed. While continuous exposure to anti-tumor cytokines typically leads to significant cellular toxicity at high doses, DBCO-cytokines conjugated onto T cell exhibited minimal cytotoxicity (Figure 3.6b, Figure 3.7a). As a control, T cells were exposed to unmodified cytokines for the same amount of time used for the cytokine

coupling reaction, and then washed away (NP + Transient IL-12); this transient cytokine exposure had modest impact on long-term T cell phenotype. In contrast, conjugated cytokines (NP + Conjugated IL-12) directed T cell differentiation in a dose-dependent manner even at 7 days after conjugation, similarly but to a lesser extent than continuous exposure to unmodified cytokine at the same concentration as used in cytokine conjugation (NP + Continuous IL-12) (Figure 3.6c-d, Figure 3.7b-c). The change in T cell phenotype with cytokine conjugation translated to functional changes, as reflected by increased cytotoxicity of Pmel-1 T cells against B16-F10 melanoma tumor cells (Figure 3.6e). IL-21 and TNF- $\alpha$  were also successfully conjugated to T cells with the same approach (Figure 3.7). Considering the biofunction of DBCO-modified cytokines, the conjugation efficiency, and the ability for conjugated cytokines to direct T cell differentiation and cytotoxic activities, DBCO-IL-12 was used in subsequent studies. Overall, these findings demonstrate that cytokine conjugation leads to long-term impact on T cell phenotype, without the toxicity associated with continuous exposure to high concentrations of soluble cytokine.

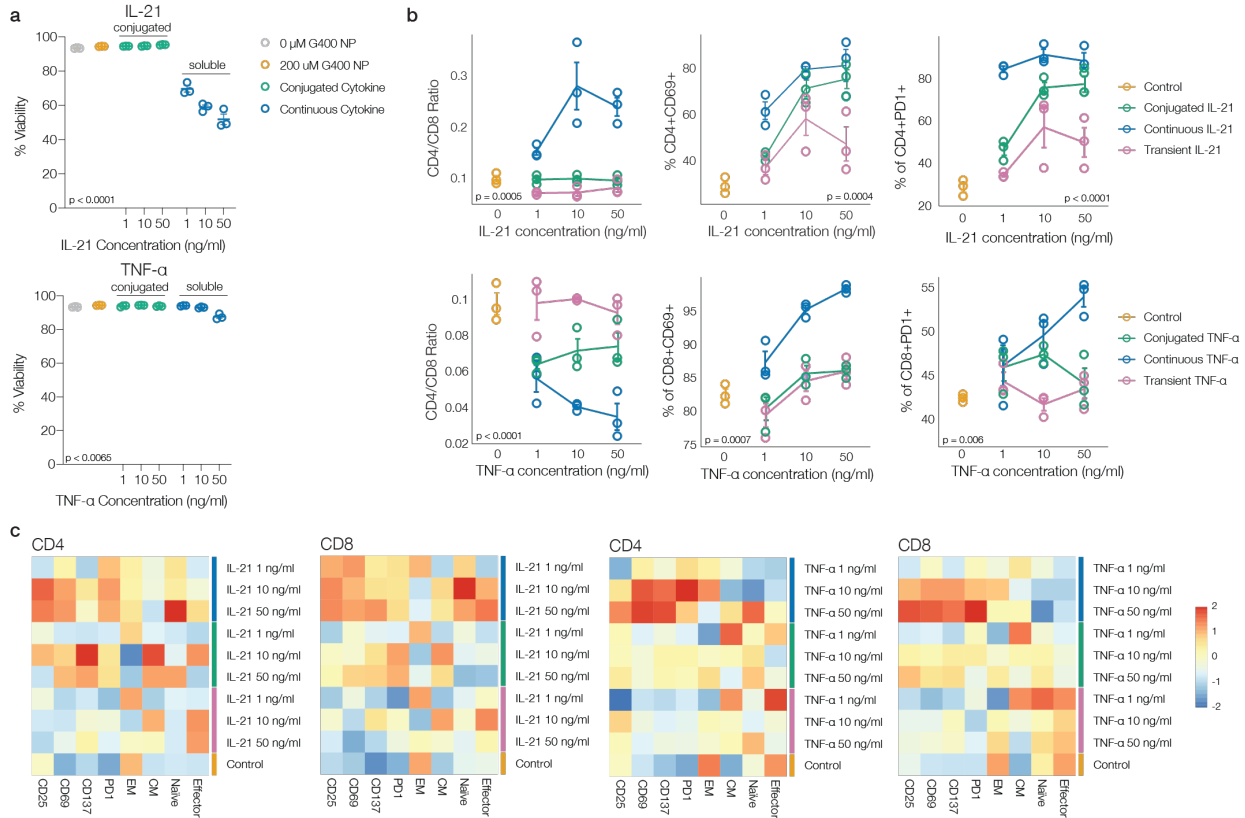


**Figure 3.7, Conjugating cytokines onto T cells affects T cell phenotype without inducing cytotoxicity.** **a**, Viability data for T cells receiving no IL-21 or TNF- $\alpha$ , conjugated with DBCO-IL-21 or DBCO-TNF- $\alpha$ , and presented with soluble IL-21 or TNF- $\alpha$  (no DBCO label) in media *in vitro* culture (n=3, two-way ANOVA test). **b**, Representative phenotyping data and **(c)** Heatmap data showing memory phenotype markers and activation and exhaustion markers, for T cells conjugated with DBCO-cytokine (“Conjugated cytokine”; green), treated with soluble cytokine (“Continuous IL-12”; blue), or temporarily exposed to cytokine for duration of reaction time (“Transient cytokine”, purple) at different cytokine concentrations (n=3, two-way ANOVA test). **d**, Cytolytic activities of Pmel-1 T cells conjugated with DBCO-cytokine, treated with soluble cytokine, or temporarily exposed to cytokine against B16-F10 tumor cells (n=3).

### 3.4.3 – Cytokine conjugation promotes T cell persistence and effector differentiation *in vivo*

Next, the effects of anti-tumor cytokine conjugation on T cells were examined *in vivo*, via the adoptive transfer of a sub-curative dose of Thy1.1+ Pmel-1 TCR-transgenic gp100-specific T cells in a B16-F10 melanoma model (Figure 3.8a). Adoptively transferred T cells conditions

included: unmodified T cells (T cells), T cells treated with G400 NPs and exposed to unmodified cytokine for the reaction time (NP + transient IL-12), T cells treated with G400 NPs and conjugated with DBCO-IL-12 (NP + Conjugated IL-12), or T cells treated with G400 NPs and injected together with the same amount of control, non-DBCO IL-12 (1.47  $\mu$ g) that was conjugated to T cells in the NP + conjugated IL-12 condition (NP + soluble IL-12). We did not observe weight loss over the course of treatment except in mice receiving unconjugated, systemic IL-12 (“NP + soluble IL-12”), indicating the IL-12 conjugated T cells were well tolerated by mice. The unmodified T cells alone, or T cells with soluble IL-12 offered minimal benefit in controlling tumor growth and prolonging mouse survival. However, IL-12 conjugation onto T cells significantly delayed tumor growth, and prolonged life span by ~50% (Figure 3.8c-d); it also significantly increased the circulating total number of T cells and number of adoptively-transferred tumor-specific T cells at peak response (Figure 3.8e-f). These effects were significantly greater than found in animals that received soluble IL-12 with ACT. Additionally, mice receiving T cells with IL-12 conjugation had a higher population of effector-like and effector-memory-like T cells, not only among the adoptively transferred T cells (Thy1.1+), but also among endogenous T cells (Thy1.2+, Figure 3.8g).

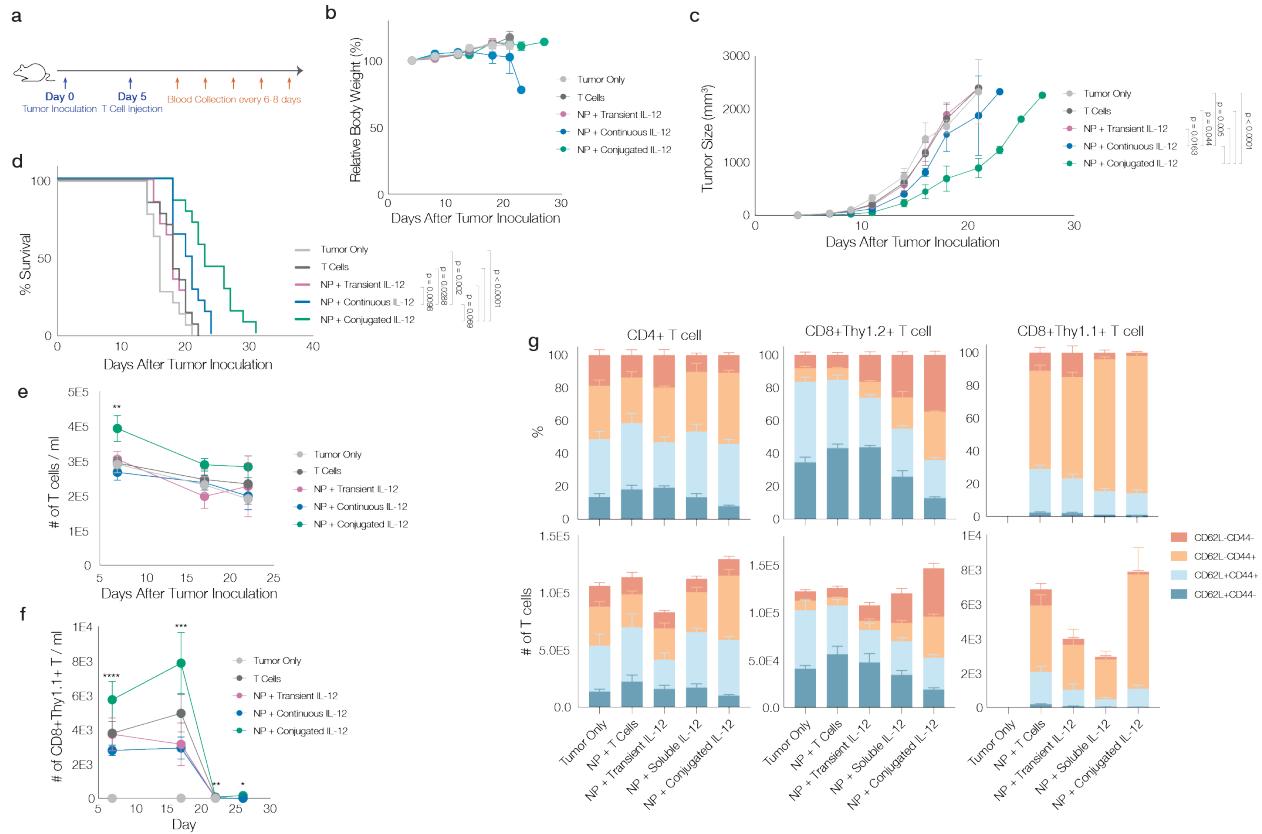


**Figure 3.8, Conjugating IL-12 on T cell surfaces increases the efficacy of subsequent adoptive T cell transfer therapies.** **a**, Schematic of animal study timeline; B16-F10 tumors were inoculated on Day 0, followed by tail vein injection of T cells on Day 5; blood was collected every 6-8 days for flow cytometry analysis after T cell injection. Animals were untreated (“Tumor only”; light grey), treated with T cells without labeling and without IL-12 conjugation (“T cells”; dark grey), treated with T cells metabolically labeled and transiently exposed to non-DBCO conjugated IL-12 prior to transfer (“NP + transient IL-12”; purple), treated with T cells that were labeled and transferred with the same quantity of soluble IL-12 (not DBCO conjugated) as was conjugated to T cells (“NP + continuous IL-12”; blue), or treated with T cells that were metabolically labeled and then conjugated with IL-12 prior to transfer (“NP + conjugated IL-12”; green). **b**, Body weight of different treatment groups over time, normalized to that of 4 days after tumor inoculation. **c**, Average tumor volume, and **(d)** mouse survival data over therapeutic study (n=7, Mantel-Cox test). **e**, Number of total T cells per 1 mL of blood and **(f)** number of CD8+Thy1.1+ Pmel-1 T cells per 1 mL of blood over therapeutic study (n=7, one-way ANOVA and Tukey’s test, \*p<0.05, \*\*p<0.01, \*\*\*p<0.001). **g**, percentage and count of T cells expressing markers indicative of different memory populations in blood on Day 17 (n=7). Total CD4+ T cells, host CD8+ T cells (Thy1.2+), and adoptively transferred CD8+ T cells (Thy 1.1+) were analyzed.



#### *3.4.4 – IL-12 conjugation enhances T cell solid tumor penetration and endogenous Th1 response*

As the increase in total T cell number in mice receiving NP + Conjugation was higher than the number of transferred Pmel-1 T cells, we next explored if the adoptively transferred T cells activated the endogenous immune system. Nine days after adoptive transfer of T cells, dendritic cells (DCs) were increased in tumors in all conditions (Figure 3.9a). However, IL-12 conjugation significantly increased both the absolute count of T cells infiltrating tumors, and the average T cell count when normalized to tumor volume, as compared to the other conditions (Figure 3.10a, Figure 3.9b). This increase was observed in both CD4<sup>+</sup> T helper cells and CD8<sup>+</sup> cytotoxic T cells (Figure 3.10b-c). IL-12 conjugation also significantly increased the number of antigen-specific Pmel-1 T cells in the tumor and tdLNs (Figure 3.10d-e). It is worth noting that the increase in total influx of T cells into the tumor (Figure 3.10a) is far greater than the increase in number of transferred Pmel-1 T cells (Figure 3.10d). Additionally, IL-12 conjugation also led to larger spleens (Figure 3.9c) as well as an increased percentage of Thy1.1<sup>+</sup> Pmel-1 T cells in tdLNs and spleens (Figure 3.10e, Figure 3.9d-e).

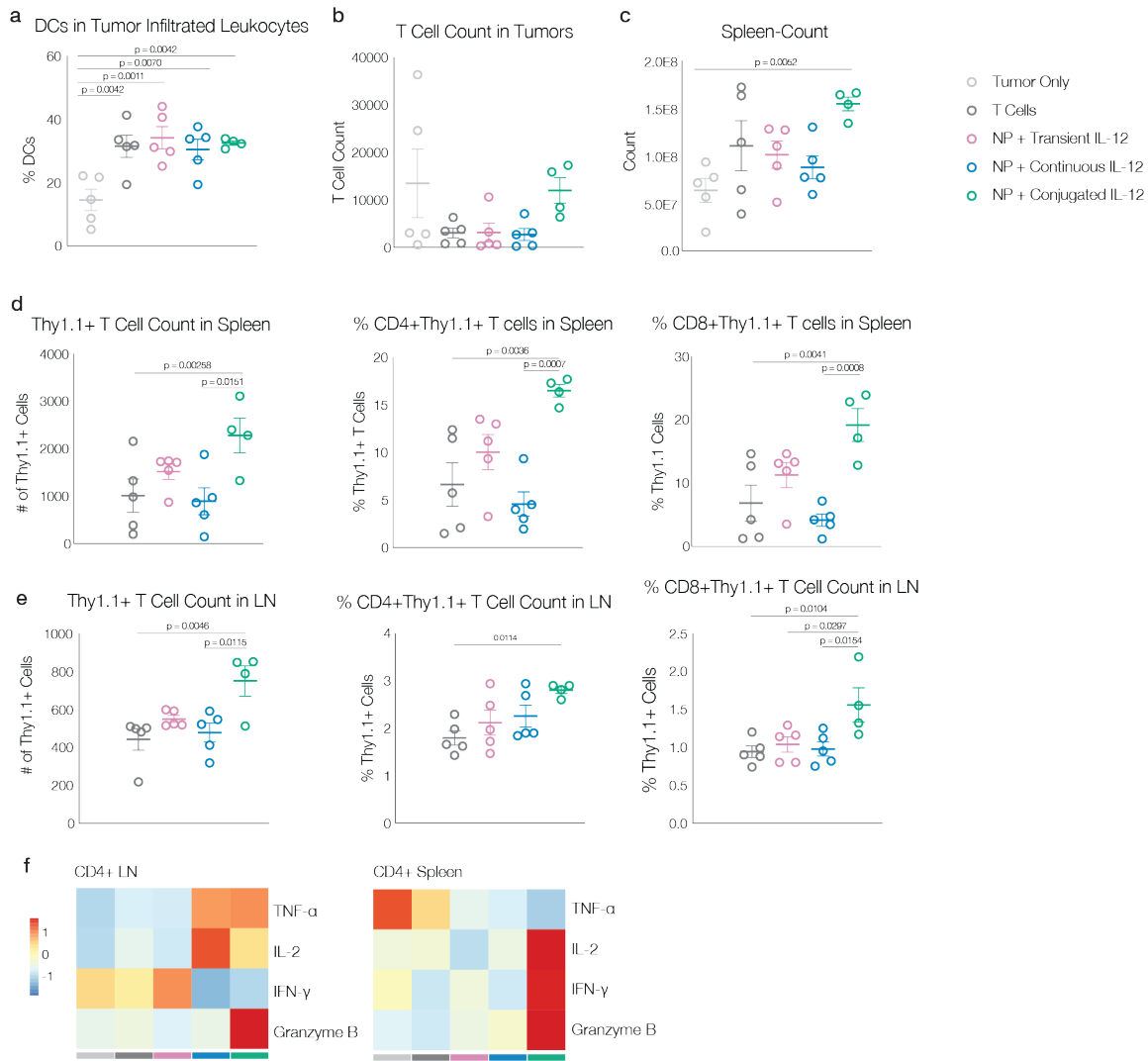


**Figure 3.9, Conjugating IL-12 on T cell surfaces increases T cell infiltration in solid tumors, increases antigen presentation, and promotes antigen spreading.** **a**, percent of DC cells in tumor infiltrated leukocytes (n=4-5). **b**, total T cell count in tumors (n=4-5). **c**, total number of leukocytes in spleen (n=4-5). **d**, total number of Thy1.1+ Pmel-1 T cells, and percent of CD4+ and CD8+ Thy1.1+ T cells in spleen (n=4-5). **e**, total number of Thy1.1+ Pmel-1 T cells, and percent of CD4+ and CD8+ Thy1.1+ T cells in tumor draining lymph nodes (n=4-5). **f**, heatmap of average expression level of Th1 cytokines in CD4+ T cells in lymph nodes and spleen after isolation and *ex vivo* antigen stimulation (n=5). Animals were untreated (“Tumor only”; light grey), treated with CAR-T cells without labeling but without IL-12 conjugation (“CAR-T”; dark grey), treated with CAR-T cells metabolically labeled and transiently exposed to non-DBCO conjugated IL-12 prior to transfer (“NP + transient IL-12”; purple), treated with CAR-T cells that were labeled and transferred with the same quantity of soluble IL-12 (not DBCO conjugated) as was conjugated to CAR-T cells (“NP + continuous IL-12”; blue), or treated with CAR-T cells that were metabolically labeled and then conjugated with IL-12 prior to transfer (“NP + conjugated IL-12”; green). (Statistical analyses performed with one-way ANOVA and Tukey’s test)

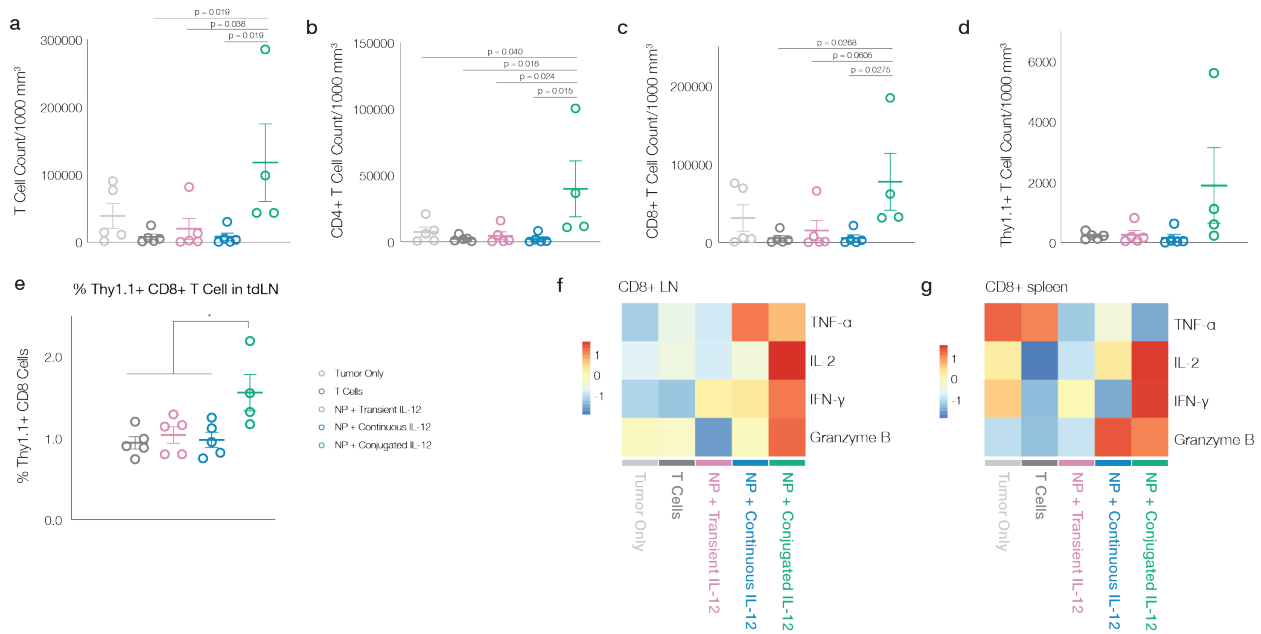


**Figure 3.10, Conjugating IL-12 on T cell surfaces increases T cell infiltration in solid tumors and effector function.** **a**, Total number of T cells per 1000 mm<sup>3</sup> tumor (n=5). **b**, Number of total CD4+ and **(c)** CD8+ T cells per 1000 mm<sup>3</sup> tumor (n=5). **d**, Number of transferred CD8+Thy1.1+ T cells per 1000 mm<sup>3</sup> tumor (n=5). **e**, Percentage of transferred Thy1.1+ CD8+ T cells among all T cell in lymph nodes (n=5). **f**, heatmap of average expression level of Th1 cytokines in CD8+ T cells isolated from lymph nodes and **(g)** from spleen following ex vivo antigen restimulation and FACs analysis (n=5). Animals were untreated (“Tumor only”; light grey), treated with T cells without labeling and without IL-12 conjugation (“T cells”; dark grey), treated with T cells metabolically labeled and transiently exposed to non-DBCO conjugated IL-12 prior to transfer (“NP + transient IL-12”; purple), treated with T cells that were labeled and transferred with the same quantity of soluble IL-12 (not DBCO conjugated) as was conjugated to T cells (“NP + continuous IL-12”; blue), or treated with T cells that were metabolically labeled and then conjugated with IL-12 prior to transfer (“NP + conjugated IL-12”; green); all data was collected 9 days after adoptive T cell transfer. All statistics were calculated with one-way ANOVA and Tukey’s test, \*p<0.05.

To better understand the function of T cells in the presence of tumor antigens, isolated T cells from spleen and tdLNs were co-cultured with B16-F10 melanoma cells for 4 hours and were stained for intracellular cytokines. In mice receiving Pmel-1 T cells with IL-12 conjugation, both CD4+ and CD8+ T cells isolated from tdLNs and spleens demonstrated higher expression levels of cytotoxic granzyme B and Th1 cytokines than T cells in the other experimental conditions (IL-2, IFN- $\gamma$ , etc.) (Figure 3.10f-g, Figure 3.9f). Additionally, the increased production of IFN- $\gamma$

could also induce increased expression of CXCL9 and CXCL10 in surrounding monocytes and improve T cell recruitment into the tumor<sup>242</sup>, which may explain the significant increase in total T cell infiltration in solid tumors (Figure 3.10a, 3.10d).

#### *3.4.5 – IL-12 conjugation to T cells activated endogenous dendritic cells and led to antigen spread*

To further understand the impact of IL-12 conjugated Pmel-1 T cells, the phenotype of tdLN DCs and antigen spread were analyzed. Mice receiving IL-12 conjugated T cells had significantly higher MHC-II expression on DCs in tdLNs than found in other conditions (Figure 3.11a-b). Additionally, DCs in spleen also demonstrated higher levels of the co-stimulatory molecule CD86 (Figure 3.11c-f) in both cDC1 and cDC2, suggesting higher levels of DC activation with IL-12 conjugation, better cross-presentation to CD8<sup>+</sup> cytotoxic T cells, and better activation of CD4<sup>+</sup> T cell responses. B16-OVA melanoma tumors were next inoculated in mice (Thy1.2<sup>+</sup>) for 5 days before Thy1.1<sup>+</sup> Pmel-1 T cells were adoptively transferred intravenously. Tumor growth and survival curve were similar to those previously observed in B16-F10 models, where IL-12 conjugated Pmel-1 T cells significantly controlled tumor growth and extended life span (Figure 12a-b). While there were initially few OVA-specific circulating T cells in any condition, a significant increase was found at day 7 in mice receiving IL-12 conjugated T cells, compared to the other conditions (Figure 3.11g-h, Figure 3.12c-d).

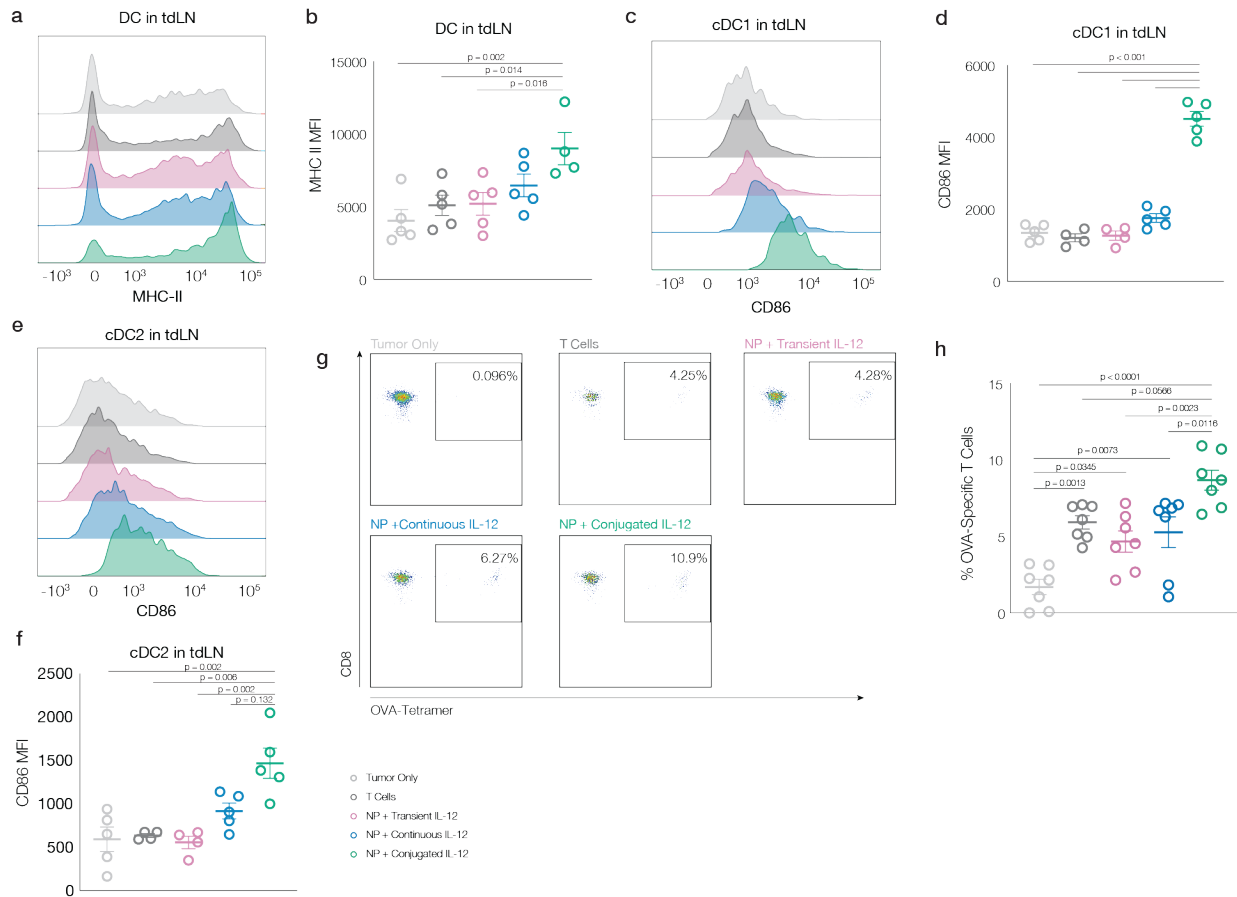


**Figure 3.11, Conjugating IL-12 on T cell surfaces activates host dendritic cells, increases antigen presentation, and promotes antigen spreading.** **a**, Representative flow cytometry histograms, and **(b)** summary MFI data for MHC-II expression in dendritic cells in tumor draining lymph nodes (n= 4-5). Representative flow cytometry histograms, and summary MFI data for CD86 expression in cDC1 **(c, d)** and cDC2 **(e, f)** in tumor draining lymph nodes (n= 4-5) 9 days after T cell adoptive transfer. **g**, Representative flow cytometry plots and **(h)** summary flow cytometry data for OVA-specific CD8+ T cells on Day 10 after T cell adoptive transfer (n= 7). Animals were untreated (“Tumor only”; light grey), treated with T cells without labeling and without IL-12 conjugation (“T cells”; dark grey), treated with T cells metabolically labeled and transiently exposed to non-DBCO conjugated IL-12 prior to transfer (“NP + transient IL-12”; purple), treated with T cells that were labeled and transferred with the same quantity of soluble IL-12 (not DBCO conjugated) as was conjugated to T cells (“NP + continuous IL-12”; blue), or treated with T cells that were metabolically labeled and then conjugated with IL-12 prior to transfer (“NP + conjugated IL-12”; green). All statistics were calculated with one-way ANOVA and Tukey’s test.

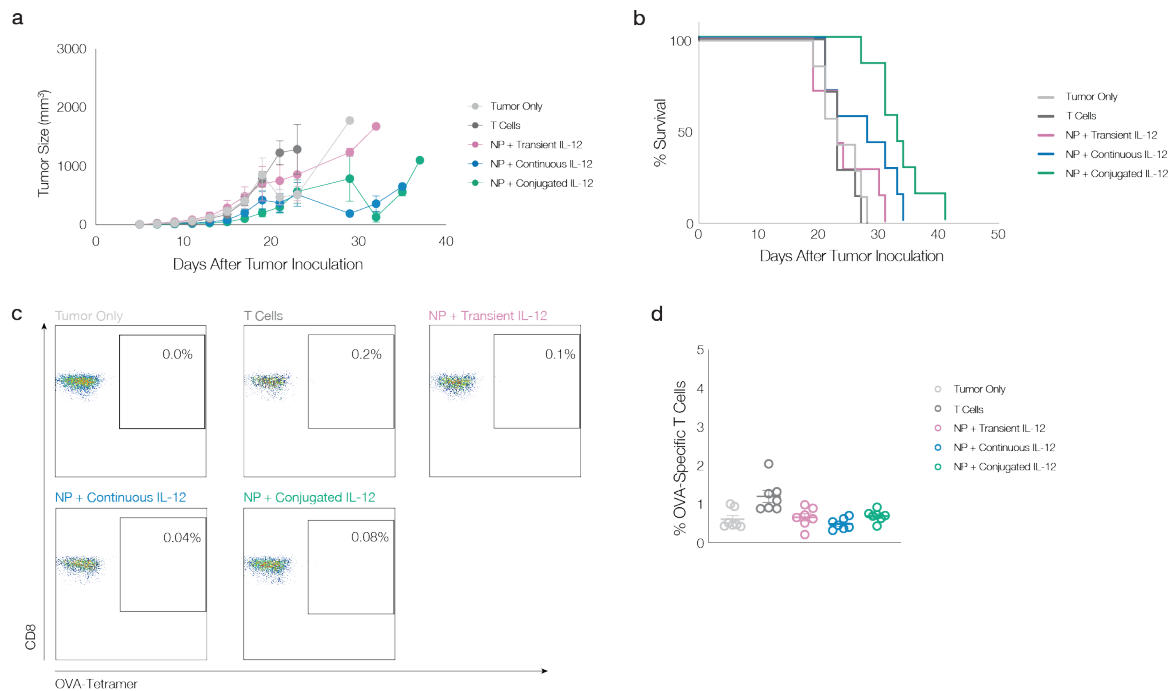


**Figure 3.12, IL-12 conjugation onto T cells in B16-OVA model.** **a**, Mouse B16-OVA tumor growth (n=7, two way-ANOVA test) and **(b)** survival (n=7, Mantel-Cox test). **c**, Representative flow cytometry plots and **(d)** summary of flow cytometry data for OVA-specific CD8<sup>+</sup> T cells on Day 2 after T cell adoptive transfer (n=7). Animals were untreated (“Tumor only”; light grey), treated with T cells without labeling and IL-12 conjugation (“T cells”; dark grey), treated with T cells metabolically labeled and transiently exposed to non-DBCO conjugated IL-12 prior to transfer (“NP + transient IL-12”; purple), treated with T cells that were labeled and transferred with the same quantify of soluble IL-12 (not DBCO conjugated) as was conjugated to T cells (“NP + continuous IL-12”; blue), or treated with T cells that were metabolically labeled and then conjugated with IL-12 prior to transfer (“NP + conjugated IL-12”; green).

### 3.4.6 – Co-conjugation of cytokines enhances ACT, and IL-12 conjugation improves sub-curative CAR-T therapy

Finally, the versatility of this approach to combine cytokines, and enhance CAR-T therapy were explored. IL-15/IL-15R $\alpha$  and IL-12 were together conjugated onto T cells, to simultaneously support T cell proliferation and T cell differentiation towards a Th1 response, respectively<sup>243</sup>. T cells were able to proliferate in vitro in the absence of IL-2 only with IL-15/IL-15R $\alpha$  conjugation

(Figure 3.13a-b). Additionally, T cells conjugated with both cytokines expressed a Th1 phenotype similar to T cells treated with soluble IL-12, indicating no detrimental impact of IL-15/IL-15R $\alpha$  co-conjugation (Figure 3.13c). In the B16-F10 melanoma model, transfer of T cells conjugated with both IL-15/IL-15R $\alpha$  and IL-12 led to better control over tumor growth and prolonged mouse survival, as compared to conjugation of either single cytokine, suggesting a synergistic effect between the proliferative ability of IL-15/IL-15R $\alpha$  and the Th1-directing ability of IL-12 (Figure 3.14a-b). Conjugation of both cytokines also significantly increased circulating T cell numbers (Figure 3.14c).

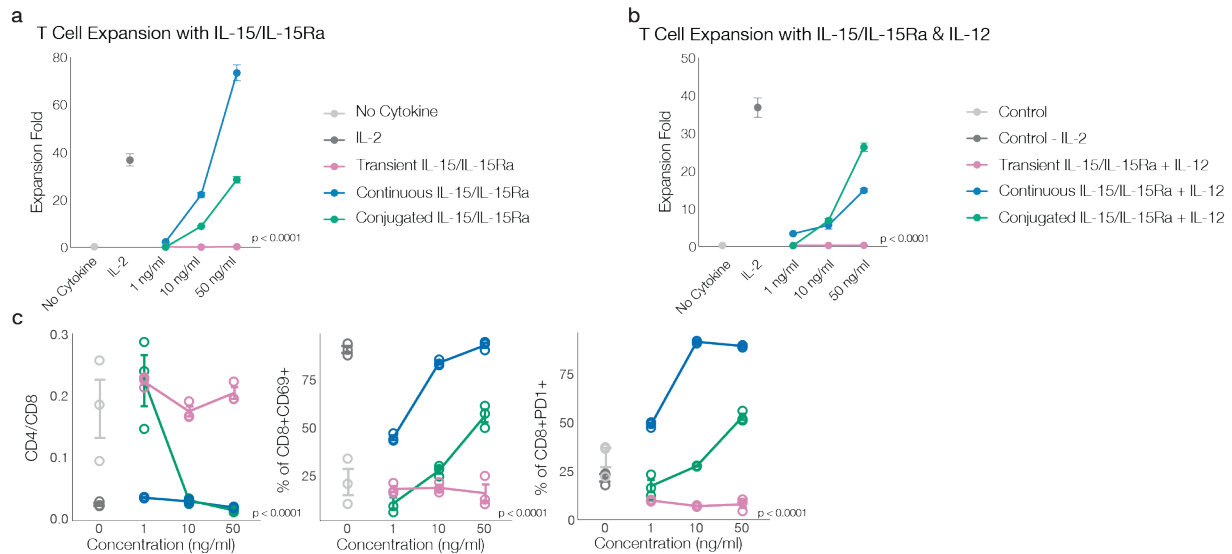


**Figure 3.13, Conjugating multiple DBCO-cytokines achieves synergistic effect on T cells. a,** Expansion data for T cells conjugated with DBCO-IL-15/IL-15R $\alpha$  (“Conjugated IL-15/IL-15R $\alpha$ ”; green), treated with continuously soluble IL-15/IL-15R $\alpha$  (“Continuous IL-15/IL-15R $\alpha$ ”; blue), or temporarily exposed to IL-15/IL-15R $\alpha$  for duration of reaction time (“Transient IL-15/IL-15R $\alpha$ ”, purple) at different IL-15/IL-15R $\alpha$  concentrations. **b,** Expansion data for T cells conjugated with both DBCO-IL-12 and DBCO-IL-15/IL-15R $\alpha$  (“Conjugated IL-15/IL-15R $\alpha$  + IL-12”; green), treated with continuously soluble IL-12 and IL-15/IL-15R $\alpha$  (“Continuous IL-15/IL-15R $\alpha$  + IL-12”; blue), or temporarily exposed to IL-12 and IL-15/IL-15R $\alpha$  for duration of reaction time (“Transient IL-15/IL-15R $\alpha$  + IL-12”, purple) at different cytokine concentrations. **c,** Representative phenotyping data showing activation and exhaustion markers, for T cells conjugated with both DBCO-IL-12 and DBCO-IL-15/IL-15R $\alpha$ , treated with soluble IL-12 and IL-15/IL-15R $\alpha$ , or temporarily exposed to IL-12 and IL-15/IL-15R $\alpha$  duration of reaction time at different cytokine concentrations. (n=3)

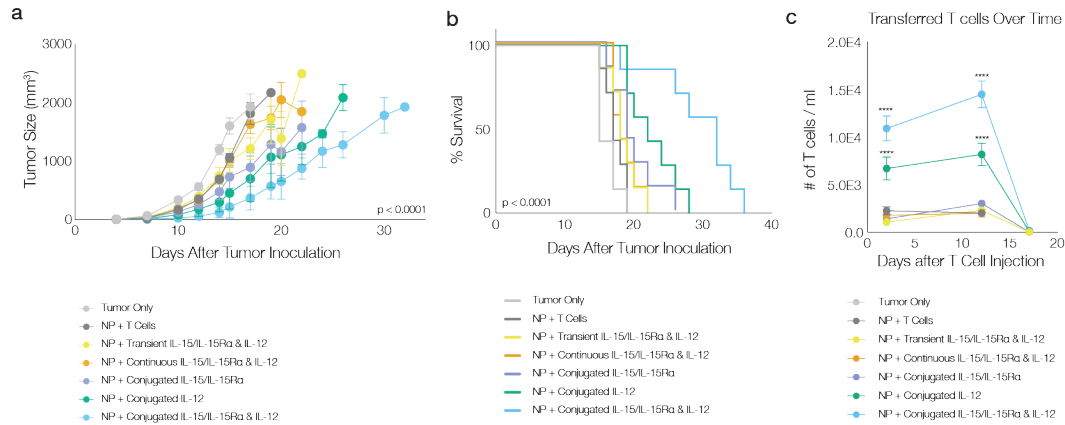


**Figure 3.14, Conjugating multiple DBCO-cytokines significantly slow tumor growth as compared to single cytokine conjugation. a,** mouse tumor growth (n=7, two-way ANOVA test) and **(b)** survival data (n=7, Mantel-Cox test) in B16-F10 melanoma model. **c,** number of Thy1.1+ CD8+ Pmel-1 T cells per 1 mL of blood over therapeutic study (n=7). Animals were untreated (“Tumor only”; light grey), treated with T cells without labeling or cytokine conjugation (“T cells”; dark grey), treated with T cells metabolically labeled and transiently exposed to non-DBCO conjugated IL-15/IL-15Rα and IL-12 (“NP + transient IL-15/IL-15Rα & IL-12”; yellow), treated with CAR-T cells that were labeled and transferred with the same quantify of soluble IL-15/IL-15Rα and IL-12 (not DBCO conjugated) as was conjugated to T cells (“NP + continuous IL-15/IL-15Rα + IL-12”; orange), treated with T cells that were metabolically labeled and conjugated with IL-15/IL-15Rα (“NP + conjugated IL-15/IL-15Rα”; orchid), treated with T cells that were metabolically labeled and conjugated with IL-12 (“NP + conjugated IL-12”, green), treated with T cells that were metabolically labeled and conjugated with IL-15/IL-15Rα and IL-12 (“NP + conjugated IL-15/IL-15Rα & IL-12”, sky blue).

The application of cytokine conjugation was next explored in the context of CAR-T therapy. NSG mice were inoculated with Raji-luc lymphoma before CD19-specific CAR-T cells were injected systemically at half of the curative dose. T cells that have no CAR vector expression showed no effect in controlling tumor growth. In comparison, metabolically labeled CAR-T cells conjugated with IL-12 significantly controlled tumor development and prolonged mice survival (Figure 3.15a-c). CAR-T cells with IL-12 conjugation also showed better proliferation in mice compared with mice receiving untreated T cells or T cells with systemic cytokine treatment (Figure 3.15d).



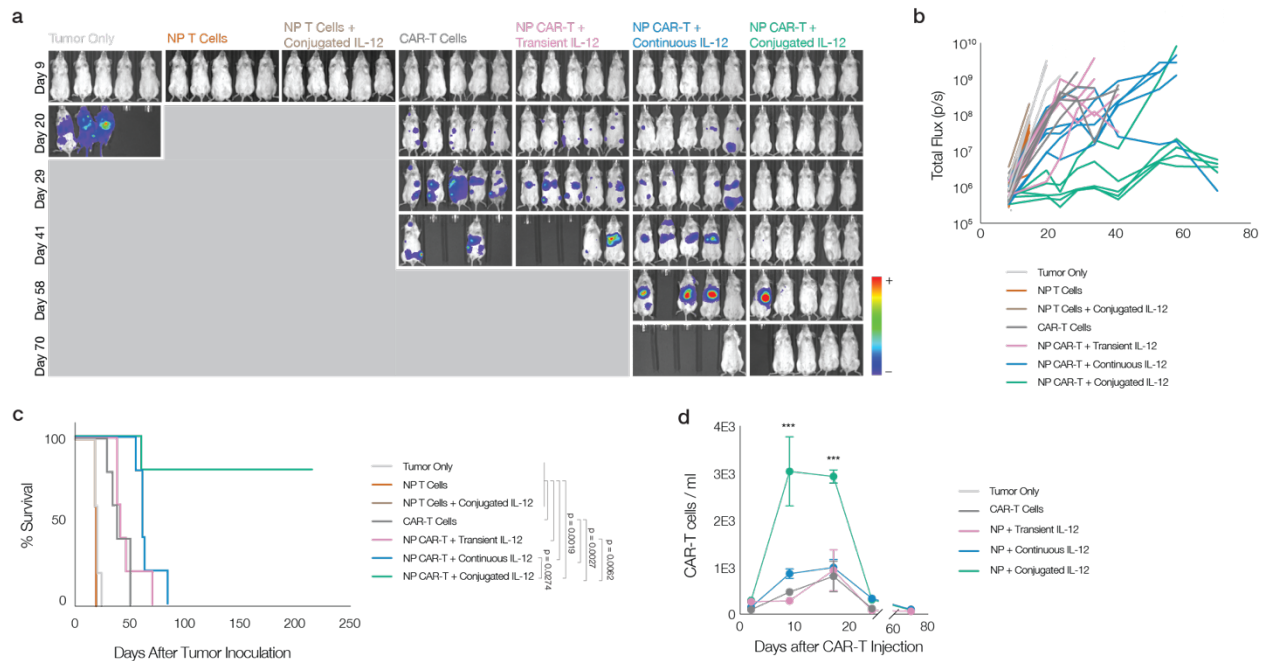


**Figure 3.15, IL-12 conjugation improves the efficacy of CAR-T therapy.** **a**, Bioluminescence image showing tumor burden in Raji xenograft model (n=5). **b**, quantification of bioluminescent signal, and **(c)** mouse survival data for Raji xenograft model (n=5, Mantel-Cox test). **d**, number of anti-CD19 CAR-T cells per 1 mL of blood over time (n=5). Animals were untreated (“Tumor only”; light grey), treated with metabolically labeled T cells without CAR vector expression (“NP T Cells”, dark orange), treated with metabolically labeled and IL-12 conjugated T cells without CAR vector expression (“NP T Cells + conjugated IL-12”), treated with CAR-T cells without labeling but without IL-12 conjugation (“CAR-T”; dark grey), treated with CAR-T cells metabolically labeled and transiently exposed to non-DBCO conjugated IL-12 prior to transfer (“NP + transient IL-12”; purple), treated with CAR-T cells that were labeled and transferred with the same quantity of soluble IL-12 (not DBCO conjugated) as was conjugated to CAR-T cells (“NP + continuous IL-12”; blue), or treated with CAR-T cells that were metabolically labeled and then conjugated with IL-12 prior to transfer (“NP + conjugated IL-12”; green).

### 3.5 – Discussion

Here we demonstrate a simple and scalable nanotechnology strategy to increase the efficacy of adoptive T cell transfer therapies. Nanoparticles fabricated from a polymer of synthetic sugar provided a potent approach to efficiently label T cells for cytokine conjugation, and direct T cell differentiation and function. T cell can be easily metabolically labeled and conjugated with anti-

tumor cytokines, or other agents, by simply adding nanoparticles and cytokines sequentially into normal T cell culture, without disrupting the conventional manufacturing processes for ACT and CAR-T therapies. T cells conjugated with the anti-tumor cytokine IL-12 demonstrated significantly better control over solid tumor growth, likely by increasing the number of adoptively transferred T cells both in circulation and the number penetrating the tumors. Additionally, IL-12 conjugation led to activation of the endogenous immune system towards a Th1 type response, enabling the recognition of tumor antigens beyond those targeted by the ACT. Finally, this approach was shown to be useful in CAR-T and human tumor models, setting the stage for future clinical use, and also serving as a versatile platform for the conjugation of multiple cytokines.

The artificial sugar nanoparticles utilize the T cell metabolic pathways to efficiently label cell surface glycoproteins with azide groups, without otherwise significantly altering the T cells, providing a chemical handle for the conjugation of various agents onto T cell surfaces. T cells were azide-labeled at ~100% efficiency, with the level of azide incorporation proportional to the sugar dose added to the culture medium. Various cytokines could, also in a dose-dependent manner, be conjugated to the T cell surface, and maintained their bioactive functions, as demonstrated by analysis of a number of phenotypic and functional features. These findings support the broad utility of metabolic labeling to enable modification of T cells.

Cytokine conjugation onto T cells via G400 NP significantly boosted the efficacy of both adoptive T cell transfers against solid tumors, and human CAR-T cells to hematologic cancer, even at significantly lower doses than previously used. The ability of IL-12 conjugation to significantly delay the progression of aggressive melanoma was likely related to the increased

number of adoptively-transferred T cells in circulation at peak response, their direction towards a more effector-memory like phenotype, and significantly increased infiltration of the solid tumor. In the CAR-T context, IL-12 conjugation allowed tumor control with a sub-curative dose, and similarly enhanced the number of circulating CAR-T cells post-infusion. The effects in both models were found with the conjugation of only 1.47  $\mu\text{g}$  IL-12 and a single T cell injection. This is a significantly lower dose as compared with previous animal studies ( $\sim 3\text{-}10$   $\mu\text{g}$  over 10 injections) and clinical trials where subjects generally receive multiple cytokine injections each week or even daily throughout the treatment<sup>194,229,230,244,245</sup>. Compared with previous strategies, our method also provided better tumor targeting and tumor-infiltration of cytokine-conjugated T cells without inducing noticeable systemic toxicity. Previous strategies increased cytokine tumor-targeting ability mostly by fusing cytokines to tumor-targeting modalities such as antibodies. However, those agents often still induced systemic toxicity given that many tumor antigens are also expressed in non-tumorous cells<sup>246-248</sup>. The findings here suggest clinical relevance, in potentially improving treatment of solid tumors, allowing treatment for patients with less available T cells, or reducing the time needed for CAR-T proliferation *ex vivo*.

Strikingly, IL-12 conjugation had a significant impact on the endogenous immune system, and orchestrated a type 1 immune response and antigen spread. This is reflected in elevated levels of Th1 cytokines in T cells isolated from spleens and tdLNs, increased activation and antigen-presentation activities of dendritic cells, and enhanced numbers of host T cells specific to antigens not targeted by the ACT. The antigen spread may result from the adoptively transferred T cells being more effective at killing cancer cells, resulting in release of more cancer-associated antigen, altered cytokine signaling by the IL-12 conjugated T cells, or by direct engagement of host immune cells with the IL-12 presented by the transferred T cells from their surface. In any

case, this finding suggests that the immediate de-bulking of tumors resulting from ACT can be enhanced by long-term immunosurveillance via mobilization of host anti-cancer immune responses resulting from the cytokine conjugation to the adoptively transferred T cells. Mobilization of host immune response and antigen spreading has been previously identified as a major contributor to ACT and CAR-T efficacy, and was observed both in patients bearing metastatic lesions and in pre-clinical animal models. However, activation of the host immune system and antigen spreading is generally achieved with the addition of another therapy. For example, chemotherapy and radiation in conjunction with CAR-T therapy helped recruit T cells to solid tumors although this could induce strong side effects<sup>249,250</sup>. CAR-T cells have also been combined with bacterial infections or checkpoint blockade, or genetically engineered to express ligands for activating cell-surface molecules<sup>251–253</sup>. In contrast to these other approaches, cytokine conjugation via metabolic labeling can mobilize a host immune response with little modification to current T cells manufacturing procedures, and without the need to orchestrate multiple therapeutic modalities.

Altogether, our findings demonstrate a simple approach to conjugate anti-tumor cytokines onto T cells, and the resulting, dramatic boost this provides to the efficacy of adoptive T cell transfer therapies at low cytokine doses. This method could be readily integrated into the current ACT and CAR-T manufacturing processes by simply adding the sugar nanoparticles to the cell culture medium during *ex vivo* T cell expansion, and including a short cytokine conjugation and wash step before transfer. The ability to conjugate multiple cytokines provides the possibility to exploit various combinations of cytokines for maximum efficacy in the future. The easy integration and versatility of this platform could transform current ACT and CAR-T therapies.

## 3.6 – Methods

### 3.6.1 – Study Design

The objective of this study was to investigate the potential of a chemical method to increase the efficacy of adoptive T cell transfer therapies against solid tumors. We developed and characterized the *in vitro* and *in vivo* effects of cytokine conjugation via metabolic labeling of T cells, as well as the impact on T cell infiltration, host immune system activation, and antigen spreading to enhance animal survival in aggressive cancer models. All animal procedures were approved by Harvard University's Institutional Animal Care and Use Committee (IACUC) and in compliance with National Institutes of Health (NIH) guidelines.

### 3.6.2 – Animal Handling

Experiments and handling of mice were conducted under federal, state, and local guidelines and with approval from Harvard University's IACUC. Five- to six-week-old female C57Bl/6 mice, TCR-transgenic Thy1.1+ Pmel mice, and Nod/SCID/IL2RG<sup>-/-</sup> (NSG) mice were purchased from the Jackson Laboratory.

### 3.6.3 – Preparation of G400 NP

Ac<sub>3</sub>ManAzAL, the monomer of G400 was first synthesized as previously described<sup>254</sup>. Ac<sub>3</sub>ManAzAL (1.0 mmol), AIBN (0.0005 mmol), and PEG DDMAT (0.0025 mmol) were then dissolved in anhydrous dimethylformamide, subjected to freeze-thaw cycle three times, and stirred at 65°C for 48 hours. G400 polymer was then obtained with precipitation in cold diethyl ether and washing with cold diethyl ether for 3 times, and then dried for future use. To obtain G400 nanoparticles, G400 polymer was dissolved in dimethylformamide at 40 mg/ml, and added

dropwise to ultrapure water on vigorous stirring. After 2 hours, the G400 NP solution was dialyzed against deionized water for 48 h, concentrated with Amicon 3k centrifugal filters, and stored at 4°C for future use.

### *3.6.4 – T cell isolation, activation, culturing, and azido-labeling*

Mouse spleens were collected and kept on ice until and throughout processing. To obtain splenocytes, spleens were compressed and passed through a 70 µm strainer, washed with PBS, and centrifuged at 300 g for 5 min at 4°C. The pellet was resuspended in 1 ml ACK buffer (Lonza, #10-548E) for 1 min; 9 ml of PBS was then added and splenocytes collected by centrifuging at 300 g for 5 min at 4 °C. Mouse Pan T cells and CD8+ T cells were isolated with magnetic-bead-based Pan T cell (Miltenyi #130-095-130) and CD8+ T cell (Miltenyi #130-104-075) isolation kit. Human PMBCs were isolated from blood samples obtained from the Specimen Bank at Brigham and Women’s Hospital, and human T cell were isolated from PBMCs with magnetic-bead-based Pan T cell (Miltenyi #130-096-535) CD8+ T cell isolation kit (Miltenyi #130-096-495) following manufacturer protocol. Mouse and human CD8+ T cells were activated with Dynabeads mouse/human T-activator respectively (ThermoFisher Scientific #11452D/#11131D) and cultured in T cell media (RPMI 1640 (Lonza #BE12-702F), 10% heat-inactivate fetal bovine serum (Gibco #10-082-147), 1% pen/strep, 55 µM β-mercaptoethanol, 10 mM HEPES, 1% 100x non-essential amino acid (Lonza #13-144E), 100 mM sodium pyruvate (Lonza #13-115E), supplemented by mouse recombinant IL-2 (BioLegend #575406) or human recombinant IL-2 (BioLegend #589106) respectively (30-200 IU/ml). T cells were azido-labelled by adding G400 NP solution directly to T cell cultures at various concentrations for 72 hours after activation.

### *3.6.5 – Flow cytometry analysis of azido-labeled T cells*

G400 NP treated T cells were washed 3 times with PBS. For flow cytometry, T cells were stained for live/dead cells, washed with PBS, fixed, and stained with DBCO-AF594 at a concentration of 1 mM at 4°C for 30 minutes. Stained T cells were then analyzed with flow.

### *3.6.6 – Imaging and Azido-signaling analysis of azido-labeled T cells with confocal imaging*

T cells were treated with G400 NP for 3 days, after which T cells were washed 3 times with PBS, and kept in G400 NP-free media for culture. At each timepoint, T cells were taken, washed with PBS 3 times, fixed and stained with DBCO-AF594 at a concentration of 1 mM at 4°C for 30 minutes, and loaded onto coverslips with ProLong Gold Antifade mountant with DAPI for confocal imaging. Z-stacks of T cells were analyzed with IMARIS imaging analysis software. Cells were identified and added as elements for analysis based on DAPI (nuclei) and AF594 (cytosol) staining. The level of azido-labeling in each cell was determined by the median intensity of AF594 on the cell surface.

### *3.6.7 – DBCO-modification of cytokines and verification*

DBCO- IL-12, IL-21, TNF- $\alpha$ , and IL-15/IL-15R $\alpha$  were obtained via reacting carrier-free cytokines with DBCO-sulfo-NHS at 1:8 molar ratio in PBS for 2 days at 4°C. The reaction mixture was then washed and concentrated with Amicon 3k centrifugal filters, and stored at -80°C for future use.

### *3.6.8 – Conjugating DBCO-modified cytokines onto T cells*

T cells were treated with 200 $\mu$ M G400 NP for 3 days, and washed with PBS 3 times. DBCO-cytokines were added to T cells for 30 minutes at 4°C. T cells were then washed 3 times with PBS before characterization or use. Cytokine-containing media before and after the reaction were collected, and ELISA was performed according to manufacturer's protocol to calculate the amount conjugated onto T cells.

### 3.6.9 – Flow cytometry for *in vitro* and *in vivo* cell analysis

CFSE staining was performed by adding T cells to 5  $\mu$ M CFSE in PBS for 30 minutes at 37°C for 20 minutes. Cells were then washed and kept in culture. Cells were stained with dead cell stain (ThermoFisher Scientific #L23105) according to manufacturer's protocol. Cells were then blocked with FcX Fc receptor blocking solution (BioLegend #101319, #422301) for 5 min and stained with surface protein antibodies for 20 min. Brilliant violet staining buffer (BD Horizon #563794) and flow cytometry staining buffer (Invitrogen #00-4222-26) were used during staining. Flow cytometry was then performed on BD Fortessa LSRII. Gating was performed based on fluorescence-minus-one controls. For blood samples from mice, 100  $\mu$ l of ACK lysis buffer was added to every 50  $\mu$ l of blood for 2 minutes to remove red blood cells. The cells were then washed and used for downstream staining. Anti-mouse and anti-human antibodies were obtained from BioLegend: Anti-mouse: CD103 (#121420), CD11b (#101263), CD11c (#117308), CD137 (#106110), CD19 (#115538, #115534), CD24 (#101826), CD25 (#101908), CD3 (#100218, #100220), CD301b (#146814), CD4 (#100559), CD40 (#124630), CD40L (#106512), CD44 (#103057), CD45 (#103132, #103114), CD62L (#104418), CD69 (#104545), CD8 (#100766), CD80 (#104743), F4/80 (#123147, #123128), I-Ab (#116406), LAG-3 (#125212), Ly-6C (#128012), MHC-II (#116406), NK-1.1 (#108748), PD-1 (#135206),



Thy1.1 (#202526), Thy1.2 (#140329), Tim3 (#134008). Anti-human: CD3 (#344808), CD4 (#344648), CD8 (#344714)

### 3.6.10 – Cytolysis Assay

1 million mouse B16-F10 cells were stained with Calcein AM (Invitrogen #C1430) for 30 min at 37 °C in dark, washed 4 times with PBS, and kept in dark on ice until use. T cells from Pmel-1 mouse spleen were isolated, treated with G400 NP for 3 days and conjugated with various DBCO-cytokines. T cells and B16-F10 melanoma cells were well mixed and seeded in 96-well U-bottom plates at different E:T ratios in 200 µl media (RPMI 1640 + 10% FBS + 1% P/S). The plate was centrifuged to collect cells to the bottom, and incubated at 37 °C for 6 hr. Supernatants were collected and their fluorescent signals measured with 485 nm excitation and 528 nm emission with a BioTek Synergy H1 plate reader. The fluorescent signals from the 528 nm channel were subtracted from the 485 nm channel, and cytolysis efficiency was calculated using  $(\text{sample well} - \text{background well}) / (\text{full-cytolysis well} - \text{background well}) * 100\%$

### 3.6.11 – CAR-T Generation

*Lentivirus construction and production:* The 2nd generation CD19 CAR construct was composed of the scFv fragment from the FMC63 antibody (GenBank: ADM64594.1) fused to the human CD8α hinge and transmembrane region (Gene bank number NP\_001759.3, aa 138-206) and linked to human 4-1BB (Gene bank number NP\_001552.2, aa 214-255) and human CD3ζ (Gene bank number NP\_000725, aa 52-163) intracellular signaling domains. To enable detection by flow cytometry, a cleavable truncated EGFR (tEGFR) was inserted to the N-terminus of the CD3ζ. Lentiviral supernatants were produced using the HEK 293T packaging line as previously described<sup>32</sup>. 100% confluent HEK 293T cells in a well of a 6-well plate was

co-transfected with 0.2 ug CAR-vector plasmid, 0.9 ug pMD2.G, 1.9 ug psPAX2 using lipofectamine 2000 (Life Technologies). The cultures were grown for 55 hr, after which the supernatants were collected, filtered to remove debris, and frozen at -80 C before use.

*CAR-T transduction:* T cells were isolated from healthy donors using the human pan-T cell isolation kit (Miltenyi Biotec) to obtain CD3<sup>+</sup> T cells. Isolated T cells were activated with Dynabead (ThermoFisher Scientific 111161D) at 1:1 ratio. After 48 h, activated T cells were transduced by adding 140  $\mu$ L of pre-warmed lentiviral supernatant containing the CD19 CAR construct. After 36 h, the media containing T cells and any remaining material were transferred to a 6-well G-Rex plate (Wilson Wolf) containing pre-warmed T cell media (described above) and expanded for 3 days. Transduced T cells were magnetically separated from Dynabeads and cryopreserved in 10% DMSO + 90% FBS. The CAR-T transduction efficiency was consistently around 25%.

### 3.6.12 – B16-F10 melanoma model

*Tumor inoculation and Pmel T cell treatment:* 100k B16-F10 melanoma cells were injected subcutaneously on the left flank of C57Bl/6 mice (female, ~6 weeks of age, Jackson Laboratory). After 5 days, tumor bearing mice were randomized and injected with either PBS, or 7 million Thy1.1<sup>+</sup> Pmel T cells via tail vein injection.

*Tumor monitoring:* size of B16-F10 melanoma was monitored over time by measuring the height, width, and length of the tumor. The total size of tumor was calculated as height\*width\*length\*0.5. Mice were euthanized if the total tumor size was over 2,000 mm<sup>3</sup>, if any of the tumor dimensions were over 20 mm, or if significant discomfort or weight loss was observed.

*Tracking of adoptively transferred T cells:* Each week, animals were bled via the tail vein and ~50  $\mu$ L blood was collected in K2-EDTA-coated collection tubes (BD). The samples were treated with ACK lysis buffer (Lonza, BioLegend), washed, and processed for flow cytometry as described above.

### 3.6.13 – Xenograft lymphoma model

*Tumor inoculation and CAR-T cell treatment:* Female NSG mice, between 6-7 wks of age were inoculated with a high dose of  $5 \times 10^5$  luciferized Raji cells (Raji-luc) intravenously on day 0. After 4 days, tumor-bearing mice were randomized into treatment groups and were treated with either mock (PBS) or  $5 \times 10^5$  CAR+ T cells.

*Tumor tracking:* Raji-luc tumor burden was monitored over time using D-Luciferin (Gold Biotechnology). Animals were anesthetized and intraperitoneally injected with D-Luciferin at 150 mg/kg. Luminescence was measured 10 minutes post injection via IVIS (Perkin Elmer). Total flux (p/s) per mouse was quantified in whole-body regions-of-interest (ROI). Animals were imaged once every 4 to 14 days. Mice were euthanized if flux from tumor was larger than 1E1, or if significant discomfort or weight loss was observed.

*Tracking of adoptively transferred CAR-T cells.* Each week, animals were bled via the tail vein and ~50  $\mu$ L blood was collected in K2-EDTA-coated collection tubes (BD). The samples were treated with ACK lysis buffer (Lonza, BioLegend), washed, and processed for flow cytometry as described above.

### 3.6.14 – Cell isolation from tumor and lymph node

Tumors and tumor-draining lymph nodes were separated from mice and mashed into small pieces. Mashed tissues were treated with 200 IU collagenase type I at 37°C for 1 hour, and were passed through pipette tips every 20 minutes. After collagenase type IV treatment, the solutions were passed through a 70 µM filter to achieve a single cell suspension. Cells from lymph node were then used for downstream analysis. Cells from tumor were spun down and treated with ACK lysis buffer to remove red blood cells, and resuspended in 1 mL RPMI media. This single cell suspension was gently added to the top of 2 mL 40% (v/v) Percoll and 2 mL 70% (v/v) Percoll to create a separation, and centrifuged at 800g for 30 minutes at room temperature. Tumor infiltrating lymphocytes were collected from the middle layer and washed with ice-cold PBS for three times before they were used for downstream analysis.

#### *3.6.15 – T cell activation assay and intracellular cytokine staining*

Mouse T cells isolated from tumor, spleen, and lymph nodes were co-cultured with B16-F10 melanoma T cells in 100 µl media. The plate was centrifuged at 1600 rpm to collect cells to the bottom. After 1 hour, GolgiPlug (BD #555029) was added according to manufacturer's protocol to stop cytokine secretion. 3 hours later, T cell and tumor cell mixtures were washed, and stained with dead cell stain, surface proteins, and intracellular cytokines with Cyto-Fast fix-perm buffer set (BioLegend #426803) according to manufacturer's protocol. Antibodies against intracellular cytokines were obtained from BioLegend: TNF- $\alpha$  (#506306), IL-2 (#503837) IFN- $\gamma$  (#505830), Granzyme B (#396404)

#### *3.6.16 – Tetramer staining*

Blood samples from mice were treated with ACK lysis buffer to remove red blood cells. 10 µl of SIINFEKL tetramer (TB-5001-4) were added to each sample, the final volume was

adjusted to 200  $\mu$ l with PBS, and the sample was incubated for 20 min at 37°C. Primary antibodies for other cell surface markers were then added and incubated for 20 min at 4°C. Cells were then washed with PBS for three times and stained with live/dead staining, and used for flow cytometry analysis.

### *3.6.17 – Statistical Analysis*

Data was represented as mean  $\pm$  SEM of biological replicates, unless otherwise stated. Detailed statistical methods are described in figure legends. Statistical testing was performed using GraphPad Prism (Version 9.02).  $p < 0.05$  was considered significant.

## **Chapter 4: Matrix viscoelasticity regulates T cell phenotype**

### **4.1 – Outline**

This chapter presents an approach to modulate T cell phenotype and function by tuning the mechanical properties of the surrounding matrices. Detailed protocols are in Appendix 2.4-2.6. Supplementary tables mentioned in this Chapter are in Appendix 1.

### **4.2 – Abstract**

The efficacy of adoptive T cell therapy is highly dependent on the generation of T cell populations that are able to both provide immediate effector function and long-term protective immunity. Inspired by the emerging consensus that T cell phenotype and function are inherently linked to their tissue localization, we present an approach to generate functionally distinct T cell populations via the physical properties of their surrounding matrix. A collagen type I based extracellular matrix (ECM) was engineered to allow for independent tuning of matrix stiffness and viscoelasticity, two features that characterize the mechanical properties of tissues. The mechanical properties of the ECM, particularly ECM viscoelasticity, regulated T cell phenotype and function, and the AP-1 pathway, which is a critical regulator of T cell fate. These observations were consistent with the profiles of T cells isolated from mechanically distinct tissues in cancer and fibrosis patients. The engineered ECM was then utilized to generate functionally distinct T cell populations from cells that received the same initial stimulation. Altogether these findings demonstrate the direct role of tissue viscoelasticity in directing T cell function and provide a strategy for generating functionally distinct T cell populations.

### 4.3 – Introduction

T cells play a critical role in the immune response to tumors and are characterized by their antigen specificity, and their long-term memory potential that establishes protective immunity<sup>1-3</sup>. Adoptive T cell therapy is an emerging area of immunotherapy where T cells are harvested from a patient, manipulated *ex vivo* and reinfused into the patient<sup>4</sup>. These T cells can either be tumor infiltrating lymphocytes (TILs), which are isolated from tumors, or more commonly autologous polyclonal T cells isolated from apheresed PBMCs<sup>5</sup>. Autologous T cells can be genetically modified into TCR T cells or Chimeric Antigen Receptor (CAR) T cells based on whether the antigen being recognized is in the presence or absence of MHC respectively<sup>5</sup>. While T cell therapy has shown remarkable promise, especially in hematological cancers, the efficacy of T cell therapies can be enhanced by generating T cell populations that provide both immediate and durable long-term protection against cancer<sup>5-8</sup>.

The generation of CAR T cells and genetically modified TCR T cells involve *ex vivo* stimulation of isolated T cells prior to genetic manipulation<sup>8,9</sup>. Approaches to T cell stimulation have evolved from the labor-intensive use of purified autologous antigen presenting cells (APCs)<sup>3,10</sup> to more efficient artificial APCs presenting aCD3/aCD28 monoclonal antibodies, supplemented with growth factors such as IL-2 for T cell expansion<sup>9,11</sup>. Activated T cells are incubated with either viral vectors or non-viral transposon systems for stable CAR or TCR expression<sup>12,13</sup>, or mRNA for more transient expression<sup>14</sup>. Most approaches aiming to generate various T cell populations *in vitro* are limited to altering the strength and duration of T cell stimulation<sup>8,15</sup>. Approaches that can further tune T cell phenotype for a given stimulation regimen could broaden the repertoire of T cells available for therapy.

Prior studies suggest that T cell phenotype is inherently linked to their location, and this is likely linked to the distinct properties of various anatomic locations<sup>16-18</sup>. In tissues, T cells encounter mechanical resistances in the form of stiffness and viscoelasticity as they engage extracellular matrices (ECM) like collagens, which are altered in pathologies like cancer and fibrosis. Stiffness describes a material's resistance to instantaneous deformation, whereas viscoelasticity is a distinct feature from stiffness that refers to a material's time-dependent mechanical response to applied stresses and strains<sup>19,20</sup>. The stress needed to maintain a particular deformation decreases more rapidly with time for minimally crosslinked, fast relaxing ECM (more viscous) than for more highly crosslinked, slow relaxing ECM (more elastic). Both tissue stiffness and viscoelasticity have been shown to independently influence the behavior of cells, including their proliferation, mobility and differentiation<sup>20</sup>.

Here, we hypothesize that functionally distinct T cell populations can be generated by selectively tuning the mechanical properties of matrices in which cells are embedded, mimicking distinct mechanical properties of the tissue microenvironment. To address this hypothesis, a collagen type 1 based ECM model was first engineered to allow for independent tuning of matrix stiffness and viscoelasticity. Collagen type 1 was utilized because it is a major ECM constituent in multiple tissues, forming the fibrillar structures that provide mechanical tissue integrity, as well as adhesion ligands for cell adhesion and migration<sup>21</sup>. To control for initial T cell activation, T cells received the same initial stimulation regimen before they were cultured in matrices with different viscoelasticity. In vivo, T cells are primed when antigen presenting cells sample, process, and present antigen to T cells on their major histocompatibility complex (MHC) proteins. However, the phenotype of these antigen presenting cells themselves could be influenced by their mechanical environment, complicating one's ability to determine how matrix



mechanical properties regulate T cell activation. Consequently, we used synthetic CD3/CD28 dynabeads, which is the industry standard for CAR-T cell activation and expansion for clinical use, and which can be easily separated from T cells via the use of magnets before the cells are seeded in collagen matrices. T cell phenotype, in vitro cytotoxic function and cytokine secretion profiles, as well as in vivo function were analyzed, as was the AP-1 pathway, which has been shown to be a critical regulator of T cell activation, differentiation and exhaustion. The profiles of T cells cultured in the distinct mechanical environments was further compared to T cells derived from mechanically distinct tissues in cancer and fibrosis patients. Together, these studies further our understanding of the role of tissue mechanical properties in directing T cell function and provide a tool for generating functionally distinct populations of T cells.

## **4.4 – Results**

### *4.4.1 – T cell phenotype varies in mechanically distinct tissues in vivo*

First, to confirm and extend previous reports that aspects of the tissue microenvironment may regulate T cell phenotype in vivo, published scRNA-seq datasets were analyzed to compare CD8<sup>+</sup> T cells located in tumors, adjacent normal tissues and blood for patients with non-small cell lung cancer (NSCLC)<sup>22</sup>, liver cancer<sup>23</sup>, and colorectal cancer<sup>24</sup>, representing diverse mechanical environments. These analyses were performed for both pan T cells and T cells with shared TCR clonotypes between the tissue types. The three tissue types were selected because they span the spectrum between very soft, fast-relaxing (blood: a viscous fluid)<sup>25</sup> and stiff, slow-relaxing (tumor)<sup>26,27</sup> tissues. Umap plots of pan T cells showed distinct localization of T cells from the different tissue compartments, with increased overlap between T cells from tumors and those from their corresponding normal tissues compared to blood (Figure 4.1a). Tumor T cell

gene signatures were generated for each tumor type by performing differential gene expression analysis between tumor derived T cells and T cells in normal tissue and blood (Appendix A1.2). These signatures were then applied to T cells from the different tissue compartments to compare their aggregate expression levels. T cells from the blood had the lowest expression of tumor T cell gene signatures, with T cells in adjacent normal tissue being intermediate (Figure 4.1b). This trend was maintained when the same analysis was performed for T cells with shared TCR clonotypes (Figure 4.1c). These results suggest that the tissue microenvironment may be playing a role in modulating T cell phenotype.

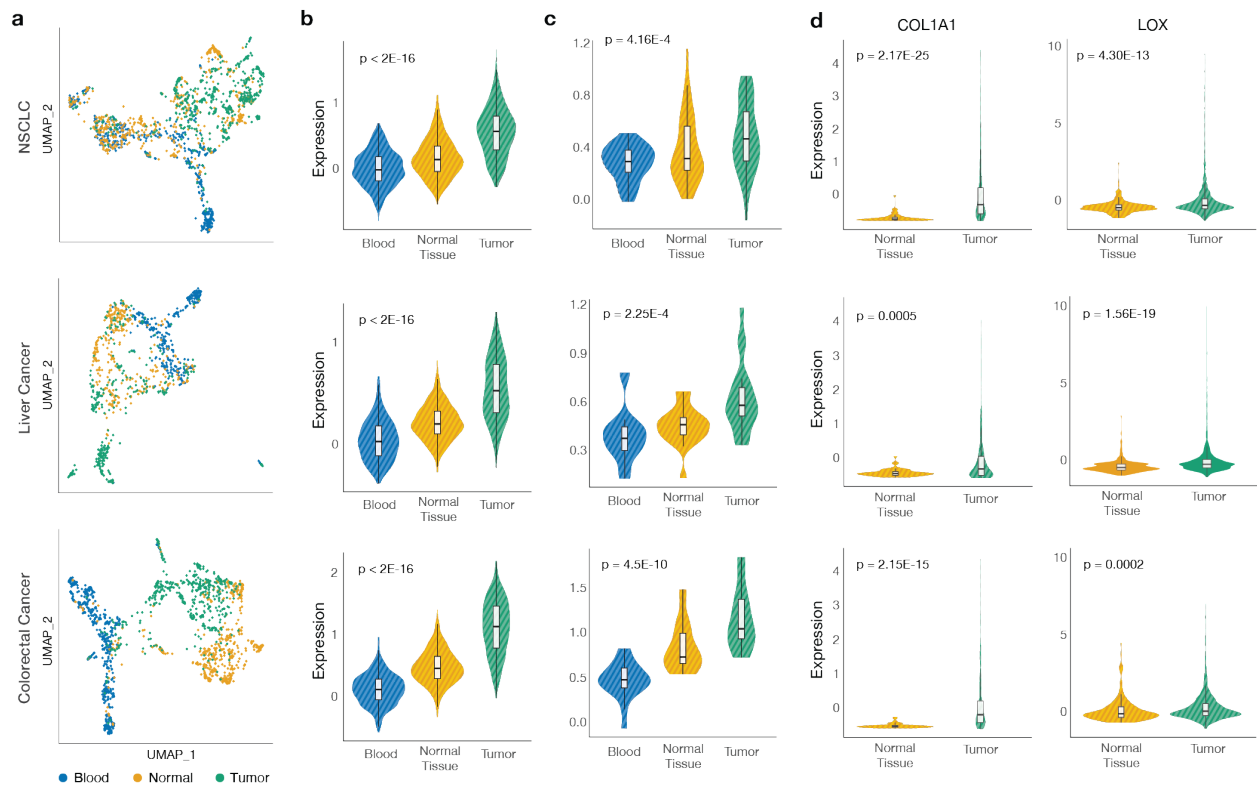


**Figure 4.1, Tissue microenvironment influences T cell phenotype.** **a.** Umap plots of pan CD8+ T cells from tumors, adjacent normal tissue and blood for NSCLC, liver cancer, and colorectal cancer. **b-c.** Violin plots comparing expression levels of tumor T cell gene signatures for T cells located in tumors, normal tissues and blood for **(b)** pan T cells or **(c)** T cells with shared TCR clonotypes. P-values were determined by performing two-tailed one-way Anova. **d.** Relative expression of collagen type I (COL1A1) and lysyl oxidase (LOX) in normal tissues and tumors from the TCGA dataset. P-values were determined by performing Wilcoxon signed-rank test.

To better correlate the observed transcriptomic differences between T cells isolated from the different tissues with their microenvironment, and to further inform our choice of ECM protein for subsequent studies, bulk sequencing from the TCGA dataset was analyzed to compare the relative expressions of canonical matrix proteins that are known to influence tissue mechanical properties. In particular, collagen type I (COL1A1) and lysyl oxidase (LOX), which is known to crosslink collagen fibers in vivo, were found to be differentially expressed in tumors relative to normal tissues for each tumor type (Figure 4.1d).

#### *4.4.2 – Synthesizing collagen-based ECM mimetic with tunable mechanical properties*

We next engineered a collagen type I based ECM model to allow for independent tuning of matrix stiffness and viscoelasticity for T cell culture. Collagen type I was first modified with norbornene (Nb), which undergoes a highly selective bioorthogonal click reaction with tetrazine (Tz) moieties via inverse electron demand Diels-Alder<sup>28</sup>. Matrix stiffness was tuned by varying the collagen concentration, while the addition of local covalent crosslinking to the Nb-modified collagen post gelation with low molecular weight Tz crosslinkers regulated matrix viscoelastic properties without changing the stiffness (Figure 4.2a, Figure 4.3a). Two collagen concentrations were utilized, as these yielded matrices which spanned the stiffness range of multiple soft tissues<sup>29</sup> (Figure 4.2b), as well as pre-malignant and malignant tumors<sup>30-34</sup>. Mechanical characterization of the matrices showed that while click crosslinking influenced matrix viscoelastic properties, as reflected in stress relaxation and loss angle of the matrices, it did not affect bulk stiffness values (Figure 4.3b-c, Figure 4.2c). Further characterization by cryo-

scanning electron microscopy (Cryo-SEM) and second harmonic generation imaging (SHG) showed that click crosslinking did not alter the fibrillar architecture or pore-size distribution of collagen matrices (Figure 4.3d-e, Figure 4.2d), and did not affect collagen fiber length, waviness or angle between the fibers (Figure 4.2e-g). Importantly, analysis of local mechanical properties with nanoindentation confirmed similar storage moduli ( $G'$ ) for each collagen concentration but significantly different loss moduli ( $G''$ ) between fast and slow relaxing matrices (Figure 4.2h-i).

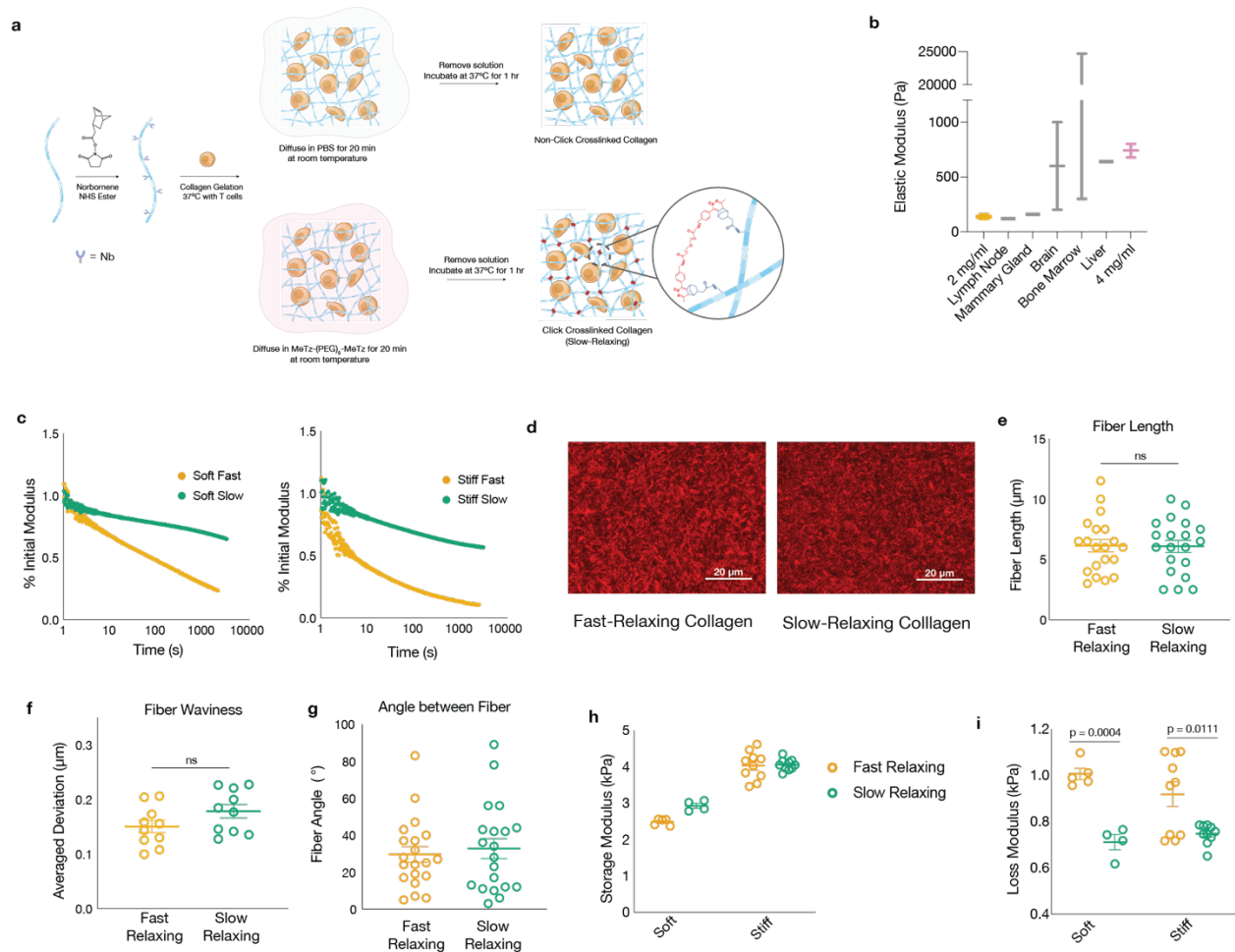


**Figure 4.2, Material synthesis and characterization.** **a.** Collagen is modified with norbornene using NHS and gelled at 37°C with T cells. A low MW divalent crosslinker containing two methyltetrazines is diffused into gels at room temperature until equilibrated with the surrounding solution, to achieve even distribution within the gel. Subsequently increasing the temperature allows covalent crosslinks to form between norbornene and methyltetrazine functionalities. **b.** Comparison of Young's moduli for soft and stiff gels to those of published different soft tissues. **c.** Stress relaxation profiles of fast relaxing and slow

relaxing, soft (left) and stiff (right) collagen matrices. **d.** SHG images for 2mg/ml fast relaxing and slow relaxing collagen gels. **e-g.** Quantification of fiber length (**e**), waviness (**f**) and angle between fibers (**g**) for fast and slow relaxing matrices. P-values were determined by performing two-tailed unpaired t-test. **h-i.** Storage and loss moduli determined using nanoindentation on collagen matrices. P-values were determined by performing two-tailed unpaired t-test for n=4 to n=10 indents.

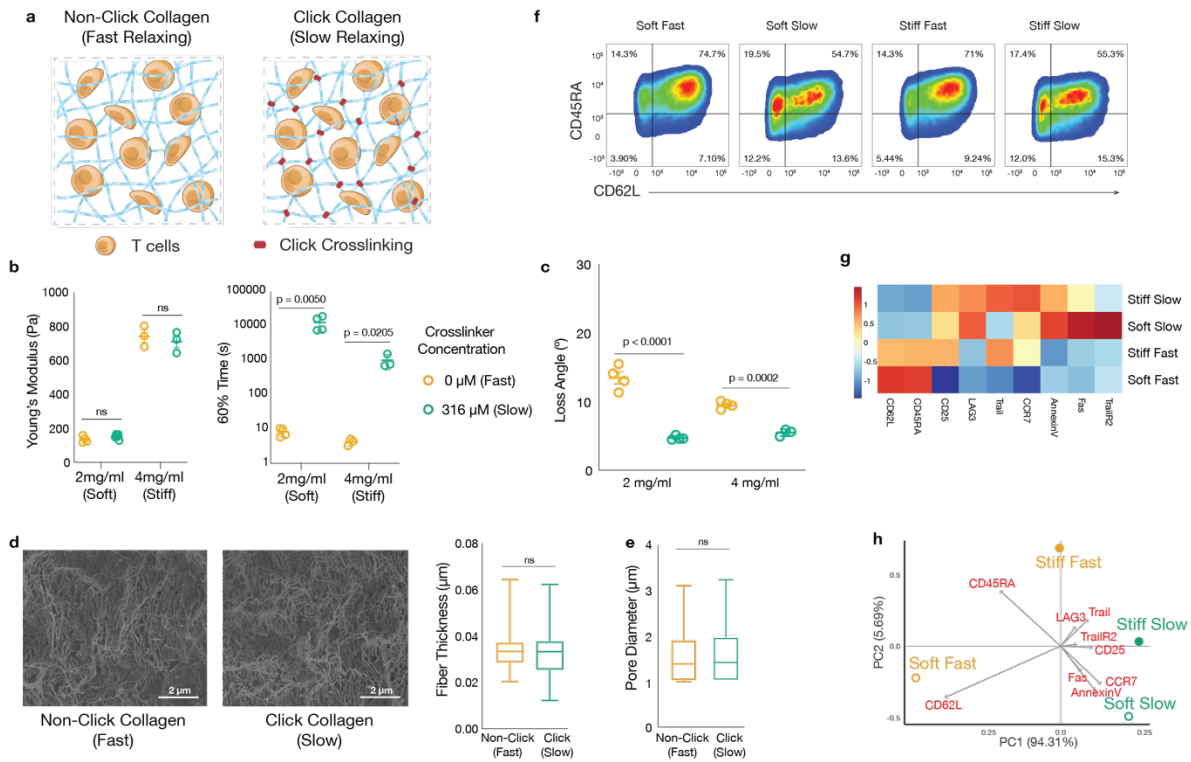


**Figure 4.3, Synthesizing collagen-based ECM mimetic with tunable mechanical properties. a.** Schematic of collagen type I based ECM mimetic showing non-click collagen (fast relaxing) and click collagen (slow relaxing) matrices. **b.** Young's moduli (left) and time values for relaxation to 60% of initially applied stress (right) for 2 mg/ml (soft) and 4 mg/ml (stiff) collagen matrices. P-values were determined by performing two-tailed unpaired t-test. Data are mean  $\pm$  s.e.m from n=3-5. Significance threshold:  $P < 0.05$  (ns=not significant). **c.** Loss angle measurements for collagen matrices. P-values were calculated by using two-tailed unpaired t-test for n=3-4 samples. **d.** Cryo-SEM images, fiber thickness and, **e.** pore size estimation for 2mg/ml fast and slow relaxing matrices showing that collagen architecture is maintained. P-values were determined using two-tailed unpaired t-test. Significance threshold:  $P < 0.05$ . **f.** Representative flow cytometry plots showing CD62L and CD45RA expression, and (**g**) relative expression levels of various markers, in CD8+ T cells cultured in slow or fast relaxing, soft or stiff collagen matrices. **h.** PCA plots showing that phenotypic differences are driven more by changes in collagen viscoelasticity than by stiffness. Data shows pooled samples for n=3.

CD8<sup>+</sup> T cells were subsequently isolated from healthy donors, activated, and subsequently cultured in fast relaxing (non-click crosslinked) or slow relaxing (click crosslinked), soft (2 mg/ml) or stiff (4 mg/ml) collagen matrices. After 3 days in the various matrices, the T cells showed notable phenotypic differences, driven more by changes in collagen viscoelasticity than by stiffness (Figure 4.3f-h). In particular, flow cytometry analysis of CD8<sup>+</sup> T cells showed higher expression of activation and inhibitory markers in slow relaxing matrices, while T cells in fast relaxing matrices exhibited higher memory marker expression, such as CD62L and CD45RA (Figure 4.3f). These observations were consistent with multiple donors and across multiple independent experiments (Figure 4.4)

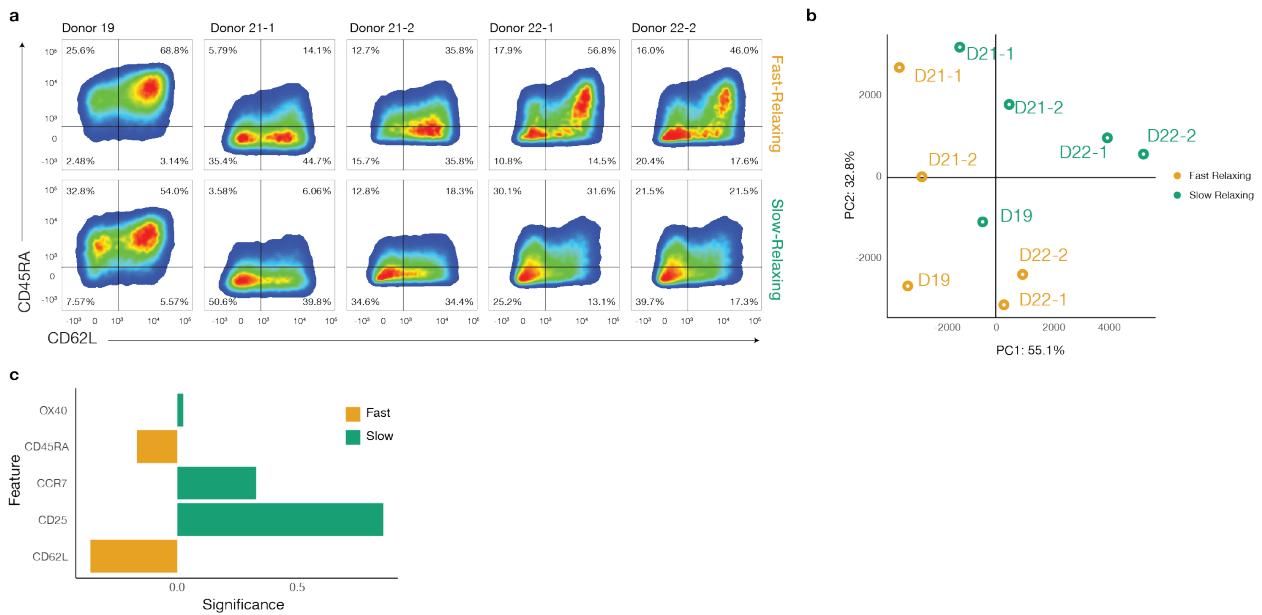


**Figure 4.4, ECM modulation of T cell phenotype using multiple donors and across independent experiments.** **a.** Representative flow cytometry plots showing CD62L and CD45RA expression for T cells cultured in soft fast and soft slow relaxing gels after 4 days of activation for multiple donors and across multiple independent studies. For donors used for independent studies, the study number is indicated after the donor number. **b.** PCA plot showing that ECM viscoelasticity drives phenotypic differences along both principal components 1 and 2. **c.** PCA loadings for PC1 showing relative importance of input features. Data shows pooled samples n=2-3 for 3 donors across 5 independent experiments.

#### *4.4.3 – Collagen modification and crosslinker have minimal effects on T cell adhesion and phenotype*

Potential effects of collagen modification and the presence of methyltetrazine crosslinkers on T cell adhesion and phenotype were next investigated. T cells that were seeded on top of unmodified and Nb-modified collagen with and without methyltetrazine crosslinkers adhered similarly to their respective collagen matrices (Figure 4.5a). In addition, T cells remained highly viable in all matrix conditions (Figure 4.5b) and had similar phenotypic profiles when they were embedded in unmodified collagen (Col) or in Nb-modified collagen (Col-Nb) (Figure 4.5c-e). The presence of methyltetrazine crosslinkers had minimal effect on T cells cultured in unmodified collagen matrices (Col (+Linkers)), but had significant effects on T cells cultured in modified collagen (Col-Nb (+Linkers)), as expected due to changes in matrix viscoelasticity from the resultant crosslinking in the latter (Figure 4.5c-e). Importantly, PCA analyses confirmed our observations, with Col-Nb (+Linkers) being most different along PC1 (Figure 4.5f).

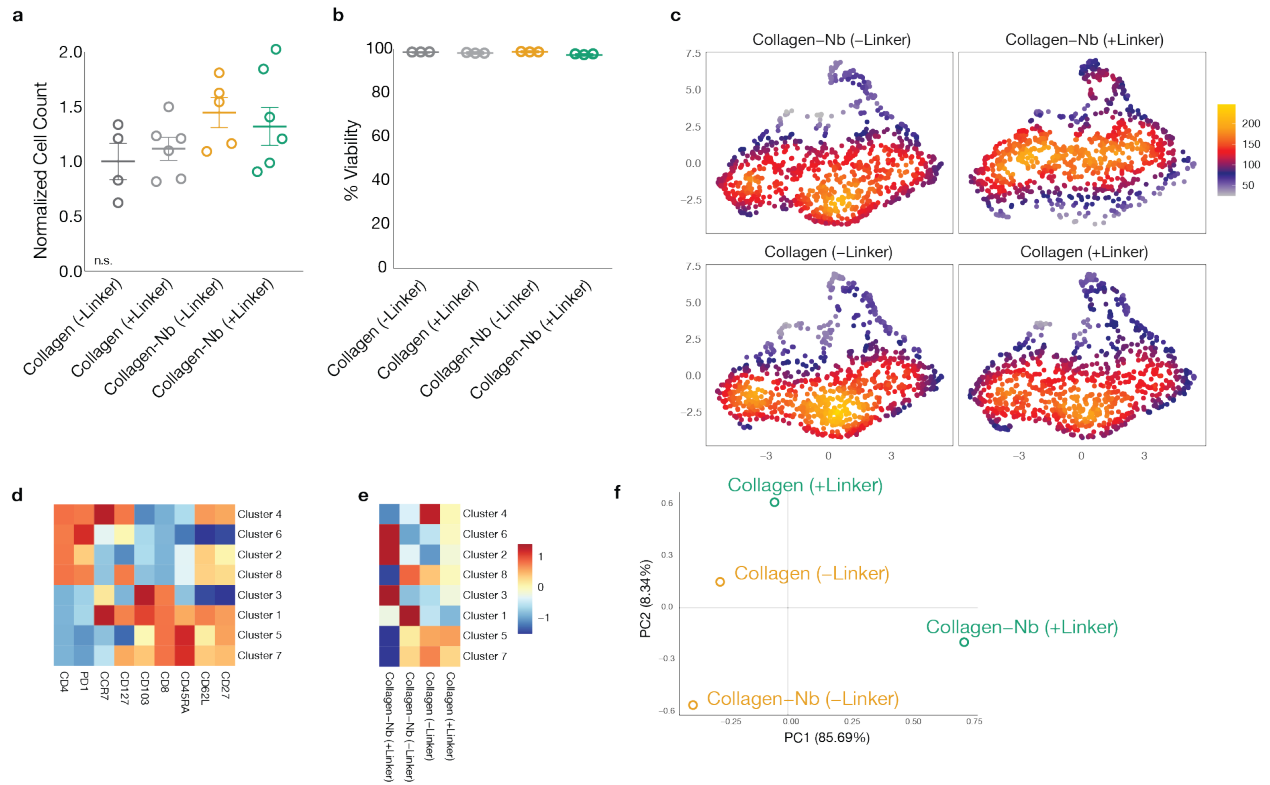


**Figure 4.5, Collagen modification and crosslinker have minimal effects on T cell adhesion and phenotype.** **a.** Adhesion of T cells seeded on top of unmodified collagen or norbornene modified collagen (Collagen-Nb) with or without methyltetrazine linkers (n=4-6 replicates). **b.** Viability of T cells embedded in collagen matrices with or without norbornene modification and crosslinker. **c.** Umap plots of T cells phenotyped by flow cytometry after embedding in collagen matrices with or without norbornene modification and crosslinker. **d-e.** K-means clustering was performed on pooled T cells from all experimental conditions. **d.** Heatmap plot showing characteristic markers for each cluster. **e.** Heatmap plot showing the frequencies of cells per condition for each cluster. **f.** PCA plot showing relative similarities between the different conditions. Data for c-f show pooled samples for n=3 replicates.

#### 4.4.4 – ECM viscoelasticity modulates T cell phenotype in complex ECM

Even though collagen type I forms a significant fraction of many tissue ECMs, the effects of viscoelasticity within the context of a more complex ECM formulation was next studied. These studies were performed with an interpenetrating network (IPN) of Matrigel and collagen type I to mimic the complexity of tissue ECM. The viscoelasticity of the collagen-Matrigel IPN was again tuned by selectively and locally crosslinking collagen-Nb within the network with low molecular



weight methyltetrazine crosslinkers. Bulk rheological characterization of the IPNs showed significant effects of click crosslinking on stress relaxation half time and loss angle (Figure 4.6a). Importantly, similar to the observations made for the collagen-only matrices, alterations in viscoelastic properties led to significant changes in T cell phenotype (Figure 4.6b-e).

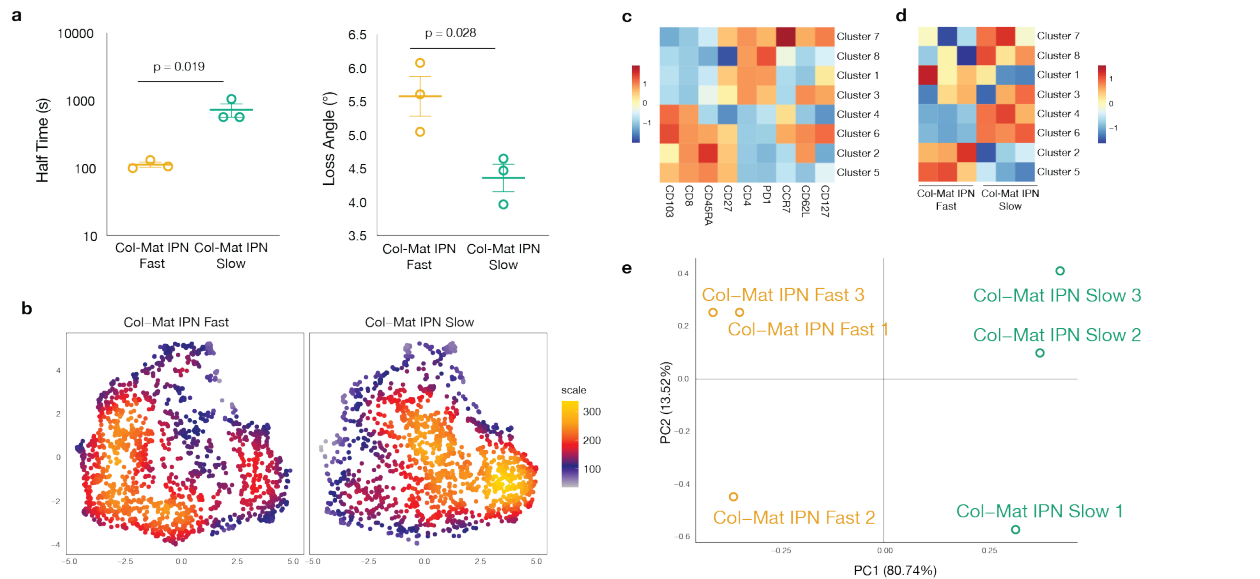


**Figure 4.6, ECM viscoelasticity modulates T cell phenotype in complex ECM. a.** Stress relaxation half time (left) and loss angle (right) measurements of fast relaxing and slow relaxing collagen-matrigel IPNs (Col-Mat IPN). P-values were determined by performing two-tailed unpaired t-test for  $n=3$  replicates. **b.** Umap plots of phenotyped T cells after embedding in fast and slow relaxing Col-Mat IPNs. Data for b shows pooled samples for  $n=3$  replicates. **c-d.** K-means clustering was performed on pooled T cells from all experimental conditions. **c.** Heatmap plot showing characteristic markers for each cluster. **d.** Heatmap plot showing the frequencies of cells per condition for each cluster. **e.** PCA plot showing relative similarities between the different conditions.

#### 4.4.5 – Extracellular matrix viscoelasticity modulates T cell transcriptomic profile

To investigate how ECM viscoelasticity drives changes in the transcriptional landscape of T cells, scRNA-seq of CD8<sup>+</sup> T cells cultured in fast relaxing and slow relaxing collagen matrices

was next performed. Umap analysis showed distinct localization of the two T cell populations (Figure 4.7a). Global differential expression identified upregulation of several conventional activation and inhibitory T cell markers, including *IL2RA* (CD25), *ENTPDI* (*CD39*) (Figure 4.7b), as well as *FAS*, *TNFRSF4* (*OX40*) and *LAG3* (Appendix A1.3) in slow-relaxing matrices compared to fast-relaxing matrices. In addition, transcription factors that have been implicated in T cell effector phenotype such as *PRDMI* (BLIMP-1) and *ZEB2* were also more highly expressed for T cells cultured in slow relaxing matrices. Of note, several genes related to the AP-1 pathway, including *JUN*, *ATF3*, *BATF* (Figure 4.7b) and *FOS* and *FOSB*, in addition to some mitogen-activated protein kinases such as MAPK8, MAPK6 and MAPK1 (Appendix A1.3) were enriched in T cells cultured in slow relaxing matrices. In contrast, T cells in fast relaxing matrices expressed higher levels of T cell memory markers and memory related transcription factors such as *CD62L*, *KLF2*, *CXCR3* and *SIPR4* (Figure 4.7b, Appendix A1.4).

We next performed consensus non-negative matrix factorization (cNMF)<sup>35</sup> to group genes into expression programs in an unsupervised manner, and investigate programs enriched for T cells in the different microenvironments. cNMF identified 15 gene expression programs, 4 of which were significantly enriched in T cells cultured in slow relaxing matrices and 2 in fast relaxing matrices (Figure 4.7c-d). Module 5 was the most notably enriched module in slow relaxing matrices and included AP-1 pathway-related genes such as *JUN*, *ATF3*, *FOS*, *FOSB* and *JUNB* (Figure 4.7d, Appendix A1.5). Unique genes from the 4 programs enriched in slow relaxing matrices were combined into the Slow-Relaxing Module (SModule), and the 2 programs associated with fast relaxing matrices were grouped into the Fast-Relaxing Module (FModule). Umap overlay of aggregate expression levels of the SModule and FModule showed distinct localizations that mapped to regions of high T cell density in slow relaxing and fast relaxing

matrices respectively (Figure 4.7e). When the expression profiles of FModule and SModule were compared between plate-cultured T cells (i.e., 2D suspension culture with no collagen matrix), and T cells embedded in fast relaxing or slow relaxing collagen matrices, T cells in the slow relaxing collagen matrices were the most different, having the lowest expression of FModule and highest expression of SModule (Figure 4.7f). Pathway enrichment analysis showed that the SModule was enriched for pathways related to TCR signaling, CD8+ T cell activation, and T cell cytotoxicity, indicating a more activated T cell state, while the FModule was enriched for genes related to leukocyte adhesion to endothelial cells (Figure 4.7g).

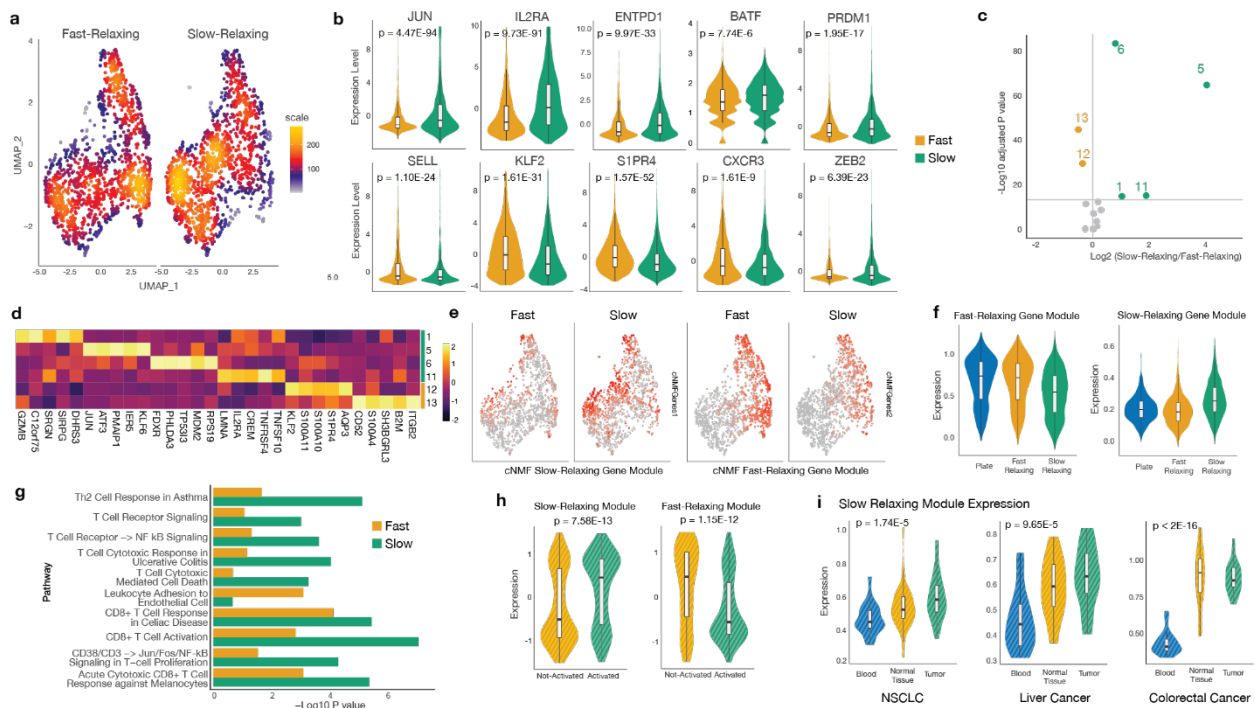


**Figure 4.7, Extracellular matrix viscoelasticity modulates T cell transcriptomic profile.** **a.** ScRNA-seq umap plots showing distinct localization of CD8+ T cells cultured in fast relaxing or slow relaxing collagen matrices. **b.** Violin plots comparing expression levels of selected genes. P-values were determined by performing differential gene expression in Seurat using a negative binomial generalized linear model. **c.** Volcano plot showing significant gene modules identified by consensus non-negative

matrix factorization (cNMF) for T cells in fast relaxing (FModule, orange) and slow relaxing matrices (SModule, green). Module 5 is the most significantly enriched module in slow relaxing matrices. P-values were determined by performing Wilcoxon Rank Sum test adjusted with FDR. Significance threshold:  $-\log_{10}(\text{Adjusted P-value}) > 15$ . **d.** Heatmap of representative genes that characterize FModule (12,13: orange) and SModule (1,2,4,11: green). Unique genes from the 4 SModule programs combined, as well as the 2 FModule programs. **e.** Umap overlay of aggregate expression levels of cNMF FModule and SModule showing distinct localizations that map to regions of high T cell density in fast relaxing and slow relaxing matrices respectively. **f.** Comparison of expression profiles of FModule and SModule between plate-cultured T cells (suspension culture; no collagen matrix condition), T cells in cultured in fast-relaxing and slow-relaxing collagen matrices. P-values were determined by performing two-tailed one-way Anova. **g.** Pathway analysis comparing enriched pathways for FModule and SModule, indicating a more activated T cell state in the SModule. **h.** Violin plots comparing expression levels of SModule and FModule in a published bulk RNA-seq dataset that profiled activated versus non-activated T cells, showing increased relative expression of SModule in activated T cells and vice versa. P-values were determined by performing Wilcoxon Rank Sum test adjusted with FDR. **i.** Violin plots comparing expression levels of SModule for T cells with shared TCR clonotypes in tumors, adjacent normal tissues and blood for NSCLC, liver cancer and colorectal cancer (same dataset used for Figure 4.1a-c). P-values were determined by performing two-tailed one-way Anova.

Next, we applied the gene modules to a series of independently published RNA-seq datasets from both in vitro and in vivo studies to correlate our observed T cell states to independent studies involving T cell activation and tissue localization respectively. In a bulk RNA-seq dataset from activated and non-activated T cells in vitro<sup>36</sup>, the SModule was significantly enriched in activated T cells while the FModule was enriched in the non-activated condition (Figure 4.7h). The SModule was then applied to CD8<sup>+</sup> T cells in tumors, adjacent normal tissue, and blood from the scRNA-seq datasets for NSCLC, liver cancer, colorectal cancer analyzed in Fig 1a-c, for both pan CD8<sup>+</sup> T cells (Figure 4.8) or T cells with shared TCR clonotypes (Figure 4.7i), in addition to a breast cancer dataset for pan CD8<sup>+</sup> T cells (Figure 4.8)<sup>37</sup>. The trends for SModule expression were consistent with those in Figure. 1a-c, with T cells in tumors having the highest expression levels among the three tissue types, T cells in blood having the lowest, and T cells in normal tissue having intermediate expression levels.

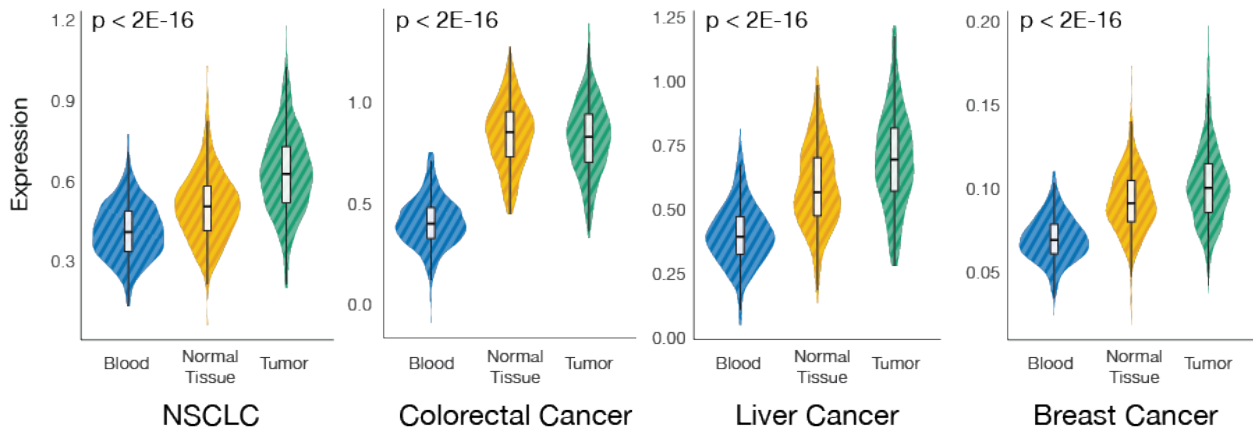


**Figure 4.8, Application of in vitro generated modules to pan T cells in tumor patients.** Violin plots comparing expression levels of SModule for pan CD8+ T cells tumors, adjacent normal tissues and blood for NSCLC, liver cancer and colorectal cancer. P-values were determined by using two-tailed one-way Anova.

#### 4.4.6 – AP-1 Pathway is enhanced in T cells cultured in slow relaxing ECM in vitro, and in tumors and fibrotic tissues in vivo

Due to the observation that multiple AP-1 related genes were enriched in T cells from slow relaxing matrices, we performed AP-1 gene enrichment analysis on the cNMF modules. We saw significant enrichment of the AP-1 pathway in cNMF Module 5 (Figure 4.9a), which was the most notable module in slow relaxing matrices. Consequently, we hypothesized that ECM viscoelasticity modulates the AP-1 pathway, which in turn drives the observed T cell phenotypic profiles. To test the relevance of this hypothesis in vivo, we investigated the expression levels of cNMF Module 5 (AP-1 Module) in T cells derived from tumors, adjacent normal tissue, and blood from scRNA-seq datasets for NSCLC, liver cancer, colorectal cancer for T cells with shared TCR clonotypes (Figure 4.9b). We observed the highest expression levels in tumors, while T cells in blood had the lowest expression levels of the AP-1 Module. T cells in adjacent normal tissues had AP-1 expression levels that were again intermediate.

To examine whether the observations of AP-1 enrichment in T cells are specific to cancer, or more broadly to conditions with altered matrix mechanics, a similar analysis was performed in the context of fibrosis. Fibrosis is generally accompanied by increased ECM deposition and crosslinking<sup>38</sup>, resulting in changes in matrix stiffness and viscoelasticity. We investigated the AP-1 pathway in T cells located in fibrotic tissues by first generating cNMF modules from CD8+ T cell data derived from a published liver cirrhosis scRNA-seq dataset<sup>39</sup> and two IPF datasets<sup>40,41</sup>, which compared fibrotic tissues to adjacent normal tissues. These cNMF modules were generated from the published datasets themselves and were independent of the modules generated in this study in vitro. We then performed AP-1 gene enrichment analyses and saw AP-1 enriched modules in all the fibrosis datasets investigated (Figure 4.9c-d). Importantly, the expression levels of the AP-1 modules were significantly higher in fibrotic tissues than in normal tissues. This trend was maintained when we investigated the expression levels of the in vitro generated AP-1 module in the fibrotic tissues (Figure 4.9e).

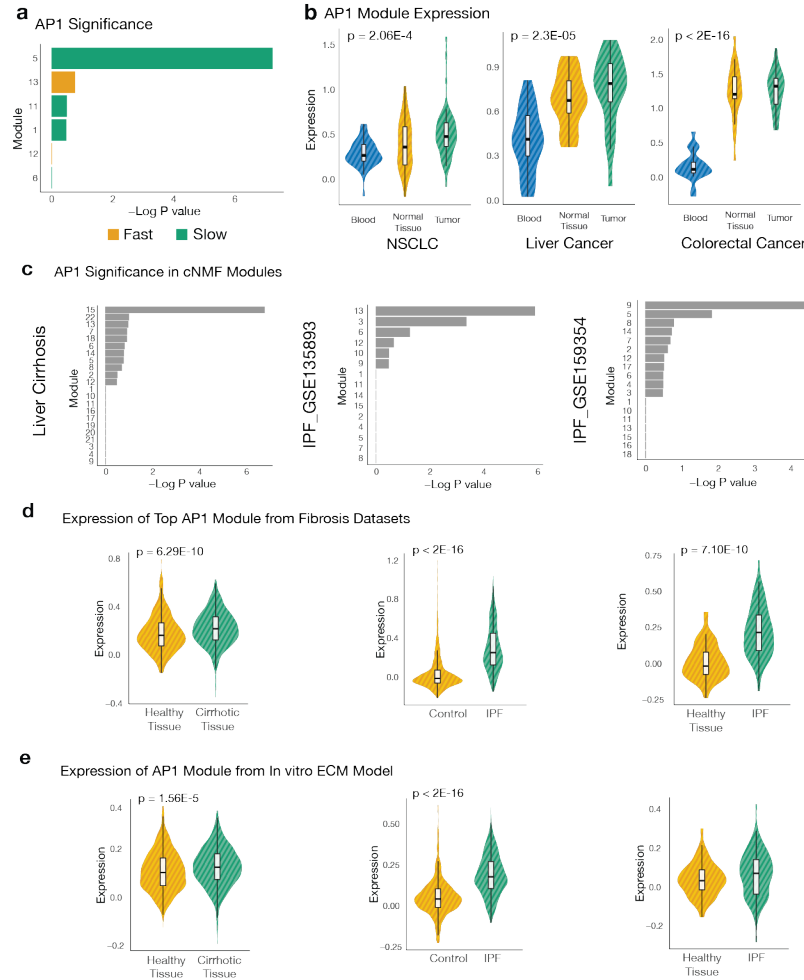


**Figure 4.9, AP-1 pathway is modulated by matrix mechanics.** **a-b.** AP-1 pathway analysis was performed on enriched cNMF modules from Fig 3. **a.** Relative significance of AP-1 related genes in cNMF modules, showing significant AP-1 enrichment in Module 5. **b.** Violin plots comparing expression levels of Module 5 (AP-1 Module) for T cells with shared TCR clonotypes in tumors, adjacent normal tissues and blood for NSCLC, liver cancer and colorectal cancer. P-values were determined by performing two-tailed one-way Anova. **c-d.** AP-1 pathway analysis was performed on cNMF modules generated from the indicated fibrosis datasets. **c.** Relative significance of AP-1 related genes in cNMF modules. **d.** Violin plots comparing the expression levels of the top AP-1 module in CD8<sup>+</sup> T cells derived from healthy and fibrotic tissues for each fibrosis study. **e.** Violin plots comparing expression levels of our *in vitro* generated AP-1 Module in CD8<sup>+</sup> T cells derived from healthy and fibrotic tissues for the same datasets. P-values were determined by using the Wilcoxon Rank Sum test.

The phosphorylation states of a number of transcription factors and kinases related to the AP-1 pathway were next examined to further probe AP-1 transcriptional regulation after T cells are cultured in collagen matrices of varying stiffness and viscoelasticity (Figure 4.10a). For all

transcription factors investigated, there was increased phosphorylation in T cells cultured in slow relaxing matrices for both CD4+ and CD8+ T cells. Principal component analysis (PCA) revealed that ECM viscoelasticity was the main driver of the differential phosphorylation states (Figure 4.10b). In addition to c-Jun and p-c-Jun, PCA loadings identified features such as pPyk2, pPlcg1, pPlcg2, pMAPK8, pMAPK14 and pCD3z as important factors underlying the observed PCA trend (Figure 4.10c).

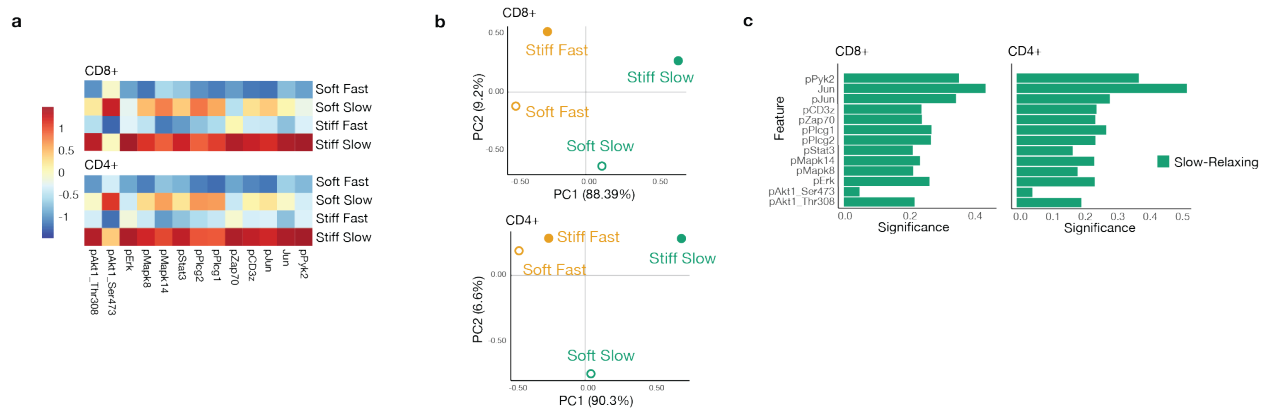


**Figure 4.10, Phosphorylation states of transcription factors and kinases known to impact or be impacted by AP-1. a.** Heatmap plots comparing expression and phosphorylation levels of different transcription factors and kinases for the different gel conditions. **b.** PCA plots comparing the relative similarities between the different collagen conditions. **c.** PCA loadings for PC1 showing the relative significance of features that drive the observations in b. Data shows pooled samples for n=3.

#### 4.4.7 – Matrix viscoelasticity impacts pattern of AP-1 protein expression

We next examined the patterns of AP-1 protein expression and their interactions, specifically with c-Jun, due to their importance in the regulation of T cell phenotype and function<sup>42</sup>. In particular, c-Jun and c-Fos are canonical AP-1 partners that have been shown to enhance IL2 production<sup>42</sup>. BATF promotes effector T cell differentiation but also drives exhaustion<sup>43–45</sup>. JunB



has been shown to enhance Th17 differentiation and IL2 production, but also promotes T cell exhaustion and effector Treg differentiation<sup>46-49</sup>. Flow cytometry analyses after culturing T cells in fast and slow relaxing matrices showed that T cells cultured in slow relaxing matrices had enhanced expression of c-Jun, c-Fos, and BATF (Figure 4.11a-b). Additionally, T cells from slow relaxing matrices exhibited higher interaction of c-Fos, JunB and BATF with c-Jun, as analyzed by c-Jun co-immunoprecipitation of cell lysates to assess AP-1 binding partners (Figure 4.11c).

The ability of c-Jun to mediate effects of viscoelasticity on T cell phenotype was directly tested by blocking c-Jun function with the SP600125 Jun N-terminal kinase inhibitor<sup>50</sup>. Umap and K-means analyses of T cell phenotypes showed that SP600125 abrogated the effects of matrix viscoelasticity (Figure 4.11d) and led to increased expression of memory markers in all conditions (Figure 4.11e). PCA analysis confirmed these results. The slow relaxing matrix without SP600125, and all conditions with SP600125 were located at the two extremes of PC1, while plate culture and fast relaxing matrix conditions without SP600125 were intermediate (Figure 4.11f). Together, these findings demonstrate that the patterns of AP-1 protein expression and their interactions with c-Jun can be modulated by ECM viscoelasticity.

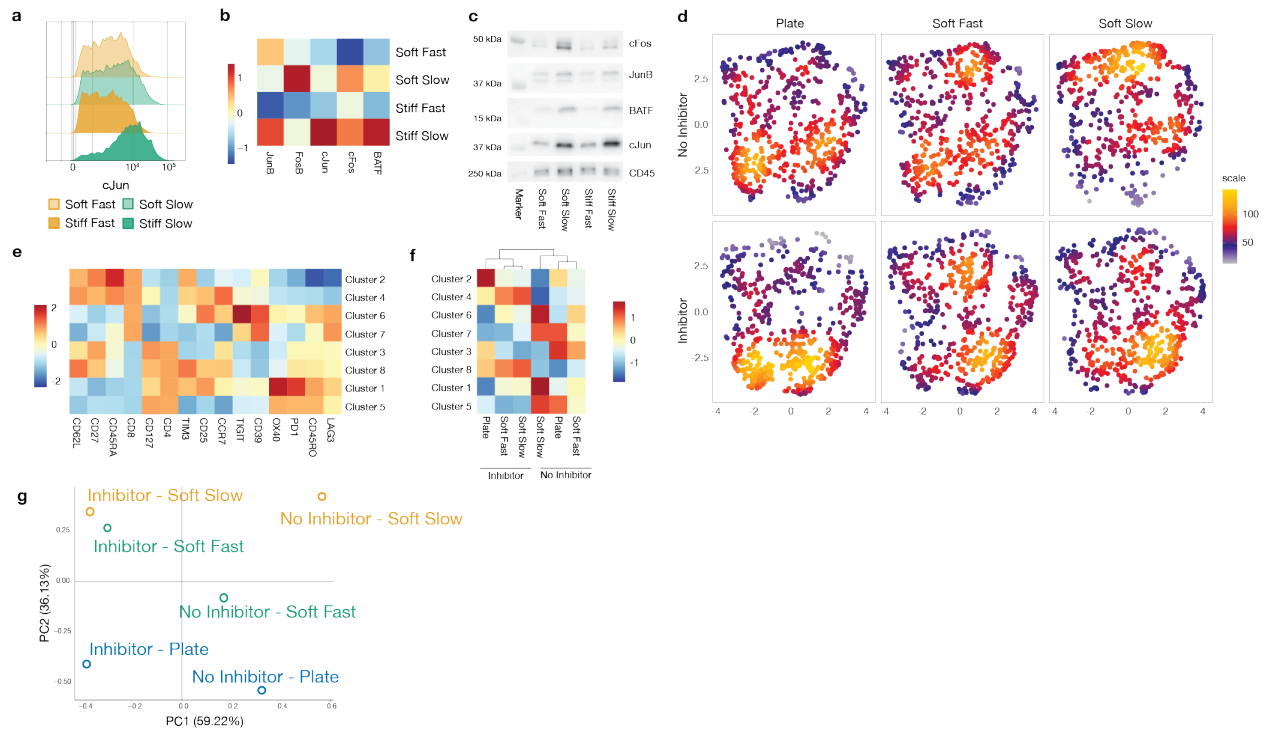


**Figure 4.11, T cell populations generated from ECM with different viscoelasticity have different patterns of AP-1 protein expression that can be abrogated by inhibitors.** **a.** Representative flow cytometry histograms showing relative expression of c-Jun for T cells cultured in fast relaxing and slow relaxing, soft and stiff matrices after acute activation. **b.** Heatmap plot showing relative expression of indicated AP-1 proteins for T cells cultured in the different collagen conditions. **c.** c-Jun co-immunoprecipitation was performed to probe for c-Jun binding partners. Western blots compare relative amounts of indicated proteins bound to c-Jun as a function of the different mechanical conditions. Data shows pooled samples n=2-4. **d.** Umap plots of plate-cultured T cells and T cells cultured in fast or slow relaxing matrices with or without the SP600125 Jun N-terminal kinase inhibitor. **e-g.** K-means clustering was performed on pooled T cells from all experimental conditions. **e.** Heatmap plot showing characteristic markers for each cluster. **f.** Heatmap plot showing the frequencies of cells per condition for each cluster. **g.** PCA plot showing the relative similarities between the different conditions.

#### 4.4.8 – ECM viscoelasticity does not select for specific T cell clones

To assess whether the observed phenotypic differences imparted by matrix viscoelasticity are due to the selection and persistence of specific T cell clones, we performed single cell RNA-sequencing with TCR sequencing using T cells from a different donor. Umap analysis on pan T cells from the different conditions showed distinct localization of T cells from plate-culture, fast

relaxing and slow relaxing matrix conditions (Figure 4.12a). The Slow-Relaxing Module (SModule), generated from the previous scRNA-seq in Figure. 3, was applied to pan T cells from this dataset to investigate consistency across different donors. The trends for SModule expression were consistent with those in Figure 4.7, with T cells cultured in slow relaxing matrices having the highest expression of SModule (Figure 4.12b).

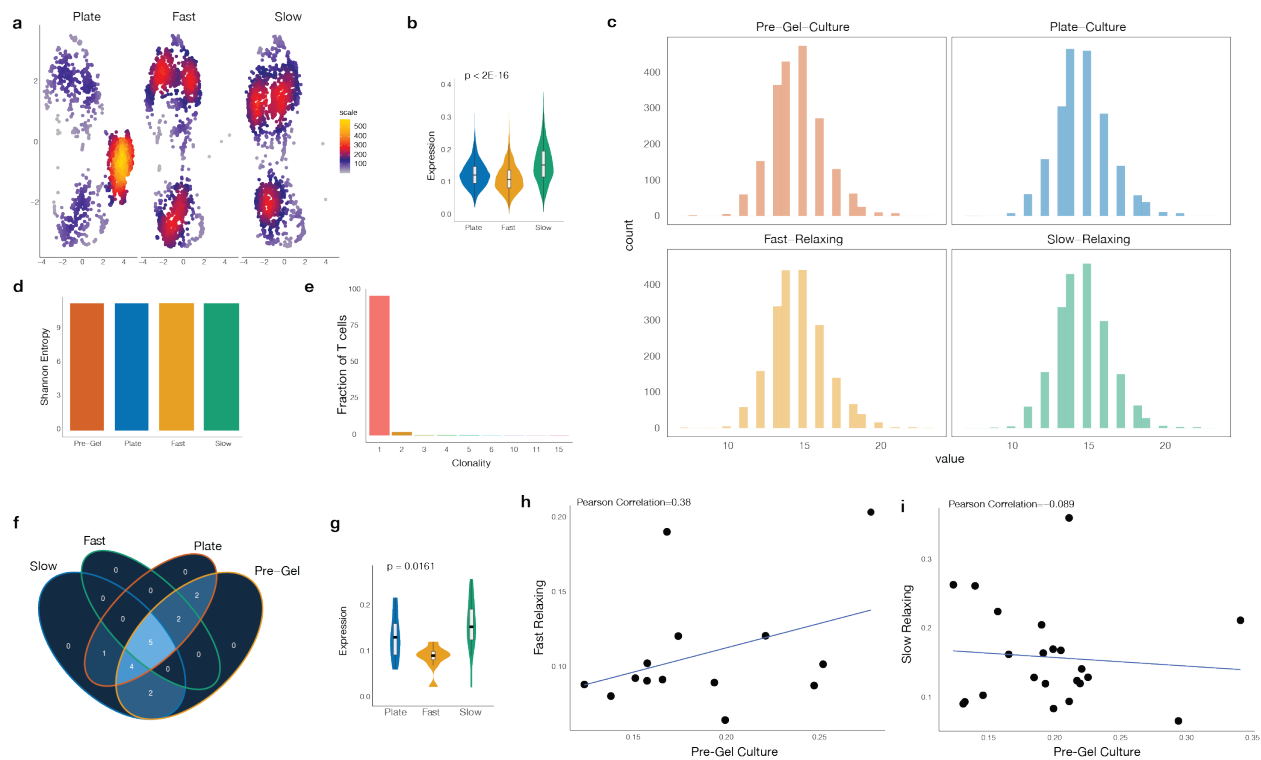


**Figure 4.12, ECM viscoelasticity does not select for specific T cell clones.** **a.** ScRNA-seq umap plots showing distinct localization of plate-cultured T cells, T cells cultured in fast relaxing or slow relaxing collagen matrices for a different donor. **b.** Violin plot comparing the expression levels of the Slow-Relaxing Module (SModule) generated in Figure 4.7 for the different matrix conditions. P-values were determined by performing two-tailed one-way Anova. **c.** Histograms showing TCR $\beta$  CDR3 length distributions. Pre-Gel condition refers to the parent T cell population before they were embedded in the matrices. **d.** Shannon entropy plot comparing clonotypic diversity between the different conditions. **e.** Plot showing the proportions of combined T cells from all experimental conditions with unique TCRs and various degrees of clonality. **f-g.** Venn diagrams showing the distribution of dominant clones (**f**) across the different conditions. **g.** Violin plot comparing the expression levels of SModule for T cells with shared TCRs. P-values were determined by performing two-tailed one-way Anova. **h-i.** Pearson

correlation plots for individual T cell clones before and after their culture in fast relaxing **(i)** or slow relaxing **(j)** collagen matrices.

To explore the potential of ECM viscoelasticity in skewing the TCR, the profile of T cell receptor  $\beta$  (TR $\beta$ ), a component of the TCR heterodimer, was investigated. Similar frequency distributions were observed for the different TR $\beta$ V genes as a function of ECM condition (Figure 4.13a). In addition, a Venn diagram of the TR $\beta$ V genes showed that 96% of the genes were present in all the conditions (Figure 4.13b). Shannon entropy, which estimates the diversity within a specific population, showed similar TR $\beta$ V diversity between T cells cultured in fast relaxing matrices, slow relaxing matrices, and plate-culture, as well as their parent T cell population (Pre-Gel) (Figure 4.13c). Importantly, when the SModule was applied to the T cells grouped by TR $\beta$ V gene, the slow relaxing matrices had the highest expression across all TR $\beta$ V genes (Figure 4.13d).



derived from the various matrix conditions were transcriptomically different, with the T cells cultured in slow relaxing matrices having the highest expression of the SModule (Figure 4.12g). We also hypothesized that if the matrix is acting by selecting specific T cell clones, whose phenotypes persist over time, then there should be a correlation between the transcriptomic profiles of those T cell clones before and after matrix culture. However, correlation analysis between individual T cell clones before and after their culture in collagen matrices showed weak correlation for the fast relaxing matrix condition (Pearson correlation=0.38) and no correlation for the slow relaxing matrix condition (Pearson correlation=-0.089) (Figure 4.12h-i). Together, these findings suggest that ECM viscoelasticity directly modulates T cell phenotype, and does not select specific T cell clones which persist over time.

#### *4.4.9 – ECM viscoelasticity imprints long-term T cell phenotype*

To investigate the extent to which the differences in T cell phenotypes persist after being exposed to matrices with different viscoelasticity, T cells were first embedded in either fast or slow relaxing collagen matrices for 3 days, after which they were cultured in suspension for 4 days. The T cells expanded and remained viable post matrix culture (Figure 4.14a). Umap, K-means and PCA analyses showed that T cell phenotypes remained distinct after 4 days of suspension culture, with T cells harvested from slow-relaxing matrices being enriched in clusters with higher expression of activation markers: clusters 4, 5, 6, 8 (Figure 4.14b-c). Importantly, this trend was maintained when the T cells harvested from the various matrix conditions were re-stimulated with dynabeads in suspension (Figure 4.14f-j).

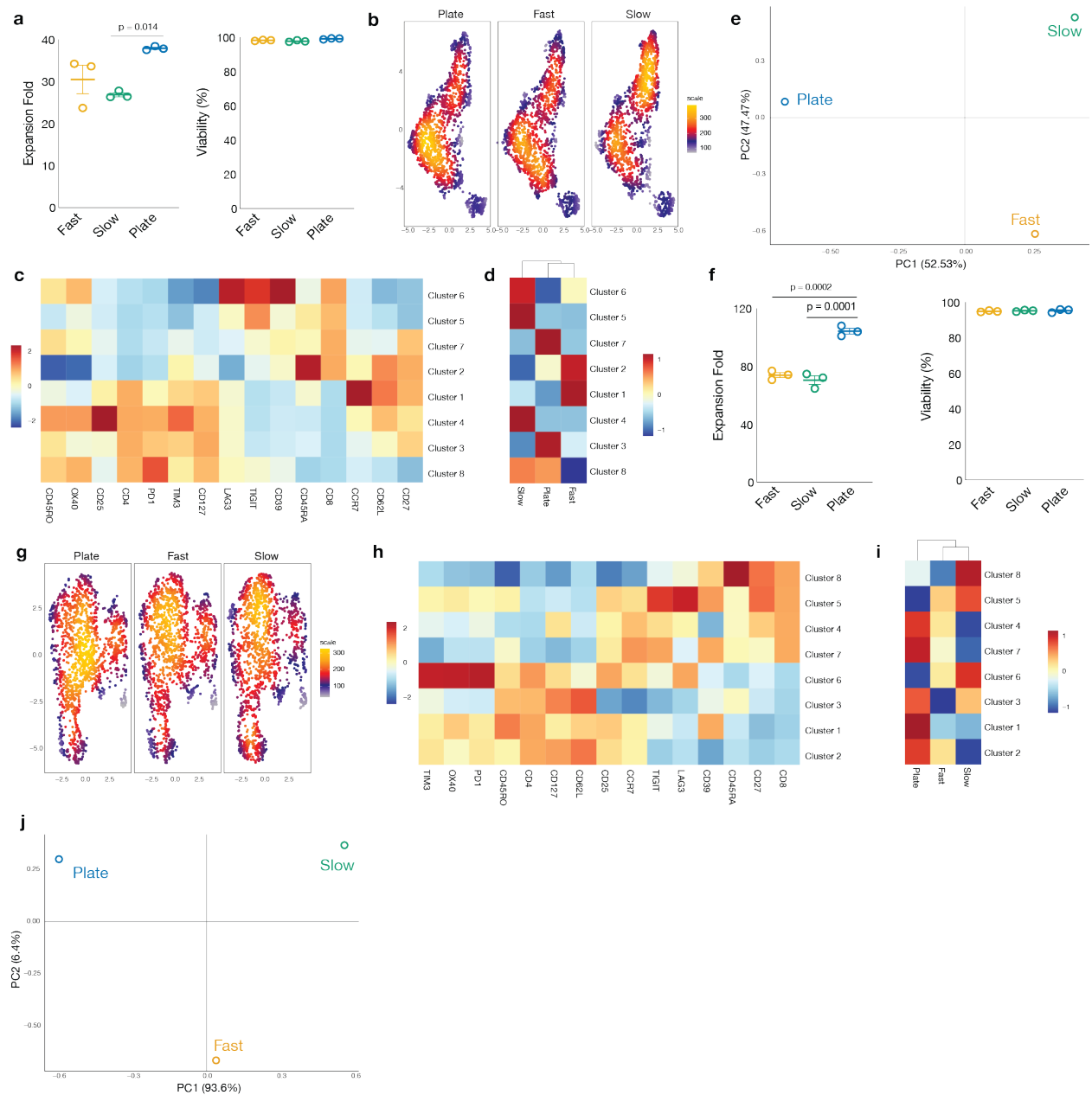


**Figure 4.14, T cell phenotypes persist after they are harvested from matrices.** T cells were first cultured on plates or in fast relaxing or slow relaxing collagen matrices, after which they were harvested and subsequently cultured in suspension with or without dynabead restimulation. **a-e.** T cell phenotyping without dynabead restimulation. **a.** Expansion fold (left) and viability (right) of T cells cultured in suspension after they were harvested from their indicated matrices. **b.** Umap plots of phenotyped T cells. **c-d.** K-means clustering was performed on pooled T cells from all experimental conditions. **c.** Heatmap plot showing characteristic markers for each cluster. **d.** Heatmap plot showing the frequencies of cells per condition for each cluster. **e.** PCA plot showing relative similarities between the different conditions. Data for b-d show pooled samples for  $n=3$  replicates. **f-j.** Similar analyses as a-e but for T cells cultured with dynabead restimulation.

To further explore the role of ECM viscoelasticity on imprinting long-term T cell phenotype, T cells were serially passaged as follows: from fast relaxing to fast relaxing matrices (Fast-Fast), from fast relaxing to slow relaxing matrices (Fast-Slow), from slow relaxing to fast relaxing matrices (Slow-Fast) and from slow relaxing to slow relaxing matrices (Slow-Slow) (Figure 4.15a). Flow cytometry analyses revealed an impact of the prior matrix condition on the phenotype of the T cells in the latter matrix. In particular, Umap, K-means and PCA analyses showed that T cells from Fast-Fast and Slow-Slow conditions were the most different, with the Fast-Slow and Slow-Fast conditions being intermediate (Figure 4.15b-e). Importantly, when the Euclidean distances between a) Fast-Fast and Fast-Slow and b) Slow-Slow and Slow-Fast conditions were compared, it was found that there was a greater distance between Fast-Fast and Fast-Slow (more dissimilar) than Slow-Slow and Slow-Fast conditions, suggesting that slow relaxing matrices had a greater impact on modulating T cells that have been previously cultured in fast relaxing matrices than vice versa (Figure 4.15f).

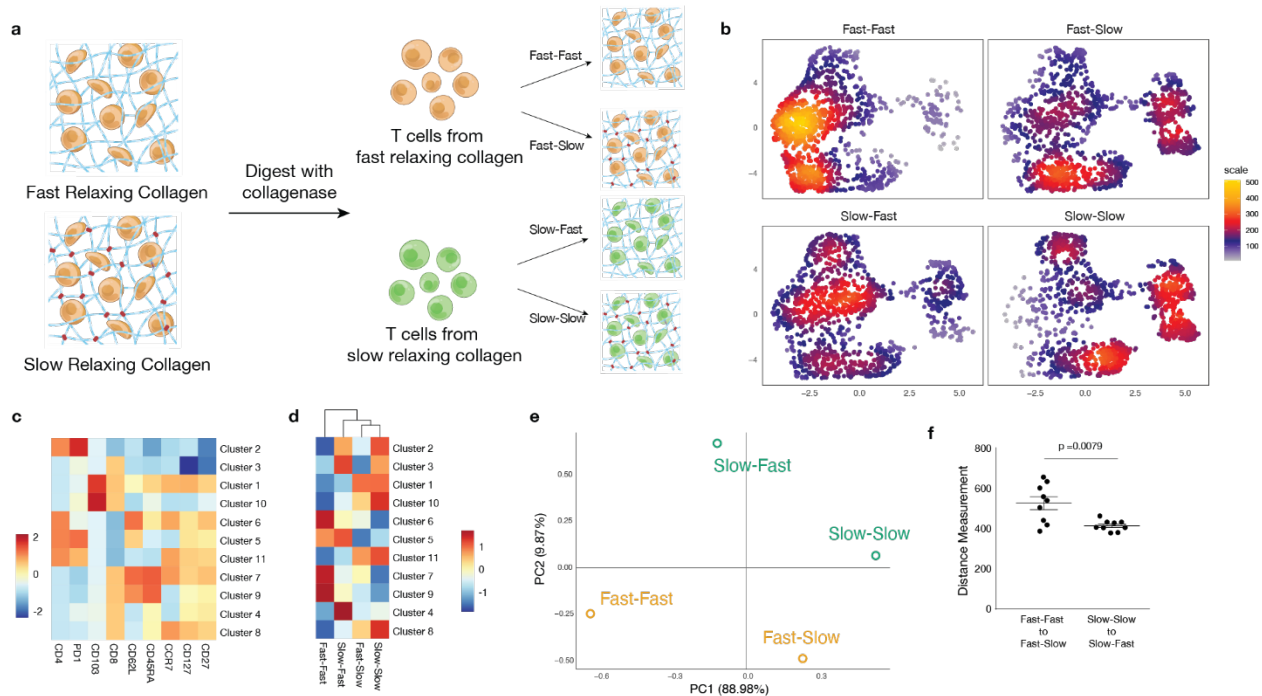




**Figure 4.15, Prior matrix condition influences the phenotype of serially passaged T cells. a.** Schematic of serial passaging experiment. T cells were either cultured in fast relaxing or slow relaxing matrices for 3 days, after which the cells were harvested and serially passaged as follows: fast relaxing to fast relaxing matrices (Fast-Fast), fast relaxing to slow relaxing matrices (Fast-Slow), slow relaxing to fast relaxing matrices (Slow-Fast) and slow relaxing to slow relaxing matrices (Slow-Slow) for an additional 4 days before analysis. **b.** Umap plots after performing flow cytometry on serially passaged T cells. **c-d.** K-means clustering was performed on pooled T cells from all experimental conditions. **c.** Heatmap plot showing characteristic markers for each cluster. **d.** Heatmap plot showing the frequencies of cells per condition for each cluster. **e.** PCA plot showing the relative similarities between the different conditions. **f.** Plot comparing the estimated Euclidean distances between the indicated conditions. P-values were determined by performing two-tailed unpaired t test with Welch's correction, with 9 pair-wise measurements from n=3 replicates.

We next profiled T cells after embedding them in collagen matrices for different timepoints (3 days and 7 days), and subsequently culturing the cells in suspension to investigate if the effects of ECM viscoelasticity on imprinting T cell phenotype is time dependent. Consistent with previous observations, T cell phenotype was modulated by ECM viscoelasticity at both harvest timepoints (Figure 4.16a-e). When T cells were harvested from collagen matrices on days 3 and 7, and subsequently cultured in suspension for 7 additional days, they maintained the T cell phenotype imprinted by the specific matrix mechanical properties in a manner dependent on the duration of initial gel culture (Figure 4.16f).

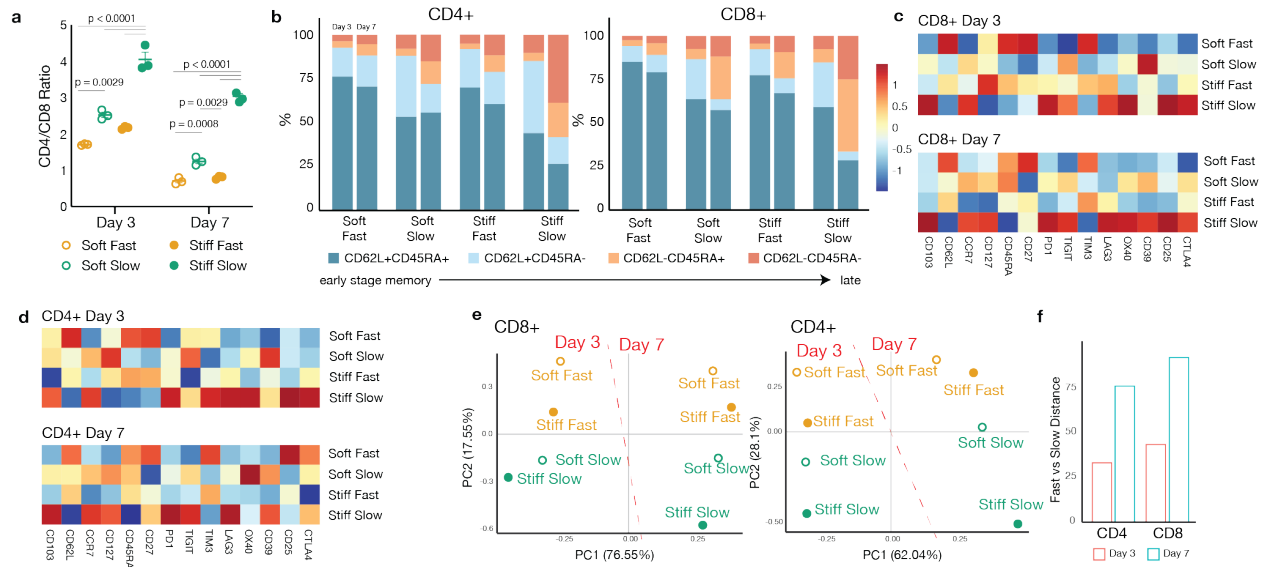
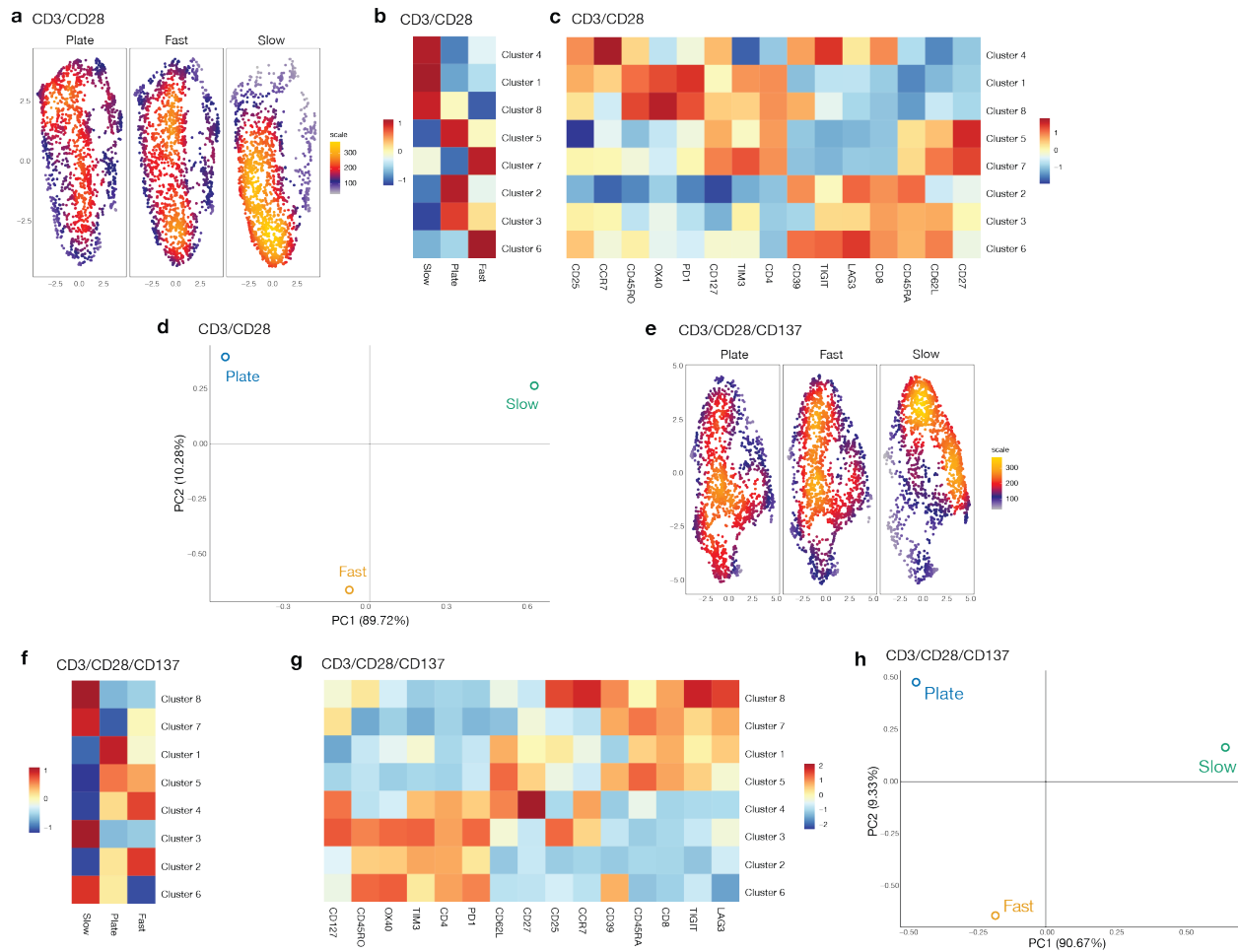


**Figure 4.16, Extended profiling and long-term imprinting of T cell Phenotype.** **a.** CD4/CD8 ratios of T cells cultured in fast relaxing and slow relaxing, soft and stiff collagen gels for 3 days and 7 days. P-values were determined by performing two-tailed one-way Anova with Tukey post-hoc test. Data shows  $n=3$  samples. **b.** CD62L and CD45RA expression profiles for CD4+ and CD8+ T cells cultured in different collagen conditions for 3 days and 7 days. **c-d.** Heatmaps for CD8+ T cells (c) and CD4+ T cells (d) showing relative marker expression levels between the different gel conditions. **e.** PCA plots showing relative similarities between the different collagen conditions for CD4+ and CD8+ T cells. **f.** Imprinting of T cell phenotype: T cells were harvested from collagen gels after 3-day and 7-day gel culture and further cultured in suspension for 7 days. The plot shows pairwise distances between T cells harvested from fast relaxing and slow relaxing collagen gels after suspension culture, showing greater differences between T cells cultured in collagen gels for 7 days. Data shows pooled samples  $n=3$ .

#### 4.4.10 – ECM viscoelasticity modulates the phenotypes of T cells subjected to different modes of prior activation

To understand the generalizability of ECM viscoelasticity in modulating T cell phenotypes in relation to mode of prior activation, T cells were either activated with CD3/CD28 or CD3/CD28/CD137 dynabeads, before embedding in collagen matrices, with the latter known to enhance memory T cell enrichment<sup>51</sup>. Consistent with previous data, flow cytometry analyses showed an impact of ECM viscoelasticity in modulating T cell phenotype after CD3/CD28 activation. Umap, K-means, and PCA analyses confirmed these differences, with T cells

harvested from slow-relaxing matrices being enriched in clusters with higher expression of activation markers: Clusters 1, 4, 8 (Figure 4.17a-d). Importantly, these phenotypic differences were maintained when the T cells were activated with CD3/CD28/CD137 dynabeads prior to matrix culture (Figure 4.17e-h).



**Extended Fig.11 ECM viscoelasticity modulates the phenotypes of T cells subjected to different modes of prior activation.** **a.** Umap plots of phenotyped T cells after stimulation with aCD3/aCD28 dynabeads. **b-c.** K-means clustering was performed on pooled T cells from all experimental conditions. **b.** Heatmap plot showing the frequencies of cells per condition for each cluster. **c.** Heatmap plot showing characteristic markers for each cluster. **d.** PCA plot showing relative similarities between the different conditions. Data for a-d show pooled samples for n=3 replicates. **e-h.** Similar analyses as a-d but for T cells stimulated with aCD3/aCD28/aCD137 dynabeads.

#### *4.4.11 – Tuning matrix viscoelasticity leads to functionally distinct T cells.*

We next investigated whether T cell populations that are functionally distinct resulted from culture in the engineered matrices with distinct levels of viscoelasticity, and how these populations would evolve when the strength of stimulation are altered. First, anti-CD19 CAR T cells were cultured in ECM with varying stiffness and viscoelasticity after exposure to different strengths of antigenic stimulation, phenotypically profiled and functionally tested for their cytotoxic potential and effector cytokine production upon co-culture with Raji tumor cells. Umap analyses of T cell phenotypes showed distinct localization of T cells cultured in fast relaxing and slow relaxing collagen matrices for all the activation regimes tested (Figure 4.18a, Figure 4.19a-b). T cells in slow relaxing matrices expressed higher levels of activation and inhibitory markers and lower levels of memory markers (Figure 4.18b-c). Functionally, anti-CD19 CAR T cells cultured in slow relaxing matrices showed higher killing of Raji tumor cells in vitro, with these differences being more substantial as the level of acute stimulation was increased (Figure 4.18d). Increased killing capacity was accompanied by higher expression of a number of effector molecules, including IL2, Granzyme B, and TNF- $\alpha$  (Figure 4.18e). The increased cytotoxicity observed for T cells cultured in slow relaxing matrices was highly positively correlated with the expression of c-Jun, c-Fos and BATF (Figure 4.19c). Similar results were obtained when the in vitro cytotoxicity experiment was repeated with a different donor, including a plate-cultured T cell condition (i.e., no collagen matrix condition). Umap, K-means, and PCA analyses of T cell cytokine profiles after co-culture of anti-CD19 CAR T cells with Raji tumor cells showed differential cytokine profiles dependent on the matrix condition (Figure 4.20a-e). This

corresponded to differences in T cell cytotoxicity, with T cells cultured in slow-relaxing matrices showing the highest killing compared with plate-cultured T cells and T cells cultured in fast-relaxing matrices (Figure 4.20f).

We next explored T cell functionality as a function of viscoelasticity for TCR T cells using a different tumor type and in a different species to understand the generalizability of these observations. We first cultured mouse Pmel-1 T cells, which recognize the gp100 epitope on B16-F10 melanoma cells<sup>52,53</sup>, in collagen matrices of different viscoelasticity, and subsequently co-cultured these T cells with B16-F10 tumor cells. Pmel-1 T cells cultured in slow relaxing matrices had the best killing relative to plate-culture and fast relaxing matrix conditions (Figure 4.20g).

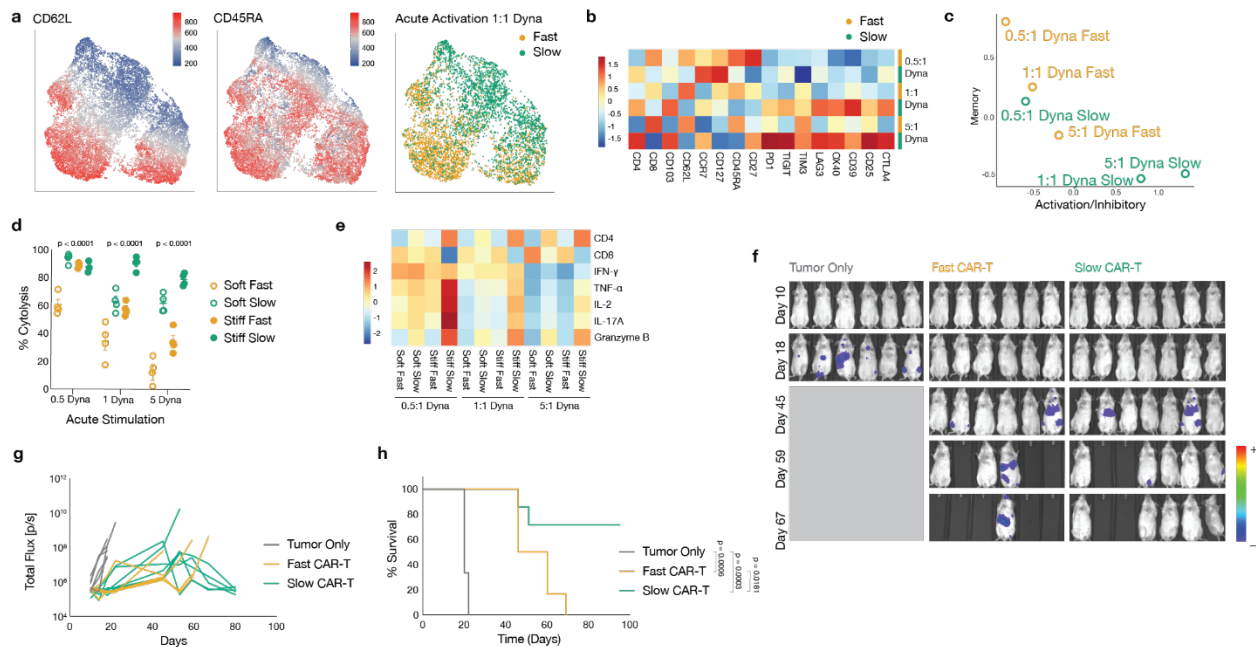


**Figure 4.18, Tuning ECM viscoelasticity results in the generation of functionally distinct T cells. a-e,** T cells were activated for 4 days using different dynabead to T cell ratios and subsequently cultured in

fast relaxing or slow relaxing matrices. **a.** Representative umap plots of CD8<sup>+</sup> T cells showing expression of CD62L (left) and CD45RA (center), as well as localization of T cells cultured in either fast relaxing or slow relaxing matrices (right). **b.** Heatmap plot showing relative marker expression as a function of fast relaxing (orange) and slow relaxing (green) matrices for the different dynabead to T cell ratios. **c.** Plot comparing memory (CD62L, CCR7, CD127, CD45RA, CD27) and activation/inhibitory (PD1, TIGIT, TIM3, LAG3, OX40, CD39, CD25, CTLA4) signatures for T cells cultured in fast relaxing and slow relaxing matrices. Data shows pooled samples n=3. **d.** Differential levels of anti-CD19 CAR T cell killing of Raji cells after culturing in different collagen conditions. P-values were calculated by using two-tailed one-way Anova for n=3-4 samples. **e.** Heatmap plot showing production of different cytokines and effector molecules by anti-CD19 CAR T cells after co-culture with Raji cells. **f-h.** Luciferized Raji xenograft lymphoma model. **f-g.** IVIS images (f) and total flux (g) of Raji tumor burden in NSG mice for the indicated conditions. **h.** Kaplan-Meier survival curves of mice from the indicated treatment groups. P-values were determined by Log-rank (Mantel-Cox) test. Data are n=6 or 7 mice per condition

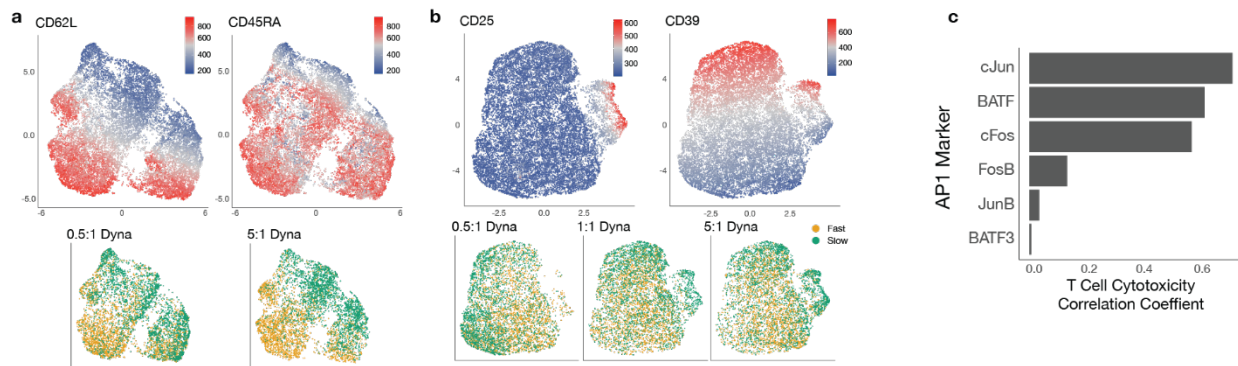


**Figure 4.19, Characterizing T cell phenotype and AP-1 correlation with T cell cytotoxicity. a.** Representative umap plots of CD8<sup>+</sup> T cells showing expression of CD62L (left) and CD45RA (right), as well as localization of T cells (bottom) cultured in either fast relaxing or slow relaxing gels, after T cells are activated with different dynabead to T cell ratios. **b.** Representative umap plots showing expression of CD25 (left), CD39 (right) and T cell localization (bottom) of the same collagen conditions used in a. Data shows pooled samples n=3. **c.** Correlation analyses showing how the expression of indicated AP-1 proteins for T cells cultured in the different mechanical conditions correlate with their observed killing of Raji cells.

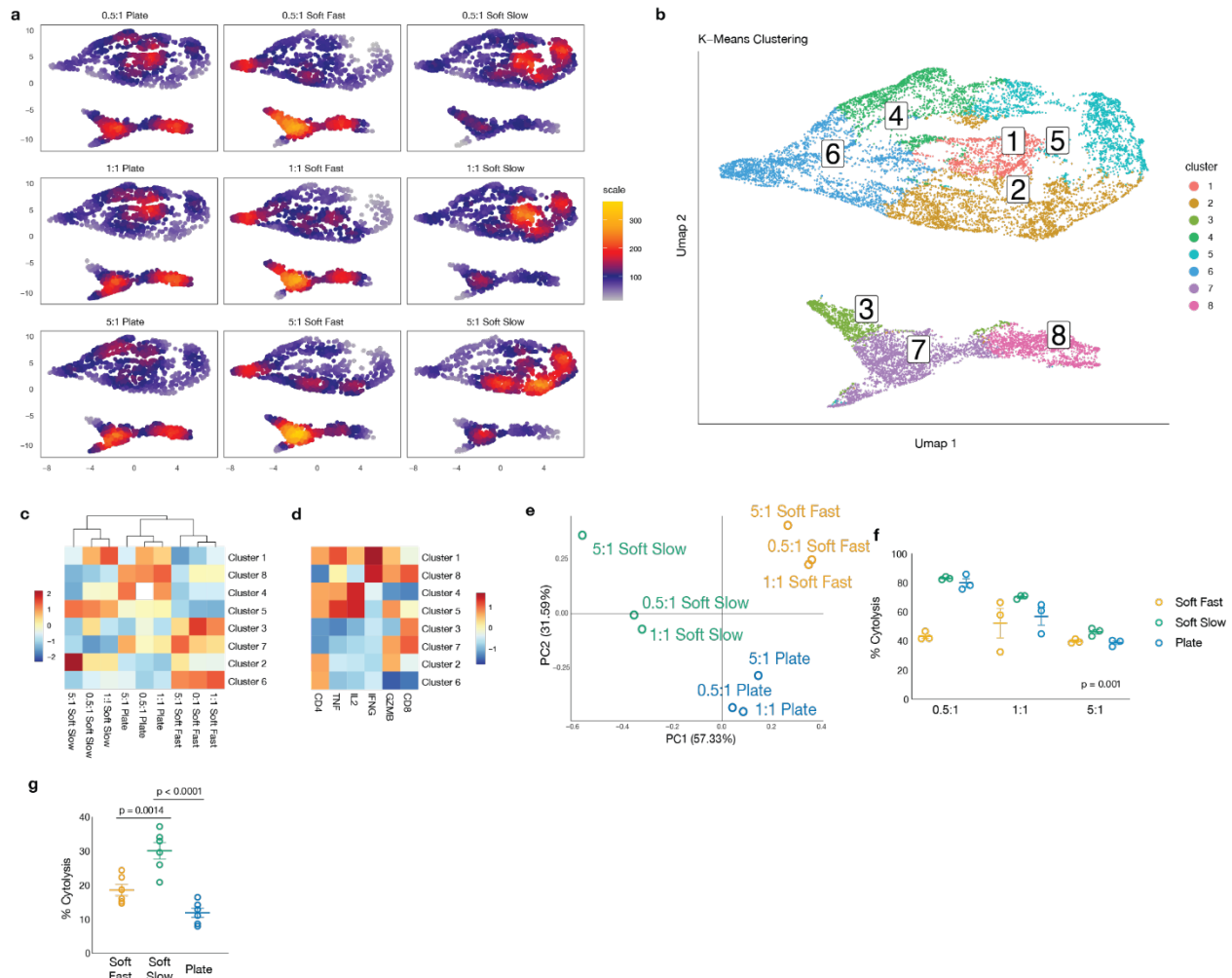


**Figure 4.20, T cells from different matrix conditions are functionally distinct against different tumor types.** **a-e.** Human anti-CD19 CAR T cells were first activated using different dynabead to T cell ratios, subsequently cultured in fast relaxing, slow relaxing matrices or plate-culture and then co-cultured with Raji tumor cells. **a.** Umap plots of anti-CD19 CAR T cells phenotyped for their intracellular cytokine profiles after co-culture with Raji tumor cells. **b-d.** K-means clustering was performed on pooled T cells from all experimental conditions **b.** Umap plot of T cells overlaid with corresponding K-means clusters. **c.** Heatmap plot showing characteristic markers for each cluster. **d.** Heatmap plot showing the frequencies of cells per condition for each cluster. **e.** PCA plot showing relative similarities between the different conditions. Data shows pooled samples n=3. **f.** Differential levels of anti-CD19 CAR T cell killing of Raji cells after plate-culture or culturing in different matrix conditions. P-values were calculated by using two-way Anova for n=3 samples per dynabead stimulation level. **g.** Mouse Pmel-1 T cells were cultured in fast relaxing, slow relaxing matrices or plate-culture and subsequently co-cultured with B16-F10 melanoma cells. Plot shows differential killing of B16-F10 tumor cells by Pmel-1 T cells. P-values were determined by performing two-tailed one-way ANOVA for n=6, 2 independent experiments.

To investigate if the in vitro functional differences corresponded to in vivo therapeutic outcomes, anti-CD19 CAR T cells cultured in fast and slow relaxing matrices were adoptively transferred into tumor-bearing mice in a luciferized Raji xenograft lymphoma model. IVIS imaging of Raji tumor burden and mouse survival showed consistency between in vitro and in vivo observations. NSG mice treated with anti-CD19 CAR T cells first cultured in slow relaxing matrices had lower tumor burden and significantly better survival than mice treated with the same number of T cells from fast relaxing matrices (Figure 4.18f-h).

#### *4.4.12 – ECM viscoelasticity modulates the phenotype and function of T cells undergoing chronic stimulation*

We sought to assess the effects of ECM viscoelasticity on T cells undergoing chronic stimulation in the matrices, specifically investigating their AP-1 protein expression and interactions, as well as their phenotype and function. To achieve chronic stimulation within the matrices, we utilized Transact, 50 nm polymeric nanoparticles conjugated with aCD3/aCD28<sup>54</sup>, as their small size is expected to minimally impact the bulk mechanics of the gel, and enable them to freely diffuse within the micron-scale pores of the gels. AP-1 protein analysis of T cells chronically stimulated in slow relaxing matrices maintained higher expression of c-Jun (Figure 4.21a-b), BATF, and JunB but expressed lower levels of c-Fos compared with cells in corresponding fast relaxing matrices (Figure 4.21b). c-Jun co-immunoprecipitation of cell lysates showed that T cells that received chronic stimulation in slow relaxing matrices had higher binding of JunB and BATF but not c-Fos (Figure 4.21c). Importantly, the amount of JunB and BATF bound to c-Jun increased markedly when the T cells were cultured in slow relaxing matrices with chronic stimulation, as compared to T cells in fast relaxing matrices (Figure 4.21c). In terms of the changes in the



individual AP-1 proteins between acute and chronic stimulation, larger increases in BATF and JunB expression were found for slow relaxing matrices after chronic stimulation, while c-Fos, FosB, and c-Jun increased more with fast relaxing matrices (Figure 4.21d).

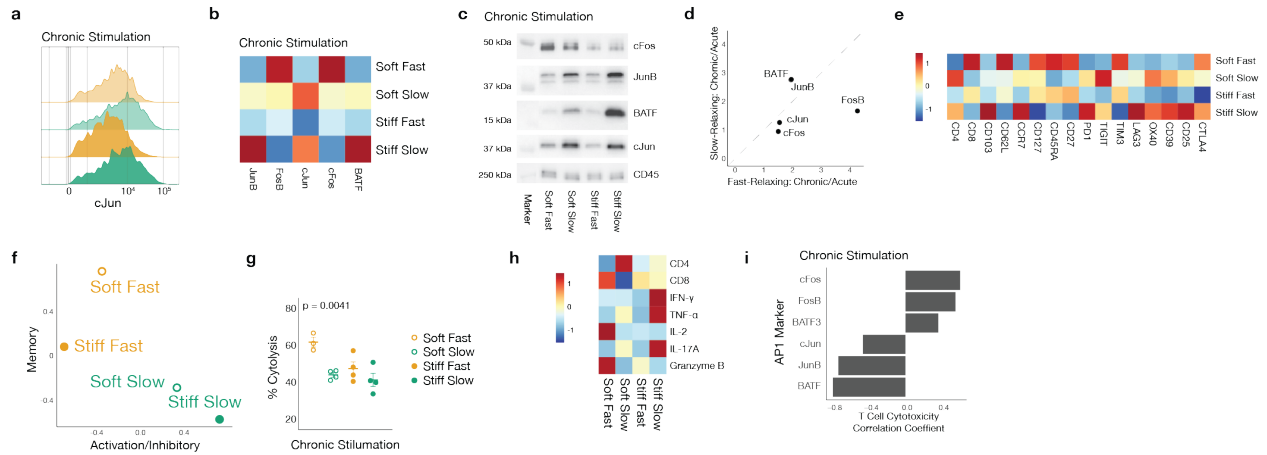


**Figure 4.21, ECM viscoelasticity modulates the phenotype and function of T cells undergoing chronic stimulation.** **a-d.** Determination of AP-1 protein expression and interactions after chronic stimulation in matrices. **a.** Representative flow cytometry histograms showing relative expression of c-Jun for T cells cultured in fast relaxing and slow relaxing, soft and stiff matrices after chronic stimulation. **b.** Heatmap plot showing relative expression of indicated AP-1 proteins for T cells cultured in the different collagen conditions after chronic stimulation. **c.** c-Jun co-immunoprecipitation was performed to probe for c-Jun binding partners. Western blots compare relative amounts of indicated proteins bound to c-Jun as a function of the different mechanical conditions. **d.** Comparison of the extent to which the individual AP-1 proteins changed between T cells with and without chronic stimulation for the different gel conditions. Data shows pooled samples n=2-4. **e-f.** T cell phenotyping after chronic stimulation in collagen matrices. **e.** Heatmap plot comparing marker expression for the different collagen conditions. **f.** Plot showing memory and activation/inhibitory signatures for T cells cultured in the different gel conditions receiving chronic stimulation. Data shows pooled samples n=2-4. **g.** Differential levels of anti-CD19 CAR T cell killing of Raji cells after chronic stimulation in collagen matrices. P-values were calculated by using two-tailed one-way Anova for n=3-4 samples. **h.** Heatmap plot showing production of different cytokines and effector molecules by chronically stimulated anti-CD19 CAR T cells after co-culture with Raji cells. **i.** Correlation analyses showing how the expression of indicated AP-1 proteins for T cells cultured in the different mechanical conditions correlate with their observed killing of Raji cells after chronic stimulation.

Finally, anti-CD19 CAR T cells were cultured in matrices with chronic stimulation, phenotypically profiled and tested for their cytotoxic potential and effector cytokine production.

Phenotypic analyses revealed that T cells in slow relaxing matrices showed higher expression of activation and inhibitory markers and lower memory marker expression (Figure 4.21e-f). In contrast to T cells without chronic stimulation, the T cells from slow relaxing matrices exhibited poorer killing capacity than those in fast relaxing matrices after chronic stimulation (Figure 4.21g). This inverse killing trend corresponded to impaired IL2 and lower Granzyme B production in T cells cultured in slow relaxing matrices, even though they generally maintained higher levels of IFN- $\gamma$  and TNF- $\alpha$  (Figure 4.21h). c-Jun, BATF and JunB expression were found to be negatively correlated with cytotoxic potential when the T cells received chronic stimulation in the matrices (Figure 4.21i), while c-Fos remained positively correlated with T cell cytotoxic potential.

#### **4.5 – Discussion**

A collagen type I based ECM model was engineered that allows for independent tuning of matrix stiffness and viscoelasticity, and used to demonstrate that the mechanical properties of tissues regulate T cell phenotype, with viscoelasticity as the dominant driver of these phenotypic differences. These observations are consistent with T cell profiles obtained from mechanically distinct tissues in cancer and fibrosis patients, and are highlighted by an enrichment in the AP-1 pathway. Importantly, functionally distinct T cell populations were generated from a population of cells that received the same prior stimulation by tuning ECM viscoelasticity.

An in vitro collagen based system was developed in which viscoelasticity can be varied independently of the initial elastic modulus by utilizing a combination of non-covalent and permanent covalent bonds. Adding covalent bonds only to regions of the network that are already

in close spatial contact (e.g., already crosslinked physically) leads to minimal changes in the moduli, but dramatic alterations in the viscoelastic properties (e.g., rate of stress relaxation). Importantly, a sequential crosslinking approach was used here, in which physical gelation occurs first, followed by local covalent crosslinking using small biorthogonal crosslinking molecules. This approach preserves a consistent collagen architecture and pore size distribution. While other studies have reported an impact of substrate stiffness on TCR interactions utilizing 2D surfaces or coated particles<sup>55-63</sup>, or on T cell activation using hydrogels with large pores that effectively create a flat/curved culture surface<sup>64</sup>, or only varying collagen density<sup>65</sup>, this is the first strategy aimed at generating functionally distinct T cell populations by tuning tissue-level viscoelasticity. This collagen system is the first to report a crosslinking mechanism that successfully decouples ECM stiffness from viscoelasticity, and the crosslinkers themselves had minimal impact on the phenotype of T cells. Modifying collagen with other click groups could expand the utility of this matrix system in the future. By demonstrating that more complex ECM can be developed by generating IPNs of collagen-Nb and other ECM proteins of interest, this system can also be used to study the impact of more complex cell-matrix interactions.

We demonstrate a direct link between ECM mechanics and T cell phenotype in vitro that it is consistent with clinical data, and is highlighted by an enrichment in the AP-1 pathway. In vitro, T cells cultured in slow relaxing collagen matrices were found to have higher expression of activation and inhibitory markers, while T cells cultured in fast relaxing matrices have higher expression of memory markers. Plate cultured T cells also showed distinct phenotypes with lower expression of activation and inhibitory markers relative to T cells cultured in slow relaxing matrices. It is important to note that plate-culture provides a mechanically diverse environment to cells. Cells engaged with the surface encounter a highly inelastic surface while those in

suspension are surrounded by a viscous cell culture medium. It could be helpful for future studies to decouple the net mechanical effects of the viscous media from the inelastic surface of the plate. *In vivo*, T cells in mechanically distinct tissue compartments are phenotypically different, as demonstrated by the transcriptomic profiles of both pan CD8<sup>+</sup> T cells and T cells with shared TCR clonotypes isolated from the blood, adjacent normal tissues and tumors of multiple tumor types. These findings are consistent with the growing acceptance that the location of T cells can be important for their phenotype, as seen in memory subtypes such as tissue resident memory T cells, which are important for the recall response to antigen<sup>17,66,67</sup>. A strikingly conserved trend was observed when T cells from blood, adjacent normal tissues, and tumors were internally compared, and when the *in vitro*-derived cNMF gene signature for T cells cultured in slow relaxing matrices was examined in these cells. The AP-1 pathway was found to be highly modulated by ECM viscoelasticity *in vitro* and showed a consistent trend between mechanically distinct tissues in multiple tumor and fibrotic studies *in vivo*. Recent studies have shown that the AP-1 pathway, specifically the activation of c-Jun in fibroblasts, is a hallmark feature and possibly a unifying mechanism for multiple fibrotic diseases<sup>68-70</sup>. While our study took an agnostic approach to investigate the effects of ECM stiffness and viscoelasticity on T cells, the convergence of the data on AP-1 is indicative of the central role it plays in the cellular response to ECM mechanics. Our findings also suggest that therapies targeting the ECM viscoelasticity may directly impact T cell biology and fate.

TCR analyses from the different matrix conditions suggested that ECM viscoelasticity directly modulates T cell phenotype and does not select for specific clones that persist over time. The weak correlation observed between T cell phenotypes before and after their culture in fast relaxing matrices, with no correlation observed in slow relaxing matrices, suggests that slow

relaxing matrices have a stronger effect on T cell phenotype than fast relaxing matrices. This is supported by the serial culture experiment, where T cells from fast relaxing matrices that were subsequently embedded in slow relaxing matrices were more impacted than T cells from slow relaxing matrices that were then embedded in fast relaxing matrices.

By tuning ECM viscoelasticity, functionally distinct T cell populations were generated, which have different patterns of AP-1 protein expression and interactions. In vitro findings suggest that slower relaxing ECM generate T cells that offer rapid response to antigen, while faster relaxing ECM may generate a slower cytotoxic response. These observations were consistent with the in vivo xenograft lymphoma model, where mice treated with T cells from slow relaxing matrices showed better therapeutic responses. Multiple studies have established that the AP-1 pathway is integral to T cell activation, effector differentiation, anergy and exhaustion<sup>43–45,47–49,71,72</sup>. Further, the relative expression of the different AP-1 proteins, and their interactions, are key to their ultimate function in T cells, and T cell exhaustion can be driven by an imbalance between activating and regulatory AP-1 complexes<sup>42</sup>. Our studies similarly find that distinct patterns of AP-1 protein expression and interactions result in T cell populations within matrices of distinct viscoelasticity, in a manner dependent on the length of stimulation.

The findings from this study support in vivo reports that tissue localization is essential to T cell fate, and identify tissue viscoelasticity as an important mechanical parameter that could be regulating T cell phenotype and function. Based on the principle, we demonstrate a strategy to generating functionally distinct T cell populations by tuning ECM viscoelasticity. Beyond the matrix platform presented and disease implications of our findings, this study motivates the

exploration of T cell manufacturing approaches that incorporate viscoelasticity as a parameter in generating the desired T cell products for specific therapeutic applications.

## **4.6 – Methods**

### *4.6.1. – Material Synthesis*

Rat Tail Collagen Type I (Corning #354236) was functionalized with 5-Norbornene-2-acetic acid succinimidyl ester (Nb-NHS) (Sigma Aldrich #776173) at a ratio of 0.1g Nb-NHS: 1g collagen. Rat tail collagen was first neutralized with NaOH to pH 7.2-7.5 and buffered with 10x DPBS to a concentration of 2mg/ml. Next, Nb-NHS was dissolved in DMSO to an initial concentration of 2mg/ml and diluted 10-fold in 1x PBS, after which the Nb-NHS solution was added to the neutralized collagen, resulting in 1mg/ml final collagen concentration. The reaction proceeded for 5 hours at 4 °C under rigorous stirring to delay collagen gelation, after which 0.1N acetic acid was added to quench the reaction and re-acidify the collagen solution. The product, Norbornene-modified collagen (Col-Nb) was dialyzed in 0.025 N acetic acid for 4 days, filtered with a 0.45um filter and then lyophilized for future use.

### *4.6.2 – Col-Nb crosslinking and T cell encapsulation in Col-Nb*

Lyophilized Col-Nb was first dissolved to 6 mg/ml in 0.025 N acetic acid at 4 °C for 48 hours. To fabricate 200 µl fast relaxing (non-click crosslinked) and slow relaxing (click crosslinked) Col-Nb gels, dissolved Col-Nb was mixed on ice with 10x PBS, Milli Q water, and neutralized with NaOH to a final pH of 7.2-7.5 and a final collagen concentration to 2 mg/ml or 4 mg/ml. Dynabead activated T cells were resuspended in PBS on ice, and 100,000 cells were added to the collagen solution for a desired final cell density of 500,000 cells/ml. The collagen-T cell solution

was then gently transferred into 10mm diameter microwells of a 6-well MatTek plate (#P06G-0-10-F) and incubated at 37 °C for 30 minutes for collagen type I gelation to occur. After collagen gelation, secondary collagen crosslinking was performed in two steps: linker diffusion step, which occurred at room temperature and resulted in minimum crosslinking, and the click reaction step, which occurred at 37 °C. For the diffusion step, the plate was cooled to room temperature for 7 min, and 4 ml of either PBS control (with DMSO vehicle solution) or Methyltetrazine-(PEG)5-Methyltetrazine crosslinker solution was added to each well to allow for crosslinker diffusion. After 20 min, the PBS or crosslinker solution was removed, and the plate was moved to 37 °C for 1 hr to allow click crosslinking to proceed. After crosslinking, collagen gels underwent two 30 mins washes with T cell media to remove excess crosslinker. T cell media was then added to maintain culture. T cells in both fast relaxing and slow relaxing matrices were exposed to the same temperatures and same amount of vehicle solution for the same time period.

#### *4.6.3 – Col-Nb-Matrigel IPN crosslinking and subsequent T cell encapsulation*

To fabricate 200 µl fast relaxing and slow relaxing Col-Nb-Matrigel IPN gels, Col-Nb solution were first neutralized as mentioned above, and Matrigel was mixed into Col-Nb solution to make a final collagen concentration of 2 mg/ml and Matrigel concentration of 4 mg/ml. Dynabead activated T cells were resuspended in PBS on ice, and 100,000 cells were added to the Col-Nb-Matrigel solution. The gel was casted and crosslinked as mentioned above.

#### *4.6.4 – Shear rheological characterization*

**Sample preparation:** Shear rheological characterization of the Col-Nb gels and Col-Nb-Matrigel IPN gels were performed on a stress-controlled, combined motor and transducer (CMT) rheometer (AR-G2, TA Instrument). A 40 mm cone geometry was used. 800 µl of collagen

solution or Col-Nb-Matrigel mixture was immediately loaded onto ice-cold Peltier plate after mixing, and gelled at 37 °C for 30 min. After gelation, the gel was submerged in PBS or MeTz-(PEG)5-MeTz crosslinker solution at different concentrations with a solution chamber, to allow diffusion to happen at 25 °C for 20 min; the solution was then removed, and the temperature raised to 37 °C to allow the click reaction to happen for 1 hr.

**Oscillatory time-sweep and Frequency sweep test:** After gelation and crosslinking were completed, oscillatory time-sweep (1 Hz, 1% strain) was conducted at 37 °C for 10 min to measure the storage modulus ( $G'$ ), loss modulus ( $G''$ ), and the loss angle ( $\delta$ , delta), followed by an oscillatory frequency sweep test (1% strain, 0.01Hz—25Hz, 37 °C).

**Shear stress relaxation test:** A shear stress relaxation test was performed by applying 20% shear strain within 1 s and then maintaining the 20% strain while recording changes in shear stress for 0.5-12 hr at 37 °C. A humidity chamber was used at all times to prevent dehydration.

#### *4.6.5 – Nanoindentation*

Characterization of local mechanical properties of collagen matrices was performed by using a 100um diameter spherical tip Agilent Technologies G200 Nano Indenter. Fast relaxing and slow relaxing matrices were indented using a surface approach frequency of 110Hz, oscillation amplitude of 500nm and contact phase change of 3 degrees. Testing frequency was performed at 110Hz with a pre-test compression of 5um.

#### *4.6.6 – SHG and Cryo-SEM imaging*



*SHG*: Pristine collagen gels were imaged via second harmonic generation using a Leica SP5 X MP Inverted Confocal Microscope at 820nm wavelength at 10x magnification. Pore size distribution was determined using Imaris.

*Cryo-SEM*: Fast relaxing (non-click) and slow relaxing (click crosslinked) Col-Nb gels were washed with ddH<sub>2</sub>O for 2 hr before imaging. The sample preparation stage, sample shuttle, and freeze fracture chamber were pre-cooled with liquid nitrogen. Col-Nb gels were cut and loaded onto metal sample plates and fast frozen by pressing firmly against liquid nitrogen slush. The sample plates were then quickly transferred to the sample shuttle and loaded onto the sample preparation state. The sample was fractured by quickly running the blade across the sample after the temperature lowered to around -153 °C. The temperature of the chamber was then raised to -100 °C for around 10 min to sublimate ~500 nm of ice. The temperature of the chamber was then lowered, and the sample transferred into the sputter chamber to sputter coat the sample with platinum palladium for ~ 12 nm thickness. The sample was then again transferred to the sample shuttle, and attached onto a pre-cooled Zeiss FESEM Ultra55 Scanning Electron Microscope for imaging. Images were obtained with a line-average of 6. Fiber thickness was measured with ImageJ.

#### ***4.6.7 – T cell isolation, activation, culturing***

*Human T cells*: human PBMCs were obtained from Brigham and Women's Hospital as de-identified apheresis collars which were processed in Ficoll gradient. Pan T cell and CD8<sup>+</sup> T cells were isolated with magnetic-bead-based Pan T cell (Miltenyi #130-096-535) CD8<sup>+</sup> T cell isolation kit (Miltenyi #130-096-495) following the manufacturer's protocol.

*Mouse T cells:* Mouse spleens were collected and kept on ice until and throughout processing. To obtain splenocytes, spleens were compressed and passed through a 70  $\mu$ m strainer, washed with PBS, and centrifuged at 300 g for 5 min at 4°C. The pellet was resuspended in 1 ml ACK buffer (Lonza, #10-548E) for 1 min; 9 ml of PBS was then added and splenocytes collected by centrifuging at 300 g for 5 min at 4 °C. Mouse Pan T cells and CD8<sup>+</sup> T cells were isolated with magnetic-bead-based CD8<sup>+</sup> T cell (Miltenyi #130-104-075) isolation kit following manufacturing's protocol.

*Human and mouse T cell activation:* T cells were activated with Dynabeads human/mouse T-activator (ThermoFisher Scientific #11131D, #11162D, #11456D) according to manufacturer's protocol, and cultured in T cell media (RPMI 1640 (Lonza #BE12-702F), 10% heat-inactivated fetal bovine serum (Gibco #10-082-147), 1% pen/strep, 55  $\mu$ M  $\beta$ -mercaptoethanol, 10 mM HEPES (Sigma Aldrich # H4034 ), 1% 100x non-essential amino acid (Lonza #13-144E), 100 mM sodium pyruvate (Lonza #13-115E), supplemented with 300U/ml recombinant human IL-2 (BioLegend #589106) or 24 ng/ml recombinant mouse IL-2 (Biolegend # 575404).

#### *4.6.8 – Tumor cell culturing*

Luciferized Raji (Raji-luc) cells were cultured with RPMI 1640 (Lonza #BE12-702F) with 10% heat-inactivated fetal bovine serum (Gibco #10-082-147) and 1% pen/strep. B16-F10 melanoma cells were cultured with high-glucose DMEM (Gibco #10564029) with 10% heat-inactivated fetal bovine serum (Gibco #10-082-147) and 1% pen/strep.

#### *4.6.9 – T Cell Isolation from Collagen Matrices*

To isolate T cells from collagen gels, collagen matrices were mechanically chopped into small pieces and digested in 100U/ml collagenase type IV (ThermoFisher Scientific #17104019) at 37°C for 1 hour in digestion media (RPMI 1640 + 10% FBS), with intermittent mechanical disruption through 1ml pipette tips. Collagenase was then quenched with MACS buffer (PBS, 0.5% BSA, 2mM EDTA), after which cells were then passed through 30µM strainers (Miltenyi #130-098-458), washed twice in PBS, and resuspended for downstream analysis.

#### *4.6.10 – Flow cytometry*

Cells isolated from Col-Nb cells were kept at 4 °C throughout immunostaining. Cells were stained with dead cell stain (ThermoFisher Scientific #L23105) according to the manufacturer's protocol. Cells were then blocked with FcX Fc receptor blocking solution (BioLegend #101319, #422301) for 20 min and stained with surface protein antibodies for 20 min. Brilliant violet staining buffer (BD Horizon #563794) and flow cytometry staining buffer (Invitrogen #00-4222-26) were used during staining. For phosphorylated protein staining, T cells were fixed/permeabilized while in collagen matrices with cold methanol for two hours to preserve the phosphorylation profile of the T cells. The gels were then digested, cells blocked with FcX Fc receptor blocking solution, and stained for phosphorylated proteins with prechilled True-Phos Perm Buffer (BioLegend #425401) according to manufacturer's protocol. Flow cytometry was then performed on a BD Fortessa LSRII. Gating was performed based on fluorescence-minus-one controls. Complete set of antibodies used for flow cytometry are listed in Supplementary Table 10.

#### *4.6.11 – Flow Cytometry Analyses*

*Mean Fluorescence Intensity (MFI) and PCA:* Compensated single cell flow cytometry intensity values were first exported from FlowJo. Using R version 4.0.5, outlier intensities were discarded (defined as outside 3 standard deviations from the mean), after which the mean was calculated per sample for each marker investigated. The MFI were then represented as heatmaps using the Pheatmap package version 1.0.12<sup>255</sup>. Principal component analyses (PCA) was then performed on the MFIs. PCA scores were plotted for the first two principal components as scatter plots and loadings for the first principal component as bar plots using ggplot2 version 3.3.3<sup>256</sup>

*Determination of Activation/Inhibitory and Memory Signatures:* To determine the relevant T cell signatures, MFI calculations performed above were first scaled per marker across all the conditions investigated. Activation/Inhibitory signatures were determined by finding the mean of the scaled MFI for the following markers: PD1, TIGIT, TIM3, LAG3, OX40, CD39, CD25, CTLA4. Memory signatures were determined as above using the following markers: CD62L, CCR7, CD127, CD45RA, CD27.

*Determination of T cell Imprinting using Distance Calculations:* To determine T cell imprinting, single cell flow cytometry intensities from T cells harvested from fast relaxing and slow relaxing collagen gels after 3 days or 7 days in culture and cultured for 7 additional days in suspension were exported from FlowJo. MFI calculations were performed as previously described. From the MFIs, pairwise Euclidean distances were calculated between fast and slow relaxing gels after 3 day harvest and 7 day harvest separately to determine the extent to which their phenotypes converge.

*Umap Analyses:* Exported single cell flow cytometry intensities were filtered to remove outlier intensities as previously described. Cells were then down sampled to keep the same number of

cells per condition, after which umap analyses were performed. Umap projections were plotted as 2D scatter plots, annotated with either the marker intensity or sample type.

#### *4.6.12 – CAR T cell Generation*

*Lentivirus generation:* 2<sup>nd</sup> generation CAR construct targeting CD19 was generated with the following composition: scFv fragment from FMC63 antibody (GenBank: ADM64594.1), human CD8 $\alpha$  hinge and transmembrane domain (Gene bank number NP\_001759.3, aa 138-206), and human CD3 $\zeta$  (Gene bank number NP\_000725, aa 52-163) intracellular signaling domain with a truncated EGFR (tEGFR) inserted at the N-terminus. Using HEK 293T cells (ATCC #CRL-3216), lentiviral supernatants were generated by co-transfecting with CAR plasmid: pMD2.G: psPAX2= 1:4.5:9:5 using lipofectamine 2000 (Thermo #11668019). After 55-60hrs, supernatants were filtered and used for T cell transduction.

*T cell Transduction:* Primary human T cells were isolated from PBMCs as previously described. 100,000 T cells were activated for 48 hours with dynabeads in a 96-well plate and 100ul T cell media, after which 100ul of lentiviral supernatant was added. T cells were transferred to 24 well plates on day 3 and probed for the expression of tEGFR via flow cytometry before seeding into collagens gels on day 4.

#### *4.6.13 – Xenograft lymphoma model*

*Tumor inoculation and CAR-T cell treatment:* Female NSG mice (Jackson, # 005557), between 5-6 wks of age were inoculated with a high dose of  $5 \times 10^5$  Raji-luc cells intravenously on day 0. After 4 days, tumor-bearing mice were randomized into treatment groups and were treated with either mock (PBS) or  $5 \times 10^5$  CAR+ T cells.

*Tumor tracking:* Raji-luc tumor burden was monitored over time using D-Luciferin (Gold Biotechnology #115144-35-9). Animals were anesthetized and intraperitoneally injected with D-Luciferin at 150 mg/kg. Luminescence was measured 10 minutes post injection via IVIS (Perkin Elmer). Total flux (p/s) per mouse was quantified in whole-body regions-of-interest (ROI). Animals were imaged once every 4 to 14 days. Mice were euthanized if flux from tumor was larger than 1E10, or if significant discomfort or weight loss was observed.

#### *4.6.14 – T cell cytotoxicity assay and Intracellular Cytokine Staining (ICS)*

*T cell Cytotoxicity Assay:* Human anti-CD19 CAR T cells were harvested from collagen matrices and co-cultured with luciferase expressing Raji cells at Effector:Target=4:1 in 100  $\mu$ l media (RPMI 1640 + 10% FBS + 1% P/S) in 96-well U bottom plates. The plate was briefly centrifuged at 300 rcf to collect cells to the bottom and placed in a 37 °C incubator for 18 hours. 100  $\mu$ l of Bright-Glo luciferase assay reagent (Promega #E2620) was added to each well, and the luciferase signal measured every 5 minutes with a BioTek Synergy H1 plate reader. Peak luciferase signal is used for analysis.

Mouse B16-F10 cells were stained with Calcein AM (Invitrogen #C1430) for 30 min at 37 °C in dark, washed 4 times with PBS, and kept in dark on ice until use. T cells from Pmel-1 mouse spleen were isolated, treated with G400 NP for 3 days and conjugated with various DBCO-cytokines. T cells and B16-F10 melanoma cells were well mixed and seeded in 96-well U-bottom plates at different E:T ratios in 200  $\mu$ l media (RPMI 1640 + 10% FBS + 1% P/S). The plate was centrifuged to collect cells to the bottom, and incubated at 37 °C for 6 hr. Supernatants were collected and their fluorescent signals measured with 485 nm excitation and 528 nm emission with a BioTek Synergy H1 plate reader. The fluorescent signals from the 528 nm

channel were subtracted from the 485 nm channel, and cytolysis efficiency was calculated using  $(\text{sample well} - \text{background well}) / (\text{full-cytolysis well} - \text{background well}) * 100\%$

*ICS:* Human anti-CD19 CAR T cells were harvested from collagen matrices and co-cultured with Raji cells at Effector:Target=1.5:1 in 100  $\mu$ l media in 96-well U bottom plates. The plate was briefly centrifuged at 300 rcf to collect cells to the bottom and placed in a 37 °C incubator. After 1 hour, GolgiPlug (BD #555029) was added according to manufacturer's protocol to stop cytokine secretion, followed by an additional 3-hour culture. T cell and tumor cell mixtures were washed, and stained with dead cell stain, surface proteins, and intracellular cytokines with Cyto-Fast fix-perm buffer set (BioLegend #426803) according to manufacturer's protocol, after which flow cytometry was performed

#### *4.6.15 – cJun Immunoprecipitation*

T cells were harvested from collagen matrices, washed with ice cold PBS, and lysed with ice cold non-denaturing buffer containing protease and phosphatase inhibitors. For every 200  $\mu$ g of protein, 12  $\mu$ g of anti-cJun-agarose-conjugated antibody was added (sc-74543 AC) and incubated at 4°C overnight with rocking. The protein bound beads were then washed with non-denaturing buffer and denatured by adding 5x reducing loading buffer (Thermo #39000), and boiled at 90°C for 5 min before use for western blots.

#### *4.6.16 – Western Blotting*

For Western blotting, samples were loaded into wells of 12% Tris-Glycine polyacrylamide protein gels (Thermo #XP00125BOX) and ran at 150V. Proteins were then transferred using the iBlot2 PVDF transfer stacks (Thermo #.IB24002). After transfer, membranes were blocked with

3% BSA for 1 hour at room temperature and blotted with primary antibodies: cJun (CST #9165S), cFos (CST #2250S), BAFT (CST #8638S), JunB (CST #3753S), CD45 (CST #13917S), at 1:1000 dilution in 3% BSA overnight with rocking. Membranes were then washed with TBST for 5 min, 3 times at room temperature and blotted with HRP-linked secondary antibodies (CST #7074S) at 1:10000 in 3% BSA for 2 hrs at room temperature. Membranes were washed with TBST 3 times, incubated with the SignalFire Elite ECL chemiluminescent substrate (CST #12757) and imaged for chemiluminescence. Complete set of antibodies used for Western blotting are listed in Supplementary Table 10.

#### *4.6.17 – cJun Inhibitor studies*

c-Jun in T cells function was inhibited with the SP600125 Jun N-terminal kinase inhibitor (CST, #SP600125). T cells were encapsulated in collagen matrices as previously described, after which the T cells were cultured in media with or without 10uM SP600125. T cells that were not exposed to inhibitor had the same amount of vehicle solution (0.1% DMSO).

#### *4.6.18 – Single Cell RNA Sequencing and Analysis*

To perform scRNA-seq CD8<sup>+</sup> T cells were harvested from collagen gels, and live cells were enriched using a dead cell removal kit (Miltenyi #130-090-101). Single cell sequencing was performed using the Chromium Single Cell 3' v3 platform (10x Genomics). Sequencing was performed by the Bauer Core Facility at Harvard University using the NovaSeq S1, aligned to the human reference genome GRCh38-3.0.0. and filtered for cells using the 10x Cell Ranger Software v 3.0.1. 4,100 and 5,500 T cells were sequenced from the slow relaxing and fast relaxing gels respectively with mean reads of 110,000 and 80,000 per cell. The median genes per



cell averaged 5000 for both conditions. Median UMI counts per cell for slow relaxing and fast relaxing gels were 33000 and 28000 respectively.

Further data processing was performed in R version 4.0.5 using Seurat version 4.0.1<sup>257</sup>. First, we filtered for genes detected in at least 10 cells and for cells with at least 200 genes. Next, we filtered out T cells with percent mitochondrial genes greater than 10% and selected for CD8A expressing cells. Using scTransform, we normalized the UMI count data by performing regularized negative binomial regression, and also regressed out the mitochondrial genes. This was followed by PCA, nearest neighbor graph determination and umap embedding. The umap cell embeddings were then plotted as scatter heatmaps using the ggpointdensity package in R<sup>258</sup>. Global differential gene expression analysis was performed by Seurat using a negative binomial generalized linear model.

#### *Consensus Non-negative Matrix Factorization (cNMF)*

cNMF was performed in Python version 3.8.8. First, SCT correct counts were imported, normalized and filtered for the top 3000 over-dispersed genes, after which factorization was performed from k=5 to k=21 with 200 NMF iterations for each k. After factorization, the optimal k was selected as a trade-off between stability and error (ie. highest stability and lowest error). The top 100 genes that characterize each usage/expression program for the selected k were then exported for downstream analysis.

The aggregate expression of the top 100 genes from each cNMF expression program was calculated for each cell in R using Seurat's AddModuleScore function. Expression programs that

were significantly enriched in T cells cultured in slow or fast relaxing gels were determined using the Wilcoxon Rank Sum Test with FDR for p-value adjustment to estimate significance. Significant gene expression programs were selected as having a  $-\log_{10}$  adjusted p-value > 15. To estimate the condition in which a specific expression module is enriched, fold change was calculated as  $\log_2(\text{mean}(\text{slow relaxing}[i])/\text{mean}(\text{fast relaxing}[i]))$ , where  $i$  is an expression program. Finally, unique genes for expression programs enriched in slow or fast relaxing gels were separately combined. Pathway analysis was performed in Enrichr<sup>259</sup> using the Elsevier Pathway Collection<sup>260</sup>. P-values were determined using the Fisher Exact Test and adjusted using FDR. The top pathway terms were selected for each condition, and the adjusted p-values for both conditions for that term were plotted against each other as bar plots.

#### *AP-1 Pathway Analysis*

AP-1 pathway analysis was performed for the top 100 genes from each enriched cNMF expression program in Enrichr using the NCI-Nature 2016 database<sup>261</sup>. The FDR adjusted p-values that correspond to the AP-1 pathway for each cNMF expression program were then ranked to identify the cNMF module with the most enrichment in the AP-1 pathway.

#### *4.6.19 – Single cell RNA and TCR Sequencing and Analysis*

T cells cultured in fast-relaxing and slow-relaxing matrices, plate-cultured T cells and the parent T cell population were separately stained with TotalSeq C 0252 anti-human Hashtag 2 (Biolegend # 394663), TotalSeq C 0253 anti-human Hashtag 3 (Biolegend # 394665), TotalSeq C 0254 anti-human Hashtag 4 (Biolegend # 394667) and TotalSeq C 0251 anti-human Hashtag 1 (Biolegend # 394661), in addition to TotalSeq C 0063 anti-human CD45RA (Biolegend # 304163).

After staining, the T cells were pooled together for sequencing. TCR sequencing was performed using the chromium single-cell RNA-seq 5' (10x) with Feature Barcoding by the Bauer Core Facility at Harvard University using the NovaSeq SP, aligned to the human reference genome GRCh38-3.0.0. and filtered for cells using the 10x Cell Ranger Software v 7.0.0. 15,544 T cells were sequenced in total with 21,263 median reads per cell and 3,688 median genes per cell. Median UMI counts per cell was 12,858, and there was a 96% mapping of reads in cells.

Further data processing was performed in R version 4.0.5 using Seurat version 4.0.1<sup>257</sup>, as previously described. After data cleaning, we demultiplexed the barcoded cells to assign each cell to their experimental condition using a 0.99 positive quantile threshold. Next, the T cell's clonotype ID, CDR3aa and TRBV gene were assigned to each cell as metadata. Using scTransform, we normalized the UMI count data by performing regularized negative binomial regression, and also regressed out the mitochondrial genes. Umap cell embeddings were then plotted as scatter heatmaps using the ggpointdensity package in R<sup>258</sup>. The aggregate expressions of the SModule and FModule were estimated by using Seurat's AddModuleScore function. Venn diagrams of the TRBV genes and distribution of dominant clonotypes (clones with >3 T cells) were implemented using the ggVennDiagram package in R<sup>262</sup>. Shannon entropy was estimated using the DescTools package in R<sup>263</sup>. To estimate proportions of T cells with unique TCRs and various degrees of clonality, the frequency of each clone was determined, sorted and plotted as bar plots.

#### *4.6.20 – Analysis of Published Single Cell and Bulk RNA Sequencing Datasets*

Single cell RNA sequencing datasets from cancer patients: colorectal cancer (GSE108989), liver cancer (GSE98638), NSCLC (GSE99254) and breast cancer (GSE114727) were imported from the GEO repository and analyzed in R using Seurat. CD8<sup>+</sup> T cells were selected by filtering for cells with  $CD8A > 0$ ,  $CD4 = 0$  and  $ITGAM = 0$ . Further analyses such as data normalization, PCA, umap embedding and differential expression were performed as detailed above. Tumor T cell gene signatures were generated by performing differential expression between T cells derived from tumors and those derived from normal tissue and blood. The aggregate expression of the significant genes in the gene signature (defined as adjusted p-value  $\leq 0.1$ , average log<sub>2</sub> fold change  $\geq 0.1$  and fraction gene expression in  $\geq 0.4$  of tumor T cells) was calculated for each T cell as previously described. The distributions of aggregate expressions for the various conditions were then represented as violin plots. Statistical analyses were performed for the 3 groups using one-way Anova.

Analyses for CD8<sup>+</sup> T cells with common TCRs in blood, normal adjacent tissues and blood were performed by first selecting T cells with common clone IDs between the three tissue types. Next, the aggregate expression of tumor T cell gene signature was calculated for each T cell as described above. To account for differences in the frequencies of T cells with a particular clonotype within the different tissues, the mean aggregate expression of the gene signatures for each T cell clonotype was estimated, as representative of that specific T cell clonotype in that tissue. The distributions of mean aggregate expressions per TCR clonotype per tissue were then represented as violin plots. Statistical analyses were performed as previously described. *In vitro* generated gene signatures (SModule and AP-1 Module), were applied to the *in vivo* datasets using Seurat's AddModuleScore function as described above.

Single cell RNA sequencing datasets from fibrosis patients: liver fibrosis (GSE136103), IPF (GSE135893, GSE159354) were also imported from the GEO repository and analyzed as described above. cNMF gene expression programs were generated from the fibrosis datasets as previously described. AP-1 pathway analyses were then for each cNMF gene expression program in Enrichr using the NCI-Nature 2016 database, and the FDR adjusted values ranked. The cNMF expression program with the highest AP-1 enrichment was selected for each dataset, and the aggregate expression of the genes that constitute this program for each T cell was estimated. The distributions of aggregate expressions were represented as violin plots, and statistical analyses were performed using the Wilcox Test. *In vitro* generated AP-1 gene signature was then applied to the *in vivo* datasets as previously described.

Bulk RNA sequencing dataset (GSE126117) was imported from the GEO repository and analyzed in R using DESeq2 version 1.30.1<sup>264</sup>. Samples were first prefiltered to remove low expressing genes (genes total counts  $\geq 10$  across all samples). Normalization was then performed using the regularized log (rlog) transformation. To find the relative expression of the cNMF generated SModule and FModule gene signatures, the rlog transformed counts were first z-scored by sample. Next, the samples were subsetted for the genes that constitute each gene signature, after which their z-scored expression distributions were visualized as violin plots. Statistical analyses were performed using the Wilcox test and adjusted with FDR.

#### 4.6.21 – Correlation Coefficient Analysis

To investigate how the expression of AP-1 proteins for T cells cultured in the different mechanical conditions correlate with their observed killing of Raji cells *in vitro*, single cell flow cytometry intensities for the various AP-1 proteins were exported from FlowJo. Using R, outlier

intensities were discarded as previously described. Each cell from a given condition was assigned an initial cytotoxicity value based on the experimentally observed Raji cell killing for that condition. Next, it was hypothesized that while the observed cytotoxicity value constituted that of the average T cell population, there is heterogeneity in the killing potential of specific T cell populations based on their AP-1 profile. To map the T cell populations to their cytotoxic potentials, T cells from the various conditions were pooled together, and K-means clustering was performed, after which the average cytotoxicity value was calculated for cells in each cluster, with the reasoning that T cells that have similar AP-1 profiles are more likely to have similar killing potentials. To find the optimum number of clusters (k-clusters), the following analyses were performed. First, the Euclidean distances of each cell to the center of each cluster was calculated to transform the single cell intensity data to single cell distance matrices, where each row is a cell and each column is the distance between that cell and the center of each cluster. By performing this transformation, cluster level information could be acquired for downstream analyses. Second, from step 1, the average Euclidean distances for cells in each cluster to all the cluster centers were calculated: groups of clusters with phenotypically similar cells (ie. have similar AP-1 profiles) will have smaller distances. Third, Random Forest regression was performed with the input as the average cluster distances determined from step 2, and the output as the average cytotoxicity for that cluster. The % variance explained from the regression analysis was then calculated. This analysis was iterated over multiple k-clusters, with the optimum k-cluster determined to be the one with the highest variance explained. For this k-cluster, the MFI of each marker was calculated per cluster, to serve as the characteristic AP-1 profile for that cluster. Finally, Pearson correlation analysis was performed between the

characteristic AP-1 protein expression per cluster and their corresponding average cytotoxicity values.

#### *4.6.22 – Statistical Analysis*

Unless otherwise specified, statistical analyses were performed on Prism Graphpad software version 9.0.2 or with R version 4.0.5. Statistical tests used two-tail one-way ANOVA and post-hoc tests for multiple comparisons, or Student's t-test or Wilcox test for comparison between two groups. P-value less than 0.05 was considered as significant unless otherwise noted. Error bars represent standard error of mean, unless otherwise noted.

## **Chapter 5: Thesis summary and future directions**

### **5.1 – Thesis Summary**

This thesis presents two systems designed to increase the efficacy of adoptive T cell therapies during the *ex vivo* manufacturing process. The first system uses azido-sugar nanoparticles to metabolically label T cells and allow for cytokine conjugation. This method is used to direct T cell differentiation, activate the host immune response, and induce antigen spreading. The second system is a collagen type 1-based ECM that allows for independent tuning of matrix stiffness and viscoelasticity. This system is used to generate phenotypically and functionally distinct T cells.

Azido-sugar nanoparticle were used to metabolically label the T cell glycocalyx with azide handles. This allowed modified, DBCO-containing anti-tumor cytokines to be conjugated onto T cell surfaces, and provide a local, concentrated signal to direct T cell differentiation. The process could be completed by simply adding nanoparticles and cytokines sequentially into T cell cultures, and could be readily integrated into the current T cell manufacturing process. By conjugating IL-12 onto T cells, this method harnessed the potent anti-tumor activity of the cytokine while significantly reducing its cytotoxicity, and significantly boosted the anti-tumor efficacy of T cells by directing them to a more effector-memory phenotype. Additionally, IL-12 conjugation activated the host immune system, encouraged T cell infiltration into solid tumors, induced antigen spreading, and achieved complete response with only half of the curative dose for CAR-T cells. Additionally, the potential use of multiple cytokines has been explored by simultaneously conjugating IL-12 and IL-15/IL-15Ra complexes, and synergistic effects from conjugating these two cytokines have been observed. Altogether, these findings demonstrated a



simple, easily integratable approach to conjugate anti-tumor cytokines onto T cells to boost the efficacy of existing ACT and CAR-T therapies.

Azido-sugar nanoparticles were used to metabolically label the T cell glycocalyx with azide handles. This allowed modified, DBCO-containing anti-tumor cytokines to be conjugated onto T cell surfaces, providing a local, concentrated signal to direct T cell differentiation. The process could be completed by simply adding nanoparticles and cytokines sequentially to T cell cultures and readily integrated into the current T cell manufacturing process. By conjugating IL-12 onto T cells, this method harnessed the potent anti-tumor activity of the cytokine while significantly reducing its cytotoxicity, and it boosted the anti-tumor efficacy of T cells by directing them to a more effector-memory phenotype. Moreover, IL-12 conjugation activated the host immune system, encouraged T cell infiltration into solid tumors, induced antigen spreading, and achieved a complete response with only half of the curative dose for CAR-T cells. Additionally, the potential use of multiple cytokines has been explored by simultaneously conjugating IL-12 and IL-15/IL-15Ra complexes, and the observed synergistic effects from this conjugation demonstrate the potential of this approach. Overall, these findings demonstrate a simple and easily integratable approach to conjugate anti-tumor cytokines onto T cells to boost the efficacy of existing ACT and CAR-T therapies.

Overall, the thesis presents two approaches for generating functionally distinct T cells that could potentially improve the efficacy of ACT and CAR-T cells in solid tumors. These approaches modulate T cell phenotype and function from two angles: one through cytokine signaling and the other through mechanical modulation. Therefore, opportunities exist to potentially integrate these two approaches by first generating more effective T cells using elastic, slow-relaxing collagen

gels, and then conjugating anti-tumor cytokines onto them right before delivery. Future optimization and potential synergies need to be explored if the methods are used in combination.

## **5.2 – Limitation of the thesis and future directions**

Although the data for each aim strongly supports the idea that T cell phenotype and function could be modulated *ex vivo* to achieve a better response *in vivo*, it is important to consider certain limitations before translating these approaches for industrial and clinical use. The following describes some limitations for Aim 1 and Aim 2.

### *5.2.1 – Limitations for Aim 1:*

1. The work presented here only explored the use of one mannose-based, azido-sugar polymer (Ac<sub>4</sub>ManAz) that is precipitated into a nanoparticle. It would be interesting to investigate whether using the monomer or polymer/nanoparticle form of azido-sugar achieves similar or different azide labeling. Additionally, exploring the use of azido-sugar developed from other base sugars, such as galactose and glucose, could potentially achieve similar azido-labeling of the T cell glycocalyx and simplify the manufacturing process needed to mass-produce azido-sugar/azido-sugar nanoparticles. These explorations could lower the barrier for technology translation.
2. Work presented in this thesis are mostly based on the single conjugation of IL-12. Conjugating both IL-12 and IL-15 at equal concentrations was briefly explored in a mouse melanoma model. It would be worthwhile to explore the use of 1) other cytokines, 2) potential combinations of two or more cytokine, and 3) the optimal molar-to-molar

ratio of each cytokine combination. Specifically, one interesting combination to explore would be IL-15, IL-7, and IL-21, as well as their individual combinations with IL-12.

These combinations have been shown to support the generation and maintenance of T<sub>SCM</sub> and T<sub>CM</sub> populations. IL-23 is also an interesting target, as overexpression of IL-23 in CAR-T cells has been linked with a superior anti-tumor response.

3. The work explored the changes in T cell phenotype and effector molecule secretion in the tumor-draining lymph nodes and spleens of mice receiving IL-12 conjugated T cells. However, little has been investigated regarding the phenotypes and functions of T cells that infiltrate the tumor, as well as the differential performance between adoptively transferred T cells and host-generated T cells inside the tumor. These aspects could potentially reveal valuable information on the T cells' response against the immunosuppressive tumor microenvironment and the activation of the host immunity.
4. The study only used the Raji lymphoma model in NSG mice to demonstrate the efficacy of cytokine conjugation in CAR-T cells. Since NSG mice lack functional adaptive immunity, and Raji lymphoma is a semi-liquid tumor, it would be valuable to replicate the study in a solid mouse tumor CAR-T model. This would allow for investigation of whether the observations seen in the B16-F10 melanoma model, such as activation of the host immune system, increased T cell infiltration into tumors, and antigen spreading, could be replicated with CAR-T cells and help to evaluate the boost in efficacy for CAR-Ts against solid tumors.
5. The improved tumor control is attributed to T cells conjugated with IL-12 having more effector-memory phenotypes and more effector functions, such as cytokine secretion. Given that an effector-dominant T cell population provides immediate tumor killing but

poor long-term control, whereas stem-cell-like-memory-dominant and central-memory-dominant T cells demonstrate better long-term control of tumors via T cell proliferation, it would be interesting to test IL-12 conjugated T cells in a less aggressive or even slow-developing tumor model to determine whether similar treatment benefits could be achieved as those observed in the aggressive melanoma model. Alternatively, a slow-developing tumor model could be used to determine whether generating a memory-concentrated population would benefit the long-term control of such tumors.

### *5.2.2 – Limitations for Aim 2:*

1. The method described in this thesis involves embedding and harvesting T cells in collagen matrices for a period of 3-7 days. This process is laborious, time-consuming, and expensive, as each gel can only yield up to 10 million T cells, requiring numerous gels to be manufactured. Consequently, integrating this process into the current CAR-T cell manufacturing pipeline may be challenging. While the work presented here demonstrates the significant impact that viscoelasticity can have on T cell function, further development and optimization are necessary to create 2D or pseudo-3D cultures that can apply this principle and imprint the effects of viscoelasticity on T cells without relying on the burdensome process of gel embedding and harvesting.
2. The TCR sequencing presented in this work has demonstrated that matrices with varying viscoelasticity directly modulate T cell phenotype without selecting for specific clones to persist over time. However, the sequencing analysis has been performed on relatively few cells, with only 3.7% of clones having two or more cells and even fewer having more

than 10 cells. To obtain more accurate results, the number of T cells should be increased, or the starting population should be enriched for several clones.

3. The study heavily relies on categorizing the "memory-ness" of in vitro T cells based on the expression of surface markers such as CD62L and CCR7. Although these surface markers can indicate "memory-ness" to a certain extent, a more rigorous method should be used to examine the functional state of T cells and establish actual T cell memory. This should include evaluating T cells' ability to live long-term and their capacity to quickly expand upon antigen restimulation. Therefore, the emphasis on surface markers expressed by T cells in Aim 2 does not adequately represent the actual memory-ness of the T cells, and a more comprehensive approach is needed to evaluate T cell memory.

### *5.2.3 - Limitations for Aim 1 and 2*

1. Both Aim 1 and Aim 2 focus on the use of T cells in adoptive cell transfer (ACT) therapies. While T cells are the most widely explored cell type for ACTs, they suffer from various limitations. First, they only kill in a CAR-specific or antigen-specific mechanism, which makes it difficult to recognize all antigens in a heterogeneous tumor. Second, T cell therapies can have strong and lethal side effects, including cytokine release syndrome and neurotoxicity. Third, CAR-T is individual specific, cannot be manufactured as off-the-shelf products, and faces long manufacturing lags for terminal stage patients. Therefore, it is worthwhile to explore ACT with other cell types, such as natural killer (NK) cells. It would be interesting to investigate whether presenting anti-tumor cytokine signaling with metabolic labeling or controlling mechanical cues presented to NK cells could similarly affect their performance in ACT. These

explorations would help in designing cell products that could potentially overcome the limitations of T cell therapies.

## Chapter 6: References

1. Rosenberg, S. A. *et al.* Observations on the systemic administration of autologous lymphokine-activated killer cells and recombinant interleukin-2 to patients with metastatic cancer. *N Engl J Med* **313**, 1485–1492 (1985).
2. Donohue, J. H. *et al.* The systemic administration of purified interleukin 2 enhances the ability of sensitized murine lymphocytes to cure a disseminated syngeneic lymphoma. *The Journal of Immunology* **132**, (1984).
3. Rosenberg, S. A. *et al.* Use of tumor-infiltrating lymphocytes and interleukin-2 in the immunotherapy of patients with metastatic melanoma. A preliminary report. *N Engl J Med* **319**, 1676–1680 (1988).
4. June, C. H., Riddell, S. R. & Schumacher, T. N. Adoptive cellular therapy: A race to the finish line. *Sci Transl Med* **7**, (2015).
5. Ping, Y., Liu, C. & Zhang, Y. T-cell receptor-engineered T cells for cancer treatment: current status and future directions. *Protein Cell* **9**, 254–266 (2018).
6. Shah, N. N. *et al.* CD4/CD8 T-Cell Selection Affects Chimeric Antigen Receptor (CAR) T-Cell Potency and Toxicity: Updated Results From a Phase I Anti-CD22 CAR T-Cell Trial. *Journal of Clinical Oncology* **38**, 1938 (2020).
7. Chmielewski, M. & Abken, H. TRUCKs: the fourth generation of CARs. <https://doi-org.ezp-prod1.hul.harvard.edu/10.1517/14712598.2015.1046430> **15**, 1145–1154 (2015).
8. Enblad, G., Karlsson, H. & Loskog, A. S. I. CAR T-Cell Therapy: The Role of Physical Barriers and Immunosuppression in Lymphoma. *Hum Gene Ther* **26**, 498–505 (2015).
9. Fang, M., Yuan, J., Peng, C. & Li, Y. Collagen as a double-edged sword in tumor progression. *Tumor Biology* **35**, 2871–2882 (2014).
10. Brandenburg, S. *et al.* IL-2 induces in vivo suppression by CD4+CD25+Foxp3+ regulatory T cells. *Eur J Immunol* **38**, 1643–1653 (2008).
11. Majzner, R. G. & Mackall, C. L. Tumor antigen escape from car t-cell therapy. *Cancer Discov* **8**, 1219–26 (2018).
12. Elosgui-Artola, A. *et al.* Matrix viscoelasticity controls spatio-temporal tissue organization. *bioRxiv* 2022.01.19.476771 (2022) doi:10.1101/2022.01.19.476771.
13. Vining, K. H. & Mooney, D. J. Mechanical forces direct stem cell behaviour in development and regeneration. *Nat Rev Mol Cell Biol* **18**, 728–742 (2017).
14. Majedi, F. S. *et al.* T-cell activation is modulated by the 3D mechanical microenvironment. *Biomaterials* **252**, (2020).

15. Morgan, R. A. *et al.* Cancer regression in patients after transfer of genetically engineered lymphocytes. *Science* **314**, 126–129 (2006).
16. Kochenderfer, J. N. *et al.* Eradication of B-lineage cells and regression of lymphoma in a patient treated with autologous T cells genetically engineered to recognize CD19. *Blood* **116**, 4099–4102 (2010).
17. Atrash, S., Bano, K., Harrison, B. & Abdallah, A. O. CAR-T treatment for hematological malignancies. *Journal of Investigative Medicine* **68**, 956–964 (2020).
18. Gill, S., Maus, M. v. & Porter, D. L. Chimeric antigen receptor T cell therapy: 25 years in the making. *Blood Rev* **30**, 157–167 (2016).
19. CAR T-Cell Therapy Approved for Multiple Myeloma - National Cancer Institute. <https://www.cancer.gov/news-events/cancer-currents-blog/2021/fda-ide-cel-car-t-multiple-myeloma>.
20. Jackson, H. J., Rafiq, S. & Brentjens, R. J. Driving CAR T-cells forward. *Nat Rev Clin Oncol* **13**, 370 (2016).
21. June, C. H., O'Connor, R. S., Kawalekar, O. U., Ghassemi, S. & Milone, M. C. CAR T cell immunotherapy for human cancer. *Science (1979)* **359**, 1361–1365 (2018).
22. Gowrishankar, K., Birtwistle, L. & Micklethwaite, K. Manipulating the tumor microenvironment by adoptive cell transfer of CAR T-cells. *Mammalian Genome* **29**, 739–756 (2018).
23. Schaft, N. The Landscape of CAR-T Cell Clinical Trials against Solid Tumors—A Comprehensive Overview. *Cancers 2020, Vol. 12, Page 2567* **12**, 2567 (2020).
24. Hou, B., Tang, Y., Li, W., Zeng, Q. & Chang, D. Efficiency of CAR-T Therapy for Treatment of Solid Tumor in Clinical Trials: A Meta-Analysis. *Dis Markers* **2019**, (2019).
25. Brentjens, R. J. *et al.* Safety and persistence of adoptively transferred autologous CD19-targeted T cells in patients with relapsed or chemotherapy refractory B-cell leukemias. *Blood* **118**, 4817–4828 (2011).
26. Valkenburg, K. C., de Groot, A. E. & Pienta, K. J. Targeting the tumour stroma to improve cancer therapy. *Nature Reviews Clinical Oncology 2018 15:6* **15**, 366–381 (2018).
27. Singh, N., Perazzelli, J., Grupp, S. A. & Barrett, D. M. Early memory phenotypes drive T cell proliferation in patients with pediatric malignancies. *Sci Transl Med* **8**, (2016).
28. Gattinoni, L., Speiser, D. E., Lichterfeld, M. & Bonini, C. T memory stem cells in health and disease. *Nature Medicine 2017 23:1* **23**, 18–27 (2017).



29. Xie, Y. *et al.* Naive tumor-specific CD4<sup>+</sup> T cells differentiated in vivo eradicate established melanoma. *Journal of Experimental Medicine* **207**, 651–667 (2010).
30. Rafiq, S., Hackett, C. S. & Brentjens, R. J. Engineering strategies to overcome the current roadblocks in CAR T cell therapy. *Nature Reviews Clinical Oncology* 2019 17:3 **17**, 147–167 (2019).
31. Kim, C. & Williams, M. A. Nature and nurture: T-cell receptor-dependent and T-cell receptor-independent differentiation cues in the selection of the memory T-cell pool. *Immunology* **131**, 310 (2010).
32. Omilusik, K. D. & Goldrath, A. W. The origins of memory T cells. *Nature* 2021 552:7685 **552**, 337–339 (2017).
33. Dutton, R. W., Bradley, L. M. & Swain, S. L. T cell memory. *Annu Rev Immunol* **16**, 201–223 (1998).
34. Kaech, S. M. & Cui, W. Transcriptional control of effector and memory CD8<sup>+</sup> T cell differentiation. *Nature Reviews Immunology* 2012 12:11 **12**, 749–761 (2012).
35. Hinrichs, C. S. *et al.* Adoptively transferred effector cells derived from naïve rather than central memory CD8<sup>+</sup> T cells mediate superior antitumor immunity. *Proc Natl Acad Sci U S A* **106**, 17469–17474 (2009).
36. Klebanoff, C. A. *et al.* Central memory self/tumor-reactive CD8<sup>+</sup> T cells confer superior antitumor immunity compared with effector memory T cells. *Proc Natl Acad Sci U S A* **102**, 9571–9576 (2005).
37. Hinrichs, C. S. *et al.* Human effector CD8<sup>+</sup> T cells derived from naive rather than memory subsets possess superior traits for adoptive immunotherapy. *Blood* **117**, 808–814 (2011).
38. Gattinoni, L. *et al.* Acquisition of full effector function in vitro paradoxically impairs the in vivo antitumor efficacy of adoptively transferred CD8<sup>+</sup> T cells. *J Clin Invest* **115**, 1616–1626 (2005).
39. Leblay, N. *et al.* Cite-Seq Profiling of T Cells in Multiple Myeloma Patients Undergoing BCMA Targeting CAR-T or Bites Immunotherapy. *Blood* **136**, 11–12 (2020).
40. Sommermeyer, D. *et al.* Chimeric antigen receptor-modified T cells derived from defined CD8<sup>+</sup> and CD4<sup>+</sup> subsets confer superior antitumor reactivity in vivo. *Leukemia* 2016 30:2 **30**, 492–500 (2015).
41. Das, R. K., Vernau, L., Grupp, S. A. & Barrett, D. M. Naïve T-cell deficits at diagnosis and after chemotherapy impair cell therapy potential in pediatric cancers. *Cancer Discov* **9**, 492–499 (2019).

42. Singh, N., Perazzelli, J., Grupp, S. A. & Barrett, D. M. Early memory phenotypes drive T cell proliferation in patients with pediatric malignancies. *Sci Transl Med* **8**, (2016).
43. Xu, Y. *et al.* Closely related T-memory stem cells correlate with in vivo expansion of CAR-CD19-T cells and are preserved by IL-7 and IL-15. *Blood* **123**, 3750–3759 (2014).
44. Klaver, Y., van Steenbergen, S. C. L., Sleijfer, S., Debets, R. & Lamers, C. H. J. T cell maturation stage prior to and during GMP processing informs on CAR T cell expansion in patients. *Front Immunol* **7**, 648 (2016).
45. Turtle, C. J. *et al.* CD19 CAR-T cells of defined CD4<sup>+</sup>:CD8<sup>+</sup> composition in adult B cell ALL patients. *J Clin Invest* **126**, 2123–2138 (2016).
46. Gattinoni, L. *et al.* Wnt signaling arrests effector T cell differentiation and generates CD8<sup>+</sup> memory stem cells. *Nature Medicine* **15**, 808–813 (2009).
47. Klebanoff, C. A. *et al.* Determinants of successful CD8<sup>+</sup> T-cell adoptive immunotherapy for large established tumors in mice. *Clinical Cancer Research* **17**, 5343–5352 (2011).
48. Oliveira, G. *et al.* Tracking genetically engineered lymphocytes long-term reveals the dynamics of t cell immunological memory. *Sci Transl Med* **7**, (2015).
49. Restifo, N. P. & Gattinoni, L. Lineage relationship of effector and memory T cells. *Curr Opin Immunol* **25**, 556–563 (2013).
50. Levine, B. L., Miskin, J., Wonnacott, K. & Keir, C. Global Manufacturing of CAR T Cell Therapy. *Mol Ther Methods Clin Dev* **4**, 92 (2017).
51. Schluns, K. S. & Lefrançois, L. Cytokine control of memory T-cell development and survival. *Nature Reviews Immunology* **3**, 269–279 (2003).
52. Alizadeh, D. *et al.* IL15 enhances CAR-T cell antitumor activity by reducing mTORC1 activity and preserving their stem cell memory phenotype. *Cancer Immunol Res* **7**, 759–772 (2019).
53. Tian, Y. & Zajac, A. J. IL-21 and T Cell Differentiation: Consider the Context. *Trends Immunol* **37**, 557–568 (2016).
54. Klebanoff, C. A. *et al.* Inhibition of AKT signaling uncouples T cell differentiation from expansion for receptor-engineered adoptive immunotherapy. *JCI Insight* **2**, (2017).
55. Funk, C. R. *et al.* PI3K $\delta/\gamma$  inhibition promotes human CART cell epigenetic and metabolic reprogramming to enhance antitumor cytotoxicity. *Blood* **139**, 523–537 (2022).
56. Raje, N. S. *et al.* Updated Clinical and Correlative Results from the Phase I CRB-402 Study of the BCMA-Targeted CAR T Cell Therapy bb21217 in Patients with Relapsed and Refractory Multiple Myeloma. *Blood* **138**, 548–548 (2021).

57. Ghassemi, S. *et al.* Rapid manufacturing of non-activated potent CAR T cells. *Nature Biomedical Engineering* 2022 6:2 **6**, 118–128 (2022).
58. Garfall, A. L. *et al.* T-cell phenotypes associated with effective CAR T-cell therapy in postinduction vs relapsed multiple myeloma. *Blood Adv* **3**, 2812–2815 (2019).
59. Cohen, A. D. *et al.* B cell maturation antigen–specific CAR T cells are clinically active in multiple myeloma. *J Clin Invest* **129**, 2210–2221 (2019).
60. Abecassis, A. *et al.* CAR-T cells derived from multiple myeloma patients at diagnosis have improved cytotoxic functions compared to those produced at relapse or following daratumumab treatment. *EJHaem* **3**, 970–974 (2022).
61. Shedlock, D. J. & Shen, H. Requirement for CD4 T cell help in generating functional CD8 T cell memory. *Science (1979)* **300**, 337–339 (2003).
62. Janssen, E. M. *et al.* CD4<sup>+</sup> T cells are required for secondary expansion and memory in CD8<sup>+</sup> T lymphocytes. *Nature* 2003 421:6925 **421**, 852–856 (2003).
63. Hung, K. *et al.* The Central Role of CD4<sup>+</sup> T Cells in the Antitumor Immune Response. *Journal of Experimental Medicine* **188**, 2357–2368 (1998).
64. Aleksandrova, K. *et al.* Functionality and Cell Senescence of CD4/ CD8-Selected CD20 CAR T Cells Manufactured Using the Automated CliniMACS Prodigy® Platform. *Transfusion Medicine and Hemotherapy* **46**, 47–54 (2019).
65. Moeller, M. *et al.* Adoptive transfer of gene-engineered CD4<sup>+</sup> helper T cells induces potent primary and secondary tumor rejection. *Blood* **106**, 2995–3003 (2005).
66. Moeller, M. *et al.* Sustained Antigen-Specific Antitumor Recall Response Mediated by Gene-Modified CD4<sup>+</sup> T Helper-1 and CD8<sup>+</sup> T Cells. *Cancer Res* **67**, 11428–11437 (2007).
67. Teoh, J. *et al.* Lisocabtagene Maraleucel (liso-cel) Manufacturing Process Control and Robustness across CD19<sup>+</sup> Hematological Malignancies. *Blood* **134**, 593–593 (2019).
68. Sommermeyer, D. *et al.* Chimeric antigen receptor-modified T cells derived from defined CD8<sup>+</sup> and CD4<sup>+</sup> subsets confer superior antitumor reactivity in vivo. *Leukemia* 2016 30:2 **30**, 492–500 (2015).
69. Gardner, R. *et al.* CD19CAR T Cell Products of Defined CD4:CD8 Composition and Transgene Expression Show Prolonged Persistence and Durable MRD-Negative Remission in Pediatric and Young Adult B-Cell ALL. *Blood* **128**, 219 (2016).
70. Gardner, R. A. *et al.* Intent-to-treat leukemia remission by CD19 CAR T cells of defined formulation and dose in children and young adults. *Blood* **129**, 3322–3331 (2017).

71. Turtle, C. J. *et al.* CD19 CAR–T cells of defined CD4+:CD8+ composition in adult B cell ALL patients. *J Clin Invest* **126**, 2123–2138 (2016).
72. Abramson, J. S. *et al.* Lisocabtagene maraleucel for patients with relapsed or refractory large B-cell lymphomas (TRANSCEND NHL 001): a multicentre seamless design study. *The Lancet* **396**, 839–852 (2020).
73. Nishimura, T. *et al.* Distinct Role of Antigen-Specific T Helper Type 1 (Th1) and Th2 Cells in Tumor Eradication in Vivo. *Journal of Experimental Medicine* **190**, 617–628 (1999).
74. Knutson, K. L. & Disis, M. L. Tumor antigen-specific T helper cells in cancer immunity and immunotherapy. *Cancer Immunology, Immunotherapy* **54**, 721–728 (2005).
75. Lorvik, K. B. *et al.* Adoptive transfer of tumor-specific Th2 cells eradicates tumors by triggering an in situ inflammatory immune response. *Cancer Res* **76**, 6864–6876 (2016).
76. Tsukamoto, H. *et al.* Soluble IL6R expressed by myeloid cells reduces tumor-specific Th1 differentiation and drives tumor progression. *Cancer Res* **77**, 2279–2291 (2017).
77. Shiao, S. L. *et al.* TH2-polarized CD4+ T Cells and macrophages limit efficacy of radiotherapy. *Cancer Immunol Res* **3**, 518–525 (2015).
78. DeNardo, D. G. *et al.* CD4+ T Cells Regulate Pulmonary Metastasis of Mammary Carcinomas by Enhancing Protumor Properties of Macrophages. *Cancer Cell* **16**, 91–102 (2009).
79. Tokumaru, Y. *et al.* Association of Th2 high tumors with aggressive features of breast cancer. [https://doi-org.ezp-prod1.hul.harvard.edu/10.1200/JCO.2020.38.15\\_suppl.e12584](https://doi-org.ezp-prod1.hul.harvard.edu/10.1200/JCO.2020.38.15_suppl.e12584) **38**, e12584–e12584 (2020).
80. Miyahara, Y. *et al.* Generation and regulation of human CD4+ IL-17-producing T cells in ovarian cancer. *Proc Natl Acad Sci U S A* **105**, 15505–15510 (2008).
81. Zhang, B. *et al.* The prevalence of Th17 cells in patients with gastric cancer. *Biochem Biophys Res Commun* **374**, 533–537 (2008).
82. Qian, X. *et al.* Interleukin-17 acts as double-edged sword in anti-tumor immunity and tumorigenesis. *Cytokine* **89**, 34–44 (2017).
83. Muranski, P. *et al.* Tumor-specific Th17-polarized cells eradicate large established melanoma. *Blood* **112**, 362–373 (2008).
84. Martin-Orozco, N. *et al.* T Helper 17 Cells Promote Cytotoxic T Cell Activation in Tumor Immunity. *Immunity* **31**, 787–798 (2009).
85. Ma, X. *et al.* Interleukin-23 engineering improves CAR T cell function in solid tumors. *Nature Biotechnology* 2020 38:4 **38**, 448–459 (2020).

86. Overacre-Delgoffe, A. E. *et al.* Microbiota-specific T follicular helper cells drive tertiary lymphoid structures and anti-tumor immunity against colorectal cancer. *Immunity* **54**, 2812-2824.e4 (2021).
87. Chaurio, R. A. *et al.* TGF- $\beta$ -mediated silencing of genomic organizer SATB1 promotes Tfh cell differentiation and formation of intra-tumoral tertiary lymphoid structures. *Immunity* **55**, 115-128.e9 (2022).
88. Nurieva, R. I. *et al.* Function of T follicular helper cells in anti-tumor immunity. *The Journal of Immunology* **202**, (2019).
89. Wang, T. *et al.* Regulation of the innate and adaptive immune responses by Stat-3 signaling in tumor cells. *Nature Medicine* *2004 10:1* **10**, 48–54 (2003).
90. Burdelya, L. *et al.* Stat3 Activity in Melanoma Cells Affects Migration of Immune Effector Cells and Nitric Oxide-Mediated Antitumor Effects. *The Journal of Immunology* **174**, 3925–3931 (2005).
91. Xue, W. *et al.* Senescence and tumour clearance is triggered by p53 restoration in murine liver carcinomas. *Nature* *2006 445:7128* **445**, 656–660 (2007).
92. Zboralski, D., Hoehlig, K., Eulberg, D., Frömming, A. & Vater, A. Increasing tumor-infiltrating T cells through inhibition of CXCL12 with NOX-A12 synergizes with PD-1 blockade. *Cancer Immunol Res* **5**, 950–956 (2017).
93. Feig, C. *et al.* Targeting CXCL12 from FAP-expressing carcinoma-associated fibroblasts synergizes with anti-PD-L1 immunotherapy in pancreatic cancer. *Proc Natl Acad Sci U S A* **110**, 20212–20217 (2013).
94. Draghiciu, O., Lubbers, J., Nijman, H. W. & Daemen, T. Myeloid derived suppressor cells—An overview of combat strategies to increase immunotherapy efficacy. <https://doi-org.ezp-prod1.hul.harvard.edu/10.4161/21624011.2014.954829> **4**, 954829 (2015).
95. Morgan, R. A. *et al.* Case Report of a Serious Adverse Event Following the Administration of T Cells Transduced With a Chimeric Antigen Receptor Recognizing ERBB2. *Molecular Therapy* **18**, 843–851 (2010).
96. Richman, S. A. *et al.* High-Affinity GD2-specific CAR T cells induce fatal encephalitis in a preclinical neuroblastoma model. *Cancer Immunol Res* **6**, 36–46 (2018).
97. Spear, P., Barber, A. & Sentman, C. L. Collaboration of chimeric antigen receptor (CAR)-expressing T cells and host T cells for optimal elimination of established ovarian tumors. <https://doi-org.ezp-prod1.hul.harvard.edu/10.4161/onci.23564> **2**, (2013).
98. Boulch, M. *et al.* A cross-talk between CAR T cell subsets and the tumor microenvironment is essential for sustained cytotoxic activity. *Sci Immunol* **6**, (2021).

99. Hanahan, D. & Coussens, L. M. Accessories to the Crime: Functions of Cells Recruited to the Tumor Microenvironment. *Cancer Cell* **21**, 309–322 (2012).
100. Xu, Y. *et al.* Glycolysis determines dichotomous regulation of T cell subsets in hypoxia. *J Clin Invest* **126**, 2678–2688 (2016).
101. Harel, M. *et al.* Proteomics of Melanoma Response to Immunotherapy Reveals Mitochondrial Dependence. *Cell* **179**, 236-250.e18 (2019).
102. Vaupel, P., Kallinowski, F., Okunieff, P. & Rallinowski, F. Blood flow, oxygen and nutrient supply, and metabolic microenvironment of human tumors: a review. *AACR* **49**, 6449–6465 (1989).
103. Kallinowski, F., Vaupel, P., Runkel, S., research, G. B.-C. & 1988, undefined. Glucose uptake, lactate release, ketone body turnover, metabolic micromilieu, and pH distributions in human breast cancer xenografts in nude rats. *AACR*.
104. Warburg, O. On the origin of cancer cells. *Science (1979)* **123**, 309–314 (1956).
105. Chang, C. H. *et al.* Posttranscriptional Control of T Cell Effector Function by Aerobic Glycolysis. *Cell* **153**, 1239–1251 (2013).
106. Chang, C. H. *et al.* Metabolic Competition in the Tumor Microenvironment Is a Driver of Cancer Progression. *Cell* **162**, 1229–1241 (2015).
107. Zhang, Y. *et al.* Enhancing CD8+ T Cell Fatty Acid Catabolism within a Metabolically Challenging Tumor Microenvironment Increases the Efficacy of Melanoma Immunotherapy. *Cancer Cell* **32**, 377-391.e9 (2017).
108. Lindau, D., Gielen, P., Kroesen, M., Wesseling, P. & Adema, G. J. The immunosuppressive tumour network: myeloid-derived suppressor cells, regulatory T cells and natural killer T cells. *Immunology* **138**, 105–115 (2013).
109. Dankner, M., Gray-Owen, S. D., Huang, Y. H., Blumberg, R. S. & Beauchemin, N. CEACAM1 as a multi-purpose target for cancer immunotherapy. <https://doi-org.ezp-prod1.hul.harvard.edu/10.1080/2162402X.2017.1328336> **6**, (2017).
110. Hurwitz, A. A. & Watkins, S. K. Immune suppression in the tumor microenvironment: A role for dendritic cell-mediated tolerization of T cells. *Cancer Immunology, Immunotherapy* **61**, 289–293 (2012).
111. Topalian, S. L. *et al.* Safety, Activity, and Immune Correlates of Anti-PD-1 Antibody in Cancer. *New England Journal of Medicine* **366**, 2443–2454 (2012).
112. Hirayama, A. v. *et al.* The response to lymphodepletion impacts PFS in patients with aggressive non-Hodgkin lymphoma treated with CD19 CAR T cells. *Blood* **133**, 1876–1887 (2019).

113. Gattinoni, L., Powell, D. J., Rosenberg, S. A. & Restifo, N. P. Adoptive immunotherapy for cancer: building on success. *Nat Rev Immunol* **6**, 383 (2006).
114. Schuster, S. J. *et al.* Tisagenlecleucel in Adult Relapsed or Refractory Diffuse Large B-Cell Lymphoma. *New England Journal of Medicine* **380**, 45–56 (2019).
115. Locke, F. L. *et al.* Long-term safety and activity of axicabtagene ciloleucel in refractory large B-cell lymphoma (ZUMA-1): a single-arm, multicentre, phase 1–2 trial. *Lancet Oncol* **20**, 31–42 (2019).
116. Munshi, N. C. *et al.* Idecabtagene Vicleucel in Relapsed and Refractory Multiple Myeloma. *New England Journal of Medicine* **384**, 705–716 (2021).
117. Ghilardi, G. *et al.* Bendamustine is safe and effective for lymphodepletion before tisagenlecleucel in patients with refractory or relapsed large B-cell lymphomas. *Annals of Oncology* **33**, 916–928 (2022).
118. Maziarz, R. T., Diaz, A., Miklos, D. & Shah, N. N. Perspective: An International Fludarabine Shortage: Supply Chain Issues Impacting Transplantation and Immune Effector Cell Therapy Delivery. *Transplant Cell Ther* (2022) doi:10.1016/J.JTCT.2022.08.002.
119. Pocaterra, A., Catucci, M. & Mondino, A. Adoptive T cell therapy of solid tumors: time to team up with immunogenic chemo/radiotherapy. *Curr Opin Immunol* **74**, 53–59 (2022).
120. Murad, J. P. *et al.* Pre-conditioning modifies the TME to enhance solid tumor CAR T cell efficacy and endogenous protective immunity. *Molecular Therapy* **29**, 2335–2349 (2021).
121. Srivastava, S. *et al.* Immunogenic Chemotherapy Enhances Recruitment of CAR-T Cells to Lung Tumors and Improves Antitumor Efficacy when Combined with Checkpoint Blockade. *Cancer Cell* **39**, 193–208.e10 (2021).
122. Menon, H. *et al.* Role of radiation therapy in modulation of the tumor stroma and microenvironment. *Front Immunol* **10**, 193 (2019).
123. Dewan, M., Galloway, A., ... N. K.-C. C. & 2009, undefined. Fractionated but Not Single-Dose Radiotherapy Induces an Immune-Mediated Abscopal Effect when Combined with Anti-CTLA-4 Antibody. *AACR*.
124. Lugade, A. A. *et al.* Local Radiation Therapy of B16 Melanoma Tumors Increases the Generation of Tumor Antigen-Specific Effector Cells That Traffic to the Tumor. *The Journal of Immunology* **174**, 7516–7523 (2005).
125. Klug, F. *et al.* Low-Dose Irradiation Programs Macrophage Differentiation to an iNOS<sup>+</sup>/M1 Phenotype that Orchestrates Effective T Cell Immunotherapy. *Cancer Cell* **24**, 589–602 (2013).

126. Curtsinger, J. M. & Mescher, M. F. Inflammatory Cytokines as a Third Signal for T Cell Activation. *Curr Opin Immunol* **22**, 333 (2010).
127. Pouw, N., Treffers-Westerlaken, E., Mondino, A., Lamers, C. & Debets, R. TCR gene-engineered T cell: Limited T cell activation and combined use of IL-15 and IL-21 ensure minimal differentiation and maximal antigen-specificity. *Mol Immunol* **47**, 1411–1420 (2010).
128. Bondanza, A. *et al.* Suicide gene therapy of graft-versus-host disease induced by central memory human T lymphocytes. *Blood* **107**, 1828–1836 (2006).
129. Mescher, M. F. Surface contact requirements for activation of cytotoxic T lymphocytes. *The Journal of Immunology* **149**, (1992).
130. Cheung, A. S., Zhang, D. K. Y., Koshy, S. T. & Mooney, D. J. Scaffolds that mimic antigen-presenting cells enable ex vivo expansion of primary T cells. *Nature Biotechnology* *2018* **36:2** **36**, 160–169 (2018).
131. Sunshine, J. C., Perica, K., Schneck, J. P. & Green, J. J. Particle shape dependence of CD8<sup>+</sup> T cell activation by artificial antigen presenting cells. *Biomaterials* **35**, 269–277 (2014).
132. Fadel, T. R. *et al.* A carbon nanotube–polymer composite for T-cell therapy. *Nature Nanotechnology* *2014* **9:8** **9**, 639–647 (2014).
133. Meyer, R. A. *et al.* Biodegradable Nanoellipsoidal Artificial Antigen Presenting Cells for Antigen Specific T-Cell Activation. *Small* **11**, 1519–1525 (2015).
134. Alvarez-Fernández, C., Escribà-Garcia, L., Vidal, S., Sierra, J. & Briones, J. A short CD3/CD28 costimulation combined with IL-21 enhance the generation of human memory stem T cells for adoptive immunotherapy. *J Transl Med* **14**, 1–10 (2016).
135. Badovinac, V. P. & Harty, J. T. Manipulating the Rate of Memory CD8<sup>+</sup> T Cell Generation after Acute Infection. *The Journal of Immunology* **179**, 53–63 (2007).
136. D’Souza, W. N. & Hedrick, S. M. Cutting Edge: Latecomer CD8 T Cells Are Imprinted with a Unique Differentiation Program. *The Journal of Immunology* **177**, 777–781 (2006).
137. Solouki, S. *et al.* TCR Signal Strength and Antigen Affinity Regulate CD8 + Memory T Cells. *The Journal of Immunology* **205**, 1217–1227 (2020).
138. Mandal, S. *et al.* Polymer-based synthetic dendritic cells for tailoring robust and multifunctional T cell responses. *ACS Chem Biol* **10**, 485–492 (2015).
139. Sun, L. *et al.* DNA-Edited Ligand Positioning on Red Blood Cells to Enable Optimized T Cell Activation for Adoptive Immunotherapy. *Angewandte Chemie International Edition* **59**, 14842–14853 (2020).



140. Zhang, D. K. Y., Cheung, A. S. & Mooney, D. J. Activation and expansion of human T cells using artificial antigen-presenting cell scaffolds. *Nature Protocols* 2020 15:3 **15**, 773–798 (2020).
141. Philipson, B. I. *et al.* 4-1BB costimulation promotes CAR T cell survival through noncanonical NF- $\kappa$ B signaling. *Sci Signal* **13**, (2020).
142. Zhang, H. *et al.* 4-1BB Is Superior to CD28 Costimulation for Generating CD8+ Cytotoxic Lymphocytes for Adoptive Immunotherapy. *The Journal of Immunology* **179**, 4910–4918 (2007).
143. Maus, M. v. *et al.* Ex vivo expansion of polyclonal and antigen-specific cytotoxic T lymphocytes by artificial APCs expressing ligands for the T-cell receptor, CD28 and 4-1BB. *Nature Biotechnology* 2002 20:2 **20**, 143–148 (2002).
144. Chacon, J. A. *et al.* Co-Stimulation through 4-1BB/CD137 Improves the Expansion and Function of CD8+ Melanoma Tumor-Infiltrating Lymphocytes for Adoptive T-Cell Therapy. *PLoS One* **8**, e60031 (2013).
145. Hernandez-Chacon, J. A. *et al.* Co-stimulation through the CD137/4-1BB pathway protects human melanoma tumor-infiltrating lymphocytes from activation-induced cell death and enhances anti-tumor effector function. *J Immunother* **34**, 236 (2011).
146. Liegel, J. *et al.* T Cells Educated By DC/AML Fusions in the Context of 4-1BB Costimulation As a Potent Strategy for Adoptive Cellular Therapy. *Blood* **134**, 2673 (2019).
147. McNamara, J. O. *et al.* Multivalent 4-1BB binding aptamers costimulate CD8+ T cells and inhibit tumor growth in mice. *J Clin Invest* **118**, 376–386 (2008).
148. Ramakrishna, V. *et al.* Characterization of the human T cell response to in vitro CD27 costimulation with varlilumab. *J Immunother Cancer* **3**, 1–13 (2015).
149. Lee, S.-J. *et al.* CD134 Costimulation Couples the CD137 Pathway to Induce Production of Supereffector CD8 T Cells That Become IL-7 Dependent. *The Journal of Immunology* **179**, 2203–2214 (2007).
150. Alves Costa Silva, C., Facchinetti, F., Routy, B. & Derosa, L. New pathways in immune stimulation: targeting OX40. *ESMO Open* **5**, e000573 (2020).
151. Hinrichs, C. S. *et al.* IL-2 and IL-21 confer opposing differentiation programs to CD8+ T cells for adoptive immunotherapy. *Blood* **111**, 5326–5333 (2008).
152. Ross, S. H. & Cantrell, D. A. Signaling and Function of Interleukin-2 in T Lymphocytes. *Annu Rev Immunol* **36**, 411 (2018).

153. Moroz, A. *et al.* IL-21 Enhances and Sustains CD8<sup>+</sup> T Cell Responses to Achieve Durable Tumor Immunity: Comparative Evaluation of IL-2, IL-15, and IL-21. *The Journal of Immunology* **173**, 900–909 (2004).
154. Guo, Y., Luan, L., Patil, N. K. & Sherwood, E. R. Immunobiology of the IL-15/IL-15R $\alpha$  complex as an antitumor and antiviral agent. *Cytokine Growth Factor Rev* **38**, 10–21 (2017).
155. Rathmell, J. C., Farkash, E. A., Gao, W. & Thompson, C. B. IL-7 Enhances the Survival and Maintains the Size of Naive T Cells. *The Journal of Immunology* **167**, 6869–6876 (2001).
156. Floros, T. & Tarhini, A. A. Anticancer Cytokines: Biology and Clinical Effects of Interferon- $\alpha$ 2, Interleukin (IL)-2, IL-15, IL-21, and IL-12. *Semin Oncol* **42**, 539–548 (2015).
157. Parlato, S. *et al.* Expression of CCR-7, MIP-3 $\beta$ , and Th-1 chemokines in type I IFN-induced monocyte-derived dendritic cells: importance for the rapid acquisition of potent migratory and functional activities. *Blood* **98**, 3022–3029 (2001).
158. Sabatino, M. *et al.* Generation of clinical-grade CD19-specific CAR-modified CD8<sup>+</sup> memory stem cells for the treatment of human B-cell malignancies. *Blood* **128**, 519–528 (2016).
159. Li, Y. *et al.* MART-1–Specific Melanoma Tumor-Infiltrating Lymphocytes Maintaining CD28 Expression Have Improved Survival and Expansion Capability Following Antigenic Restimulation In Vitro. *The Journal of Immunology* **184**, 452–465 (2010).
160. Yang, S. *et al.* Modulating the differentiation status of ex vivo-cultured anti-tumor T cells using cytokine cocktails. *Cancer Immunology, Immunotherapy* **62**, 727–736 (2013).
161. Cui, W., Joshi, N. S., Jiang, A. & Kaech, S. M. Effects of Signal 3 during CD8 T cell priming: Bystander production of IL-12 enhances effector T cell expansion but promotes terminal differentiation. *Vaccine* **27**, 2177–2187 (2009).
162. Crompton, J. G. *et al.* Akt inhibition enhances expansion of potent tumor-specific lymphocytes with memory cell characteristics. *Cancer Res* **75**, 296–305 (2015).
163. van der Waart, A. B. *et al.* Inhibition of Akt signaling promotes the generation of superior tumor-reactive T cells for adoptive immunotherapy. *Blood* **124**, 3490–3500 (2014).
164. Eid, R. A. *et al.* Akt1 and -2 inhibition diminishes terminal differentiation and enhances central memory CD8<sup>+</sup> T-cell proliferation and survival. *Oncoimmunology* **4**, (2015).
165. Urak, R. *et al.* Ex vivo Akt inhibition promotes the generation of potent CD19CAR T cells for adoptive immunotherapy. *J Immunother Cancer* **5**, 1–13 (2017).

166. Zheng, W. *et al.* PI3K orchestration of the in vivo persistence of chimeric antigen receptor-modified T cells. *Leukemia* 2018 32:5 **32**, 1157–1167 (2018).
167. Petersen, C. T. *et al.* Improving T-cell expansion and function for adoptive T-cell therapy using ex vivo treatment with PI3K $\delta$  inhibitors and VIP antagonists. *Blood Adv* **2**, 210–223 (2018).
168. Zheng, W. *et al.* PI3K orchestration of the in vivo persistence of chimeric antigen receptor-modified T cells. *Leukemia* 2018 32:5 **32**, 1157–1167 (2018).
169. Bowers, J. S. *et al.* PI3K $\delta$  inhibition enhances the antitumor fitness of adoptively transferred CD8<sup>+</sup> T cells. *Front Immunol* **8**, 1221 (2017).
170. Mineharu, Y., Kamran, N., Lowenstein, P. R. & Castro, M. G. Blockade of mTOR signaling via rapamycin combined with immunotherapy augments antiglioma cytotoxic and memory T-Cell functions. *Mol Cancer Ther* **13**, 3024–3036 (2014).
171. Chatterjee, S. *et al.* Targeting PIM kinase with PD1 inhibition improves immunotherapeutic antitumor t-cell response. *Clinical Cancer Research* **25**, 1036–1049 (2019).
172. Sauer, S. *et al.* T cell receptor signaling controls Foxp3 expression via PI3K, Akt, and mTOR. *Proc Natl Acad Sci U S A* **105**, 7797–7802 (2008).
173. Sukumar, M., Kishton, R. J. & Restifo, N. P. Metabolic reprogramming of anti-tumor immunity. *Curr Opin Immunol* **46**, 14–22 (2017).
174. O’Sullivan, D. & Pearce, E. L. Targeting T cell metabolism for therapy. *Trends Immunol* **36**, 71–80 (2015).
175. Sukumar, M. *et al.* Inhibiting glycolytic metabolism enhances CD8<sup>+</sup> T cell memory and antitumor function. *J Clin Invest* **123**, 4479–4488 (2013).
176. Cantor, J. R. *et al.* Physiologic Medium Rewires Cellular Metabolism and Reveals Uric Acid as an Endogenous Inhibitor of UMP Synthase. *Cell* **169**, 258-272.e17 (2017).
177. Geiger, R. *et al.* L-Arginine Modulates T Cell Metabolism and Enhances Survival and Anti-tumor Activity. *Cell* **167**, 829-842.e13 (2016).
178. Balmer, M. L. *et al.* Memory CD8<sup>+</sup> T Cells Require Increased Concentrations of Acetate Induced by Stress for Optimal Function. *Immunity* **44**, 1312–1324 (2016).
179. Huang, Y. *et al.* Resuscitating cancer immunosurveillance: Selective stimulation of DLL1-notch signaling in T cells rescues T-cell function and inhibits tumor growth. *Cancer Res* **71**, 6122–6131 (2011).

180. Biktasova, A. K. *et al.* Multivalent forms of the notch ligand DLL-1 enhance antitumor T-cell immunity in lung cancer and improve efficacy of EGFR-targeted therapy. *Cancer Res* **75**, 4728–4741 (2015).
181. Kondo, T. *et al.* Notch-mediated conversion of activated T cells into stem cell memory-like T cells for adoptive immunotherapy. *Nature Communications* **2017 8:1 8**, 1–14 (2017).
182. Ando, M. *et al.* Rejuvenating Effector/Exhausted CAR T Cells to Stem Cell Memory-Like CAR T Cells By Resting Them in the Presence of CXCL12 and the NOTCH Ligand. *Cancer Research Communications* **1**, 41–55 (2021).
183. Janghorban, M., Xin, L., Rosen, J. M. & Zhang, X. H. F. Notch signaling as a regulator of the tumor immune response: To target or not to target? *Front Immunol* **9**, 1649 (2018).
184. Muralidharan, S. *et al.* Activation of Wnt Signaling Arrests Effector Differentiation in Human Peripheral and Cord Blood-Derived T Lymphocytes. *The Journal of Immunology* **187**, 5221–5232 (2011).
185. Muranski, P. *et al.* Th17 Cells Are Long Lived and Retain a Stem Cell-like Molecular Signature. *Immunity* **35**, 972–985 (2011).
186. D’Souza, W. N., Chang, C.-F., Fischer, A. M., Li, M. & Hedrick, S. M. The Erk2 MAPK Regulates CD8 T Cell Proliferation and Survival. *The Journal of Immunology* **181**, 7617–7629 (2008).
187. Boni, A. *et al.* Selective BRAFV600E inhibition enhances T-cell recognition of melanoma without affecting lymphocyte function. *Cancer Res* **70**, 5213–5219 (2010).
188. Gurusamy, D. *et al.* Multi-phenotype CRISPR-Cas9 Screen Identifies p38 Kinase as a Target for Adoptive Immunotherapies. *Cancer Cell* **37**, 818-833.e9 (2020).
189. Hao, M. *et al.* Combination of metabolic intervention and T cell therapy enhances solid tumor immunotherapy. *Sci Transl Med* **12**, 6667 (2020).
190. Liu, Y. *et al.* Cytokine conjugation to enhance T cell therapy. *Proceedings of the National Academy of Sciences* **120**, e2213222120 (2022).
191. Yeku, O. O., Purdon, T. J., Koneru, M., Spriggs, D. & Brentjens, R. J. Armored CAR T cells enhance antitumor efficacy and overcome the tumor microenvironment. *Scientific Reports* **2017 7:1 7**, 1–14 (2017).
192. Chmielewski, M. & Abken, H. CAR T cells transform to trucks: Chimeric antigen receptor-redirected T cells engineered to deliver inducible IL-12 modulate the tumour stroma to combat cancer. *Cancer Immunology, Immunotherapy* **61**, 1269–1277 (2012).

193. Zhang, S., Zhao, J., Bai, X., Handley, M. & Shan, F. Biological effects of IL-15 on immune cells and its potential for the treatment of cancer. *Int Immunopharmacol* **91**, 107318 (2021).
194. Tang, L. *et al.* Enhancing T cell therapy through TCR-signaling-responsive nanoparticle drug delivery. *Nature Biotechnology* 2018 36:8 **36**, 707–716 (2018).
195. Wang, H. *et al.* Metabolic labeling and targeted modulation of dendritic cells. *Nature Materials* 2020 19:11 **19**, 1244–1252 (2020).
196. Luo, Y. *et al.* IL-12 nanochaperone-engineered CAR T cell for robust tumor-immunotherapy. *Biomaterials* **281**, 121341 (2022).
197. Jones, R. B. *et al.* Antigen recognition-triggered drug delivery mediated by nanocapsule-functionalized cytotoxic T-cells. *Biomaterials* **117**, 44–53 (2017).
198. Stephan, M. T., Moon, J. J., Um, S. H., Bersthteyn, A. & Irvine, D. J. Therapeutic cell engineering with surface-conjugated synthetic nanoparticles. *Nature Medicine* 2010 16:9 **16**, 1035–1041 (2010).
199. Sanz-Ortega, L. *et al.* T cells loaded with magnetic nanoparticles are retained in peripheral lymph nodes by the application of a magnetic field. *J Nanobiotechnology* **17**, 1–20 (2019).
200. Siriwon, N. *et al.* CAR-T cells surface-engineered with drug-encapsulated nanoparticles can ameliorate intratumoral T-cell hypofunction. *Cancer Immunol Res* **6**, 812–824 (2018).
201. Nie, W. *et al.* Magnetic Nanoclusters Armed with Responsive PD-1 Antibody Synergistically Improved Adoptive T-Cell Therapy for Solid Tumors. *ACS Nano* **13**, 1469–1478 (2019).
202. Stadtmauer, E. A. *et al.* CRISPR-engineered T cells in patients with refractory cancer. *Science (1979)* **367**, (2020).
203. Narayan, V. *et al.* PSMA-targeting TGF $\beta$ -insensitive armored CAR T cells in metastatic castration-resistant prostate cancer: a phase 1 trial. *Nature Medicine* 2022 28:4 **28**, 724–734 (2022).
204. Kloss, C. C. *et al.* Dominant-Negative TGF- $\beta$  Receptor Enhances PSMA-Targeted Human CAR T Cell Proliferation And Augments Prostate Cancer Eradication. *Molecular Therapy* **26**, 1855–1866 (2018).
205. Zebley, C. C. *et al.* CD19-CAR T cells undergo exhaustion DNA methylation programming in patients with acute lymphoblastic leukemia. *Cell Rep* **37**, 110079 (2021).
206. Prinzing, B. *et al.* Deleting DNMT3A in CAR T cells prevents exhaustion and enhances antitumor activity. *Sci Transl Med* **13**, (2021).

207. Zhang, L. *et al.* Tumor-infiltrating lymphocytes genetically engineered with an inducible gene encoding interleukin-12 for the immunotherapy of metastatic melanoma. *Clinical Cancer Research* **21**, 2278–2288 (2015).
208. Ghassemi, S. *et al.* Reducing Ex Vivo Culture Improves the Antileukemic Activity of Chimeric Antigen Receptor (CAR) T Cells. *Cancer Immunol Res* **6**, 1100–1109 (2018).
209. Flinn, I. W. *et al.* A First-in-Human Study of YTB323, a Novel, Autologous CD19-Directed CAR-T Cell Therapy Manufactured Using the Novel T-Charge™ platform, for the Treatment of Patients (Pts) with Relapsed/Refractory (r/r) Diffuse Large B-Cell Lymphoma (DLBCL). *Blood* **138**, 740–740 (2021).
210. Sperling, A. S. *et al.* P1446: PHASE I STUDY DATA UPDATE OF PHE885, A FULLY HUMAN BCMA-DIRECTED CAR-T CELL THERAPY MANUFACTURED USING THE T-CHARGE™ PLATFORM FOR PATIENTS WITH RELAPSED/REFRACTORY (R/R) MULTIPLE MYELOMA (MM). *Hemasphere* **6**, 1329–1330 (2022).
211. Nawaz, W. *et al.* AAV-mediated in vivo CAR gene therapy for targeting human T-cell leukemia. *Blood Cancer Journal* 2021 11:6 **11**, 1–12 (2021).
212. Agarwalla, P. *et al.* Bioinstructive implantable scaffolds for rapid in vivo manufacture and release of CAR-T cells. *Nature Biotechnology* 2022 40:8 **40**, 1250–1258 (2022).
213. Agarwal, S. *et al.* In Vivo Generation of CAR T Cells Selectively in Human CD4+ Lymphocytes. *Molecular Therapy* **28**, 1783–1794 (2020).
214. Rurik, J. G. *et al.* CAR T cells produced in vivo to treat cardiac injury. *Science* (1979) **375**, 91–96 (2022).
215. Parayath, N. N., Stephan, S. B., Koehne, A. L., Nelson, P. S. & Stephan, M. T. In vitro-transcribed antigen receptor mRNA nanocarriers for transient expression in circulating T cells in vivo. *Nat Commun* **11**, (2020).
216. Saitakis, M. *et al.* Different TCR-induced T lymphocyte responses are potentiated by stiffness with variable sensitivity. *Elife* **6**, (2017).
217. O'Connor, R. *et al.* Substrate rigidity regulates human T cell activation and proliferation. *The Journal of Immunology* **188**, (2012).
218. Majedi, F. S. *et al.* T-cell activation is modulated by the 3D mechanical microenvironment. *Biomaterials* **252**, 120058 (2020).
219. Jiang, J. & Ahuja, S. Addressing Patient to Patient Variability for Autologous CAR T Therapies. *J Pharm Sci* **110**, 1871–1876 (2021).

220. Mueller-schoell, A. *et al.* Early Survival Prediction Framework in CD19-Specific CAR-T Cell Immunotherapy Using a Quantitative Systems Pharmacology Model. *Cancers* 2021, Vol. 13, Page 2782 **13**, 2782 (2021).
221. Weiss, T., Weller, M., Guckenberger, M., Sentman, C. L. & Roth, P. NKG2D-based CAR T cells and radiotherapy exert synergistic efficacy in glioblastoma. *Cancer Res* **78**, 1031–1043 (2018).
222. Grosser, R., Cherkassky, L., Chintala, N. & Adusumilli, P. S. Combination Immunotherapy with CAR T Cells and Checkpoint Blockade for the Treatment of Solid Tumors. *Cancer Cell* **36**, 471–482 (2019).
223. Song, W. & Zhang, M. Use of CAR-T cell therapy, PD-1 blockade, and their combination for the treatment of hematological malignancies. *Clinical Immunology* **214**, 108382 (2020).
224. Liu, Y. *et al.* Intravenous injection of the oncolytic virus M1 awakens antitumor T cells and overcomes resistance to checkpoint blockade. *Cell Death & Disease* 2020 *11*:12 **11**, 1–13 (2020).
225. Park, A. K. *et al.* Effective combination immunotherapy using oncolytic viruses to deliver CAR targets to solid tumors. *Sci Transl Med* **12**, 1863 (2020).
226. Lanitis, E., Irving, M. & Coukos, G. Targeting the tumor vasculature to enhance T cell activity. *Curr Opin Immunol* **33**, 55–63 (2015).
227. Chmielewski, M., Kopecky, C., Hombach, A. A. & Abken, H. IL-12 release by engineered T cells expressing chimeric antigen receptors can effectively muster an antigen-independent macrophage response on tumor cells that have shut down tumor antigen expression. *Cancer Res* **71**, 5697–5706 (2011).
228. Fu, R. *et al.* Delivery Techniques for Enhancing CAR T Cell Therapy against Solid Tumors. *Adv Funct Mater* **31**, 2009489 (2021).
229. Motzer, R. J. *et al.* Phase I trial of subcutaneous recombinant human interleukin-12 in patients with advanced renal cell carcinoma. *Clinical Cancer Research* **4**, 1183–1191 (1998).
230. Sangro, B. *et al.* Phase I trial of intratumoral injection of an adenovirus encoding interleukin-12 for advanced digestive tumors. *Journal of Clinical Oncology* **22**, 1389–1397 (2004).
231. Bortolanza, S. *et al.* Treatment of pancreatic cancer with an oncolytic adenovirus expressing interleukin-12 in Syrian hamsters. *Molecular Therapy* **17**, 614–622 (2009).
232. Guo, N. *et al.* Study of recombinant human interleukin-12 for treatment of complications after radiotherapy for tumor patients. *World J Clin Oncol* **8**, 158–167 (2017).

233. Bhatia, S. *et al.* Recombinant interleukin-21 plus sorafenib for metastatic renal cell carcinoma: A phase 1/2 study. *J Immunother Cancer* **2**, 1–11 (2014).
234. Conlon, K. C. *et al.* Redistribution, Hyperproliferation, Activation of Natural Killer Cells and CD8 T Cells, and Cytokine Production During First-in-Human Clinical Trial of Recombinant Human Interleukin-15 in Patients With Cancer. *Journal of Clinical Oncology* **33**, 74 (2015).
235. Floros, T. & Tarhini, A. A. Anticancer Cytokines: Biology and Clinical Effects of Interferon- $\alpha$ 2, Interleukin (IL)-2, IL-15, IL-21, and IL-12. *Semin Oncol* **42**, 539–548 (2015).
236. Hotz, C. *et al.* Local delivery of mRNA-encoding cytokines promotes antitumor immunity and tumor eradication across multiple preclinical tumor models. *Sci Transl Med* **13**, (2021).
237. Wyatt Shields, C. *et al.* Cellular backpacks for macrophage immunotherapy. *Sci Adv* **6**, (2020).
238. Saxon, E. & Bertozzi, C. R. Cell surface engineering by a modified Staudinger reaction. *Science (1979)* **287**, 2007–2010 (2000).
239. Prescher, J. A., Dube, D. H. & Bertozzi, C. R. Chemical remodelling of cell surfaces in living animals. *Nature* **430**, 873–877 (2004).
240. Du, J. *et al.* Metabolic glycoengineering: Sialic acid and beyond. *Glycobiology* **19**, 1382–1401 (2009).
241. Wang, H. *et al.* Metabolic labeling and targeted modulation of dendritic cells. *Nature Materials* **19**, 1244–1252 (2020).
242. Tokunaga, R. *et al.* CXCL9, CXCL10, CXCL11/CXCR3 axis for immune activation - a target for novel cancer therapy. *Cancer Treat Rev* **63**, 40 (2018).
243. Sato, N., Patel, H. J., Waldmann, T. A. & Tagaya, Y. The IL-15/IL-15R $\alpha$  on cell surfaces enables sustained IL-15 activity and contributes to the long survival of CD8 memory T cells. *Proc Natl Acad Sci U S A* **104**, 588–593 (2007).
244. Smyth, M. J., Taniguchi, M. & Street, S. E. A. The Anti-Tumor Activity of IL-12: Mechanisms of Innate Immunity That Are Model and Dose Dependent. *The Journal of Immunology* **165**, 2665–2670 (2000).
245. Chiodoni, C. *et al.* Different requirements for  $\alpha$ -galactosylceramide and recombinant IL-12 antitumor activity in the treatment of C-26 colon carcinoma hepatic metastases. *Eur J Immunol* **31**, 3101–3110 (2001).



246. Fallon, J. K., Vandevener, A. J., Schlom, J. & Greiner, J. W. Enhanced antitumor effects by combining an IL-12/anti-DNA fusion protein with avelumab, an anti-PD-L1 antibody. *Oncotarget* **8**, 20558 (2017).
247. Xue, D., Hsu, E., Fu, Y. X. & Peng, H. Next-generation cytokines for cancer immunotherapy. *Antib Ther* **4**, 123–133 (2021).
248. Pogue, S. L. *et al.* Targeting Attenuated Interferon- $\alpha$  to Myeloma Cells with a CD38 Antibody Induces Potent Tumor Regression with Reduced Off-Target Activity. *PLoS One* **11**, e0162472 (2016).
249. Srivastava, S. *et al.* Immunogenic Chemotherapy Enhances Recruitment of CAR-T Cells to Lung Tumors and Improves Antitumor Efficacy when Combined with Checkpoint Blockade. *Cancer Cell* **39**, 193-208.e10 (2021).
250. Geyer, M. B. *et al.* Safety and tolerability of conditioning chemotherapy followed by CD19-targeted CAR T cells for relapsed/refractory CLL. *JCI Insight* **4**, (2019).
251. Chapuis, A. G. *et al.* T-Cell Therapy Using Interleukin-21–Primed Cytotoxic T-Cell Lymphocytes Combined With Cytotoxic T-Cell Lymphocyte Antigen-4 Blockade Results in Long-Term Cell Persistence and Durable Tumor Regression. *Journal of Clinical Oncology* **34**, 3787 (2016).
252. Xin, G. *et al.* Pathogen-boosted adoptive cell transfer therapy induces endogenous antitumor immunity through antigen spreading. *Cancer Immunol Res* **8**, 7–18 (2020).
253. Etxeberria, I. *et al.* Intratumor Adoptive Transfer of IL-12 mRNA Transiently Engineered Antitumor CD8<sup>+</sup> T Cells. *Cancer Cell* **36**, 613-629.e7 (2019).
254. Wang, H. *et al.* Metabolic labeling and targeted modulation of dendritic cells. *Nature Materials* **2020 19:11 19**, 1244–1252 (2020).
255. CRAN - Package pheatmap. <https://cran.r-project.org/web/packages/pheatmap/index.html>.
256. Wickham, H. ggplot2. (2016) doi:10.1007/978-3-319-24277-4.
257. Hao, Y. *et al.* Integrated analysis of multimodal single-cell data. *Cell* **184**, 3573-3587.e29 (2021).
258. Package ‘ggpointdensity’ Type Package Title A Cross Between a 2D Density Plot and a Scatter Plot. (2022).
259. Xie, Z. *et al.* Gene Set Knowledge Discovery with Enrichr. *Curr Protoc* **1**, (2021).
260. Biological research – Pathway Studio | Elsevier. <https://www-elsevier-com.ezp-prod1.hul.harvard.edu/solutions/pathway-studio-biological-research>.

261. The NCI-Nature Pathway Interaction Database: A cell signaling resource - Google Search. <https://www.google.com/search?client=firefox-b-1-d&q=The+NCI-Nature+Pathway+Interaction+Database%3A+A+cell+signaling+resource>.
262. Gao, C.-H., Yu, G. & Cai, P. ggVennDiagram: An Intuitive, Easy-to-Use, and Highly Customizable R Package to Generate Venn Diagram. *Front Genet* **12**, (2021).
263. Tools for Descriptive Statistics • DescTools. <https://andrisignorell.github.io/DescTools/>.
264. Love, M. I., Huber, W. & Anders, S. Moderated estimation of fold change and dispersion for RNA-seq data with DESeq2. *Genome Biology* **2014 15:12** **15**, 1–21 (2014).
265. Terrén, I. *et al.* Cytokine-Induced Memory-Like NK Cells: From the Basics to Clinical Applications. *Front Immunol* **13**, (2022).
266. Cózar, B. *et al.* Tumor-infiltrating natural killer cells. *Cancer Discov* **11**, 34 (2021).
267. Davis, Z. B., Felices, M., Verneris, M. R. & Miller, J. S. Natural Killer Cell Adoptive Transfer Therapy: Exploiting the First Line of Defense Against Cancer. *Cancer J* **21**, 486 (2015).
268. Miller, J. S. & Geller, M. A. Use of allogeneic NK cells for cancer immunotherapy. *Immunotherapy* **3**, 1445 (2011).
269. Berrien-Elliott, M. M., Wagner, J. A. & Fehniger, T. A. Human Cytokine-Induced Memory-Like Natural Killer Cells. *J Innate Immun* **7**, 563 (2015).
270. Romee, R. *et al.* Cytokine-induced memory-like natural killer cells exhibit enhanced responses against myeloid leukemia. *Sci Transl Med* **8**, (2016).
271. Granzin, M. *et al.* Shaping of Natural Killer Cell Antitumor Activity by Ex Vivo Cultivation. *Front Immunol* **8**, (2017).
272. Denman, C. J. *et al.* Membrane-Bound IL-21 Promotes Sustained Ex Vivo Proliferation of Human Natural Killer Cells. *PLoS One* **7**, e30264 (2012).
273. Campbell, J. J. *et al.* Unique Subpopulations of CD56+ NK and NK-T Peripheral Blood Lymphocytes Identified by Chemokine Receptor Expression Repertoire. *The Journal of Immunology* **166**, 6477–6482 (2001).
274. Cooper, M. A. *et al.* Human natural killer cells: a unique innate immunoregulatory role for the CD56bright subset. *Blood* **97**, 3146–3151 (2001).
275. Carrega, P. *et al.* Natural killer cells infiltrating human nonsmall-cell lung cancer are enriched in CD56brightCD16– cells and display an impaired capability to kill tumor cells. *Cancer* **112**, 863–875 (2008).

276. Wang, M. *et al.* Automation Platform for CAR-T Manufacturing: The Benefits and the Clinical Outcomes. *Blood* **134**, 1960 (2019).
277. Driving the next wave of innovation in CAR T-cell therapies | McKinsey. <https://www.mckinsey.com/industries/life-sciences/our-insights/driving-the-next-wave-of-innovation-in-car-t-cell-therapies>.
278. Lee, D. W. *et al.* ASTCT Consensus Grading for Cytokine Release Syndrome and Neurologic Toxicity Associated with Immune Effector Cells. *Biology of Blood and Marrow Transplantation* **25**, 625–638 (2019).
279. Santomasso, B., Bachier, C., Westin, J., Rezvani, K. & Shpall, E. J. The Other Side of CAR T-Cell Therapy: Cytokine Release Syndrome, Neurologic Toxicity, and Financial Burden. *American Society of Clinical Oncology Educational Book* 433–444 (2019) doi:10.1200/edbk\_238691.
280. Hay, K. A. *et al.* Kinetics and biomarkers of severe cytokine release syndrome after CD19 chimeric antigen receptor–modified T-cell therapy. *Blood* **130**, 2295 (2017).
281. Tedesco, V. E. & Mohan, C. Biomarkers for Predicting Cytokine Release Syndrome following CD19-Targeted CAR T Cell Therapy. *J Immunol* **206**, 1561–1568 (2021).
282. Hartmann, J., Schübler-Lenz, M., Bondanza, A. & Buchholz, C. J. Clinical development of CAR T cells—challenges and opportunities in translating innovative treatment concepts. *EMBO Mol Med* **9**, 1183–1197 (2017).
283. The Digital Edge in CAR-T Manufacturing and Delivery | BCG. <https://www.bcg.com/publications/2021/car-t-cell-therapy-digital-supply-chain>.
284. Levine, B. L., Miskin, J., Wonnacott, K. & Keir, C. Global Manufacturing of CAR T Cell Therapy. *Mol Ther Methods Clin Dev* **4**, 92–101 (2017).
285. Salih, H. R. & Jung, G. The challenges of translation. *EMBO Mol Med* **11**, e10874 (2019).
286. le Gouill, S. *et al.* Is Good Clinical Practice Becoming Poor Clinical Care? *Hemasphere* **1**, (2017).
287. Ahmed, N. *et al.* Socioeconomic and Racial Disparity in Chimeric Antigen Receptor T Cell Therapy Access. *Transplant Cell Ther* **28**, 358–364 (2022).
288. Burki, T. K. CAR T-cell therapy roll-out in low-income and middle-income countries. *Lancet Haematol* **8**, e252–e253 (2021).
289. Port to patient: Improving country cold chains for COVID-19 vaccines | McKinsey. <https://www.mckinsey.com/industries/public-and-social-sector/our-insights/port-to-patient-improving-country-cold-chains-for-covid-19-vaccines>.

290. Angel, S. *et al.* Toward Optimal Cryopreservation and Storage for Achievement of High Cell Recovery and Maintenance of Cell Viability and T Cell Functionality. *Biopreserv Biobank* **14**, 539–547 (2016).
291. Ivanics, T. *et al.* Patient-derived xenograft cryopreservation and reanimation outcomes are dependent on cryoprotectant type. *Lab Invest* **98**, 947–956 (2018).

## Appendices

### Appendix 1: Tables for Chapter 4

#### A1.1 – Donor information

Data	Donor
Figure 2f-h	Donor 19
Figure 3	Donor 22
Figure 4a-c	Donor 2
Figure 4d-g	Donor 22
Figure 5	Donor 2
Figure 6	Donor 3
Figure 7	Donor 2
Extended Figure 2	Donor 19
	Donor 21
	Donor 22
Extended Figure 3a	Donor D
Extended Figure 3b-e	Donor 2
Extended Figure 4	Donor 2
Extended Figure 7	Donor 2
Extended Figure 8	Donor 2
Extended Figure 9	Donor 22
Extended Figure 10	Donor 2
Extended Figure 11	Donor 21
Extended Figure 12	Donor 2
Extended Figure 13a-f	Donor 1
Extended Figure 13g	Pmel-1 (mouse)
Extended Figure 14	Donor 2

#### A1.2 – Tumor cell gene signature

Tumor Type	NSCLC				
Gene	p_val	avg_log2FC	pct.1	pct.2	p_val_adj
LSP1	0	0.315605759	0.956	0.88	0
CLIC1	0	0.364526517	0.926	0.831	0
LCK	0	0.152559854	0.92	0.817	0
APOBEC3C	0	0.643877388	0.85	0.656	0
EWSR1	0	0.32813207	0.824	0.668	0
TBC1D10C	0	0.19823389	0.818	0.707	0
IDH2	0	0.908921284	0.718	0.527	0
HERPUD1	0	0.424504198	0.708	0.562	0
RHOH	0	0.259839354	0.702	0.554	0
FKBP1A	0	0.321407853	0.686	0.54	0
CXCR3	0	1.243652717	0.686	0.396	0
SURF4	0	0.516253093	0.664	0.471	0

CD27-AS1	0	0.507138858	0.654	0.446	0
SIT1	0	0.464945968	0.638	0.451	0
DEF6	0	0.506205229	0.636	0.519	0
PDIA6	0	0.630654331	0.628	0.43	0
BST2	0	0.70945336	0.614	0.473	0
ARID5A	0	0.680922542	0.61	0.415	0
PSTPIP1	0	0.387492738	0.604	0.452	0
SLC3A2	0	0.284462038	0.602	0.447	0
CHST12	0	0.415009075	0.576	0.423	0
GLIPR2	0	0.376326737	0.574	0.442	0
UBE2I	0	0.381847947	0.566	0.434	0
HM13	0	0.433879426	0.562	0.417	0
EIF3I	0	0.419605596	0.556	0.407	0
DAXX	0	0.426498426	0.546	0.386	0
NUDC	0	0.369109473	0.542	0.42	0
C19orf66	0	0.378964619	0.538	0.4	0
PSMC2	0	0.301268408	0.538	0.379	0
ATF4	0	0.445612403	0.532	0.385	0
ATP6V0E2	0	0.694618703	0.524	0.353	0
TRAT1	0	0.3947112	0.512	0.401	0
MAGED2	0	0.297925787	0.5	0.357	0
ATP6V1C2	0	0.609680633	0.496	0.344	0
RBBP7	0	0.309180105	0.488	0.377	0
VDAC1	0	0.742205098	0.476	0.29	0
PLEKHF1	0	0.372183146	0.476	0.32	0
IFI35	0	0.973090511	0.47	0.278	0
PIN1	0	0.482101438	0.454	0.33	0
NXF1	0	0.384749767	0.452	0.356	0
TWF2	0	0.369766136	0.438	0.319	0
GORASP2	0	0.390199125	0.42	0.305	0
PPP1CC	0	0.434434807	0.418	0.27	0
STIP1	0	0.336964893	0.416	0.295	0
RHOC	0	0.676232645	0.408	0.244	0
UBE2A	0	0.365928686	0.406	0.273	0
CYB5R3	0	0.372443226	0.404	0.281	0
EMC7	0	0.458653054	0.4	0.279	0
HMG1	1.18E-304	0.275055487	0.716	0.611	1.75E-300
CHMP2A	6.07E-304	0.351429543	0.5	0.372	8.97E-300
HNRNPR	2.79E-301	0.231090119	0.676	0.556	4.12E-297
SASH3	3.03E-292	0.18092478	0.772	0.655	4.48E-288
ABI3	2.00E-284	0.247591996	0.648	0.478	2.96E-280
EIF2S1	7.11E-282	0.341902051	0.41	0.291	1.05E-277
ANGPTL6	1.21E-280	0.432886445	0.482	0.329	1.79E-276
PSMC4	7.38E-278	0.312417657	0.44	0.333	1.09E-273
TMCO1	6.75E-271	0.253635205	0.582	0.436	9.98E-267
IRF9	5.95E-269	0.214124805	0.678	0.605	8.79E-265
PPT1	5.69E-266	0.243354616	0.552	0.347	8.42E-262
CASP4	5.37E-258	0.235875277	0.624	0.484	7.93E-254
CANX	1.84E-252	0.210204744	0.628	0.52	2.72E-248
GABARAPL2	3.10E-249	0.230617871	0.586	0.501	4.58E-245
MDH1	1.32E-248	0.230865928	0.57	0.455	1.95E-244
RNH1	4.53E-245	0.276624602	0.486	0.414	6.69E-241
TLR9	3.87E-235	0.3793981	0.42	0.292	5.72E-231
MIR497HG	8.07E-233	0.385859811	0.484	0.35	1.19E-228
TSPO	5.72E-231	0.28820725	0.628	0.498	8.46E-227
ATP5C1	9.30E-226	0.208113654	0.634	0.548	1.37E-221

NRBP1	1.15E-224	0.239568513	0.514	0.38	1.70E-220
SHISA5	2.54E-222	0.157774922	0.83	0.75	3.75E-218
PTBP1	1.60E-221	0.276533499	0.538	0.39	2.37E-217
MRPS18B	8.70E-216	0.272981862	0.408	0.324	1.29E-211
TAF7	1.42E-213	0.182874384	0.708	0.549	2.10E-209
SEC11C	9.36E-205	0.312287983	0.448	0.327	1.38E-200
LY6G5B	3.03E-204	0.228856543	0.626	0.522	4.48E-200
RNASET2	1.36E-201	0.291585429	0.468	0.35	2.00E-197
PYURF	4.04E-196	0.187499594	0.564	0.454	5.98E-192
ATP6AP1	9.12E-194	0.237163722	0.47	0.346	1.35E-189
HLA-DQA1	2.07E-192	0.279977695	0.456	0.374	3.05E-188
ADRM1	1.00E-189	0.267978654	0.496	0.377	1.48E-185
LAPTM4A	5.06E-189	0.256721162	0.446	0.319	7.47E-185
COX5A	1.69E-188	0.282957811	0.566	0.451	2.49E-184
AHSA1	1.57E-185	0.275695761	0.414	0.312	2.32E-181
GLUL	6.50E-180	0.147731479	0.55	0.503	9.61E-176
FSCN3	1.23E-179	0.374275721	0.542	0.406	1.82E-175
ANXA7	2.36E-179	0.182440792	0.61	0.472	3.49E-175
ABHD3	1.13E-177	0.258676368	0.44	0.315	1.68E-173
BABAM1	1.06E-165	0.228973186	0.516	0.422	1.57E-161
PPP2R1A	6.38E-163	0.204631597	0.548	0.42	9.44E-159
HNRNPC	5.53E-162	0.134423712	0.924	0.846	8.18E-158
RNF31	7.64E-159	0.157577424	0.71	0.63	1.13E-154
SEN3-EIF4A1	3.01E-158	0.121538166	0.846	0.747	4.44E-154
ANXA11	2.71E-146	0.181521315	0.642	0.5	4.01E-142
GRB2	1.60E-144	0.189942968	0.622	0.524	2.36E-140
GSTO1	9.59E-135	0.268097157	0.414	0.33	1.42E-130
CLPP	2.96E-132	0.270845091	0.406	0.321	4.38E-128
DDX39A	3.17E-129	0.17964204	0.518	0.431	4.68E-125
COPE	8.61E-129	0.158669401	0.78	0.678	1.27E-124
HOMER3	4.83E-127	0.223317374	0.722	0.624	7.14E-123
GABARAPL1	4.79E-126	0.187883242	0.438	0.354	7.09E-122
CYCS	2.25E-123	0.187409709	0.552	0.422	3.33E-119
PRDX5	1.17E-121	0.242203954	0.508	0.428	1.72E-117
TUFM	4.47E-121	0.157029119	0.558	0.474	6.61E-117
PSMD13	1.43E-119	0.16729788	0.58	0.445	2.12E-115
BUB3	3.76E-117	0.116647239	0.768	0.652	5.56E-113
NAPA	3.97E-114	0.169809185	0.61	0.483	5.86E-110
CTSC	1.85E-105	0.102254049	0.79	0.696	2.73E-101
BUD23	1.17E-101	0.221873548	0.41	0.325	1.72E-97
PDIA3	1.11E-99	0.10767974	0.854	0.736	1.64E-95
EMC4	6.43E-99	0.17213228	0.508	0.436	9.50E-95
BRK1	1.04E-92	0.145479226	0.648	0.536	1.53E-88
CASC4	4.81E-92	0.179918126	0.45	0.365	7.11E-88
PMF1-BGLAP	5.55E-89	0.227102642	0.508	0.362	8.20E-85
NAPA-AS1	2.68E-88	0.319007137	0.462	0.359	3.95E-84
MIR4632	8.00E-81	0.441677749	0.41	0.276	1.18E-76
AP3S1	1.08E-78	0.189085721	0.4	0.319	1.59E-74
CD5	3.95E-78	0.119428817	0.622	0.516	5.84E-74
PUF60	5.17E-77	0.139927417	0.534	0.407	7.65E-73
ADIPOR1	2.67E-75	0.165254266	0.424	0.331	3.95E-71
KIAA0391	2.17E-74	0.106322564	0.724	0.652	3.20E-70
C1orf43	4.58E-74	0.142065422	0.48	0.381	6.77E-70
RTFDC1	8.46E-73	0.15133036	0.488	0.395	1.25E-68
H2AFZ	1.66E-72	0.115910773	0.638	0.584	2.45E-68
LMAN2	1.20E-70	0.116652002	0.672	0.555	1.77E-66

MFSD10	8.57E-69	0.141927135	0.538	0.418	1.27E-64
SRI	2.28E-61	0.130330282	0.586	0.507	3.37E-57
DERL1	1.03E-60	0.138241136	0.472	0.347	1.52E-56
CD2BP2	1.12E-59	0.151602966	0.408	0.305	1.65E-55
OSTF1	1.35E-59	0.111265151	0.668	0.554	1.99E-55
DPM1	3.06E-59	0.169653491	0.408	0.287	4.52E-55
PQLC3	4.99E-56	0.136319642	0.418	0.337	7.38E-52
MTG1	4.20E-54	0.155183694	0.464	0.351	6.20E-50
MIR4721	1.04E-52	0.239014161	0.424	0.37	1.53E-48
MEAF6	7.15E-49	0.117350568	0.518	0.39	1.06E-44
PEBP1	2.05E-48	0.102108903	0.616	0.554	3.03E-44
UQCRC1	5.12E-48	0.118164282	0.504	0.376	7.57E-44
PRELID1	4.93E-46	0.132550926	0.546	0.437	7.28E-42
CCT6A	5.28E-39	0.101235832	0.486	0.411	7.81E-35
NDUFAF3	2.06E-38	0.160314728	0.416	0.305	3.05E-34
TMEM9B	2.08E-38	0.105429076	0.452	0.355	3.08E-34
PPP4C	3.16E-38	0.122737198	0.504	0.378	4.67E-34
ERGIC3	1.98E-37	0.108436612	0.444	0.356	2.93E-33
NDUFA10	2.10E-33	0.112485492	0.418	0.294	3.10E-29
SDF4	2.67E-30	0.11938785	0.43	0.335	3.95E-26
GAPDH	1.20E-25	0.961083836	0.996	0.959	1.77E-21
HSPA1A	6.11E-24	3.2639292	0.51	0.21	9.03E-20
RPS19BP1	1.52E-23	0.130917034	0.4	0.343	2.25E-19
MEA1	1.41E-22	0.116665967	0.434	0.339	2.08E-18
HSPA1B	1.81E-22	3.457474215	0.416	0.145	2.67E-18
ITGAE	9.64E-18	2.199586786	0.702	0.362	1.42E-13
RGS1	3.80E-15	1.911438756	0.858	0.459	5.61E-11
CD82	5.10E-13	2.030090619	0.65	0.281	7.54E-09
ITM2C	7.35E-13	2.461333457	0.552	0.161	1.09E-08
COTL1	1.26E-11	1.267470721	0.88	0.607	1.86E-07
HLA-A	3.17E-11	0.314780372	1	1	4.68E-07
CD74	3.27E-11	0.724811275	0.976	0.942	4.84E-07
DUSP4	5.41E-11	2.656409801	0.402	0.101	7.99E-07
HAVCR2	1.26E-09	2.568488304	0.422	0.118	1.87E-05
CAPG	1.55E-09	2.035092655	0.56	0.197	2.28E-05
CXCR6	1.61E-09	1.486833464	0.804	0.437	2.37E-05
JUN	2.13E-09	1.715358669	0.652	0.279	3.14E-05
ITGA1	5.84E-09	1.871755244	0.614	0.199	8.64E-05
LDHA	1.05E-08	0.977602196	0.894	0.718	0.000155
RBPJ	1.57E-08	1.49501811	0.676	0.374	0.000232
GZMA	1.71E-08	0.7544964	0.946	0.843	0.000253
STK17B	5.10E-08	0.608225499	0.988	0.904	0.000753
PDCD1	7.01E-08	1.814091254	0.492	0.222	0.001036
TBCD	1.60E-07	1.420019309	0.628	0.333	0.00237
ZFP36L1	1.74E-07	0.772178451	0.866	0.733	0.002573
HLA-J	2.54E-07	0.337438729	0.998	0.999	0.003757
CD8A	4.42E-07	0.366193309	0.998	0.998	0.006539
PDE4DIP	5.35E-07	1.531240193	0.574	0.251	0.007905
SP140	8.46E-07	0.933919804	0.766	0.578	0.012502
HLA-B	8.50E-07	0.182973873	1	1	0.012555
TNFAIP3	9.49E-07	1.03589458	0.782	0.535	0.01403
CTSD	1.56E-06	0.871838356	0.854	0.627	0.023032
SIRPG	2.27E-06	1.357267607	0.588	0.306	0.033522
CD96	4.13E-06	0.674736079	0.942	0.78	0.061031
CD2	4.54E-06	0.453192871	0.99	0.947	0.067058
KLFL-CMTM1	5.38E-06	0.836069102	0.76	0.542	0.079535



SLA	6.27E-06	0.683451097	0.926	0.791	0.092721
-----	----------	-------------	-------	-------	----------

Tumor Type	Liver Cancer				
Gene	p_val	avg_log2FC	pct.1	pct.2	p_val_adj
CLIC1	0	0.4043869	0.973	0.872	0
ARPC1B	0	0.28312867	0.96	0.863	0
KLRC4-KLRK1	0	0.1772679	0.943	0.898	0
KLRK1	0	0.14160059	0.94	0.893	0
HLA-DPB1	0	0.67368582	0.933	0.797	0
SASH3	0	0.17040322	0.92	0.873	0
CTSD	0	1.083624	0.907	0.723	0
IQGAP1	0	0.26352799	0.897	0.818	0
APOBEC3C	0	0.76923673	0.893	0.753	0
WDR1	0	0.27994045	0.893	0.842	0
EWSR1	0	0.23371604	0.887	0.828	0
BUB3	0	0.28418475	0.877	0.762	0
UBE2L6	0	0.4384349	0.867	0.747	0
RHOH	0	0.29705064	0.857	0.725	0
PARK7	0	0.30164241	0.84	0.752	0
PRKAR1A	0	0.24281201	0.84	0.75	0
CD27	0	1.02791162	0.837	0.658	0
CD84	0	0.35871146	0.833	0.708	0
MCL1	0	0.50497017	0.827	0.73	0
ACTR2	0	0.23515349	0.823	0.755	0
MAP4K1	0	0.41008755	0.82	0.713	0
CD27-AS1	0	1.02095287	0.813	0.628	0
VCP	0	0.3211456	0.813	0.715	0
STAT3	0	0.69980546	0.807	0.702	0
IDH2	0	0.69156692	0.797	0.657	0
SLFN12L	0	0.47887452	0.793	0.658	0
AP2M1	0	0.32581647	0.79	0.687	0
LASP1	0	0.77033592	0.777	0.628	0
YARS	0	0.5123993	0.777	0.582	0
INPP4B	0	0.30261734	0.77	0.652	0
CHST12	0	0.68592236	0.767	0.573	0
PTPN6	0	0.24005566	0.763	0.703	0
ABI3	0	0.40251189	0.757	0.587	0
RALY	0	0.38330319	0.747	0.662	0
IGFLR1	0	0.70400358	0.747	0.575	0
SIRPG	0	1.08946908	0.743	0.513	0
PPP2CA	0	0.30455062	0.737	0.635	0
ITGB7	0	0.25826907	0.73	0.61	0
GBP4	0	0.81352105	0.723	0.513	0
PSMA4	0	0.34032029	0.713	0.6	0
ARID5A	0	0.63127036	0.71	0.512	0
UBA1	0	0.39324201	0.707	0.535	0
SEC11A	0	0.41005101	0.7	0.51	0
GSDMD	0	0.34998998	0.697	0.558	0
PDIA6	0	0.35047842	0.69	0.628	0
PSMB2	0	0.38978703	0.69	0.543	0
HIF1A	0	0.32082517	0.687	0.547	0
OS9	0	0.28217323	0.68	0.582	0

FASLG	0	1.01648057	0.677	0.448	0
BST2	0	0.65455383	0.677	0.518	0
ANXA5	0	0.51239525	0.673	0.532	0
SAMD9L	0	0.31939202	0.67	0.538	0
DNAJA1	0	0.32334933	0.667	0.578	0
SYNGR2	0	0.45303959	0.667	0.51	0
CXCR3	0	0.85690763	0.663	0.427	0
P2RY10	0	0.776599	0.643	0.46	0
PLEKHF1	0	0.47735512	0.643	0.482	0
PMF1	0	0.68970196	0.64	0.448	0
GPR174	0	0.7838842	0.637	0.44	0
NCKAP1L	0	0.44216086	0.633	0.457	0
OAS2	0	0.48135664	0.633	0.478	0
CTSA	0	0.54698783	0.63	0.455	0
PPM1G	0	0.55430689	0.623	0.423	0
ELMO1	0	0.36214549	0.623	0.48	0
HK1	0	0.38574366	0.617	0.437	0
DCAF11	0	0.50352011	0.617	0.415	0
CISH	0	0.38605088	0.613	0.505	0
NASP	0	0.51358735	0.61	0.475	0
PPM1M	0	0.39589058	0.607	0.42	0
CDC123	0	0.61953845	0.603	0.432	0
RIF1	0	0.48278897	0.597	0.443	0
HOPX	0	0.54861948	0.593	0.503	0
BATF	0	0.5179137	0.59	0.395	0
COQ10B	0	0.42157083	0.587	0.352	0
PMF1-BGLAP	0	0.62888963	0.583	0.405	0
MAP2K3	0	0.60109058	0.583	0.415	0
GALM	0	0.64155952	0.577	0.42	0
SLC4A5	0	0.68276006	0.573	0.388	0
ABHD3	0	0.4891797	0.563	0.4	0
VDAC1	0	0.43364165	0.553	0.368	0
DYX1C1-CCPG1	0	0.44074611	0.54	0.408	0
TRAFD1	0	0.54503559	0.533	0.393	0
PFKP	0	0.58080531	0.53	0.403	0
AP2S1	0	0.61723421	0.527	0.342	0
IFI35	0	0.52362527	0.513	0.372	0
CYC1	0	0.54824767	0.503	0.352	0
TOR1A	0	0.56755204	0.493	0.313	0
EIF2AK1	0	0.45444616	0.473	0.39	0
CMTM3	0	0.47348962	0.463	0.358	0
DNAJB11	0	0.4670248	0.453	0.31	0
MAD2L2	0	0.88834023	0.45	0.232	0
PLSCR1	0	0.72933381	0.45	0.255	0
BAK1	0	0.76411756	0.437	0.263	0
ASNA1	0	0.57602674	0.433	0.295	0
SAE1	0	0.47594973	0.43	0.318	0
ZNF394	0	0.68397251	0.43	0.31	0
IRF7	0	0.77992087	0.423	0.257	0
MCM5	0	0.90732312	0.413	0.258	0
TMED7	0	0.73060978	0.413	0.275	0
CD101	0	0.50805471	0.41	0.293	0
JMJD6	0	0.60201169	0.403	0.247	0
KIAA1033	0	0.46294299	0.403	0.34	0
GTF3C6	1.79E-307	0.54729298	0.56	0.387	2.46E-303
CCPG1	1.08E-306	0.39118242	0.55	0.425	1.48E-302

PRPF31	3.79E-303	0.43418059	0.497	0.347	5.21E-299
NUP62	1.26E-300	0.45092656	0.463	0.333	1.74E-296
PSMG2	1.40E-300	0.42415574	0.513	0.4	1.93E-296
PLA2G16	2.52E-292	0.59824572	0.47	0.257	3.46E-288
OGDH	4.43E-285	0.36945604	0.537	0.435	6.09E-281
PSMD3	5.57E-270	0.51392736	0.44	0.297	7.65E-266
EMC3	2.07E-268	0.45290345	0.513	0.358	2.84E-264
CD244	5.41E-265	0.29921327	0.57	0.502	7.43E-261
HSPD1	3.86E-264	0.32201599	0.637	0.552	5.30E-260
HM13	6.32E-262	0.30563879	0.657	0.553	8.68E-258
HCP5	1.28E-258	0.23726613	0.657	0.545	1.76E-254
AIP	5.23E-252	0.30124906	0.737	0.607	7.19E-248
RAB11B	2.37E-250	0.41132604	0.623	0.502	3.25E-246
WSB1	4.39E-248	0.2266544	0.753	0.647	6.03E-244
GGA1	1.40E-247	0.34729135	0.567	0.427	1.93E-243
RASSF5	3.67E-247	0.1785541	0.873	0.805	5.04E-243
TMX4	9.70E-247	0.31746349	0.61	0.47	1.33E-242
IRF9	1.05E-237	0.21526658	0.827	0.747	1.44E-233
ECHS1	1.04E-236	0.46611725	0.4	0.272	1.42E-232
SURF4	1.52E-231	0.20467637	0.807	0.712	2.09E-227
CTBS	1.18E-226	0.43053727	0.4	0.27	1.62E-222
ACO2	1.11E-225	0.33465002	0.517	0.397	1.52E-221
C17orf62	2.04E-225	0.23461182	0.827	0.693	2.80E-221
SDHA	1.06E-220	0.23032168	0.743	0.643	1.45E-216
USP4	7.72E-219	0.29399546	0.557	0.47	1.06E-214
POLG	5.05E-215	0.38015427	0.44	0.348	6.94E-211
RNF10	4.85E-213	0.29392671	0.613	0.517	6.66E-209
VPS4A	2.68E-211	0.37240691	0.467	0.413	3.68E-207
RAB11FIP1	5.56E-208	0.35508302	0.467	0.335	7.63E-204
SQRDL	1.06E-206	0.30324457	0.607	0.437	1.46E-202
TRAPPC3	1.10E-206	0.40969903	0.43	0.313	1.51E-202
ARHGEF39	4.65E-206	0.34014321	0.63	0.502	6.38E-202
SMC5	2.23E-204	0.3178789	0.58	0.462	3.06E-200
FERMT3	1.34E-201	0.19828604	0.83	0.75	1.84E-197
BECN1	5.96E-199	0.26782993	0.617	0.502	8.19E-195
PDGFRA	3.62E-198	0.4105999	0.483	0.355	4.97E-194
CNTRL	3.76E-197	0.25252135	0.703	0.58	5.16E-193
SRSF2	3.34E-196	0.16339163	0.857	0.848	4.58E-192
ZBTB38	9.42E-194	0.21215848	0.737	0.602	1.29E-189
ARPC5	1.16E-192	0.16632224	0.883	0.782	1.59E-188
PRDX6	3.36E-192	0.27165278	0.64	0.523	4.61E-188
RHOC	5.47E-188	0.31289901	0.58	0.415	7.51E-184
NAPA	1.72E-187	0.27139551	0.703	0.573	2.36E-183
MDH2	4.99E-187	0.26436224	0.67	0.555	6.85E-183
FPGS	1.45E-184	0.3599848	0.48	0.373	1.99E-180
GPI	3.80E-183	0.19129139	0.803	0.673	5.22E-179
ACLY	1.14E-181	0.30052359	0.513	0.395	1.56E-177
RNF31	1.02E-180	0.17863489	0.853	0.777	1.41E-176
SLC3A2	6.72E-178	0.23397016	0.677	0.558	9.23E-174
ARPC5L	1.05E-177	0.29061003	0.713	0.55	1.44E-173
CLTA	6.33E-177	0.34047402	0.563	0.402	8.69E-173
BCL2L1	6.09E-174	0.35711453	0.46	0.355	8.37E-170
CYLD	6.42E-174	0.20124355	0.763	0.637	8.82E-170
STXBP2	6.63E-174	0.31399767	0.57	0.472	9.11E-170
CCT6A	3.43E-173	0.24802707	0.663	0.55	4.71E-169
PYCARD	1.77E-172	0.52295	0.437	0.288	2.43E-168

TSTA3	6.26E-170	0.35051522	0.45	0.36	8.59E-166
ST6GALNAC6	4.23E-169	0.28988728	0.567	0.435	5.82E-165
USP20	5.40E-169	0.31208994	0.45	0.397	7.42E-165
ATP6V1C2	4.49E-168	0.31199924	0.6	0.525	6.17E-164
GRB2	5.31E-168	0.21509479	0.753	0.683	7.29E-164
LAMP2	4.94E-163	0.25308545	0.557	0.457	6.78E-159
SDF4	8.18E-161	0.30978727	0.57	0.457	1.12E-156
TMEM59	7.66E-160	0.15954204	0.9	0.818	1.05E-155
SEPHS2	9.51E-160	0.29300708	0.493	0.362	1.31E-155
FAM50A	5.49E-159	0.36801005	0.477	0.38	7.54E-155
TOB2	4.02E-157	0.35862312	0.49	0.393	5.51E-153
PI4KB	4.11E-157	0.28090939	0.52	0.397	5.64E-153
ATP5C1	2.04E-156	0.22444426	0.71	0.6	2.81E-152
CSR1	4.13E-155	0.32252006	0.46	0.338	5.67E-151
MFSD10	2.84E-152	0.24760263	0.63	0.51	3.89E-148
NDUFA9	1.92E-147	0.2828109	0.543	0.403	2.64E-143
COMMD7	6.31E-145	0.2549793	0.61	0.425	8.66E-141
PSPC1	1.45E-141	0.34240419	0.487	0.34	2.00E-137
SLAMF1	1.82E-141	0.17124199	0.697	0.61	2.50E-137
SLC38A10	1.43E-140	0.32658031	0.443	0.375	1.97E-136
FYT1D1	3.30E-140	0.23769243	0.61	0.44	4.53E-136
NELFCD	1.34E-136	0.22177292	0.65	0.485	1.84E-132
UTY	2.09E-136	0.26384397	0.52	0.442	2.87E-132
AK3	2.09E-135	0.29363236	0.437	0.325	2.86E-131
DDB1	6.49E-135	0.20537139	0.617	0.548	8.91E-131
DCTN1	4.32E-132	0.24340007	0.473	0.397	5.93E-128
ANXA11	4.36E-132	0.18422965	0.75	0.665	5.99E-128
U2AF1	1.08E-131	0.23505111	0.743	0.647	1.48E-127
PTK2B	1.37E-130	0.17607813	0.797	0.658	1.88E-126
PPT1	2.86E-130	0.20355226	0.58	0.447	3.93E-126
SF3B3	1.17E-128	0.19898507	0.623	0.51	1.61E-124
TIMMDC1	3.26E-128	0.28937359	0.517	0.347	4.48E-124
DCXR	1.69E-127	0.36892827	0.437	0.348	2.33E-123
PRELID1	2.70E-127	0.26126818	0.683	0.555	3.71E-123
RBM22	4.44E-124	0.25798282	0.487	0.382	6.10E-120
HSH2D	7.96E-124	0.28325657	0.5	0.393	1.09E-119
EIF2AK2	2.45E-123	0.24155445	0.557	0.417	3.36E-119
NAA50	1.54E-121	0.19942291	0.64	0.485	2.12E-117
KDEL2	3.08E-121	0.25401222	0.5	0.392	4.23E-117
GIGYF2	1.07E-120	0.25294918	0.553	0.42	1.47E-116
VAMP5	3.80E-119	0.38830169	0.49	0.368	5.22E-115
PSMA5	5.61E-118	0.18005096	0.79	0.68	7.71E-114
SLBP	1.58E-117	0.24781939	0.49	0.368	2.17E-113
CCDC107	2.97E-117	0.25233665	0.62	0.507	4.08E-113
DNTTIP2	6.27E-117	0.21127776	0.567	0.458	8.61E-113
MXD3	2.30E-116	0.30136548	0.677	0.56	3.16E-112
PPP5C	2.32E-116	0.34597554	0.413	0.275	3.18E-112
PSMB6	4.36E-116	0.28752387	0.55	0.443	5.99E-112
PTBP1	5.78E-116	0.19887407	0.703	0.62	7.94E-112
ZMYM5	1.74E-115	0.26851295	0.473	0.338	2.39E-111
CAT	1.86E-115	0.25624524	0.457	0.327	2.55E-111
PPP1CA	9.67E-113	0.12881183	0.923	0.858	1.33E-108
PLEKHB2	1.30E-112	0.20012765	0.567	0.455	1.78E-108
USP39	2.72E-111	0.26218113	0.42	0.338	3.73E-107
ERP44	1.58E-109	0.20764536	0.623	0.515	2.16E-105
LAMTOR1	3.43E-109	0.25712258	0.58	0.457	4.71E-105

CD247	3.66E-109	0.12624124	0.883	0.775	5.03E-105
AP3M1	4.55E-109	0.24085223	0.423	0.32	6.25E-105
EIF4A3	2.38E-108	0.2438621	0.483	0.363	3.27E-104
RAB4B	3.64E-107	0.28285659	0.5	0.357	5.00E-103
TWF2	1.37E-106	0.22494572	0.58	0.478	1.88E-102
DCAF7	5.12E-106	0.19611443	0.613	0.46	7.03E-102
TAX1BP1	2.84E-104	0.15386717	0.797	0.737	3.90E-100
PSTPIP1	1.58E-103	0.15671509	0.743	0.653	2.16E-99
DNAJC1	6.13E-103	0.25693563	0.617	0.465	8.42E-99
LAP3	7.97E-103	0.28647836	0.463	0.295	1.09E-98
COMT	1.85E-100	0.27646019	0.463	0.352	2.54E-96
TBCC	4.43E-100	0.1994031	0.62	0.508	6.09E-96
MAF1	9.03E-100	0.18372021	0.7	0.585	1.24E-95
SPG21	2.60E-98	0.27134866	0.443	0.275	3.56E-94
SAR1B	3.84E-98	0.26365747	0.427	0.338	5.28E-94
VPS33A	6.97E-98	0.20622531	0.617	0.53	9.57E-94
RPS6KA1	2.13E-97	0.18814647	0.6	0.432	2.93E-93
WDR54	1.41E-96	0.30148528	0.407	0.252	1.94E-92
PSMF1	1.16E-95	0.19424355	0.633	0.533	1.59E-91
DNAJC3	5.49E-95	0.19742931	0.573	0.462	7.53E-91
POLR2G	1.04E-94	0.19342614	0.753	0.6	1.43E-90
TCIRG1	1.57E-94	0.14574512	0.78	0.663	2.16E-90
MGAT1	2.17E-94	0.17020479	0.677	0.598	2.98E-90
ELMSAN1	1.11E-93	0.20720578	0.577	0.463	1.52E-89
TBC1D10A	1.66E-93	0.24524342	0.443	0.383	2.29E-89
MIA-RAB4B	2.77E-93	0.26784412	0.49	0.353	3.81E-89
CSNK1A1	4.81E-93	0.15898992	0.737	0.665	6.61E-89
RTCA	4.49E-92	0.26008551	0.447	0.337	6.17E-88
COPE	7.80E-91	0.15876325	0.857	0.76	1.07E-86
U2AF1L4	5.81E-90	0.30386764	0.4	0.332	7.97E-86
NUMA1	8.44E-90	0.18641841	0.583	0.467	1.16E-85
HADHA	7.01E-89	0.16429904	0.66	0.512	9.63E-85
TMEM50A	1.52E-88	0.1400449	0.833	0.723	2.09E-84
CCSER2	2.27E-87	0.1674236	0.67	0.588	3.11E-83
CRKL	1.71E-86	0.21836018	0.437	0.348	2.34E-82
PSD4	2.13E-86	0.21921465	0.467	0.378	2.92E-82
PPP6R1	1.22E-85	0.21370625	0.52	0.417	1.67E-81
HELZ	1.57E-85	0.14816964	0.71	0.627	2.15E-81
RAB5C	1.19E-84	0.1982229	0.653	0.553	1.64E-80
TRABD	3.07E-84	0.18736379	0.637	0.55	4.21E-80
OVCA2	6.44E-84	0.26157553	0.48	0.397	8.84E-80
LAX1	9.90E-82	0.21940351	0.403	0.347	1.36E-77
CAPN1	1.07E-80	0.2049914	0.513	0.41	1.47E-76
GTF3C1	1.23E-80	0.21716049	0.483	0.367	1.69E-76
SRSF4	1.42E-80	0.17614425	0.657	0.542	1.95E-76
PSMB10	1.93E-80	0.12804178	0.893	0.847	2.66E-76
SP110	6.71E-80	0.14875889	0.82	0.698	9.21E-76
TMEM33	3.57E-79	0.20081967	0.503	0.368	4.90E-75
COG4	5.01E-79	0.22541965	0.417	0.283	6.88E-75
DDX3Y	2.21E-78	0.15904511	0.527	0.45	3.04E-74
ADA	1.72E-77	0.20032055	0.473	0.34	2.36E-73
NDUFA10	6.05E-76	0.18666146	0.49	0.4	8.31E-72
NUDT21	5.07E-75	0.19825845	0.54	0.385	6.97E-71
LSM10	1.92E-74	0.27795336	0.42	0.327	2.63E-70
CHKB-CPT1B	3.54E-74	0.2088622	0.54	0.353	4.86E-70
UBA2	3.57E-73	0.24554816	0.477	0.377	4.90E-69

PQLC3	1.27E-72	0.20037836	0.483	0.39	1.74E-68
MIR3661	5.24E-72	0.34457072	0.623	0.5	7.20E-68
RTN3	2.46E-71	0.21680164	0.417	0.318	3.37E-67
ATP6VOD1	2.77E-71	0.18377685	0.517	0.438	3.81E-67
TMEM134	2.95E-71	0.29431693	0.443	0.335	4.06E-67
NUDT5	8.47E-71	0.23060496	0.54	0.395	1.16E-66
SIT1	1.19E-70	0.13526083	0.76	0.678	1.63E-66
UBE2A	2.59E-70	0.19991496	0.497	0.373	3.56E-66
CHKB	3.87E-70	0.21546922	0.493	0.33	5.32E-66
RTCB	8.28E-69	0.19253738	0.45	0.352	1.14E-64
PSMD8	6.42E-68	0.16515695	0.717	0.575	8.81E-64
DR1	1.92E-67	0.17906452	0.57	0.452	2.64E-63
PIN1	6.19E-67	0.2159778	0.58	0.458	8.51E-63
STAT5A	1.12E-66	0.19514492	0.5	0.352	1.54E-62
RGL4	4.71E-66	0.25494582	0.517	0.405	6.47E-62
SYNCRIP	5.17E-66	0.1845362	0.533	0.418	7.10E-62
RCN2	6.17E-66	0.20701077	0.427	0.33	8.48E-62
ATRX	7.88E-66	0.10187259	0.863	0.813	1.08E-61
RHBDD2	1.16E-65	0.18866995	0.553	0.387	1.59E-61
PSMD9	3.28E-65	0.22727741	0.467	0.355	4.51E-61
CNTD1	1.04E-64	0.25753026	0.54	0.407	1.42E-60
GATSL3	2.98E-64	0.21603804	0.467	0.397	4.10E-60
COPB1	5.50E-63	0.13466882	0.677	0.578	7.56E-59
PARL	7.22E-63	0.23213807	0.407	0.278	9.92E-59
CD5	8.28E-63	0.11038853	0.797	0.712	1.14E-58
CDKL3	7.04E-61	0.22514132	0.653	0.543	9.67E-57
COMMD8	4.96E-60	0.18580073	0.493	0.372	6.81E-56
DDX39A	6.14E-59	0.13527939	0.667	0.593	8.43E-55
DDB2	1.75E-58	0.19277302	0.427	0.337	2.41E-54
CLK3	4.28E-58	0.16836188	0.5	0.405	5.87E-54
DOK2	7.48E-58	0.14113043	0.683	0.523	1.03E-53
C7orf25	1.87E-56	0.15129146	0.74	0.618	2.57E-52
VPS26A	4.07E-55	0.16754318	0.487	0.365	5.59E-51
DEF6	1.11E-54	0.1163744	0.767	0.708	1.52E-50
ACTL6A	2.00E-54	0.19407391	0.42	0.298	2.75E-50
HOMER3	2.66E-54	0.17403809	0.823	0.737	3.65E-50
STT3B	4.82E-54	0.17882893	0.467	0.383	6.61E-50
TBCB	4.99E-54	0.15275315	0.727	0.562	6.86E-50
SCAPER	9.05E-54	0.17517058	0.46	0.352	1.24E-49
ARHGEF6	1.12E-53	0.12504014	0.693	0.558	1.54E-49
GDI2	1.52E-53	0.11060005	0.74	0.69	2.09E-49
CCNH	2.04E-53	0.12660932	0.703	0.578	2.81E-49
CHMP5	8.02E-53	0.20210306	0.447	0.34	1.10E-48
DHX15	8.83E-53	0.1330924	0.557	0.478	1.21E-48
UBE2N	2.13E-52	0.12443841	0.727	0.597	2.92E-48
PSMC2	3.98E-52	0.14682937	0.563	0.44	5.46E-48
MIA2	8.94E-52	0.17522837	0.563	0.443	1.23E-47
KDM5D	3.12E-51	0.14560532	0.51	0.398	4.28E-47
CHFR	1.22E-50	0.1913879	0.473	0.345	1.68E-46
SYS1	3.56E-50	0.18478103	0.44	0.302	4.89E-46
STARD3NL	3.77E-50	0.19495327	0.42	0.32	5.17E-46
GART	6.17E-50	0.19232292	0.407	0.338	8.47E-46
ACSL5	1.08E-47	0.12080328	0.627	0.518	1.48E-43
PTPA	1.38E-47	0.20279034	0.463	0.35	1.90E-43
SNRPA	2.41E-47	0.24325041	0.443	0.348	3.31E-43
PSMA2	2.86E-47	0.13010342	0.763	0.652	3.93E-43

MTCH1	1.18E-46	0.16031413	0.497	0.405	1.61E-42
NFX1	1.30E-46	0.15149997	0.463	0.405	1.78E-42
FLII	1.66E-46	0.12586416	0.603	0.52	2.29E-42
SERPINB1	2.76E-46	0.12552454	0.613	0.543	3.78E-42
WHSC1L1	3.14E-46	0.14958551	0.623	0.51	4.31E-42
DPH1	1.53E-45	0.15802234	0.557	0.475	2.10E-41
PPM1B	2.53E-45	0.15523434	0.513	0.387	3.48E-41
LOC374443	3.19E-45	0.12712157	0.657	0.552	4.38E-41
SLC25A39	7.27E-45	0.16950756	0.45	0.353	9.98E-41
RHOG	2.80E-44	0.1156884	0.69	0.608	3.85E-40
TLR9	3.58E-44	0.18975489	0.567	0.442	4.91E-40
TSPYL2	5.00E-44	0.16302156	0.44	0.307	6.87E-40
CLIP1	1.43E-42	0.15337809	0.487	0.377	1.96E-38
TXN2	1.45E-42	0.16728037	0.497	0.388	1.98E-38
PITPNB	1.54E-42	0.22906356	0.48	0.333	2.12E-38
DHPS	1.98E-42	0.15964158	0.517	0.407	2.72E-38
CYB5B	6.21E-42	0.13727924	0.573	0.475	8.53E-38
CHIC2	2.14E-41	0.1996052	0.513	0.372	2.94E-37
RBM42	2.43E-41	0.18425974	0.513	0.37	3.34E-37
FBXL5	2.77E-41	0.11025001	0.637	0.547	3.81E-37
TERF1	3.10E-41	0.21405181	0.43	0.322	4.26E-37
PARP10	2.56E-40	0.12903796	0.587	0.478	3.51E-36
TRPC4AP	1.15E-39	0.12550477	0.623	0.523	1.57E-35
HEXB	1.60E-39	0.15997405	0.52	0.38	2.19E-35
ELAVL1	8.55E-39	0.19068619	0.453	0.307	1.17E-34
BRK1	9.29E-39	0.11732018	0.767	0.645	1.28E-34
KRAS	5.96E-38	0.15607844	0.517	0.355	8.18E-34
SH2D3C	8.22E-37	0.12456087	0.607	0.492	1.13E-32
RAD51L3-RFFL	9.74E-37	0.14880094	0.507	0.375	1.34E-32
OTUB1	3.46E-36	0.12904111	0.663	0.588	4.76E-32
ATF2	4.31E-35	0.138934	0.493	0.368	5.92E-31
PSMA6	4.98E-35	0.12019526	0.67	0.555	6.85E-31
CSNK2B	1.26E-34	0.1072726	0.727	0.613	1.73E-30
C19orf66	1.44E-34	0.11197892	0.637	0.585	1.97E-30
ITGB2-AS1	3.69E-34	0.11519857	0.583	0.503	5.07E-30
CMTM7	4.33E-34	0.15348292	0.5	0.385	5.95E-30
IWS1	1.89E-33	0.13511382	0.5	0.428	2.60E-29
GPR18	3.49E-33	0.12232241	0.483	0.385	4.79E-29
DDX23	4.93E-33	0.11149426	0.5	0.462	6.77E-29
PRDX5	9.30E-33	0.15316696	0.653	0.528	1.28E-28
CDK12	1.84E-32	0.1628435	0.493	0.397	2.53E-28
MRPL9	3.89E-32	0.13467488	0.48	0.388	5.34E-28
GOLPH3	5.36E-31	0.1313321	0.487	0.373	7.35E-27
ATP6AP1	5.12E-30	0.10155216	0.59	0.477	7.03E-26
NUTF2	8.58E-30	0.18214809	0.46	0.367	1.18E-25
NARF	1.98E-29	0.12280517	0.503	0.43	2.71E-25
AP5M1	4.15E-29	0.1223413	0.457	0.367	5.70E-25
EMC7	7.78E-29	0.13797004	0.5	0.35	1.07E-24
AP3S1	8.51E-29	0.14834482	0.483	0.357	1.17E-24
RFFL	1.14E-28	0.12696087	0.45	0.347	1.56E-24
BLOC1S2	2.14E-28	0.13399903	0.51	0.388	2.94E-24
PPP1R7	6.70E-28	0.13714363	0.523	0.415	9.20E-24
NAA60	8.99E-28	0.14108609	0.48	0.297	1.23E-23
HAT1	1.43E-27	0.13530578	0.457	0.348	1.96E-23
EIF1B	1.49E-27	0.15341036	0.47	0.363	2.04E-23
TMED5	1.72E-27	0.10191575	0.557	0.505	2.36E-23

CD2BP2	2.14E-27	0.11589714	0.53	0.392	2.95E-23
HEXA	2.27E-27	0.10489076	0.56	0.475	3.12E-23
TALDO1	2.48E-27	0.13158162	0.54	0.387	3.40E-23
PECAM1	1.96E-26	0.16147032	0.423	0.322	2.69E-22
EMC4	2.85E-26	0.10948472	0.637	0.513	3.92E-22
MCRIP1	4.13E-26	0.13682148	0.527	0.437	5.67E-22
NCAPH2	1.23E-25	0.14174561	0.413	0.327	1.69E-21
COG1	1.64E-25	0.10246816	0.577	0.495	2.26E-21
UQCRC1	1.74E-24	0.10034643	0.593	0.458	2.40E-20
YIPF5	2.39E-24	0.11406815	0.417	0.378	3.28E-20
GUSB	2.66E-24	0.11745989	0.423	0.353	3.65E-20
SZRD1	5.61E-24	0.11416554	0.507	0.432	7.70E-20
MIR2110	2.22E-23	0.2831283	0.427	0.303	3.05E-19
BABAM1	2.94E-23	0.11180259	0.55	0.44	4.04E-19
GAPDH	3.67E-23	0.8713297	1	0.985	5.04E-19
POLDIP3	7.51E-23	0.10630562	0.473	0.342	1.03E-18
ACAA1	2.25E-22	0.10946578	0.447	0.357	3.10E-18
SIPA1	6.56E-22	0.12322605	0.423	0.367	9.01E-18
MOB4	1.26E-21	0.10448674	0.483	0.352	1.73E-17
CHMP1A	3.33E-21	0.10782454	0.447	0.368	4.57E-17
HAVCR2	2.00E-20	4.06200842	0.577	0.157	2.74E-16
NMRAL1	9.76E-20	0.13571974	0.417	0.33	1.34E-15
TACC3	4.01E-19	0.11007616	0.41	0.317	5.51E-15
SDHC	2.80E-18	0.16352467	0.43	0.297	3.84E-14
LSM1	3.37E-18	0.15341899	0.423	0.295	4.63E-14
SNRPC	7.68E-18	0.13684769	0.473	0.378	1.06E-13
WBSCR22	3.61E-17	0.10536819	0.533	0.407	4.96E-13
MRPL28	6.27E-17	0.13616876	0.41	0.28	8.61E-13
FBXW2	3.73E-16	0.1032147	0.453	0.347	5.12E-12
CCS	3.86E-16	0.11418482	0.41	0.303	5.30E-12
CCL4L1	6.62E-16	1.79297053	0.82	0.653	9.09E-12
NR4A2	1.05E-15	2.92025084	0.673	0.273	1.44E-11
TPT1	5.76E-15	0.98963711	0.993	0.983	7.92E-11
DUSP4	1.51E-14	3.63661232	0.447	0.123	2.08E-10
PDCD1	2.60E-14	2.76936246	0.667	0.298	3.57E-10
DCTN3	4.97E-14	0.10962321	0.483	0.367	6.83E-10
LOC642361	3.06E-13	0.20730549	0.41	0.303	4.20E-09
HSP90AA1	1.34E-12	0.95437774	0.953	0.947	1.84E-08
RGS1	2.69E-12	2.14880723	0.857	0.498	3.70E-08
ITGAE	1.69E-11	2.19152779	0.61	0.393	2.32E-07
TNFRSF9	2.44E-11	3.4332531	0.44	0.118	3.35E-07
CD74	2.25E-10	0.8527746	0.98	0.947	3.09E-06
APOBEC3F	3.74E-10	1.44104357	0.823	0.59	5.14E-06
COTL1	6.60E-10	1.30126662	0.913	0.708	9.06E-06
ZFP36L1	1.04E-09	0.86333718	0.953	0.908	1.42E-05
PHLDA1	4.27E-09	2.75834458	0.46	0.157	5.86E-05
ENTPD1	4.72E-09	2.85181152	0.4	0.173	6.48E-05
HLA-DQB1	6.67E-09	1.59420334	0.723	0.467	9.16E-05
IFI6	7.82E-09	1.4535713	0.727	0.478	0.000107
CD8A	8.02E-09	0.48320137	1	1	0.00011
IL2RB	1.18E-08	1.11663394	0.9	0.748	0.000163
HLA-DPB2	1.53E-08	0.62650895	0.463	0.265	0.00021
CCL4	4.78E-08	1.15546083	0.89	0.765	0.000656
TOX	6.65E-08	1.68939149	0.687	0.388	0.000913
WARS	7.55E-08	1.89042599	0.583	0.353	0.001037
LYST	8.15E-08	1.30070076	0.857	0.615	0.00112



TNFAIP3	8.85E-08	1.3482656	0.807	0.618	0.001215
HLA-DRA	9.20E-08	1.74367062	0.723	0.433	0.001264
FABP5	1.17E-07	1.53578332	0.407	0.145	0.00161
LSP1	1.21E-07	0.606982	0.98	0.942	0.001664
CCL3	1.23E-07	2.17554077	0.557	0.278	0.001684
APOBEC3G	1.30E-07	1.0094219	0.923	0.788	0.001792
ITM2A	1.87E-07	1.09159553	0.873	0.72	0.002573
ID2	2.47E-07	0.85713649	0.96	0.843	0.003397
TIGIT	2.73E-07	1.3737434	0.85	0.552	0.003746
HLA-DRB6	2.77E-07	1.13079092	0.857	0.637	0.003809
RPL19P12	3.21E-07	0.88858311	0.527	0.528	0.004404
MIR155HG	7.08E-07	2.29134852	0.42	0.145	0.00973
APOBEC3D	7.23E-07	1.22830358	0.733	0.505	0.009926
ICOS	9.72E-07	1.73924152	0.64	0.318	0.013352
HLA-DRB1	1.06E-06	1.08747931	0.873	0.71	0.014584
SRGN	1.52E-06	0.61636657	0.977	0.913	0.020854
RPL28	1.54E-06	0.71124527	0.967	0.967	0.021118
IFNG	1.70E-06	2.0672754	0.547	0.21	0.023362
OASL	2.70E-06	1.79577815	0.587	0.272	0.037035
SMG1P3	3.09E-06	0.93592484	0.763	0.585	0.042504
IFITM3	3.91E-06	0.71185169	0.823	0.812	0.053638
STK17B	5.46E-06	0.437938	0.997	0.978	0.075025

Tumor Type	Colorectal Cancer					
Gene	p_val	avg_log2FC	pct.1	pct.2	p_val_adj	
RAN	0	0.309943707		0.916	0.831	0
CTSD	0	0.546407672		0.889	0.799	0
IDH2	0	0.647575567		0.88	0.787	0
FKBP1A	0	0.653110723		0.864	0.719	0
UBE2L6	0	0.485805933		0.833	0.731	0
PSMA2	0	0.339372819		0.789	0.704	0
C7orf25	0	0.361202463		0.764	0.666	0
DRAP1	0	0.489310854		0.731	0.631	0
CASP4	0	0.39832039		0.722	0.616	0
BST2	0	0.530849657		0.66	0.536	0
OCIAD2	0	0.522910262		0.622	0.476	0
PMF1-BGLAP	0	0.560309382		0.567	0.434	0
EMC7	0	0.386388127		0.56	0.463	0
PIN1	0	0.41251513		0.551	0.417	0
RTRAF	0	0.453027085		0.533	0.483	0
SERTAD1	0	0.680997557		0.524	0.398	0
IFI35	0	0.457716599		0.498	0.394	0
PDCL3	0	0.555468344		0.46	0.343	0
ASNA1	0	0.614504421		0.447	0.312	0
IRF7	0	0.707481199		0.444	0.328	0
MAD2L2	0	0.5523493		0.409	0.299	0
BUD31	2.65E-273	0.333223469		0.642	0.586	4.14E-269
UBE2F-SCLY	1.30E-269	0.450510381		0.416	0.298	2.03E-265
RABAC1	6.50E-268	0.325099886		0.724	0.606	1.01E-263
NUDC	1.50E-260	0.297221885		0.664	0.596	2.34E-256
SLC25A5-AS1	2.85E-260	0.510309014		0.547	0.427	4.45E-256
ZNHIT3	5.67E-259	0.402449151		0.458	0.377	8.85E-255

SAE1	3.21E-246	0.346778948	0.407	0.362	5.00E-242
LSM2	5.54E-227	0.424138768	0.427	0.302	8.64E-223
GABARAPL2	7.41E-225	0.231813346	0.72	0.643	1.16E-220
PSMA4	2.47E-207	0.229464052	0.669	0.621	3.85E-203
MIR3661	1.52E-194	0.459075868	0.607	0.457	2.37E-190
COPE	1.38E-188	0.197222741	0.833	0.81	2.15E-184
TMEM109	2.57E-188	0.220482541	0.598	0.571	4.01E-184
CHST12	1.99E-186	0.247884701	0.638	0.502	3.11E-182
PSMA6	7.66E-185	0.199667088	0.72	0.706	1.20E-180
CXCL13	8.05E-159	7.542730798	0.633	0.139	1.26E-154
GSTO1	6.01E-149	0.289295355	0.529	0.442	9.38E-145
MRPS16	1.61E-143	0.286968384	0.567	0.482	2.52E-139
EMC4	1.61E-131	0.197948848	0.664	0.581	2.52E-127
HOMER3	1.76E-129	0.22739524	0.764	0.742	2.75E-125
PSMB6	6.82E-127	0.218303458	0.656	0.541	1.06E-122
PSMB3	9.64E-111	0.184570477	0.747	0.679	1.50E-106
SELENOT	3.23E-106	0.133577902	0.809	0.739	5.05E-102
PSMD8	5.88E-106	0.171231288	0.704	0.638	9.18E-102
SDHD	1.64E-101	0.18409658	0.664	0.587	2.56E-97
PRDX5	9.98E-97	0.201551644	0.691	0.609	1.56E-92
FDPS	3.67E-87	0.19593735	0.489	0.458	5.73E-83
ANXA2	7.87E-87	0.129595133	0.76	0.737	1.23E-82
VKORC1	4.07E-86	0.235602952	0.424	0.373	6.35E-82
STXBP2	3.93E-85	0.200413646	0.518	0.492	6.14E-81
GDI1	6.47E-81	0.212615824	0.562	0.526	1.01E-76
MEAF6	8.59E-78	0.150359584	0.598	0.561	1.34E-73
SNRNP40	2.11E-75	0.181990803	0.473	0.428	3.30E-71
RBM42	1.02E-71	0.225341302	0.46	0.309	1.59E-67
NDUFB5	2.41E-68	0.197379548	0.404	0.368	3.76E-64
GPX4	5.54E-68	0.172712819	0.633	0.617	8.65E-64
UBE2N	1.08E-67	0.111318313	0.738	0.738	1.68E-63
NR1H2	6.79E-65	0.156921071	0.522	0.452	1.06E-60
FBXO7	1.16E-64	0.1254277	0.656	0.573	1.82E-60
GTF3C6	1.99E-63	0.206851712	0.493	0.4	3.11E-59
CSNK2B	1.97E-61	0.129997292	0.711	0.67	3.07E-57
PLTP	1.06E-60	0.280159525	0.507	0.374	1.65E-56
PSMD11	1.07E-60	0.139875884	0.6	0.54	1.67E-56
HSPA1A	7.71E-56	3.621174331	0.767	0.542	1.20E-51
LY6G5B	1.51E-52	0.121033586	0.709	0.657	2.36E-48
CCDC12	1.79E-52	0.150275069	0.658	0.569	2.80E-48
PRSS53	2.93E-52	0.180693448	0.453	0.4	4.57E-48
EHMT1	1.40E-51	0.185478153	0.46	0.41	2.19E-47
SIT1	1.55E-51	0.109346928	0.693	0.621	2.43E-47
AIP	2.69E-51	0.119771198	0.624	0.617	4.21E-47
TXNDC12	2.10E-46	0.123556243	0.567	0.557	3.27E-42
HSP90AA1	8.56E-45	1.504595448	0.998	0.984	1.34E-40
CFLAR-AS1	1.04E-41	0.196607621	0.504	0.441	1.62E-37
FAM166A	4.76E-38	0.204124205	0.491	0.449	7.43E-34
IDH3B	1.08E-36	0.102082775	0.556	0.554	1.68E-32
HSPA1L	1.05E-32	3.179851504	0.602	0.364	1.64E-28
HSPA1B	4.55E-32	3.129605596	0.689	0.392	7.10E-28
HLA-DRB1	4.17E-31	1.628375726	0.973	0.866	6.51E-27
DNAJB1	5.07E-30	1.737729205	0.913	0.923	7.91E-26
HAVCR2	1.94E-28	3.28115701	0.704	0.273	3.02E-24
HLA-DRB6	2.61E-28	1.571487613	0.964	0.791	4.08E-24
TALDO1	2.65E-27	0.108022557	0.558	0.456	4.14E-23

HLA-DRB5	3.29E-27	1.521961279	0.953	0.796	5.13E-23
RBPJ	3.21E-26	2.327765846	0.831	0.516	5.02E-22
CD74	8.38E-26	1.07081663	1	0.992	1.31E-21
HLA-DRA	1.66E-25	2.205660672	0.893	0.619	2.59E-21
HSPB1	3.54E-24	2.41603832	0.573	0.389	5.52E-20
HSPA8	8.85E-24	0.918051738	0.998	0.999	1.38E-19
CD82	1.10E-22	2.278441769	0.809	0.459	1.72E-18
AP2S1	6.05E-22	0.136224958	0.422	0.352	9.44E-18
GAPDH	4.58E-21	0.690259051	0.998	0.999	7.14E-17
HSPH1	4.61E-21	1.975916356	0.784	0.653	7.20E-17
APOBEC3G	3.41E-20	1.467764851	0.947	0.812	5.32E-16
HLA-DPA1	5.13E-20	0.993278771	0.989	0.957	8.01E-16
NAPA-AS1	9.65E-20	0.142808874	0.569	0.468	1.51E-15
HSP90AB1	4.42E-19	1.033002738	0.996	0.962	6.91E-15
DUSP4	5.71E-19	2.151976066	0.818	0.421	8.91E-15
APOBEC3C	3.55E-18	1.291204842	0.929	0.821	5.54E-14
CTLA4	4.07E-18	2.833366858	0.498	0.214	6.35E-14
GZMB	5.58E-18	1.556972181	0.953	0.803	8.72E-14
UBB	1.12E-17	0.487312859	1	0.999	1.75E-13
VCAM1	1.69E-17	3.246131131	0.542	0.129	2.64E-13
HLA-DQB1	1.63E-16	1.627862345	0.867	0.568	2.54E-12
NUTF2	8.30E-16	0.101769696	0.438	0.406	1.29E-11
LOC100507412	5.78E-15	1.820073289	0.496	0.502	9.02E-11
SAMSN1	8.97E-15	1.324816842	0.967	0.736	1.40E-10
MEA1	1.69E-14	0.103059412	0.456	0.389	2.64E-10
HSPE1	5.42E-14	1.325304639	0.751	0.623	8.46E-10
DUSP10	8.39E-14	1.937802712	0.702	0.378	1.31E-09
PHLDA1	2.34E-13	1.930821441	0.7	0.386	3.65E-09
HSPD1	3.52E-13	1.388392433	0.793	0.724	5.49E-09
ANXA2P2	5.93E-13	0.134399598	0.562	0.541	9.26E-09
SLC5A3	1.64E-12	1.607257363	0.664	0.479	2.56E-08
LDHA	3.49E-12	0.863145723	0.993	0.943	5.44E-08
BHLHE40-AS1	7.26E-12	1.910498013	0.544	0.22	1.13E-07
HLA-DQA1	8.28E-12	1.849395813	0.616	0.349	1.29E-07
IFI6	8.48E-12	1.562374885	0.624	0.434	1.32E-07
ADAM19	9.54E-12	1.615153646	0.673	0.463	1.49E-07
HMGB2	1.74E-11	1.108278956	0.916	0.74	2.72E-07
OASL	2.09E-11	1.850428904	0.693	0.337	3.26E-07
MRPL51	3.35E-11	0.102131499	0.438	0.389	5.23E-07
CXCR6	3.53E-11	1.487381009	0.838	0.63	5.51E-07
PDCD1	4.43E-11	1.967868735	0.611	0.302	6.92E-07
MIR155HG	8.44E-11	2.347501764	0.467	0.169	1.32E-06
ANXA5	1.31E-10	1.238775334	0.869	0.676	2.05E-06
UBC	2.97E-10	0.378890715	1	1	4.63E-06
NAB1	4.21E-10	2.121571808	0.478	0.217	6.57E-06
LYST	5.16E-10	1.198530639	0.882	0.647	8.06E-06
HLA-DMA	5.18E-10	1.594095818	0.676	0.394	8.09E-06
PDE4DIP	6.50E-10	1.638918668	0.64	0.372	1.01E-05
NDFIP2	8.97E-10	1.988960301	0.562	0.269	1.40E-05
CXCR4	1.08E-09	0.774315057	0.996	0.976	1.69E-05
HLA-DQB2	1.58E-09	1.71359467	0.491	0.209	2.46E-05
DNAJA1	2.36E-09	1.002895617	0.918	0.796	3.68E-05
TBCD	2.63E-09	1.424649193	0.724	0.463	4.11E-05
ZNF683	3.72E-09	1.970425298	0.562	0.262	5.81E-05
CCL3	4.35E-09	1.758178908	0.651	0.352	6.79E-05
LAG3	4.50E-09	1.343641355	0.72	0.442	7.03E-05

CD2	5.03E-09	0.608051244	0.989	0.969	7.86E-05
FABP5	7.13E-09	1.394917049	0.491	0.17	0.000111
BHLHE40	1.46E-08	1.37241657	0.738	0.472	0.000228
CD44	2.09E-08	0.603944345	0.991	0.963	0.000326
HLA-A	3.30E-08	0.215056589	1	1	0.000515
IVNS1ABP	4.88E-08	0.945588243	0.933	0.749	0.000762
LGALS3	5.93E-08	1.596718974	0.58	0.296	0.000925
IFI16	1.18E-07	0.700480812	0.944	0.874	0.001848
ICOS	1.73E-07	1.129437594	0.771	0.631	0.002695
RNF19A	2.05E-07	0.910002685	0.889	0.733	0.003196
COTL1	2.32E-07	0.789133105	0.933	0.854	0.003624
NEAT1	2.60E-07	0.8114303	0.887	0.883	0.004055
CD38	2.71E-07	1.759732288	0.456	0.222	0.004231
ENTPD1	3.13E-07	1.51492875	0.556	0.377	0.004891
SLC38A2	3.28E-07	0.927848107	0.824	0.716	0.005122
GGA2	4.44E-07	1.264117817	0.669	0.432	0.006925
EDARADD	5.05E-07	0.881204597	0.687	0.677	0.007883
ACP5	5.25E-07	1.471716488	0.578	0.322	0.008188
H3F3B	5.36E-07	0.315175576	1	1	0.008369
AHSA1	6.42E-07	1.220705694	0.66	0.446	0.010018
TOB1	8.16E-07	0.897892549	0.864	0.762	0.012735
ITM2A	8.17E-07	0.774209969	0.902	0.817	0.012754
H2AFZ	8.48E-07	0.773276431	0.884	0.782	0.013242
CCL4	1.17E-06	0.819535851	0.971	0.851	0.01822
DDIT4	1.27E-06	0.921999408	0.884	0.694	0.019897
HLA-DPB1	1.58E-06	0.60198576	0.976	0.909	0.024703
CACYBP	1.61E-06	1.010780716	0.702	0.569	0.025182
ARID5B	1.97E-06	1.01023218	0.762	0.596	0.030802
BTG1	2.02E-06	0.494024442	0.996	0.977	0.031516
ITGAE	2.31E-06	0.944023453	0.893	0.623	0.036033
FUT8	2.69E-06	1.515736773	0.469	0.248	0.042055
ABCG1	2.81E-06	1.687617124	0.436	0.187	0.04382
SLF1	3.65E-06	1.28338366	0.627	0.336	0.057011
ITM2C	3.68E-06	1.060773507	0.8	0.486	0.057513
MX1	4.01E-06	1.439349155	0.48	0.329	0.06252
TANK	5.07E-06	0.81977818	0.876	0.733	0.079154
CKS2	5.84E-06	1.331157808	0.493	0.279	0.091183
BTG3	5.99E-06	1.323765448	0.56	0.32	0.09353

### A1.3 – Differential gene expression for slow relaxing gels

Gene	p_val	avg_logFC	pct.1	pct.2	p_val_adj
MIF	5.07E-187	0.31671551	1	0.999	8.95E-183
RPSA	3.61E-176	0.17285624	1	1	6.38E-172
RPS29	1.03E-175	0.15838452	1	1	1.83E-171
RPS20	1.86E-164	0.19344148	1	1	3.28E-160
RPL37A	2.80E-155	0.17449325	1	1	4.95E-151
RPL23	6.31E-152	0.25947876	1	1	1.12E-147
LIMA1	2.05E-147	0.45935271	0.976	0.957	3.62E-143
OAZ1	3.19E-144	0.1733194	1	1	5.63E-140
MDM2	2.15E-135	0.58751257	0.879	0.793	3.80E-131

FDXR	3.62E-130	0.53747734	0.875	0.773	6.40E-126
PHPT1	8.94E-130	0.32258951	0.999	1	1.58E-125
RPL9	1.14E-124	0.16739618	1	1	2.02E-120
FOSB	6.87E-124	0.6475612	0.509	0.216	1.21E-119
SRGN	1.45E-119	0.36059921	1	0.998	2.56E-115
RPS27L	3.12E-119	0.33763741	1	1	5.51E-115
SOD1	5.47E-119	0.24982025	1	0.999	9.68E-115
RPL27A	3.73E-105	0.15131437	1	1	6.60E-101
ATF3	5.65E-104	0.56523021	0.518	0.273	9.99E-100
ANKRD28	6.57E-100	0.38661568	0.826	0.678	1.16E-95
JUN	2.53E-98	0.56617572	0.72	0.545	4.47E-94
RPL6	4.43E-98	0.13268816	1	1	7.83E-94
IL2RA	5.51E-95	0.45214134	0.993	0.988	9.73E-91
CREM	5.93E-94	0.39169457	0.966	0.938	1.05E-89
DUSP4	6.31E-94	0.40153934	0.944	0.923	1.11E-89
RPL38	7.41E-93	0.14269749	1	1	1.31E-88
TRIAP1	4.90E-89	0.32514453	0.955	0.923	8.65E-85
PHLDA3	1.66E-88	0.48865346	0.653	0.384	2.93E-84
TSC22D3	8.00E-86	0.45784679	0.626	0.378	1.41E-81
HIC1	6.90E-85	0.36120945	0.862	0.754	1.22E-80
RPL5	1.95E-78	0.14461746	1	1	3.44E-74
HSP90AA1	1.64E-76	0.21905763	0.999	1	2.89E-72
SUPT4H1	6.53E-75	0.24682142	0.992	0.99	1.15E-70
CRIP1	5.76E-74	0.29975106	0.946	0.904	1.02E-69
RPS27	6.07E-73	0.11395788	1	1	1.07E-68
SEC11C	7.74E-73	0.26330034	0.997	0.998	1.37E-68
NDUFAF8	1.03E-71	0.21616956	0.998	0.996	1.82E-67
RPL4	3.81E-70	0.11615389	1	1	6.74E-66
IDS	1.75E-67	0.26472964	0.926	0.886	3.09E-63
RPL24	1.81E-67	0.10266967	1	1	3.20E-63
DUSP1	3.98E-67	0.36261752	0.366	0.168	7.03E-63
RPL21	3.87E-66	0.10043611	1	1	6.83E-62
ISCU	6.93E-66	0.23754171	0.99	0.971	1.23E-61
CD70	1.04E-65	0.41987781	0.932	0.904	1.84E-61
ASB2	2.29E-65	0.2881546	0.932	0.89	4.05E-61
MT-ND2	5.67E-64	0.16914385	1	1	1.00E-59
RPL7	2.39E-63	0.1311718	1	1	4.22E-59
UBB	1.13E-62	0.14842215	1	1	2.00E-58
CYCS	1.86E-62	0.20434394	1	1	3.29E-58
KLF6	1.28E-61	0.35735101	0.893	0.862	2.27E-57
PSMB7	8.92E-61	0.17090797	1	0.999	1.58E-56
CDKN1A	3.68E-60	0.48751705	0.608	0.405	6.50E-56
LMNA	4.97E-60	0.40439124	0.913	0.876	8.79E-56
TP53I3	7.32E-60	0.41990035	0.276	0.146	1.29E-55
FAM3C	1.61E-59	0.28684356	0.842	0.748	2.85E-55
NPM1	1.92E-59	0.21223514	1	1	3.39E-55
TPRG1	3.87E-59	0.54693736	0.628	0.515	6.85E-55
CYP1B1	2.43E-58	0.62182681	0.428	0.247	4.29E-54
LDLRAD4	9.18E-58	0.34484049	0.533	0.355	1.62E-53
FOS	9.94E-58	0.57919573	0.359	0.141	1.76E-53
RPL27	5.57E-57	0.09886246	1	1	9.84E-53
RPS19	1.07E-56	0.11062084	1	1	1.88E-52
BAX	1.64E-56	0.19472775	0.999	1	2.90E-52
MIR155HG	1.83E-56	0.37290446	0.544	0.362	3.23E-52
MYL9	2.21E-55	0.44872206	0.368	0.193	3.91E-51
CYTIP	4.38E-55	0.2370593	0.994	0.99	7.74E-51

GADD45A	1.06E-54	0.40504012	0.701	0.588	1.87E-50
MT-ND4L	3.91E-54	0.19862037	0.998	1	6.91E-50
MUC20-OT1	2.15E-53	0.25386651	0.874	0.821	3.80E-49
TFRC	3.14E-53	0.23609054	0.975	0.967	5.56E-49
TNFAIP3	5.38E-53	0.30934253	0.424	0.23	9.50E-49
RRM2B	1.11E-52	0.26716311	0.485	0.295	1.96E-48
RPS17	1.13E-52	0.19044296	0.993	0.985	2.00E-48
GALM	3.59E-52	0.26655758	0.956	0.943	6.34E-48
RPS2	2.65E-51	0.12031696	1	1	4.68E-47
GPR183	3.25E-51	0.3339499	0.775	0.663	5.75E-47
RPL37	4.21E-51	0.0780897	1	1	7.44E-47
TIGAR	6.40E-51	0.27315693	0.704	0.529	1.13E-46
LRPAP1	5.19E-50	0.17642327	0.995	0.984	9.18E-46
SELENOH	6.76E-50	0.17819581	0.999	0.998	1.20E-45
CD2	2.41E-49	0.20788107	0.997	0.998	4.25E-45
RPL15	3.80E-49	0.07765484	1	1	6.72E-45
RPS16	1.39E-48	0.07670444	1	1	2.46E-44
RNF19A	1.90E-48	0.28429115	0.72	0.593	3.36E-44
MTRNR2L8	3.39E-48	0.36682938	0.623	0.477	5.99E-44
SYTL3	1.34E-47	0.24923444	0.822	0.712	2.38E-43
SKP1	1.94E-47	0.12478349	1	1	3.43E-43
DDB2	2.34E-46	0.23221123	0.94	0.923	4.14E-42
TNFRSF10B	9.21E-45	0.22988768	0.372	0.2	1.63E-40
ASCC3	1.20E-44	0.22602756	0.918	0.866	2.12E-40
RPS11	2.98E-44	0.08749518	1	1	5.27E-40
STK17A	4.68E-44	0.21239017	0.984	0.975	8.27E-40
ARPC2	6.36E-44	0.09241237	1	1	1.12E-39
ACO44849.1	1.05E-43	0.17679469	0.238	0.096	1.86E-39
GPX4	1.38E-43	0.14800793	1	1	2.44E-39
MICAL2	1.55E-43	0.25149929	0.582	0.401	2.74E-39
XPC	1.88E-43	0.2518012	0.816	0.73	3.33E-39
BLOC1S2	1.26E-42	0.19928864	0.956	0.941	2.22E-38
TMEM67	2.71E-42	0.16922749	0.246	0.1	4.79E-38
LPXN	6.39E-42	0.20399764	0.944	0.91	1.13E-37
BSG	1.42E-41	0.14636965	0.999	0.997	2.51E-37
RDH10	1.65E-41	0.2940056	0.48	0.32	2.92E-37
DRAM1	1.67E-41	0.21646072	0.39	0.23	2.94E-37
IFNG	3.14E-41	0.61304351	0.46	0.353	5.54E-37
HSPA1B	1.33E-39	0.20834839	0.3	0.163	2.36E-35
MIR34AHG	1.37E-39	0.18238207	0.208	0.076	2.41E-35
MRPS6	3.51E-39	0.16564389	0.995	0.994	6.20E-35
JAML	5.84E-39	0.25405215	0.861	0.813	1.03E-34
CCDC90B	5.95E-39	0.20989585	0.838	0.764	1.05E-34
RPL22	9.54E-39	0.07527254	1	1	1.69E-34
CCT7	1.41E-38	0.14278006	1	1	2.50E-34
EZR	1.49E-38	0.15364949	0.999	1	2.63E-34
SLC1A4	1.89E-38	0.22909518	0.514	0.347	3.35E-34
PPP1R2	1.17E-37	0.1736537	0.975	0.973	2.06E-33
ACO20916.1	2.10E-37	0.19074218	0.27	0.122	3.71E-33
ENTPD1	5.64E-37	0.27451241	0.641	0.507	9.97E-33
PHLDA1	2.47E-36	0.30493532	0.72	0.623	4.37E-32
HIPK1	3.66E-36	0.20868453	0.584	0.407	6.47E-32
HSPH1	5.04E-36	0.19245336	0.994	0.996	8.91E-32
MYB	9.56E-36	0.30991292	0.677	0.538	1.69E-31
EHD4	1.63E-35	0.22743389	0.56	0.416	2.87E-31
MYH10	2.15E-35	0.23410291	0.309	0.168	3.80E-31

NPM3	2.21E-35	0.22244575	0.879	0.839	3.91E-31
RPS13	2.31E-35	0.07991098	1	1	4.09E-31
RGCC	3.03E-35	0.242608	0.73	0.669	5.35E-31
FBXO22	3.11E-35	0.20212164	0.891	0.853	5.50E-31
NCS1	4.91E-35	0.23534278	0.369	0.217	8.68E-31
DNAJA1	5.70E-35	0.15827871	1	1	1.01E-30
SAT1	1.32E-34	0.23681317	0.935	0.928	2.34E-30
SELENOS	1.48E-34	0.17444307	0.987	0.972	2.61E-30
RPS5	1.86E-34	0.08259429	1	1	3.29E-30
NAP1L1	1.89E-34	0.11208863	1	1	3.34E-30
RPL36	1.93E-34	0.08805034	1	1	3.41E-30
PPP1R15A	2.13E-34	0.2224616	0.9	0.882	3.77E-30
MT2A	2.55E-34	0.25444673	0.99	0.988	4.51E-30
ITM2A	3.10E-34	0.25925384	0.739	0.67	5.48E-30
C6orf48	3.13E-34	0.20364921	0.78	0.669	5.52E-30
NSA2	1.71E-33	0.12447813	0.999	0.999	3.02E-29
NKD2	2.07E-33	0.24683332	0.387	0.231	3.66E-29
PGM2L1	2.51E-33	0.22862955	0.536	0.41	4.43E-29
PLIN2	8.61E-33	0.20997819	0.912	0.888	1.52E-28
SPRYD7	9.43E-33	0.19385328	0.568	0.403	1.67E-28
MAPK8	9.67E-33	0.21602608	0.582	0.447	1.71E-28
APLP2	1.48E-32	0.19475875	0.627	0.485	2.62E-28
DHRS3	1.66E-32	0.26566087	0.569	0.418	2.94E-28
GATA3	1.81E-32	0.2305215	0.952	0.942	3.20E-28
TOMM5	2.72E-32	0.15091775	0.982	0.972	4.80E-28
NR3C1	2.91E-32	0.21881077	0.751	0.654	5.15E-28
NOP53	8.43E-32	0.13290424	0.999	0.999	1.49E-27
MYADM	8.56E-32	0.22254084	0.654	0.514	1.51E-27
DYNLL1	2.49E-31	0.11779648	1	1	4.39E-27
UBE2S	9.43E-31	0.17875795	0.999	1	1.67E-26
BBC3	3.15E-30	0.22790642	0.375	0.24	5.57E-26
TM7SF3	4.53E-30	0.18642202	0.824	0.763	8.01E-26
NDUFS5	5.85E-30	0.09342455	1	1	1.03E-25
HSPA1A	6.80E-30	0.25046152	0.823	0.813	1.20E-25
CCNG1	1.12E-29	0.18136468	0.896	0.859	1.99E-25
PSMB1	1.47E-29	0.08865283	1	1	2.60E-25
DAPP1	1.57E-29	0.20518085	0.649	0.525	2.77E-25
ZMAT3	1.71E-29	0.22494792	0.362	0.226	3.02E-25
USP12	2.23E-29	0.18851789	0.621	0.475	3.95E-25
SESN1	2.76E-29	0.17892448	0.291	0.15	4.88E-25
RALB	9.38E-29	0.20898255	0.746	0.664	1.66E-24
PLCG2	9.60E-29	0.19836814	0.589	0.45	1.70E-24
AEN	9.85E-29	0.19646743	0.549	0.388	1.74E-24
RPL7A	1.01E-28	0.07763269	1	1	1.79E-24
VDR	1.75E-28	0.18153899	0.448	0.315	3.09E-24
IKBIP	2.57E-28	0.15236948	0.97	0.973	4.54E-24
TRIM22	3.14E-28	0.24572945	0.461	0.302	5.55E-24
PMAIP1	3.64E-28	0.25514	0.815	0.744	6.43E-24
SMIM3	4.30E-28	0.19559514	0.74	0.649	7.60E-24
MBD2	4.38E-28	0.13156637	0.99	0.991	7.74E-24
EEF2	5.16E-28	0.10409005	1	1	9.12E-24
RBM8A	6.33E-28	0.11068375	0.999	1	1.12E-23
AHI1	9.08E-28	0.21761841	0.75	0.68	1.60E-23
TPM4	1.37E-27	0.12278545	0.999	1	2.42E-23
XRCC6	1.72E-27	0.10158972	1	1	3.04E-23
UBE2M	1.99E-27	0.11272225	0.998	1	3.51E-23

SCCPDH	2.03E-27	0.18300639	0.686	0.567	3.58E-23
ZEB2	3.61E-27	0.19850028	0.425	0.295	6.39E-23
SLC27A2	3.81E-27	0.19476075	0.785	0.716	6.73E-23
EVI5	4.81E-27	0.19282988	0.35	0.216	8.50E-23
TRIB1	7.23E-27	0.17858874	0.318	0.188	1.28E-22
PPP1R14B	7.45E-27	0.14606717	1	1	1.32E-22
SLC7A5	8.27E-27	0.20724621	0.74	0.676	1.46E-22
FAM107B	9.96E-27	0.16407773	0.981	0.987	1.76E-22
YBX1	1.07E-26	0.09278166	1	1	1.89E-22
ACSL4	1.18E-26	0.19865215	0.892	0.878	2.09E-22
PAM16	1.32E-26	0.11086259	0.203	0.092	2.33E-22
FAS	1.95E-26	0.18338726	0.779	0.686	3.44E-22
PVT1	3.30E-26	0.18783984	0.523	0.377	5.83E-22
IFT57	3.45E-26	0.18422754	0.701	0.598	6.10E-22
ARL3	4.29E-26	0.15785719	0.922	0.897	7.59E-22
MLF2	4.66E-26	0.14358755	0.958	0.946	8.24E-22
VPS41	1.15E-25	0.16620767	0.64	0.492	2.03E-21
ODC1	1.38E-25	0.1946662	0.969	0.972	2.44E-21
ACOT9	1.74E-25	0.17402801	0.72	0.61	3.08E-21
HIBCH	2.31E-25	0.16856561	0.67	0.544	4.09E-21
NME2	2.85E-25	0.12673597	0.311	0.182	5.04E-21
PTP4A2	3.11E-25	0.11035437	1	1	5.50E-21
TRAF1	3.45E-25	0.19275107	0.651	0.526	6.10E-21
ARF5	3.70E-25	0.14620619	0.89	0.828	6.55E-21
TIPARP	5.50E-25	0.18490354	0.646	0.51	9.72E-21
C20orf204	5.85E-25	0.22073242	0.327	0.205	1.03E-20
CHKA	7.34E-25	0.15728269	0.386	0.258	1.30E-20
PYHIN1	7.40E-25	0.22117205	0.533	0.406	1.31E-20
NFE2L3	8.80E-25	0.18821741	0.458	0.325	1.55E-20
TAF3	9.76E-25	0.16046554	0.831	0.782	1.73E-20
CD86	1.10E-24	0.18006953	0.525	0.388	1.95E-20
PHB	2.03E-24	0.114545	1	0.999	3.60E-20
LIF	2.10E-24	0.27819352	0.596	0.477	3.71E-20
NFAT5	2.46E-24	0.18300438	0.482	0.353	4.36E-20
SYNGR2	2.85E-24	0.18425643	0.76	0.719	5.03E-20
HIST1H2BJ	3.14E-24	0.16991879	0.306	0.186	5.55E-20
PSMB6	3.55E-24	0.09094886	1	1	6.28E-20
SLC39A8	3.63E-24	0.15218251	0.825	0.746	6.41E-20
CCR4	4.60E-24	0.17048073	0.288	0.164	8.13E-20
EIF3J	4.91E-24	0.12243775	0.994	0.995	8.67E-20
CD82	7.61E-24	0.21942235	0.643	0.543	1.34E-19
ZMPSTE24	8.23E-24	0.16004061	0.715	0.594	1.45E-19
SERTAD1	1.04E-23	0.16938531	0.513	0.382	1.84E-19
ARPC4	1.10E-23	0.10222616	1	0.999	1.95E-19
IER3	1.14E-23	0.37260374	0.414	0.305	2.02E-19
IL9R	1.14E-23	0.20301541	0.498	0.342	2.02E-19
DENR	1.58E-23	0.12739302	0.974	0.974	2.79E-19
RPL7L1	3.82E-23	0.14277076	0.982	0.984	6.76E-19
MPDU1	5.28E-23	0.13618509	0.914	0.885	9.34E-19
CD38	7.35E-23	0.18992481	0.857	0.856	1.30E-18
PRPF6	7.67E-23	0.13012706	0.973	0.959	1.36E-18
SRM	8.38E-23	0.15240654	0.998	1	1.48E-18
RILPL2	8.99E-23	0.1572994	0.927	0.912	1.59E-18
AHRR	9.52E-23	0.13546965	0.336	0.205	1.68E-18
GPATCH4	1.08E-22	0.15154865	0.97	0.968	1.90E-18
TUBB6	1.14E-22	0.25516894	0.469	0.349	2.02E-18



F2R	1.59E-22	0.19736253	0.594	0.472	2.80E-18
RPS3A	1.94E-22	0.06092202	1	1	3.44E-18
CD3D	2.01E-22	0.11312213	1	1	3.56E-18
KPNA4	2.72E-22	0.14243969	0.868	0.804	4.80E-18
ST13	3.01E-22	0.10850778	1	1	5.32E-18
BOP1	3.85E-22	0.14473217	0.933	0.924	6.80E-18
ATP6V0E1	4.63E-22	0.09950343	0.999	1	8.18E-18
SLA	4.91E-22	0.19912647	0.72	0.658	8.68E-18
SURF4	5.22E-22	0.11801497	0.989	0.994	9.23E-18
NINJ1	5.78E-22	0.18519862	0.562	0.456	1.02E-17
ELL2	5.81E-22	0.1847341	0.519	0.391	1.03E-17
RPS4X	6.46E-22	0.05857822	1	1	1.14E-17
MRPL47	8.07E-22	0.10808141	0.992	0.992	1.43E-17
DNAJB6	9.68E-22	0.12840157	0.965	0.958	1.71E-17
INPP5F	1.01E-21	0.1322794	0.309	0.188	1.79E-17
RNF19B	1.06E-21	0.15085874	0.36	0.254	1.88E-17
ECHS1	1.09E-21	0.11789136	0.987	0.98	1.93E-17
PRDM1	1.10E-21	0.18779129	0.71	0.604	1.95E-17
PPIL4	1.77E-21	0.15479522	0.631	0.51	3.13E-17
RPL23A	1.80E-21	0.05302165	1	1	3.19E-17
FHL2	2.08E-21	0.15387379	0.272	0.173	3.68E-17
RPS25	2.76E-21	0.05264088	1	1	4.88E-17
RPS9	4.15E-21	0.04983351	1	1	7.34E-17
CHSY1	4.66E-21	0.15116226	0.487	0.359	8.23E-17
UBE2V1	4.68E-21	0.12881932	0.361	0.232	8.27E-17
PRMT1	4.99E-21	0.13361994	0.999	1	8.81E-17
LAX1	5.03E-21	0.15377826	0.386	0.264	8.90E-17
ACO20571.1	5.32E-21	0.16961061	0.398	0.272	9.41E-17
TMF1	5.33E-21	0.14659494	0.946	0.92	9.41E-17
LYST	5.89E-21	0.1714316	0.566	0.437	1.04E-16
HSDL2	7.94E-21	0.155103	0.644	0.528	1.40E-16
SMIM30	9.13E-21	0.1596858	0.704	0.594	1.61E-16
PITRM1	1.11E-20	0.14272451	0.515	0.381	1.96E-16
CCP110	1.20E-20	0.15765652	0.699	0.597	2.11E-16
ZBED2	1.28E-20	0.25261334	0.216	0.116	2.26E-16
NQO1	1.88E-20	0.16186471	0.861	0.835	3.33E-16
NOL7	2.33E-20	0.10125346	0.999	1	4.11E-16
RPL18A	2.71E-20	0.05540866	1	1	4.79E-16
KRTCAP2	2.93E-20	0.12513061	0.954	0.924	5.18E-16
PLK3	3.21E-20	0.16265375	0.581	0.449	5.67E-16
PHB2	3.57E-20	0.0963475	1	1	6.30E-16
AEBP2	4.05E-20	0.14944097	0.63	0.492	7.15E-16
CTLA4	4.07E-20	0.19962173	0.291	0.169	7.19E-16
KIF3B	4.10E-20	0.15346462	0.537	0.425	7.25E-16
RFTN1	4.78E-20	0.15051737	0.66	0.534	8.45E-16
BIRC3	5.03E-20	0.20769396	0.532	0.394	8.89E-16
YPEL5	5.20E-20	0.16349884	0.376	0.244	9.19E-16
PSMD4	5.28E-20	0.09804509	0.998	0.994	9.33E-16
DNLZ	5.36E-20	0.09661269	0.201	0.102	9.48E-16
KCNK1	7.52E-20	0.20860117	0.416	0.289	1.33E-15
STAU1	8.55E-20	0.12889911	0.888	0.861	1.51E-15
IARS2	8.93E-20	0.12834062	0.902	0.863	1.58E-15
MCL1	9.16E-20	0.15144009	0.868	0.854	1.62E-15
ACO60780.1	9.55E-20	0.12670543	0.296	0.18	1.69E-15
KIF2A	1.27E-19	0.11161307	0.996	0.997	2.25E-15
SLC2A1	1.35E-19	0.14932142	0.746	0.684	2.38E-15

MLF1	1.37E-19	0.15397958	0.555	0.41	2.43E-15
FTL	2.03E-19	0.10859325	1	1	3.58E-15
FTH1	2.14E-19	0.09992304	1	1	3.78E-15
GLO1	2.15E-19	0.1084564	0.995	0.995	3.81E-15
SNRPB	2.57E-19	0.07005113	1	1	4.54E-15
GK	2.73E-19	0.16242721	0.446	0.333	4.82E-15
SQSTM1	2.73E-19	0.14456304	0.951	0.942	4.83E-15
NME1	2.74E-19	0.11370958	1	0.999	4.84E-15
EID1	3.32E-19	0.09008054	0.998	1	5.86E-15
MYOF	3.37E-19	0.13050691	0.27	0.173	5.96E-15
SNHG19	3.43E-19	0.15751177	0.432	0.32	6.07E-15
BUD31	3.58E-19	0.09096963	1	1	6.33E-15
MRPL45	3.62E-19	0.13413757	0.757	0.668	6.39E-15
CCDC86	4.80E-19	0.18832915	0.798	0.766	8.48E-15
PSMB10	5.02E-19	0.13075625	0.806	0.73	8.87E-15
RPL13A	5.73E-19	0.05914374	1	1	1.01E-14
RPL17	6.52E-19	0.12115442	0.916	0.898	1.15E-14
DNAJC18	6.56E-19	0.15314262	0.488	0.375	1.16E-14
GPR171	6.60E-19	0.1676823	0.92	0.897	1.17E-14
NDFIP2	7.23E-19	0.16686693	0.79	0.718	1.28E-14
MYL6	7.56E-19	0.07631588	1	1	1.34E-14
YWHAE	8.75E-19	0.09044692	0.999	1	1.55E-14
RDX	8.76E-19	0.14199443	0.828	0.778	1.55E-14
IER5	9.72E-19	0.16163049	0.796	0.772	1.72E-14
RPS28	9.79E-19	0.05437467	1	1	1.73E-14
SAP18	1.17E-18	0.07610126	1	1	2.07E-14
PPAN	1.37E-18	0.15780567	0.695	0.616	2.42E-14
SLC25A4	1.47E-18	0.18120486	0.702	0.585	2.60E-14
EBNA1BP2	1.65E-18	0.11865102	0.993	0.994	2.91E-14
ACO09948.1	1.71E-18	0.12686025	0.352	0.244	3.03E-14
RAB11FIP1	1.78E-18	0.12687083	0.986	0.984	3.15E-14
BCAS4	1.89E-18	0.14997498	0.9	0.877	3.33E-14
C12orf75	2.58E-18	0.10042572	1	1	4.56E-14
RPP30	2.70E-18	0.12826388	0.931	0.92	4.77E-14
STAT3	2.72E-18	0.15306179	0.744	0.66	4.80E-14
ATP8B4	3.28E-18	0.15874613	0.502	0.366	5.80E-14
CXorf40B	3.80E-18	0.1317264	0.477	0.351	6.72E-14
SNAPC1	4.78E-18	0.14205448	0.515	0.386	8.45E-14
CMSS1	5.90E-18	0.12777128	0.939	0.935	1.04E-13
PMPCA	6.23E-18	0.1248831	0.89	0.858	1.10E-13
VDAC2	6.57E-18	0.08589789	1	1	1.16E-13
BZW1	6.64E-18	0.09043307	1	1	1.17E-13
NTPCR	7.22E-18	0.13268069	0.711	0.603	1.28E-13
SH2D1A	7.84E-18	0.13808558	0.937	0.926	1.39E-13
MAPK6	7.85E-18	0.1420907	0.8	0.747	1.39E-13
TP53TG1	7.87E-18	0.1510547	0.465	0.36	1.39E-13
NOP14	8.16E-18	0.13158494	0.933	0.923	1.44E-13
GBP2	8.53E-18	0.14570025	0.929	0.927	1.51E-13
PEBP1	8.79E-18	0.10103985	1	1	1.55E-13
PAAF1	9.39E-18	0.13223461	0.576	0.446	1.66E-13
SLC7A6	1.05E-17	0.13803223	0.477	0.357	1.86E-13
CD109	1.10E-17	0.11565107	0.265	0.168	1.94E-13
CYTH2	1.25E-17	0.14039961	0.555	0.429	2.21E-13
GJB6	1.29E-17	0.30371382	0.265	0.188	2.28E-13
EVL	1.33E-17	0.11834352	0.998	1	2.35E-13
EIF4G2	1.46E-17	0.094533	0.999	1	2.57E-13

SRI	1.52E-17	0.09094986	1	1	2.68E-13
YPEL2	1.58E-17	0.14765414	0.296	0.203	2.79E-13
KPNA1	1.65E-17	0.13315253	0.584	0.459	2.92E-13
GPN3	1.70E-17	0.11855358	0.917	0.898	3.00E-13
PPP1R16B	1.72E-17	0.12934892	0.425	0.293	3.03E-13
SEMA4D	2.32E-17	0.13528521	0.884	0.862	4.10E-13
ATP2C1	2.38E-17	0.13478899	0.489	0.372	4.21E-13
SLC5A3	2.99E-17	0.14673061	0.543	0.438	5.28E-13
PNO1	3.12E-17	0.13393212	0.846	0.804	5.52E-13
MRPL27	4.81E-17	0.09579208	0.998	0.998	8.51E-13
IL12RB2	5.12E-17	0.11083998	0.26	0.159	9.05E-13
KIF3A	5.17E-17	0.14844402	0.818	0.774	9.14E-13
IKZF3	5.56E-17	0.1704505	0.595	0.504	9.83E-13
ITPR1	7.22E-17	0.16972061	0.504	0.408	1.28E-12
2-Sep	7.76E-17	0.10714561	0.972	0.972	1.37E-12
INPP1	1.00E-16	0.13182648	0.44	0.323	1.77E-12
PLIN3	1.06E-16	0.14432537	0.724	0.636	1.87E-12
SCRIB	1.11E-16	0.1169319	0.351	0.232	1.96E-12
KMT2A	1.12E-16	0.1259429	0.938	0.929	1.99E-12
TOGARAM1	1.21E-16	0.11412252	0.326	0.216	2.14E-12
EIF6	1.30E-16	0.09387687	0.997	0.997	2.29E-12
ACBD6	1.40E-16	0.12227518	0.901	0.875	2.48E-12
HERC5	1.46E-16	0.17829534	0.418	0.308	2.59E-12
AQP11	1.46E-16	0.11460979	0.236	0.15	2.59E-12
ACAT1	1.75E-16	0.11346322	0.979	0.978	3.09E-12
PPFIBP1	1.99E-16	0.15274084	0.22	0.131	3.52E-12
RPL18	2.06E-16	0.04837145	1	1	3.65E-12
HSPD1	2.14E-16	0.1271321	1	1	3.78E-12
PSMD13	2.26E-16	0.07982128	0.999	1	4.00E-12
RELB	2.76E-16	0.14426143	0.446	0.317	4.87E-12
UTP20	2.80E-16	0.14248324	0.6	0.477	4.95E-12
GSPT1	3.21E-16	0.10092199	0.995	0.998	5.68E-12
TRAF4	3.28E-16	0.14166795	0.548	0.451	5.79E-12
NT5C3B	3.28E-16	0.12366998	0.853	0.808	5.79E-12
GOLGB1	3.45E-16	0.15797271	0.874	0.863	6.10E-12
PTPN22	3.96E-16	0.13754253	0.866	0.855	7.01E-12
HDLBP	3.99E-16	0.11394598	0.939	0.917	7.05E-12
MT1E	4.00E-16	0.18260739	0.887	0.878	7.07E-12
MAN1C1	4.38E-16	0.13444366	0.316	0.214	7.74E-12
ABCC1	4.58E-16	0.12026893	0.406	0.284	8.10E-12
SOS2	4.75E-16	0.11193298	0.299	0.192	8.39E-12
RAB3GAP1	5.31E-16	0.1211965	0.397	0.284	9.39E-12
RBM19	5.42E-16	0.12746365	0.542	0.42	9.57E-12
NMNAT1	5.78E-16	0.09322901	0.225	0.13	1.02E-11
UHRF1BP1L	6.22E-16	0.12712248	0.547	0.416	1.10E-11
ARL2BP	6.45E-16	0.12681286	0.731	0.632	1.14E-11
ORAI2	6.82E-16	0.14044853	0.757	0.702	1.21E-11
PSMD8	7.04E-16	0.06289292	1	1	1.24E-11
ELMO1	7.66E-16	0.13032431	0.679	0.558	1.35E-11
SSBP1	8.13E-16	0.07639031	0.999	1	1.44E-11
CTNS	8.14E-16	0.11557687	0.286	0.194	1.44E-11
ZEB1	8.28E-16	0.1377721	0.665	0.565	1.46E-11
RPL22L1	8.47E-16	0.15179163	0.997	0.996	1.50E-11
C16orf87	9.63E-16	0.13159844	0.846	0.834	1.70E-11
KPNB1	1.14E-15	0.09333464	0.999	0.999	2.02E-11
RRP12	1.15E-15	0.12212537	0.416	0.297	2.02E-11

FAM241A	1.16E-15	0.13566587	0.445	0.32	2.06E-11
GCNT1	1.36E-15	0.10944922	0.316	0.212	2.41E-11
EIF3F	1.39E-15	0.06710042	1	1	2.46E-11
C12orf45	1.41E-15	0.12538241	0.814	0.742	2.49E-11
NCOA3	1.46E-15	0.14295653	0.701	0.608	2.58E-11
CCNK	1.51E-15	0.11622493	0.862	0.811	2.66E-11
HSPB1	1.53E-15	0.14519709	0.885	0.87	2.71E-11
TNFRSF11A	1.63E-15	0.11652438	0.298	0.208	2.89E-11
CSNK1G1	1.65E-15	0.13472867	0.546	0.435	2.92E-11
ATP6V0A2	1.76E-15	0.13304979	0.616	0.508	3.11E-11
GLS	2.12E-15	0.11614615	0.935	0.92	3.76E-11
GTF2B	2.75E-15	0.10683384	0.921	0.904	4.87E-11
PDLIM5	2.83E-15	0.12473507	0.443	0.342	5.00E-11
C4orf48	3.03E-15	0.09556869	0.99	0.987	5.36E-11
NUDC	3.30E-15	0.08320216	1	1	5.83E-11
CSNK1A1	3.81E-15	0.09195829	0.994	0.995	6.74E-11
CDYL2	3.91E-15	0.09343401	0.227	0.138	6.90E-11
WDR43	3.91E-15	0.12683689	0.962	0.972	6.92E-11
EIF1AX	4.08E-15	0.0969825	0.996	0.998	7.22E-11
PHLPP1	4.12E-15	0.11048361	0.311	0.217	7.28E-11
ZNF654	4.47E-15	0.11024434	0.303	0.208	7.91E-11
COQ2	4.54E-15	0.13330358	0.564	0.459	8.03E-11
RHOC	4.68E-15	0.14136491	0.908	0.883	8.27E-11
PHF19	4.92E-15	0.09594931	1	1	8.69E-11
SMG6	5.93E-15	0.12408625	0.805	0.742	1.05E-10
AL135925.1	6.08E-15	0.09715747	0.238	0.15	1.07E-10
DNAJA4	6.29E-15	0.10828472	0.332	0.234	1.11E-10
MRPL52	6.68E-15	0.07488787	0.999	1	1.18E-10
TRA2A	6.87E-15	0.12333221	0.73	0.645	1.21E-10
IL13	6.88E-15	0.5669031	0.31	0.194	1.22E-10
LETM1	6.91E-15	0.11692891	0.82	0.751	1.22E-10
DHX16	7.26E-15	0.11939019	0.704	0.607	1.28E-10
SLC35E4	7.53E-15	0.11485657	0.332	0.226	1.33E-10
EED	8.38E-15	0.1243725	0.791	0.741	1.48E-10
NUB1	8.42E-15	0.11902357	0.88	0.846	1.49E-10
SLC39A6	8.47E-15	0.12663164	0.576	0.459	1.50E-10
POLR2H	8.58E-15	0.09414408	0.994	0.995	1.52E-10
STAM	9.41E-15	0.13032809	0.601	0.494	1.66E-10
HTATIP2	9.45E-15	0.1201684	0.928	0.922	1.67E-10
PSMD9	9.56E-15	0.11669733	0.6	0.488	1.69E-10
STOML2	9.95E-15	0.08288617	1	0.999	1.76E-10
SBDS	1.25E-14	0.10832134	0.919	0.912	2.22E-10
ESRRA	1.30E-14	0.12195405	0.691	0.584	2.31E-10
QTRT1	1.34E-14	0.12156082	0.567	0.452	2.38E-10
TCTN3	1.36E-14	0.14572559	0.603	0.528	2.41E-10
MORN2	1.68E-14	0.10140906	0.327	0.223	2.98E-10
IL5	1.90E-14	0.55529788	0.346	0.24	3.36E-10
TUFM	1.90E-14	0.07995761	1	1	3.36E-10
CERS6	2.07E-14	0.12424229	0.373	0.285	3.67E-10
PFDN6	2.47E-14	0.09656542	0.972	0.965	4.37E-10
COTL1	2.55E-14	0.08579111	1	1	4.50E-10
STRBP	2.65E-14	0.12848748	0.602	0.498	4.69E-10
PELO	3.66E-14	0.12507764	0.772	0.712	6.47E-10
MTCH1	3.83E-14	0.09588009	0.99	0.986	6.77E-10
EMC7	4.03E-14	0.08891715	0.989	0.988	7.12E-10
EXOSC1	4.20E-14	0.09943344	0.951	0.935	7.42E-10

MBNL1	4.41E-14	0.10719525	0.978	0.974	7.80E-10
ATAD3B	5.11E-14	0.1205384	0.865	0.831	9.04E-10
SERTAD2	5.49E-14	0.11715509	0.397	0.298	9.70E-10
BCLAF1	5.92E-14	0.09432423	0.995	0.996	1.05E-09
DNAJC2	6.44E-14	0.10944454	0.948	0.948	1.14E-09
ETFB	6.44E-14	0.10091203	0.989	0.996	1.14E-09
REEP3	6.51E-14	0.12444781	0.672	0.546	1.15E-09
TNFAIP8	6.98E-14	0.10457979	0.978	0.98	1.23E-09
C11orf98	7.32E-14	0.08923929	0.257	0.169	1.29E-09
PTGER4	7.56E-14	0.14182186	0.451	0.339	1.34E-09
AC016831.7	7.60E-14	0.10471095	0.326	0.228	1.34E-09
AOAH	7.68E-14	0.14641996	0.486	0.378	1.36E-09
PTP4A1	7.74E-14	0.11469925	0.86	0.801	1.37E-09
ZFAS1	8.21E-14	0.1053783	0.999	1	1.45E-09
CIB2	8.41E-14	0.08370414	0.205	0.118	1.49E-09
TMEM173	8.43E-14	0.12265688	0.946	0.956	1.49E-09
PSMD11	9.13E-14	0.09036053	0.996	0.994	1.61E-09
TMEM243	9.93E-14	0.1190581	0.869	0.864	1.76E-09
UBE2D4	9.94E-14	0.10121797	0.354	0.258	1.76E-09
MIB1	1.03E-13	0.12533513	0.511	0.398	1.81E-09
ST8SIA4	1.04E-13	0.12689322	0.818	0.78	1.84E-09
C3orf14	1.04E-13	0.16318268	0.572	0.473	1.85E-09
STAT1	1.05E-13	0.17460192	0.921	0.916	1.85E-09
HSF1	1.08E-13	0.1085427	0.846	0.797	1.90E-09
EIF4H	1.08E-13	0.08607198	0.993	0.996	1.92E-09
ZNF282	1.12E-13	0.11821289	0.412	0.313	1.97E-09
LAPTM5	1.12E-13	0.118879	0.986	0.986	1.98E-09
EIF5B	1.16E-13	0.0792938	1	1	2.05E-09
DCTN2	1.27E-13	0.08885334	0.988	0.976	2.24E-09
UQCRC2	1.28E-13	0.09268933	0.998	0.997	2.27E-09
MAP9	1.40E-13	0.11781398	0.405	0.298	2.47E-09
SMAP2	1.42E-13	0.0964264	0.992	0.994	2.51E-09
BMI1	1.52E-13	0.11301501	0.428	0.326	2.69E-09
DESI1	1.59E-13	0.10337052	0.981	0.984	2.80E-09
LACTB	1.59E-13	0.13395725	0.542	0.432	2.81E-09
SMARCA2	1.73E-13	0.124522	0.876	0.86	3.06E-09
RAD51C	1.75E-13	0.10104107	0.977	0.976	3.09E-09
SLIRP	1.90E-13	0.08618624	0.998	1	3.36E-09
BTBD10	2.01E-13	0.11388698	0.519	0.404	3.55E-09
ARL13B	2.03E-13	0.11132676	0.432	0.326	3.59E-09
AGK	2.18E-13	0.11604952	0.556	0.436	3.85E-09
GCC2	2.23E-13	0.11730445	0.915	0.908	3.94E-09
PDE4A	2.26E-13	0.12332915	0.602	0.497	3.99E-09
RHBDD2	2.28E-13	0.13187628	0.532	0.445	4.03E-09
LRP5	2.43E-13	0.09118231	0.203	0.126	4.30E-09
LAGE3	2.52E-13	0.09095613	0.989	0.991	4.45E-09
SDHB	2.54E-13	0.08845415	0.989	0.984	4.49E-09
DTWD1	3.02E-13	0.11072041	0.433	0.323	5.33E-09
NFIL3	3.09E-13	0.12832757	0.742	0.674	5.47E-09
SMG1	3.12E-13	0.11295818	0.819	0.771	5.51E-09
AC099552.1	3.36E-13	0.13922642	0.218	0.136	5.94E-09
BCS1L	3.55E-13	0.11976395	0.622	0.518	6.28E-09
OXS1	3.56E-13	0.11309605	0.771	0.706	6.29E-09
FAH	4.00E-13	0.1247885	0.834	0.792	7.07E-09
MED21	4.07E-13	0.11301301	0.599	0.475	7.19E-09
SLAMF7	4.42E-13	0.14347124	0.391	0.292	7.81E-09

NDUFAF6	4.65E-13	0.11547478	0.64	0.528	8.22E-09
SRA1	4.79E-13	0.09041992	0.986	0.981	8.46E-09
SKIL	4.97E-13	0.11193555	0.328	0.244	8.78E-09
MRPL42	5.43E-13	0.09328638	0.961	0.964	9.60E-09
MCOLN2	5.45E-13	0.12005835	0.476	0.373	9.63E-09
PHLDA2	5.91E-13	0.209323	0.273	0.198	1.05E-08
LRR61	6.01E-13	0.10425525	0.38	0.279	1.06E-08
GPR68	6.16E-13	0.11932385	0.449	0.348	1.09E-08
NUTM2B-AS1	6.21E-13	0.11478384	0.744	0.691	1.10E-08
TRAF3IP2	6.69E-13	0.10347372	0.288	0.216	1.18E-08
CCNB1IP1	6.79E-13	0.11322968	0.754	0.677	1.20E-08
TIMM50	6.98E-13	0.09922821	0.922	0.897	1.23E-08
WDR46	7.85E-13	0.09867542	0.926	0.911	1.39E-08
ATP10D	8.10E-13	0.09152144	0.241	0.171	1.43E-08
PTMS	8.76E-13	0.14979554	0.786	0.747	1.55E-08
QSOX1	8.90E-13	0.09641031	0.328	0.224	1.57E-08
TIGIT	9.42E-13	0.17265268	0.826	0.825	1.67E-08
DMXL1	1.02E-12	0.10895484	0.39	0.296	1.80E-08
BMS1	1.05E-12	0.1036176	0.934	0.936	1.85E-08
BOLA3	1.06E-12	0.07731373	0.997	0.999	1.88E-08
SMKR1	1.11E-12	0.11400231	0.275	0.185	1.96E-08
HADHB	1.16E-12	0.09737806	0.912	0.892	2.04E-08
YIF1A	1.23E-12	0.09445218	0.95	0.932	2.17E-08
PRR13	1.28E-12	0.07279049	0.999	1	2.26E-08
POLR2A	1.28E-12	0.09593149	0.97	0.968	2.27E-08
OSTF1	1.30E-12	0.09167614	0.996	0.996	2.29E-08
DDX27	1.43E-12	0.09220929	0.96	0.955	2.52E-08
C1QBP	1.43E-12	0.10560327	1	1	2.54E-08
CDC123	1.44E-12	0.07992546	0.997	0.997	2.55E-08
NAB1	1.45E-12	0.09229773	0.289	0.203	2.56E-08
AUH	1.46E-12	0.11960061	0.63	0.512	2.58E-08
CDC34	1.47E-12	0.10173075	0.819	0.759	2.60E-08
SPTLC1	1.49E-12	0.10736802	0.752	0.674	2.63E-08
SLC39A14	1.57E-12	0.11038281	0.356	0.269	2.78E-08
NMT2	1.69E-12	0.12288167	0.501	0.395	2.98E-08
SLC39A1	1.71E-12	0.10677422	0.78	0.726	3.02E-08
NAP1L4	1.79E-12	0.08218067	0.997	0.999	3.17E-08
PIDD1	1.86E-12	0.11997453	0.478	0.384	3.28E-08
PRDM2	1.92E-12	0.11562511	0.728	0.662	3.40E-08
TNFRSF8	1.95E-12	0.15018811	0.516	0.44	3.44E-08
ALYREF	2.04E-12	0.07890771	0.995	0.997	3.61E-08
ELOB	2.17E-12	0.05136816	1	1	3.83E-08
PSMA7	2.26E-12	0.0467043	1	1	4.00E-08
OLA1	2.27E-12	0.0898264	0.983	0.981	4.02E-08
U2AF1L4	2.28E-12	0.11706998	0.46	0.37	4.04E-08
AIFM1	2.33E-12	0.0940502	0.931	0.909	4.12E-08
PDCD4	2.41E-12	0.13673073	0.577	0.479	4.26E-08
PKM	2.55E-12	0.08417678	0.999	1	4.51E-08
TRIP11	2.86E-12	0.11851499	0.787	0.731	5.06E-08
TNFRSF4	2.89E-12	0.381305	0.278	0.198	5.12E-08
CISD2	2.90E-12	0.08655148	0.982	0.986	5.12E-08
CD6	2.96E-12	0.13079532	0.797	0.757	5.23E-08
SMARCB1	3.03E-12	0.08273584	0.988	0.987	5.36E-08
LRIF1	3.13E-12	0.11848697	0.677	0.563	5.54E-08
ACTG1	3.16E-12	0.06091059	1	1	5.58E-08
EIF4A2	3.25E-12	0.10833456	0.936	0.93	5.74E-08

CCSER2	3.30E-12	0.12378058	0.633	0.54	5.83E-08
ARID3B	3.37E-12	0.10948046	0.488	0.378	5.95E-08
GTF2I	3.58E-12	0.09698812	0.951	0.936	6.32E-08
ETS1	3.64E-12	0.10997444	0.966	0.949	6.44E-08
BRD9	3.65E-12	0.10284881	0.803	0.737	6.44E-08
TTLL5	3.89E-12	0.0828192	0.249	0.167	6.87E-08
DNAJC21	3.96E-12	0.08575058	0.989	0.989	7.01E-08
RPS27A	4.03E-12	0.03801653	1	1	7.12E-08
ENY2	4.12E-12	0.06925402	0.998	0.997	7.28E-08
NCOA1	4.34E-12	0.11069276	0.458	0.367	7.67E-08
TARSL2	4.38E-12	0.10948824	0.428	0.334	7.75E-08
CITED2	4.45E-12	0.1392024	0.636	0.558	7.87E-08
GAMT	4.64E-12	0.12309769	0.841	0.812	8.21E-08
PGAM1	5.08E-12	0.07363416	1	1	8.97E-08
LIAS	5.22E-12	0.10747895	0.611	0.509	9.22E-08
CSE1L	5.48E-12	0.0997056	0.908	0.886	9.69E-08
SNX10	5.93E-12	0.10215615	0.902	0.892	1.05E-07
BTF3	6.54E-12	0.04851106	1	1	1.16E-07
CCL3	6.72E-12	0.57407387	0.356	0.233	1.19E-07
PPP2CB	6.88E-12	0.10306142	0.466	0.378	1.22E-07
CD226	6.93E-12	0.12305808	0.658	0.555	1.23E-07
HNRNPLL	7.27E-12	0.10807818	0.659	0.553	1.28E-07
DDX1	7.33E-12	0.09177811	0.962	0.962	1.29E-07
ZCCHC2	7.67E-12	0.11043483	0.518	0.422	1.36E-07
CGAS	7.98E-12	0.10860151	0.858	0.851	1.41E-07
PIGX	8.16E-12	0.09727503	0.906	0.897	1.44E-07
EIF3I	8.42E-12	0.05916328	1	1	1.49E-07
SPATS2	8.76E-12	0.11087939	0.563	0.476	1.55E-07
MYBBP1A	8.76E-12	0.11167157	0.486	0.39	1.55E-07
TMEM30A	8.82E-12	0.11436111	0.559	0.459	1.56E-07
NCEH1	8.93E-12	0.09147689	0.306	0.219	1.58E-07
GRK3	9.15E-12	0.11086955	0.378	0.286	1.62E-07
RNF121	9.58E-12	0.1001657	0.385	0.288	1.69E-07
SLC9A7	1.01E-11	0.09046561	0.31	0.214	1.79E-07
IL2RB	1.02E-11	0.11102435	0.904	0.882	1.81E-07
AIFM2	1.08E-11	0.10915028	0.659	0.545	1.90E-07
ACTA2	1.14E-11	0.12884162	0.395	0.301	2.02E-07
TOMM22	1.14E-11	0.08411642	0.997	0.998	2.02E-07
APOBEC3C	1.17E-11	0.10776429	0.948	0.933	2.06E-07
ESYT2	1.19E-11	0.12094216	0.606	0.518	2.10E-07
SLAIN1	1.25E-11	0.10467403	0.413	0.329	2.20E-07
TMEM68	1.31E-11	0.10129898	0.408	0.326	2.31E-07
PINK1	1.32E-11	0.07961763	0.21	0.129	2.33E-07
STAG1	1.39E-11	0.10599524	0.744	0.654	2.45E-07
CRK	1.41E-11	0.09255497	0.322	0.229	2.50E-07
NFKB2	1.44E-11	0.12871211	0.524	0.406	2.55E-07
SUSD6	1.44E-11	0.09834986	0.383	0.283	2.55E-07
TRIM26	1.47E-11	0.11014602	0.662	0.569	2.59E-07
PSMC6	1.59E-11	0.08204457	0.986	0.986	2.81E-07
SPG7	1.59E-11	0.10369336	0.74	0.67	2.82E-07
SH2D2A	1.60E-11	0.10647514	0.926	0.91	2.83E-07
ANKRA2	1.64E-11	0.0938516	0.298	0.208	2.89E-07
TRIP6	1.70E-11	0.11790717	0.361	0.283	3.01E-07
ADI1	1.72E-11	0.10014594	0.909	0.89	3.05E-07
ASH1L	1.76E-11	0.11625495	0.636	0.546	3.10E-07
PPM1D	1.79E-11	0.09174615	0.284	0.204	3.17E-07

RAPGEF1	1.83E-11	0.11119474	0.665	0.574	3.23E-07
BRMS1L	1.83E-11	0.08569628	0.28	0.204	3.24E-07
RABGGTB	1.83E-11	0.10706057	0.704	0.621	3.24E-07
SF3B6	1.91E-11	0.06656677	1	1	3.37E-07
IFRD1	1.94E-11	0.11056705	0.515	0.424	3.43E-07
CCDC34	2.07E-11	0.10554003	0.874	0.862	3.66E-07
RELL1	2.15E-11	0.0890546	0.307	0.215	3.81E-07
POLR3H	2.23E-11	0.11097709	0.742	0.676	3.94E-07
MPZL3	2.25E-11	0.09778645	0.326	0.24	3.98E-07
NOC3L	2.25E-11	0.11417762	0.825	0.797	3.98E-07
LRRFIP2	2.28E-11	0.10448979	0.816	0.771	4.03E-07
KIF5C	2.32E-11	0.1108181	0.428	0.326	4.10E-07
PACSIN2	2.56E-11	0.10119412	0.439	0.35	4.53E-07
TRAF3IP1	2.68E-11	0.0992643	0.344	0.259	4.73E-07
TNPO1	2.69E-11	0.100242	0.856	0.832	4.76E-07
IFITM1	2.70E-11	0.12421887	0.545	0.471	4.77E-07
OXCT1	2.70E-11	0.08503535	0.984	0.981	4.78E-07
MRPL49	2.78E-11	0.10605019	0.697	0.63	4.91E-07
TGIF1	2.82E-11	0.08169138	0.218	0.143	4.98E-07
REV3L	2.85E-11	0.114762	0.55	0.464	5.04E-07
C7orf50	3.05E-11	0.09242706	0.918	0.894	5.39E-07
LAG3	3.26E-11	0.14108606	0.721	0.685	5.76E-07
SNRPC	3.31E-11	0.06370385	0.999	1	5.84E-07
NUDT5	3.32E-11	0.07064322	0.998	0.996	5.87E-07
HSP90AB1	3.35E-11	0.09003596	1	1	5.92E-07
HNRNPAB	3.41E-11	0.08297175	0.999	0.999	6.02E-07
SLC35D1	3.56E-11	0.09240837	0.355	0.264	6.30E-07
WDR1	3.59E-11	0.06337529	0.999	1	6.35E-07
ANAPC11	3.99E-11	0.07278576	0.999	0.998	7.05E-07
CSTF3	4.24E-11	0.10710146	0.616	0.522	7.50E-07
PNMA1	4.62E-11	0.09391788	0.378	0.294	8.16E-07
TOR1A	4.81E-11	0.08885481	0.92	0.899	8.51E-07
CXorf40A	4.90E-11	0.08496967	0.297	0.209	8.65E-07
ARID3A	5.16E-11	0.10752164	0.423	0.336	9.13E-07
ATAD1	5.26E-11	0.10101653	0.613	0.514	9.29E-07
DUSP10	5.34E-11	0.09347622	0.305	0.22	9.43E-07
DAAM1	5.36E-11	0.11731642	0.475	0.367	9.48E-07
HAGH	5.39E-11	0.09388448	0.891	0.864	9.52E-07
DYNC2L1	5.41E-11	0.08994485	0.299	0.209	9.56E-07
EMG1	5.74E-11	0.09669877	0.919	0.923	1.01E-06
TAF1D	6.03E-11	0.09296482	0.981	0.984	1.07E-06
ZFP36L1	6.12E-11	0.1353987	0.488	0.406	1.08E-06
DCUN1D3	6.13E-11	0.07946654	0.219	0.142	1.08E-06
HBS1L	6.23E-11	0.0947658	0.908	0.872	1.10E-06
ITPRIPL2	6.27E-11	0.08575767	0.229	0.158	1.11E-06
RPIA	6.27E-11	0.09408487	0.886	0.868	1.11E-06
AKAP17A	6.44E-11	0.10985016	0.711	0.65	1.14E-06
MTIF2	6.48E-11	0.10427316	0.734	0.671	1.15E-06
MRPL1	6.77E-11	0.0887027	0.947	0.942	1.20E-06
RGS1	7.03E-11	0.1239651	0.205	0.12	1.24E-06
TMEM99	7.30E-11	0.09663436	0.384	0.291	1.29E-06
EAF2	7.61E-11	0.11456419	0.768	0.718	1.35E-06
GFOD2	7.65E-11	0.08195293	0.296	0.213	1.35E-06
FAM229B	7.90E-11	0.07157852	0.206	0.136	1.40E-06
MT1X	8.12E-11	0.09612029	0.96	0.956	1.43E-06
TTC4	8.30E-11	0.08232976	0.306	0.218	1.47E-06



KIF1B	8.39E-11	0.10403639	0.417	0.328	1.48E-06
PSMD2	8.51E-11	0.06664433	0.998	0.998	1.50E-06
PRKACA	8.89E-11	0.09715423	0.486	0.388	1.57E-06
HIPK2	8.97E-11	0.11122564	0.365	0.27	1.59E-06
PPIL1	9.09E-11	0.09645146	0.822	0.766	1.61E-06
ETV6	9.25E-11	0.09400262	0.36	0.273	1.64E-06
METTL8	9.56E-11	0.10467691	0.476	0.381	1.69E-06
PPFIA1	1.02E-10	0.10366258	0.552	0.45	1.81E-06
SNX9	1.08E-10	0.11475697	0.432	0.346	1.92E-06
CCT6A	1.10E-10	0.0727232	0.999	1	1.95E-06
NUDT4	1.12E-10	0.1045109	0.537	0.436	1.98E-06
FBXW11	1.21E-10	0.10015186	0.539	0.437	2.14E-06
ZNF326	1.26E-10	0.09789083	0.882	0.847	2.23E-06
BAZ1A	1.28E-10	0.0840215	0.984	0.989	2.26E-06
FARSA	1.40E-10	0.08871023	0.929	0.921	2.47E-06
MYO1C	1.46E-10	0.09520366	0.358	0.265	2.59E-06
PCNP	1.49E-10	0.08068688	0.974	0.974	2.63E-06
POLR1C	1.49E-10	0.09815355	0.491	0.384	2.63E-06
TGFBR3	1.51E-10	0.10712274	0.253	0.18	2.66E-06
TERF2IP	1.55E-10	0.07487692	0.993	0.994	2.74E-06
TCP1	1.56E-10	0.0767655	0.999	0.999	2.77E-06
YWHAQ	1.64E-10	0.06411547	0.999	1	2.90E-06
DPCD	1.65E-10	0.08185969	0.289	0.206	2.92E-06
HUWE1	1.72E-10	0.09184153	0.958	0.959	3.03E-06
GAB3	1.73E-10	0.09434406	0.317	0.235	3.05E-06
IFT46	1.78E-10	0.07343638	0.243	0.166	3.15E-06
AIM2	1.83E-10	0.13341935	0.497	0.394	3.23E-06
ZNRF1	1.86E-10	0.10779135	0.508	0.42	3.28E-06
KIF1BP	1.87E-10	0.09933117	0.481	0.378	3.30E-06
DDI2	1.91E-10	0.09233035	0.372	0.266	3.38E-06
TP53I13	2.05E-10	0.09926811	0.64	0.548	3.62E-06
DYNC1H1	2.12E-10	0.09162483	0.965	0.97	3.74E-06
STK38L	2.14E-10	0.09244196	0.367	0.276	3.78E-06
CHORDC1	2.16E-10	0.09511259	0.952	0.951	3.82E-06
RIC3	2.37E-10	0.08906326	0.265	0.192	4.18E-06
TAX1BP1	2.48E-10	0.09342604	0.966	0.955	4.39E-06
CFLAR	2.53E-10	0.10572721	0.886	0.863	4.47E-06
AAMP	2.67E-10	0.0877745	0.893	0.867	4.72E-06
EIF3D	2.75E-10	0.06557255	1	1	4.86E-06
GFM1	2.77E-10	0.09803341	0.722	0.654	4.89E-06
SAMD10	2.79E-10	0.0853515	0.334	0.236	4.93E-06
GLIPR1	2.79E-10	0.1133717	0.817	0.775	4.94E-06
ADIPOR1	2.85E-10	0.0883223	0.872	0.838	5.05E-06
ZNF880	2.89E-10	0.10172996	0.405	0.315	5.10E-06
NEAT1	2.95E-10	0.17081577	0.97	0.976	5.21E-06
PSMC4	3.03E-10	0.06801939	0.996	0.997	5.36E-06
NUTM2A-AS1	3.08E-10	0.09220334	0.425	0.33	5.45E-06
NDFIP1	3.17E-10	0.10721501	0.812	0.793	5.61E-06
SLCO4A1	3.24E-10	0.10154283	0.693	0.605	5.73E-06
IRGQ	3.25E-10	0.0717782	0.214	0.143	5.74E-06
RRP9	3.27E-10	0.10581733	0.74	0.701	5.78E-06
RPS3	3.38E-10	0.03475063	1	1	5.98E-06
LETM2	3.58E-10	0.07664444	0.209	0.139	6.33E-06
CRYBG1	3.64E-10	0.09870577	0.824	0.802	6.44E-06
ZZEF1	3.65E-10	0.0907245	0.393	0.301	6.45E-06
CD96	3.65E-10	0.10620736	0.9	0.893	6.46E-06

FDX1	3.72E-10	0.09072555	0.972	0.973	6.58E-06
AHCYL2	3.73E-10	0.07455016	0.2	0.138	6.59E-06
STAMBP	3.78E-10	0.10035963	0.679	0.59	6.69E-06
UBR3	3.78E-10	0.08515149	0.315	0.226	6.69E-06
TLE3	3.89E-10	0.10092798	0.46	0.361	6.88E-06
VMP1	4.10E-10	0.09879	0.948	0.938	7.24E-06
UBFD1	4.11E-10	0.09510085	0.478	0.388	7.26E-06
SSH1	4.25E-10	0.09212685	0.372	0.281	7.50E-06
BATF	4.38E-10	0.0975499	0.953	0.949	7.74E-06
ANXA7	4.41E-10	0.07688274	0.977	0.978	7.79E-06
FAM222B	4.83E-10	0.07720269	0.265	0.189	8.54E-06
SLC3A2	5.28E-10	0.10425226	0.988	0.991	9.33E-06
STIP1	5.43E-10	0.0720383	0.998	0.999	9.60E-06
FBRS	5.53E-10	0.09751642	0.684	0.595	9.78E-06
VDAC3	5.62E-10	0.06256114	0.999	1	9.93E-06
SELENOM	5.78E-10	0.07430473	0.204	0.13	1.02E-05
MT1G	5.83E-10	0.16789394	0.25	0.161	1.03E-05
TAOK1	5.95E-10	0.10102396	0.483	0.383	1.05E-05
ABI2	6.04E-10	0.09955208	0.529	0.431	1.07E-05
SCOC	6.30E-10	0.09449816	0.737	0.663	1.11E-05
SUDS3	6.32E-10	0.09209962	0.792	0.724	1.12E-05
HSD17B10	6.46E-10	0.06792041	0.999	0.999	1.14E-05
PON2	6.50E-10	0.10244484	0.279	0.205	1.15E-05
CSDE1	6.81E-10	0.06572753	0.997	0.998	1.20E-05
MAP3K2	6.82E-10	0.10116448	0.656	0.566	1.21E-05
EIF3A	6.86E-10	0.06789464	0.999	1	1.21E-05
STK11	6.91E-10	0.09697552	0.662	0.58	1.22E-05
PRADC1	7.13E-10	0.09560494	0.655	0.562	1.26E-05
NAT10	7.14E-10	0.10287775	0.625	0.517	1.26E-05
AP1S1	7.80E-10	0.08059342	0.961	0.96	1.38E-05
SLC52A2	7.81E-10	0.08599804	0.888	0.849	1.38E-05
ADO	7.92E-10	0.08253663	0.294	0.213	1.40E-05
SLC25A20	7.94E-10	0.09056082	0.381	0.29	1.40E-05
SENP6	7.94E-10	0.09945976	0.724	0.662	1.40E-05
EIF3G	8.77E-10	0.0565601	1	1	1.55E-05
CCDC88A	8.85E-10	0.10886643	0.391	0.31	1.56E-05
ADRM1	9.12E-10	0.06511054	1	0.999	1.61E-05
SPATA2	9.22E-10	0.07879505	0.311	0.233	1.63E-05
SLC25A6	9.41E-10	0.05032421	1	1	1.66E-05
CLPTM1L	9.41E-10	0.08106288	0.969	0.971	1.66E-05
HMCES	9.55E-10	0.09689978	0.719	0.649	1.69E-05
MICAL3	9.59E-10	0.08496367	0.322	0.23	1.70E-05
NOP58	9.74E-10	0.07613503	0.996	0.997	1.72E-05
KDSR	1.05E-09	0.10621697	0.545	0.446	1.85E-05
REPS1	1.06E-09	0.0924545	0.492	0.41	1.87E-05
UPF1	1.06E-09	0.09772689	0.576	0.477	1.88E-05
MLEC	1.07E-09	0.07292199	0.994	0.99	1.88E-05
GLA	1.15E-09	0.09472413	0.722	0.674	2.03E-05
GCN1	1.17E-09	0.09528849	0.534	0.433	2.07E-05
PKN2	1.18E-09	0.09559512	0.45	0.362	2.09E-05
CPPED1	1.18E-09	0.10592433	0.71	0.627	2.09E-05
MED19	1.18E-09	0.09801445	0.614	0.518	2.09E-05
IFT74	1.18E-09	0.09825166	0.48	0.386	2.09E-05
P4HA2	1.20E-09	0.08904756	0.278	0.206	2.11E-05
TRIM28	1.22E-09	0.07443894	0.992	0.993	2.15E-05
CSNK1G3	1.26E-09	0.0957972	0.472	0.38	2.22E-05

SPINT2	1.33E-09	0.13924466	0.265	0.189	2.36E-05
PUM1	1.34E-09	0.09737416	0.755	0.694	2.36E-05
CTU2	1.35E-09	0.09481688	0.586	0.467	2.38E-05
OTUD1	1.38E-09	0.07806303	0.214	0.142	2.44E-05
SERAC1	1.40E-09	0.07701005	0.247	0.165	2.48E-05
TM2D3	1.41E-09	0.09421907	0.604	0.509	2.49E-05
RHOA	1.44E-09	0.05290738	1	1	2.55E-05
DNAAF2	1.51E-09	0.09598005	0.498	0.417	2.67E-05
LRIG1	1.54E-09	0.07977242	0.279	0.2	2.73E-05
SLC2A8	1.63E-09	0.09298433	0.386	0.299	2.88E-05
SDC4	1.63E-09	0.07864313	0.217	0.147	2.89E-05
SNHG8	1.66E-09	0.08240774	0.992	0.993	2.93E-05
PHACTR4	1.66E-09	0.09849818	0.626	0.538	2.93E-05
NOTCH1	1.66E-09	0.09157412	0.406	0.314	2.93E-05
LSM11	1.66E-09	0.07809586	0.3	0.212	2.94E-05
HIP1R	1.69E-09	0.08251801	0.327	0.248	2.99E-05
CCL4	1.70E-09	0.6205642	0.235	0.169	3.00E-05
ETF1	1.70E-09	0.08338911	0.962	0.958	3.01E-05
MRPL21	1.79E-09	0.06834225	0.997	0.994	3.16E-05
CREG1	1.83E-09	0.09201586	0.406	0.316	3.24E-05
C12orf57	1.98E-09	0.09000433	0.982	0.976	3.50E-05
CSTF2	2.01E-09	0.09268475	0.58	0.489	3.55E-05
SKAP2	2.11E-09	0.10563019	0.592	0.504	3.73E-05
VPS37A	2.20E-09	0.09042155	0.491	0.397	3.90E-05
PRCP	2.26E-09	0.08509157	0.351	0.272	3.99E-05
PAQR3	2.27E-09	0.07255397	0.234	0.163	4.01E-05
ILF2	2.29E-09	0.06263584	1	1	4.04E-05
TXNL4B	2.36E-09	0.0861034	0.408	0.317	4.17E-05
MYO1G	2.43E-09	0.07414042	0.996	0.995	4.29E-05
PDCD11	2.55E-09	0.09761025	0.788	0.746	4.50E-05
MRPS33	2.62E-09	0.07059665	0.99	0.992	4.63E-05
NFKBIB	2.68E-09	0.08241367	0.865	0.844	4.74E-05
TICAM1	2.79E-09	0.08307305	0.351	0.267	4.93E-05
MRPL23	2.81E-09	0.06786981	0.994	0.989	4.96E-05
NSMCE2	2.83E-09	0.10462721	0.73	0.681	5.00E-05
ACO16831.1	2.84E-09	0.07511621	0.222	0.15	5.02E-05
SELENOO	2.93E-09	0.08677674	0.397	0.307	5.18E-05
UQCRH	2.99E-09	0.04346691	1	1	5.28E-05
CD84	3.03E-09	0.11220425	0.595	0.524	5.36E-05
TNIK	3.05E-09	0.10421961	0.659	0.562	5.39E-05
C16orf45	3.22E-09	0.08740415	0.34	0.264	5.70E-05
RYBP	3.28E-09	0.10473948	0.54	0.468	5.80E-05
FGFR1	3.29E-09	0.12581764	0.639	0.571	5.81E-05
DDOST	3.37E-09	0.07283355	0.982	0.975	5.96E-05
LARP4	3.61E-09	0.08937929	0.831	0.783	6.39E-05
EI24	3.67E-09	0.09362526	0.762	0.697	6.49E-05
MPC1	3.69E-09	0.08412415	0.894	0.871	6.52E-05
CXCR4	3.75E-09	0.12072809	0.809	0.802	6.63E-05
WBP11	3.78E-09	0.0745455	0.973	0.974	6.68E-05
DUSP18	3.78E-09	0.0713309	0.226	0.149	6.68E-05
TBC1D13	3.87E-09	0.06879131	0.239	0.156	6.84E-05
PRDX3	4.01E-09	0.07132751	0.998	1	7.10E-05
TVP23B	4.03E-09	0.0756625	0.294	0.22	7.13E-05
UBN2	4.05E-09	0.0735439	0.247	0.18	7.16E-05
IQCB1	4.11E-09	0.09324958	0.551	0.459	7.27E-05
VDAC1	4.29E-09	0.06777955	0.999	1	7.58E-05

GNPAT	4.30E-09	0.08854708	0.72	0.629	7.61E-05
APAF1	4.32E-09	0.09165949	0.44	0.354	7.64E-05
CEP85L	4.33E-09	0.10131123	0.532	0.456	7.65E-05
SGMS1	4.35E-09	0.09234052	0.379	0.307	7.69E-05
CASK	4.42E-09	0.09356878	0.424	0.349	7.82E-05
TRAF3	4.43E-09	0.09461749	0.59	0.502	7.83E-05
TCOF1	4.50E-09	0.08477026	0.943	0.932	7.95E-05
SPAG9	4.63E-09	0.09346518	0.713	0.65	8.19E-05
LSM12	4.66E-09	0.07856728	0.958	0.949	8.24E-05
PSEN2	4.70E-09	0.06451694	0.2	0.14	8.31E-05
MED6	4.92E-09	0.0819808	0.864	0.83	8.70E-05
SMG5	4.94E-09	0.08020444	0.336	0.262	8.73E-05
NCLN	4.97E-09	0.09229516	0.643	0.547	8.79E-05
PASK	4.98E-09	0.08639523	0.298	0.222	8.81E-05
SMARCC1	4.99E-09	0.07862184	0.964	0.965	8.83E-05
PPME1	5.08E-09	0.08945618	0.457	0.371	8.98E-05
RALGDS	5.15E-09	0.09919668	0.553	0.464	9.10E-05
RPL19	5.17E-09	0.03366406	1	1	9.14E-05
OAT	5.25E-09	0.09362079	0.578	0.496	9.28E-05
GDAP1	5.38E-09	0.07871064	0.312	0.232	9.51E-05
B3GALNT2	5.51E-09	0.06511469	0.215	0.15	9.74E-05
PER1	5.53E-09	0.06771817	0.239	0.165	9.77E-05
ARL6IP5	5.58E-09	0.07108916	0.998	0.998	9.86E-05
UBAP2L	5.65E-09	0.08351107	0.844	0.797	9.99E-05
CARS	5.76E-09	0.09362855	0.902	0.892	0.000102
GLRX3	6.09E-09	0.06988038	0.992	0.992	0.000108
KLHL18	6.26E-09	0.09086351	0.502	0.394	0.000111
COPS2	6.43E-09	0.0806517	0.914	0.908	0.000114
COQ8A	6.47E-09	0.08486925	0.369	0.285	0.000114
DEF8	6.69E-09	0.08932438	0.707	0.628	0.000118
PLEKHB2	6.84E-09	0.08139812	0.911	0.903	0.000121
RAD21	6.87E-09	0.08166832	0.998	0.999	0.000122
5-Mar	6.90E-09	0.08924724	0.599	0.503	0.000122
ITPR2	6.99E-09	0.10428089	0.444	0.36	0.000124
CASC4	7.05E-09	0.09307221	0.634	0.546	0.000125
SMPD4	7.06E-09	0.08774539	0.726	0.659	0.000125
LRWD1	7.11E-09	0.09103908	0.595	0.49	0.000126
PRKAR2A	7.33E-09	0.09328071	0.709	0.65	0.00013
FAM216A	7.42E-09	0.1076079	0.642	0.562	0.000131
GALNT2	7.48E-09	0.08379918	0.334	0.252	0.000132
PCM1	7.62E-09	0.08571861	0.932	0.944	0.000135
NPEPPS	7.98E-09	0.09119024	0.698	0.622	0.000141
CNIH4	7.99E-09	0.07792958	0.956	0.948	0.000141
AC058791.1	8.12E-09	0.10763522	0.523	0.438	0.000144
CCDC51	8.23E-09	0.08893869	0.636	0.549	0.000145
C11orf24	8.36E-09	0.09437294	0.61	0.493	0.000148
METTL2A	8.36E-09	0.09042607	0.61	0.524	0.000148
THG1L	8.57E-09	0.09102727	0.617	0.516	0.000152
MXD4	8.59E-09	0.11485407	0.438	0.38	0.000152
FURIN	8.74E-09	0.11466206	0.844	0.822	0.000155
SDCBP	9.02E-09	0.09751981	0.842	0.816	0.000159
OSBPL3	9.51E-09	0.09282932	0.532	0.444	0.000168
RTCB	9.51E-09	0.06947474	0.985	0.978	0.000168
ZMAT5	9.62E-09	0.08972701	0.538	0.444	0.00017
RBPJ	9.79E-09	0.10679797	0.931	0.929	0.000173
GTF2H2C	1.04E-08	0.06722531	0.25	0.178	0.000185

DKC1	1.10E-08	0.08845112	0.981	0.99	0.000195
GFPT1	1.11E-08	0.09362526	0.623	0.54	0.000196
ING4	1.12E-08	0.07737998	0.289	0.214	0.000197
LCMT1	1.14E-08	0.08074507	0.827	0.765	0.000202
HGS	1.16E-08	0.0885678	0.619	0.53	0.000205
CHD1	1.16E-08	0.08582973	0.867	0.854	0.000206
AIMP1	1.17E-08	0.07360359	0.968	0.976	0.000206
ZNF626	1.19E-08	0.06522604	0.205	0.136	0.00021
TRAP1	1.22E-08	0.0862885	0.937	0.922	0.000215
AHCY	1.24E-08	0.07694028	0.967	0.96	0.000218
UPF2	1.30E-08	0.08161483	0.891	0.88	0.00023
ITGAE	1.32E-08	0.07937226	0.926	0.921	0.000233
ST3GAL1	1.33E-08	0.08708742	0.86	0.842	0.000236
HIP1	1.34E-08	0.06732994	0.206	0.144	0.000237
GOLGA4	1.38E-08	0.09515065	0.92	0.917	0.000244
SESN2	1.42E-08	0.10317265	0.299	0.216	0.000251
PARL	1.43E-08	0.07932062	0.892	0.881	0.000252
NEU1	1.46E-08	0.09436276	0.552	0.466	0.000258
LRRC75A	1.47E-08	0.10281718	0.382	0.31	0.00026
TRIT1	1.47E-08	0.07861593	0.358	0.276	0.00026
NDUFV3	1.56E-08	0.07810889	0.885	0.882	0.000276
EPB41L4A-AS1	1.58E-08	0.0964467	0.513	0.422	0.000279
RUNDC1	1.63E-08	0.07579384	0.288	0.21	0.000288
ELAVL1	1.71E-08	0.07038935	0.976	0.975	0.000302
UBR5	1.72E-08	0.09385252	0.673	0.6	0.000303
DNMT3A	1.72E-08	0.09182619	0.408	0.348	0.000304
RHOH	1.72E-08	0.09177796	0.85	0.825	0.000305
ARIH1	1.73E-08	0.08918242	0.541	0.446	0.000305
MRRF	1.74E-08	0.08384316	0.475	0.392	0.000308
BRWD1	1.76E-08	0.08911148	0.544	0.458	0.000311
CNEP1R1	1.83E-08	0.06816138	0.254	0.186	0.000324
AC092069.1	1.89E-08	0.0713309	0.212	0.147	0.000334
RPLP1	1.92E-08	0.03044071	1	1	0.00034
CLEC16A	1.94E-08	0.07522342	0.299	0.218	0.000342
RNF130	1.96E-08	0.06700758	0.22	0.152	0.000347
SMARCA5	2.06E-08	0.07543757	0.984	0.984	0.000363
FOXO3	2.07E-08	0.07392219	0.251	0.187	0.000366
COX20	2.12E-08	0.07143126	0.987	0.986	0.000375
C18orf32	2.13E-08	0.06151183	0.21	0.146	0.000376
GRINA	2.22E-08	0.07499673	0.279	0.19	0.000393
PRPF31	2.24E-08	0.06687267	0.99	0.984	0.000396
PTCD1	2.25E-08	0.06890718	0.276	0.204	0.000397
FBL	2.31E-08	0.06452849	0.996	0.999	0.000408
PCBP2	2.33E-08	0.05229597	1	1	0.000413
AAED1	2.45E-08	0.08899988	0.494	0.403	0.000433
ITPA	2.49E-08	0.07134478	0.962	0.957	0.00044
TM9SF2	2.57E-08	0.08343867	0.862	0.86	0.000455
TNK2	2.66E-08	0.0722169	0.283	0.201	0.000471
SBNO1	2.74E-08	0.07776472	0.91	0.906	0.000485
AKIRIN1	2.84E-08	0.08409124	0.892	0.873	0.000502
PLEKHA5	2.85E-08	0.08937231	0.333	0.266	0.000504
ARIH2	2.93E-08	0.07601811	0.917	0.897	0.000517
HAUS6	2.93E-08	0.08599495	0.75	0.687	0.000518
ARHGAP10	3.07E-08	0.09475017	0.586	0.502	0.000543
IFRD2	3.08E-08	0.08472188	0.934	0.923	0.000544
SP110	3.08E-08	0.08838289	0.922	0.924	0.000544

POLR2F	3.08E-08	0.06636054	0.986	0.992	0.000545
SUPT5H	3.17E-08	0.07833595	0.908	0.897	0.000561
HTT	3.19E-08	0.08859691	0.606	0.514	0.000563
LRBA	3.26E-08	0.09399813	0.57	0.482	0.000576
GAS2L1	3.35E-08	0.07332793	0.229	0.159	0.000592
AFF4	3.46E-08	0.08923113	0.534	0.443	0.000612
MAEA	3.50E-08	0.08526655	0.672	0.582	0.000619
SLC12A6	3.53E-08	0.08034913	0.302	0.223	0.000623
RPP40	3.56E-08	0.08212296	0.413	0.329	0.00063
NENF	3.60E-08	0.0699222	0.963	0.959	0.000636
INTS13	3.66E-08	0.08401337	0.772	0.705	0.000647
PGAP1	3.70E-08	0.09512734	0.443	0.378	0.000653
FRMD4B	3.70E-08	0.1069874	0.818	0.809	0.000653
NT5DC1	3.72E-08	0.08593348	0.802	0.769	0.000658
AC008105.3	3.76E-08	0.09076581	0.37	0.296	0.000664
ERAL1	4.05E-08	0.08201786	0.669	0.586	0.000716
GTF2E2	4.08E-08	0.07653734	0.886	0.867	0.000721
MRPL22	4.08E-08	0.06098027	0.994	0.997	0.000722
UTP4	4.17E-08	0.08743027	0.72	0.672	0.000736
COX17	4.19E-08	0.05640082	0.998	0.998	0.000741
TTC38	4.29E-08	0.06957167	0.274	0.193	0.000759
HADHA	4.38E-08	0.06741898	0.994	0.99	0.000775
MCCC2	4.49E-08	0.08650344	0.624	0.521	0.000794
KDM5B	4.59E-08	0.10137722	0.413	0.33	0.00081
HMG4	4.69E-08	0.06855476	0.243	0.179	0.000828
STK26	4.77E-08	0.08971774	0.684	0.614	0.000842
TPD52L2	4.78E-08	0.08601506	0.657	0.576	0.000845
SARS	4.80E-08	0.07508079	0.985	0.983	0.000849
SEC16A	4.83E-08	0.08867883	0.591	0.49	0.000854
PPAT	4.84E-08	0.09233657	0.698	0.63	0.000856
XPNPEP3	4.92E-08	0.07222072	0.317	0.238	0.00087
TNFAIP1	4.97E-08	0.06122346	0.219	0.154	0.000878
YIPF6	5.12E-08	0.08686417	0.576	0.491	0.000905
KRR1	5.14E-08	0.0684616	0.985	0.985	0.000909
LEO1	5.17E-08	0.0814702	0.95	0.951	0.000914
MED1	5.25E-08	0.08785028	0.645	0.58	0.000928
IFT43	5.26E-08	0.0663297	0.245	0.176	0.00093
ADGRE5	5.34E-08	0.09457401	0.863	0.848	0.000944
BBS4	5.58E-08	0.07338109	0.305	0.236	0.000986
OSGEP	5.84E-08	0.07509045	0.839	0.817	0.001033
AK6	5.85E-08	0.07828694	0.947	0.951	0.001033
ATP5MD	5.88E-08	0.0458075	1	1	0.00104
DNAJB2	6.00E-08	0.08113291	0.385	0.294	0.00106
DAD1	6.05E-08	0.05538514	0.999	1	0.00107
ORC6	6.08E-08	0.08000397	0.929	0.938	0.001075
RFX7	6.42E-08	0.07275382	0.285	0.204	0.001136
CLCN7	6.59E-08	0.06648974	0.239	0.183	0.001165
BAZ2A	6.75E-08	0.08998315	0.629	0.54	0.001192
MTRNR2L12	6.94E-08	0.07671292	0.997	0.998	0.001227
ACSL5	7.00E-08	0.08361729	0.674	0.586	0.001236
TMEM185A	7.21E-08	0.06895038	0.278	0.207	0.001274
SERBP1	7.27E-08	0.05330962	1	1	0.001284
RBM18	7.55E-08	0.08129893	0.669	0.591	0.001334
AP4S1	7.66E-08	0.06654615	0.276	0.199	0.001353
PAIP1	7.75E-08	0.08461138	0.65	0.57	0.001369
SINHCAF	7.87E-08	0.07762812	0.944	0.943	0.001391

TOR1AIP2	7.96E-08	0.08688589	0.599	0.504	0.001406
TM9SF4	8.10E-08	0.08178404	0.46	0.38	0.001431
OTUD7B	8.12E-08	0.06540792	0.238	0.17	0.001436
CYB5R3	8.19E-08	0.07527925	0.85	0.834	0.001447
SGTA	8.25E-08	0.07653247	0.847	0.813	0.001458
UTP14A	8.40E-08	0.08501618	0.804	0.769	0.001484
REEP5	8.63E-08	0.05937889	0.999	1	0.001525
UBXN7	8.74E-08	0.08255553	0.425	0.338	0.001545
BTRC	8.75E-08	0.06182841	0.229	0.165	0.001546
VGLL4	8.78E-08	0.08471946	0.674	0.594	0.001552
MPZL1	9.08E-08	0.07463803	0.342	0.262	0.001605
ZW10	9.24E-08	0.07903165	0.452	0.37	0.001633
PTGES3	9.34E-08	0.05442942	1	1	0.001652
GPATCH2	9.41E-08	0.08552217	0.565	0.469	0.001664
RPL12	1.00E-07	0.03761318	1	1	0.001771
FAM98A	1.01E-07	0.08757336	0.693	0.626	0.001782
TLK2	1.03E-07	0.08515781	0.543	0.431	0.001822
DENND3	1.05E-07	0.08602301	0.426	0.345	0.001856
CSNK2A2	1.07E-07	0.07447913	0.894	0.881	0.001883
PFDN2	1.11E-07	0.06160995	0.999	1	0.001957
YY1	1.11E-07	0.06585761	0.986	0.991	0.001965
MORC4	1.12E-07	0.06388286	0.211	0.15	0.001977
AAGAB	1.15E-07	0.08134564	0.594	0.505	0.002033
FANK1	1.16E-07	0.22832223	0.296	0.222	0.002043
YBX3	1.16E-07	0.07652421	0.993	0.99	0.002054
NAT9	1.17E-07	0.06781223	0.288	0.216	0.002063
DCUN1D5	1.17E-07	0.07379276	0.98	0.978	0.002068
P2RY10	1.17E-07	0.09492408	0.568	0.484	0.002072
POLDIP2	1.22E-07	0.07057087	0.92	0.908	0.002153
SF3A3	1.23E-07	0.06799616	0.976	0.976	0.002167
SMARCD1	1.23E-07	0.07939782	0.76	0.714	0.002181
TANK	1.28E-07	0.08382719	0.867	0.868	0.00227
TAB3	1.33E-07	0.06064472	0.204	0.145	0.002343
POLH	1.33E-07	0.08344942	0.363	0.29	0.002359
HRAS	1.34E-07	0.07045892	0.95	0.958	0.002374
SAR1B	1.35E-07	0.06992274	0.937	0.917	0.002387
RPP21	1.37E-07	0.05845712	0.205	0.136	0.002417
USP42	1.38E-07	0.0769292	0.371	0.289	0.002435
RNF41	1.38E-07	0.07563926	0.398	0.322	0.00244
PSMD1	1.38E-07	0.06151495	0.998	0.998	0.00244
NUTF2	1.42E-07	0.06409337	0.987	0.981	0.002502
CRTC3	1.43E-07	0.08391108	0.712	0.621	0.002529
PBXIP1	1.45E-07	0.09727335	0.411	0.33	0.002567
DCAF13	1.46E-07	0.07209603	0.957	0.96	0.002582
SF3B2	1.50E-07	0.05628131	0.998	0.999	0.002648
KTN1	1.53E-07	0.06746217	0.993	0.994	0.002701
KIN	1.54E-07	0.0823048	0.679	0.588	0.002728
NDUFA9	1.54E-07	0.06071024	0.99	0.986	0.00273
RNASEK	1.58E-07	0.06195059	0.2	0.141	0.002799
COX11	1.60E-07	0.07704063	0.843	0.812	0.00283
RAB3IP	1.61E-07	0.0769285	0.342	0.271	0.002843
ZDHC5	1.61E-07	0.08084726	0.488	0.408	0.002843
PDSS1	1.61E-07	0.08232567	0.526	0.434	0.002854
GINM1	1.63E-07	0.08257507	0.618	0.534	0.002877
NEK6	1.70E-07	0.07586868	0.242	0.186	0.003002
RAE1	1.73E-07	0.07510122	0.856	0.824	0.003062

AFTPH	1.79E-07	0.08580518	0.528	0.435	0.003155
HCFC2	1.81E-07	0.06709738	0.26	0.19	0.003207
RNF40	1.84E-07	0.07829982	0.505	0.415	0.003248
DNAJA3	1.94E-07	0.08294999	0.698	0.633	0.003422
WDR74	1.96E-07	0.08027067	0.812	0.772	0.003458
ZC2HC1A	1.96E-07	0.0711814	0.206	0.141	0.003461
SVIP	1.96E-07	0.0787054	0.89	0.867	0.003467
MIIP	1.97E-07	0.09432533	0.94	0.944	0.003479
MAPKBP1	2.00E-07	0.06157806	0.214	0.154	0.003537
SPAG1	2.03E-07	0.07934396	0.366	0.29	0.00358
NAPA	2.04E-07	0.07111592	0.904	0.881	0.003603
ABRAXAS2	2.05E-07	0.07650939	0.443	0.365	0.003624
METTL17	2.06E-07	0.07864506	0.56	0.471	0.003643
ASCC1	2.10E-07	0.07799446	0.448	0.363	0.003713
KIF1C	2.11E-07	0.0679667	0.286	0.222	0.003728
ATP5F1C	2.15E-07	0.04535981	1	1	0.003801
KCNN4	2.15E-07	0.09230344	0.48	0.413	0.003805
NGDN	2.16E-07	0.07819224	0.686	0.613	0.003825
POLR3G	2.19E-07	0.09405298	0.503	0.393	0.003872
SCLY	2.21E-07	0.06664062	0.291	0.218	0.003908
RPS24	2.21E-07	0.03062499	1	1	0.003909
CBL	2.23E-07	0.0828513	0.55	0.466	0.003941
PCNX2	2.27E-07	0.06112015	0.215	0.159	0.004016
BCL2L1	2.29E-07	0.08349624	0.578	0.488	0.004042
SRPRB	2.38E-07	0.07303209	0.899	0.884	0.004204
PPP1CC	2.40E-07	0.06152456	0.994	0.994	0.004248
NSUN3	2.48E-07	0.06746151	0.305	0.228	0.004392
KRCC1	2.54E-07	0.09259912	0.512	0.404	0.004483
RNF114	2.58E-07	0.07608859	0.812	0.76	0.004556
MBTPS1	2.58E-07	0.08213907	0.532	0.441	0.00456
REXO4	2.63E-07	0.07915131	0.778	0.727	0.004648
GNA12	2.66E-07	0.06643606	0.279	0.215	0.0047
CMTM6	2.72E-07	0.07936915	0.956	0.95	0.004802
NFYC	2.73E-07	0.07546581	0.773	0.736	0.004829
HSDL1	2.75E-07	0.06076037	0.246	0.184	0.004862
DHX33	2.77E-07	0.08544924	0.521	0.428	0.004904
C1orf35	2.83E-07	0.07605844	0.844	0.814	0.005003
GNP2	2.89E-07	0.07801302	0.647	0.556	0.005115
FYTTD1	2.95E-07	0.08709658	0.609	0.536	0.005206
ZBTB40	2.95E-07	0.05668184	0.201	0.146	0.005212
DPH7	2.98E-07	0.08044427	0.564	0.47	0.005269
AAK1	3.01E-07	0.07598148	0.942	0.941	0.005324
RPL28	3.01E-07	0.02753332	1	1	0.005329
TSPYL1	3.04E-07	0.07840645	0.436	0.344	0.005371
SRP14	3.04E-07	0.03398873	1	1	0.005375
TNFRSF9	3.09E-07	0.07822789	0.229	0.165	0.005458
DNAJB1	3.12E-07	0.08752685	0.724	0.694	0.005521
INPP5D	3.15E-07	0.08535828	0.714	0.66	0.005569
C2orf74	3.15E-07	0.08239563	0.546	0.454	0.005571
POLK	3.16E-07	0.08282207	0.576	0.475	0.005583
RORA	3.20E-07	0.11360044	0.638	0.6	0.005659
SHOC2	3.22E-07	0.08086637	0.621	0.524	0.005692
ARHGEF12	3.22E-07	0.08026826	0.323	0.258	0.005698
HIF1A	3.33E-07	0.08056472	0.848	0.813	0.00589
NEMF	3.35E-07	0.07386706	0.917	0.903	0.005913
UBASH3B	3.48E-07	0.09044499	0.52	0.454	0.006154



CHCHD10	3.51E-07	0.06620906	0.999	1	0.006206
CLPB	3.51E-07	0.07725056	0.538	0.449	0.006212
ZBTB11	3.52E-07	0.08492347	0.532	0.446	0.006215
SLC35F2	3.58E-07	0.07540916	0.375	0.287	0.006322
WDR55	3.62E-07	0.07970674	0.624	0.547	0.006403
PUS1	3.63E-07	0.08436407	0.678	0.614	0.006409
VEZT	3.64E-07	0.08182484	0.503	0.416	0.006436
DUSP14	3.65E-07	0.08517732	0.497	0.421	0.006456
ACTR3	3.81E-07	0.04904363	1	1	0.006727
LIN7C	3.81E-07	0.07821731	0.486	0.405	0.00673
ZBTB43	3.82E-07	0.08555888	0.462	0.386	0.006745
SCAF1	3.88E-07	0.07641557	0.526	0.434	0.006854
INPP4A	3.90E-07	0.09090105	0.594	0.518	0.006885
TUBD1	4.03E-07	0.06173023	0.242	0.174	0.007132
ARID4B	4.04E-07	0.07646729	0.93	0.919	0.007139
PRKAB1	4.05E-07	0.07802629	0.346	0.282	0.007157
SETD1B	4.07E-07	0.06070253	0.238	0.175	0.007199
PHKB	4.09E-07	0.07994964	0.504	0.43	0.007227
MIR222HG	4.14E-07	0.07002707	0.268	0.2	0.007318
MACF1	4.16E-07	0.08785377	0.966	0.972	0.007357
CDK13	4.18E-07	0.08155978	0.701	0.625	0.007389
MFHAS1	4.28E-07	0.0877554	0.697	0.653	0.007566
TRPC4AP	4.29E-07	0.07881874	0.556	0.484	0.007585
PLBD2	4.33E-07	0.05366814	0.203	0.142	0.007645
ERI2	4.33E-07	0.06110969	0.24	0.178	0.007661
ACOX3	4.39E-07	0.05518183	0.211	0.148	0.007752
MPP6	4.41E-07	0.07901214	0.411	0.34	0.007788
AGFG1	4.42E-07	0.07866291	0.713	0.651	0.007817
ATXN2	4.48E-07	0.08255153	0.614	0.544	0.007914
NDUFAF5	4.52E-07	0.07788985	0.528	0.432	0.007994
NKAP	4.56E-07	0.07523381	0.842	0.805	0.008052
DDX56	4.61E-07	0.0730662	0.852	0.826	0.00814
BSPRY	4.70E-07	0.0595611	0.202	0.141	0.00831
DCAF6	4.75E-07	0.07494238	0.436	0.359	0.008395
ZNF562	4.76E-07	0.06706937	0.271	0.21	0.00842
SCO1	4.79E-07	0.07562273	0.79	0.746	0.008475
PSMD3	4.86E-07	0.05962278	0.994	0.99	0.008584
WDR4	4.92E-07	0.07947734	0.524	0.435	0.008689
YIPF2	4.94E-07	0.07508169	0.468	0.384	0.008738
FBXL20	5.01E-07	0.06470234	0.24	0.174	0.00886
VAT1	5.06E-07	0.05496253	0.216	0.152	0.008935
LINC00539	5.06E-07	0.06000481	0.201	0.147	0.008942
RSL24D1	5.14E-07	0.06269753	0.997	1	0.009077
TP53BP1	5.14E-07	0.08046338	0.473	0.4	0.009085
AC084033.3	5.18E-07	0.08058927	0.803	0.753	0.009164
BIRC6	5.25E-07	0.07881797	0.793	0.746	0.009283
RRP15	5.27E-07	0.07873507	0.82	0.774	0.00931
RALGAPB	5.33E-07	0.07043771	0.351	0.276	0.009428
TBCC	5.37E-07	0.08032456	0.586	0.514	0.0095
SELENOW	5.60E-07	0.05722071	0.998	1	0.009895
TRAF2	5.66E-07	0.07906727	0.592	0.522	0.010006
EIF3E	5.70E-07	0.04984986	1	1	0.010078
DNAJA2	5.85E-07	0.06480512	0.964	0.974	0.010336
ARID4A	5.88E-07	0.08533077	0.738	0.703	0.01039
LRRC8B	5.90E-07	0.06111882	0.269	0.194	0.010432
PPP4R3A	6.01E-07	0.07780905	0.84	0.819	0.010616

TAGLN2	6.04E-07	0.04689031	1	1	0.01067
DCP1B	6.04E-07	0.06139226	0.255	0.18	0.010679
FASTKD2	6.05E-07	0.0785978	0.597	0.51	0.010699
GSS	6.06E-07	0.07587571	0.808	0.761	0.010714
TMEM115	6.18E-07	0.0745814	0.433	0.361	0.01092
TNIP1	6.21E-07	0.07292033	0.888	0.882	0.010979
SELENOT	6.26E-07	0.06024549	0.986	0.988	0.011059
AC090152.1	6.31E-07	0.07742221	0.283	0.224	0.011162
EIF2AK4	6.40E-07	0.08173505	0.604	0.534	0.011304
DPP3	6.42E-07	0.06788827	0.882	0.862	0.011353
GRPEL1	6.67E-07	0.06853128	0.976	0.984	0.011791
CPOX	6.68E-07	0.07936591	0.673	0.598	0.011806
SUGP2	6.71E-07	0.0804233	0.664	0.599	0.011855
AKAP8L	6.77E-07	0.07981201	0.725	0.647	0.011969
PSMB3	7.13E-07	0.03959644	1	1	0.0126
HECTD1	7.28E-07	0.07752572	0.758	0.701	0.01286
UBL7	7.34E-07	0.07705003	0.661	0.574	0.012967
EPRS	7.36E-07	0.0629306	0.996	0.997	0.013
PSMC2	7.38E-07	0.06225884	0.977	0.973	0.013052
MARK4	7.43E-07	0.06117071	0.273	0.207	0.013124
CCT5	7.46E-07	0.05473397	1	1	0.013194
PRELID1	7.47E-07	0.04749754	1	1	0.013208
AC016831.5	7.58E-07	0.08964421	0.522	0.44	0.013393
ATP2B4	7.67E-07	0.08541379	0.712	0.664	0.013565
ASXL1	7.85E-07	0.06816407	0.908	0.894	0.013866
ALDOA	7.91E-07	0.07405821	0.554	0.469	0.013986
ACSF3	8.00E-07	0.07562621	0.514	0.428	0.014135
CCT8	8.06E-07	0.04906035	1	1	0.014254
FYN	8.11E-07	0.08217955	0.85	0.841	0.014337
SEC11A	8.24E-07	0.04782809	1	1	0.014564
GCAT	8.38E-07	0.07977047	0.513	0.435	0.014807
CETN2	8.39E-07	0.0714974	0.397	0.317	0.014836
LMAN1	8.58E-07	0.0643013	0.992	0.995	0.015166
XRCC5	8.60E-07	0.04431579	1	1	0.015208
MAP4	8.63E-07	0.07161708	0.921	0.921	0.01526
LEF1	8.85E-07	0.1119515	0.397	0.335	0.015646
MAN1A1	8.87E-07	0.07949647	0.484	0.406	0.015676
AKT3	9.09E-07	0.07121998	0.31	0.245	0.01606
SLC31A1	9.23E-07	0.0692269	0.356	0.272	0.016317
TWNK	9.27E-07	0.06475442	0.28	0.219	0.016378
FLYWCH1	9.33E-07	0.07211753	0.409	0.341	0.016484
WBP4	9.38E-07	0.07201745	0.88	0.864	0.016579
RBM17	9.51E-07	0.05650826	0.998	1	0.016806
RPS8	9.61E-07	0.02825045	1	1	0.016982
TMED3	9.68E-07	0.06740873	0.934	0.93	0.017108
SNRNP25	9.68E-07	0.05806199	0.991	0.986	0.017118
CMC2	9.74E-07	0.06061529	0.981	0.985	0.017222
TIMM9	9.77E-07	0.07579279	0.82	0.794	0.017264
MTO1	9.89E-07	0.07965413	0.597	0.522	0.017478
POLB	1.00E-06	0.07127062	0.36	0.289	0.017682
PCNA	1.00E-06	0.06775382	0.996	0.997	0.017721
CHPF	1.01E-06	0.07609818	0.407	0.326	0.017803
ETNK1	1.01E-06	0.07576162	0.711	0.633	0.017811
ZNF322	1.03E-06	0.05875452	0.226	0.159	0.018174
RAP2C	1.03E-06	0.07354721	0.418	0.332	0.018293
HERC2	1.04E-06	0.07977581	0.58	0.499	0.018349

IDH3A	1.04E-06	0.07970674	0.819	0.791	0.01846
ZNF213	1.05E-06	0.05429858	0.215	0.163	0.018608
TRIM44	1.05E-06	0.08363296	0.446	0.372	0.01861
MKRN1	1.06E-06	0.08125808	0.633	0.552	0.018803
AGFG2	1.09E-06	0.06617142	0.32	0.245	0.019237
PNPLA2	1.09E-06	0.07825462	0.561	0.468	0.019274
MTHFD1L	1.10E-06	0.08051287	0.706	0.643	0.019441
RBM42	1.11E-06	0.06385367	0.955	0.95	0.019677
IFT27	1.13E-06	0.077023	0.509	0.434	0.019886
FAM120AOS	1.13E-06	0.07584306	0.722	0.656	0.019904
SOAT1	1.13E-06	0.07988365	0.532	0.453	0.019928
RAB1A	1.13E-06	0.06683669	0.891	0.887	0.020033
DPP9	1.14E-06	0.07218859	0.762	0.695	0.020177
NABP1	1.16E-06	0.07860199	0.336	0.268	0.020473
IFT22	1.16E-06	0.07489865	0.452	0.375	0.02055
JMJD1C	1.18E-06	0.08348067	0.646	0.588	0.020907
AMFR	1.19E-06	0.07213653	0.408	0.332	0.021083
ABCC4	1.21E-06	0.05708339	0.21	0.158	0.021395
FAM72A	1.25E-06	0.05521855	0.2	0.144	0.022154
CMPK1	1.27E-06	0.06479263	0.947	0.944	0.022525
ZFYVE16	1.28E-06	0.06064398	0.232	0.176	0.02254
GATB	1.28E-06	0.06840972	0.388	0.312	0.022711
BSDC1	1.31E-06	0.07513614	0.432	0.366	0.023157
PIGN	1.31E-06	0.06515315	0.308	0.234	0.023159
UBR4	1.31E-06	0.07533129	0.726	0.685	0.023218
E2F7	1.32E-06	0.06807863	0.256	0.188	0.023391
VKORC1L1	1.33E-06	0.0766268	0.663	0.582	0.023536
SORT1	1.35E-06	0.07071911	0.326	0.245	0.023896
LAPTM4A	1.36E-06	0.07581585	0.683	0.631	0.024068
WDR73	1.38E-06	0.07517788	0.504	0.431	0.024364
MYL6B	1.40E-06	0.06296887	0.968	0.961	0.02466
CLK1	1.40E-06	0.0807309	0.508	0.436	0.024692
C5orf22	1.42E-06	0.06523401	0.3	0.226	0.025061
TUSC2	1.42E-06	0.06676818	0.897	0.882	0.025083
ACBD5	1.42E-06	0.07689014	0.508	0.434	0.025092
FAM104A	1.43E-06	0.06811289	0.909	0.921	0.025318
MAPK1	1.44E-06	0.07060863	0.877	0.859	0.025378
SMIM4	1.44E-06	0.07176906	0.858	0.838	0.025455
ZNF506	1.44E-06	0.06148655	0.276	0.202	0.025485
SDCCAG8	1.44E-06	0.07542376	0.337	0.275	0.025523
PRMT7	1.46E-06	0.07772239	0.509	0.431	0.025798
ACOT7	1.47E-06	0.06310916	0.945	0.935	0.026014
MTMR14	1.52E-06	0.07119996	0.78	0.725	0.026951
PSTPIP2	1.55E-06	0.07162815	0.209	0.161	0.027472
PABPN1	1.56E-06	0.06325341	0.95	0.945	0.02755
TOMM40	1.56E-06	0.0724828	0.99	0.995	0.027575
GLUD1	1.57E-06	0.06953254	0.844	0.804	0.027728
PTRH1	1.57E-06	0.07511781	0.599	0.524	0.027749
POMT1	1.58E-06	0.06206097	0.299	0.24	0.027969
CTNNB1	1.58E-06	0.08078164	0.635	0.566	0.027976
SP140	1.61E-06	0.07494385	0.93	0.935	0.028396
DPY30	1.61E-06	0.05960018	0.97	0.955	0.02852
RPGR	1.62E-06	0.08000216	0.41	0.336	0.028601
CPT1A	1.62E-06	0.08028499	0.49	0.398	0.028653
CYHR1	1.65E-06	0.07506057	0.536	0.449	0.0291
MDH2	1.65E-06	0.04425098	1	1	0.029227

ENDOD1	1.67E-06	0.0724935	0.355	0.284	0.029465
HLA-C	1.67E-06	0.0440369	1	1	0.029526
SPATC1L	1.69E-06	0.06864193	0.34	0.273	0.029833
RPE	1.70E-06	0.07427137	0.552	0.472	0.029975
CCR7	1.70E-06	0.17664278	0.4	0.304	0.03012
SPATS2L	1.72E-06	0.08274929	0.824	0.81	0.030398
CCT3	1.76E-06	0.05146326	1	1	0.031115
SGK1	1.76E-06	0.08371717	0.248	0.172	0.031195
CELF1	1.77E-06	0.07039182	0.843	0.816	0.031331
ZNF706	1.83E-06	0.05445681	0.998	1	0.032308
USP11	1.83E-06	0.07873808	0.511	0.436	0.032395
RC3H1	1.86E-06	0.06933334	0.377	0.299	0.032862
TRAPPC12	1.88E-06	0.07243603	0.534	0.455	0.033239
ANAPC10	1.90E-06	0.07138086	0.698	0.633	0.033662
BDP1	1.91E-06	0.07349788	0.932	0.934	0.033685
SLC35F5	1.91E-06	0.05928124	0.262	0.205	0.033847
NCOA2	1.93E-06	0.07624352	0.459	0.397	0.034034
CDS2	1.97E-06	0.07215657	0.706	0.642	0.034814
MYO6	1.98E-06	0.06524392	0.242	0.182	0.03503
XRRA1	2.05E-06	0.05631213	0.234	0.177	0.03625
PUM3	2.06E-06	0.07127781	0.949	0.964	0.036358
NIPA2	2.09E-06	0.06812467	0.836	0.815	0.036969
ZCCHC4	2.14E-06	0.05436652	0.225	0.169	0.037749
NCBP3	2.14E-06	0.07373916	0.793	0.761	0.037803
SNTB2	2.16E-06	0.07423513	0.459	0.384	0.038197
GNL1	2.17E-06	0.07080443	0.8	0.746	0.038356
CYSTM1	2.17E-06	0.07596007	0.704	0.654	0.03844
CASC3	2.19E-06	0.07586287	0.608	0.528	0.038627
MAP7D3	2.19E-06	0.07399475	0.816	0.786	0.03869
CTNNA1	2.20E-06	0.08270701	0.47	0.398	0.038872
UQCC2	2.20E-06	0.05135184	0.998	1	0.038959
STRAP	2.26E-06	0.05594379	0.993	0.994	0.039883
PIP5K1C	2.26E-06	0.05918125	0.227	0.165	0.039938
ADAT2	2.26E-06	0.05915621	0.283	0.222	0.04003
NLE1	2.29E-06	0.07392648	0.456	0.385	0.040477
TMEM165	2.29E-06	0.06374551	0.937	0.929	0.040499
DDX49	2.32E-06	0.06361279	0.892	0.868	0.040975
CASP3	2.35E-06	0.07212187	0.923	0.916	0.041587
CCDC127	2.36E-06	0.07282327	0.506	0.426	0.041675
NUDT15	2.40E-06	0.07335867	0.713	0.65	0.042447
NFKBIE	2.40E-06	0.06709747	0.342	0.276	0.042471
AP2B1	2.41E-06	0.06047227	0.972	0.961	0.042538
DFFA	2.44E-06	0.07126926	0.872	0.852	0.043087
CSRNP1	2.44E-06	0.0649916	0.275	0.197	0.043121
SCPEP1	2.52E-06	0.09421336	0.524	0.456	0.044472
CPEB4	2.59E-06	0.07012352	0.314	0.248	0.045737
TOB2	2.59E-06	0.07122924	0.384	0.313	0.045771
CDC26	2.59E-06	0.06240633	0.949	0.93	0.045785
GTPBP4	2.61E-06	0.0638868	0.981	0.985	0.046046
GEMIN5	2.65E-06	0.0735571	0.448	0.37	0.04684
CWC25	2.67E-06	0.07540398	0.702	0.651	0.047128
RANGAP1	2.68E-06	0.0705234	0.885	0.864	0.04744
AL355338.1	2.71E-06	0.06016852	0.258	0.185	0.047936
YTHDF1	2.74E-06	0.07380398	0.567	0.482	0.04847
DOLPP1	2.75E-06	0.05490829	0.256	0.194	0.048568
RNF5	2.77E-06	0.07352114	0.711	0.641	0.048992

PRDX1	2.78E-06	0.05467931	1	1	0.049154
NEK1	2.79E-06	0.07412726	0.398	0.332	0.049352
ALKBH1	2.80E-06	0.05306972	0.236	0.177	0.049578
BMP2K	2.82E-06	0.06130053	0.257	0.206	0.049895
ALKBH8	2.83E-06	0.05431346	0.223	0.17	0.050019
FAM117A	2.83E-06	0.07673513	0.519	0.432	0.050062
CCT4	2.83E-06	0.05158755	1	1	0.050083
STRN3	2.86E-06	0.070111	0.395	0.324	0.050518
PSMC1	2.90E-06	0.04839342	0.996	0.999	0.051338
PTTG1IP	2.91E-06	0.07742438	0.612	0.513	0.051376
WEE1	2.91E-06	0.07763016	0.619	0.564	0.051404
KAT6B	2.91E-06	0.07910351	0.484	0.42	0.051423
POLR1A	2.91E-06	0.06857964	0.372	0.31	0.051505
AHR	2.92E-06	0.06736258	0.307	0.241	0.05161
PPA1	2.94E-06	0.0497195	1	1	0.051947
TAP1	2.94E-06	0.06358209	0.995	0.996	0.052048
TMEM184B	2.95E-06	0.05759024	0.255	0.194	0.052199
GINS4	2.98E-06	0.07496656	0.605	0.527	0.05261
IRF2BP2	3.00E-06	0.08265794	0.556	0.492	0.052966
PMPCB	3.01E-06	0.06072466	0.949	0.938	0.053118
DDX31	3.08E-06	0.06520319	0.341	0.267	0.054372
SIRT5	3.08E-06	0.05161792	0.201	0.149	0.054387
APOBEC3F	3.09E-06	0.05690109	0.232	0.17	0.05466
UPRT	3.10E-06	0.0550539	0.244	0.181	0.054794
ZNF451	3.11E-06	0.0743641	0.68	0.608	0.055025
FRAT2	3.12E-06	0.06587092	0.348	0.278	0.055125
WDR59	3.16E-06	0.06331603	0.305	0.244	0.055803
PANK2	3.20E-06	0.0680937	0.864	0.839	0.056595
SEC62	3.22E-06	0.0555315	0.988	0.993	0.056886
MRPS26	3.24E-06	0.06294379	0.978	0.978	0.05722
FAM160B1	3.25E-06	0.07232066	0.42	0.342	0.057364
SDHA	3.26E-06	0.05910435	0.97	0.972	0.057575
UBE2Q1	3.26E-06	0.06771357	0.811	0.768	0.057659
ZNF146	3.26E-06	0.07463422	0.559	0.484	0.057706
MAP3K20	3.27E-06	0.0786279	0.41	0.354	0.057802
TRIP10	3.30E-06	0.05812082	0.238	0.184	0.058266
PEX13	3.33E-06	0.06670053	0.376	0.306	0.058903
SLC25A14	3.37E-06	0.05300554	0.218	0.167	0.059509
ATXN1	3.38E-06	0.08283911	0.65	0.585	0.059799
METTL1	3.39E-06	0.07635475	0.461	0.389	0.059847
TRIM37	3.40E-06	0.06719457	0.377	0.299	0.060019
TIA1	3.40E-06	0.07327328	0.659	0.581	0.06011
NUP188	3.42E-06	0.07244773	0.66	0.588	0.060362
ZBTB4	3.44E-06	0.05900005	0.23	0.177	0.060808
DCTPP1	3.46E-06	0.06092936	0.994	0.998	0.061204
PHTF2	3.46E-06	0.07570535	0.769	0.742	0.06124
PRKAG2	3.47E-06	0.06797298	0.39	0.321	0.061385
CCDC92	3.54E-06	0.06553517	0.318	0.242	0.062601
PEA15	3.56E-06	0.07147658	0.462	0.381	0.062887
SAE1	3.58E-06	0.05715373	0.98	0.979	0.063308
PLPP1	3.59E-06	0.09654282	0.334	0.287	0.06354
SZRD1	3.64E-06	0.05885143	0.967	0.967	0.064337
FAM208B	3.65E-06	0.07333837	0.53	0.446	0.06447
NARF	3.74E-06	0.06652119	0.933	0.935	0.06604
ZNF292	3.89E-06	0.07580101	0.81	0.783	0.068668
CHIC2	3.89E-06	0.06507526	0.336	0.262	0.06881

RCC1	3.90E-06	0.07025789	0.846	0.822	0.068945
NIN	4.04E-06	0.08645608	0.646	0.572	0.07149
PDE12	4.07E-06	0.07283732	0.6	0.529	0.071876
SNX14	4.09E-06	0.07220971	0.624	0.539	0.072272
MAGOHB	4.09E-06	0.05842873	0.984	0.98	0.072309
NCAPH2	4.11E-06	0.06860892	0.818	0.79	0.072729
TATDN1	4.12E-06	0.0749757	0.678	0.582	0.072852
PITPNA	4.17E-06	0.06811275	0.789	0.742	0.073677
NEK7	4.23E-06	0.07472355	0.474	0.403	0.074783
PRELID3B	4.24E-06	0.06018394	0.965	0.966	0.074989
MRPS35	4.25E-06	0.06187335	0.948	0.946	0.075155
EXT1	4.30E-06	0.05165233	0.201	0.143	0.076007
PELI1	4.33E-06	0.06764455	0.301	0.239	0.076504
CLUH	4.38E-06	0.07429036	0.441	0.369	0.07741
ANKIB1	4.49E-06	0.07290677	0.505	0.424	0.079329
BBS7	4.52E-06	0.06880564	0.466	0.394	0.079925
ZNF830	4.66E-06	0.07398539	0.583	0.516	0.082425
LRRC40	4.66E-06	0.06995859	0.556	0.473	0.082438
ORMDL1	4.67E-06	0.05443671	0.988	0.987	0.082466
SETD7	4.88E-06	0.0542958	0.222	0.166	0.086317
FBXO38	4.90E-06	0.0595323	0.282	0.216	0.08653
EIF2B4	5.01E-06	0.06831183	0.451	0.365	0.088509
MAN2A2	5.06E-06	0.06033046	0.287	0.219	0.08936
NUBPL	5.09E-06	0.05120909	0.218	0.164	0.08989
MPC2	5.09E-06	0.05357844	0.992	0.992	0.089996
GDI2	5.10E-06	0.04706653	0.999	0.999	0.09014
ZDHC14	5.11E-06	0.05665578	0.211	0.153	0.090329
MED23	5.18E-06	0.06795685	0.376	0.296	0.091642
EXT2	5.26E-06	0.06313054	0.338	0.266	0.092966
BTBD6	5.31E-06	0.06789034	0.788	0.754	0.093799
FAM96B	5.34E-06	0.04049292	1	1	0.094335
LRCH3	5.38E-06	0.0687314	0.371	0.308	0.095062
TRIM33	5.40E-06	0.07269938	0.643	0.556	0.095479
UHRF2	5.42E-06	0.07205073	0.504	0.421	0.095831
EFTUD2	5.45E-06	0.0632435	0.876	0.866	0.096252
BRAF	5.45E-06	0.0723264	0.478	0.409	0.096398
TNPO3	5.59E-06	0.06822275	0.769	0.714	0.098859
TRAPPC4	5.60E-06	0.05515714	0.977	0.98	0.098897
NHP2	5.60E-06	0.04686085	0.999	0.999	0.098992
HSP90B1	5.64E-06	0.05453102	1	1	0.099711

#### A1.4 – Differential gene expression for fast relaxing gels

Gene	p_val	avg_logFC	pct.1	pct.2	p_val_adj
LY6E	8.82E-122	-0.39441365	0.961	0.991	1.56E-117
DBI	7.22E-117	-0.20178047	1	1	1.28E-112
CISH	2.56E-111	-0.39238347	0.84	0.947	4.53E-107
ITGB2	5.91E-108	-0.3798376	0.899	0.966	1.04E-103
SCD	3.25E-106	-0.43068177	0.355	0.598	5.74E-102
IER2	2.38E-104	-0.40987754	0.94	0.984	4.20E-100
ISG20	8.88E-103	-0.5939776	0.438	0.668	1.57E-98

AES	3.23E-96	-0.24741893	0.999	1	5.71E-92
S100A4	9.19E-94	-0.62490947	0.909	0.972	1.62E-89
GSTK1	2.13E-93	-0.25327847	0.996	0.999	3.76E-89
CFL1	1.94E-90	-0.13655425	1	1	3.42E-86
AGTRAP	7.54E-88	-0.40598398	0.512	0.722	1.33E-83
NDUFB8	1.80E-85	-0.16646237	1	1	3.18E-81
LIMD2	1.76E-78	-0.28354392	0.981	0.996	3.11E-74
PIM1	6.38E-78	-0.29640013	0.937	0.979	1.13E-73
SNHG25	1.22E-77	-0.28820468	0.694	0.835	2.15E-73
SIT1	1.23E-76	-0.30446602	0.906	0.967	2.18E-72
EBP	1.46E-75	-0.22615101	0.998	1	2.59E-71
ATP5F1D	3.62E-75	-0.16072348	1	1	6.41E-71
BLOC1S1	1.57E-72	-0.22595513	0.986	0.998	2.77E-68
SREBF1	5.60E-71	-0.29971465	0.235	0.458	9.90E-67
CORO1A	5.96E-71	-0.15164259	0.999	1	1.05E-66
FKBP11	8.89E-70	-0.27690616	0.906	0.967	1.57E-65
LST1	7.83E-69	-0.37820337	0.578	0.764	1.38E-64
S100A6	1.10E-68	-0.31583973	1	1	1.95E-64
GPSM3	7.86E-67	-0.22116097	0.988	0.997	1.39E-62
COX8A	3.26E-65	-0.13576049	1	1	5.77E-61
FDPS	1.54E-63	-0.18948831	1	1	2.73E-59
GLIPR2	8.19E-62	-0.31440122	0.493	0.646	1.45E-57
TIMP1	5.60E-61	-0.42059246	0.657	0.824	9.89E-57
EMP3	6.23E-61	-0.25199375	0.995	0.999	1.10E-56
PFN1	9.66E-61	-0.10979127	1	1	1.71E-56
SERF2	1.93E-58	-0.1186684	1	1	3.40E-54
NDUFC2	2.80E-58	-0.15474671	1	1	4.94E-54
MRPL54	9.25E-58	-0.1712633	0.994	0.999	1.63E-53
S1PR4	8.86E-57	-0.30881257	0.945	0.984	1.57E-52
CD52	5.69E-55	-0.47809687	0.934	0.964	1.00E-50
MT-ATP6	1.08E-54	-0.17188139	1	1	1.90E-50
LAMTOR4	3.19E-52	-0.16825673	0.995	1	5.64E-48
GMFG	5.72E-52	-0.13780526	1	1	1.01E-47
PDLIM2	1.05E-51	-0.26242478	0.685	0.83	1.86E-47
MT-CO3	2.08E-51	-0.17503321	1	1	3.68E-47
ABCG1	3.85E-51	-0.20859058	0.103	0.267	6.80E-47
CYBA	5.37E-51	-0.16178717	1	1	9.49E-47
NCR3	1.63E-50	-0.32334719	0.758	0.863	2.88E-46
FXYD5	3.94E-50	-0.17621116	0.998	1	6.96E-46
MT-ND6	8.17E-50	-0.21566336	0.99	0.998	1.44E-45
H2AFV	1.12E-49	-0.17377793	0.998	0.998	1.98E-45
TEX264	6.25E-49	-0.20989724	0.92	0.966	1.10E-44
PTGER2	2.60E-48	-0.27197494	0.717	0.824	4.59E-44
BIN2	1.06E-47	-0.260957	0.871	0.93	1.88E-43
IDH2	1.66E-47	-0.2596754	0.918	0.97	2.94E-43
CSTB	1.78E-46	-0.15213158	0.999	1	3.15E-42
ICAM3	4.74E-46	-0.19879811	0.963	0.982	8.39E-42
DPP4	2.14E-45	-0.29151674	0.568	0.696	3.77E-41
TBC1D10C	3.25E-43	-0.20659373	0.947	0.981	5.74E-39
FADS2	4.50E-43	-0.19600117	0.086	0.214	7.95E-39
TSPAN32	5.76E-43	-0.24731134	0.2	0.364	1.02E-38
CCND3	6.58E-43	-0.17319914	0.995	0.999	1.16E-38
SH3BGR13	8.44E-42	-0.22930036	1	1	1.49E-37
DDT	1.25E-41	-0.14125685	0.999	1	2.22E-37
S100A10	1.52E-41	-0.18514	1	1	2.68E-37
MYL12A	1.78E-41	-0.1280073	1	1	3.14E-37

TMSB10	3.20E-41	-0.14189644	1	1	5.66E-37
RIPOR2	2.54E-40	-0.30203988	0.522	0.686	4.50E-36
PPIB	2.24E-39	-0.12124325	1	1	3.97E-35
PSME1	2.01E-38	-0.12631278	1	1	3.56E-34
CCDC167	2.89E-38	-0.17483538	0.971	0.984	5.11E-34
PYCARD	3.43E-38	-0.23023885	0.901	0.946	6.07E-34
LAT	6.15E-38	-0.18479141	0.978	0.99	1.09E-33
TRADD	2.66E-37	-0.20698718	0.852	0.911	4.70E-33
GIMAP4	6.58E-36	-0.30678144	0.539	0.652	1.16E-31
UCP2	6.76E-36	-0.25011831	0.844	0.929	1.20E-31
KLF2	9.10E-36	-0.34089894	0.795	0.901	1.61E-31
RRAS2	5.45E-35	-0.21449181	0.649	0.758	9.64E-31
OXLD1	7.46E-35	-0.1890456	0.756	0.844	1.32E-30
MZB1	8.21E-35	-0.28010986	0.607	0.726	1.45E-30
PLP2	8.30E-35	-0.20531977	0.938	0.965	1.47E-30
XBP1	1.70E-34	-0.2260868	0.862	0.935	3.00E-30
TSTA3	2.96E-34	-0.17118425	0.958	0.985	5.23E-30
SSBP4	4.53E-34	-0.15413067	0.983	0.991	8.01E-30
CDK2AP2	7.81E-34	-0.17350286	0.966	0.984	1.38E-29
MT-CYB	9.48E-34	-0.13162456	0.999	1	1.68E-29
CDC25B	1.68E-33	-0.26104381	0.825	0.899	2.97E-29
CTSC	6.13E-33	-0.18563244	0.985	0.993	1.08E-28
OSM	7.87E-33	-0.29217217	0.661	0.799	1.39E-28
ERP29	1.42E-32	-0.1234363	0.998	0.998	2.50E-28
COX7A2	2.80E-32	-0.11458303	1	1	4.95E-28
HCST	3.43E-32	-0.20864158	0.967	0.988	6.06E-28
SMDT1	4.80E-32	-0.1431894	0.979	0.996	8.48E-28
FADS1	5.10E-32	-0.20369442	0.148	0.269	9.01E-28
SKAP1	1.18E-31	-0.1659768	0.947	0.972	2.09E-27
VAMP5	1.20E-31	-0.19233668	0.906	0.953	2.13E-27
PRNP	1.56E-31	-0.21301135	0.559	0.658	2.76E-27
MAZ	1.64E-31	-0.1396353	0.985	0.996	2.89E-27
RFLNB	3.45E-31	-0.2185158	0.846	0.91	6.10E-27
MOSPD3	6.64E-31	-0.23917836	0.588	0.696	1.17E-26
FBXO5	1.18E-30	-0.23097153	0.739	0.835	2.08E-26
CTSW	2.26E-30	-0.33879937	0.738	0.829	4.00E-26
CD300A	2.30E-30	-0.16373431	0.113	0.238	4.07E-26
ANXA5	2.39E-30	-0.18858698	0.954	0.976	4.23E-26
LTB	2.54E-30	-0.4196394	0.881	0.958	4.49E-26
NDUFB1	5.97E-30	-0.1323823	0.993	0.998	1.05E-25
UPP1	7.93E-30	-0.21736376	0.798	0.886	1.40E-25
MT-ND4	1.38E-29	-0.11511877	1	1	2.45E-25
DOK2	1.48E-29	-0.18011532	0.96	0.977	2.62E-25
MATK	1.70E-29	-0.2293543	0.361	0.482	3.01E-25
TGFB1	2.29E-29	-0.14271414	0.988	0.993	4.04E-25
VSIR	5.53E-29	-0.25175612	0.46	0.591	9.77E-25
SELL	6.24E-29	-0.28254595	0.354	0.468	1.10E-24
RNPEPL1	8.81E-29	-0.17702427	0.872	0.93	1.56E-24
SAMD3	9.76E-29	-0.25015484	0.272	0.42	1.73E-24
ATP5F1E	1.02E-28	-0.07973043	1	1	1.80E-24
HMGB2	1.31E-28	-0.15817073	0.998	0.999	2.31E-24
LPGAT1	1.32E-28	-0.21653505	0.55	0.647	2.34E-24
CCDC28B	1.48E-28	-0.18694271	0.718	0.785	2.61E-24
RPL41	1.17E-27	-0.05898883	1	1	2.07E-23
FDFT1	1.30E-27	-0.16438075	0.937	0.967	2.29E-23
IMP3	1.53E-27	-0.13473007	0.973	0.992	2.70E-23



RNF145	1.60E-27	-0.1656459	0.794	0.855	2.83E-23
CARD16	2.03E-27	-0.18565044	0.689	0.776	3.59E-23
PSMB8	2.81E-27	-0.09258473	1	1	4.96E-23
RNF187	3.90E-27	-0.14823891	0.917	0.963	6.90E-23
SMIM26	5.12E-27	-0.13470457	0.963	0.987	9.05E-23
NACA	7.20E-27	-0.06845312	1	1	1.27E-22
ARPC1B	8.14E-27	-0.1023531	1	1	1.44E-22
SELPLG	8.44E-27	-0.20247787	0.807	0.886	1.49E-22
TUBA4A	1.34E-26	-0.13342951	0.997	0.999	2.37E-22
STMN1	1.42E-26	-0.11937173	1	1	2.52E-22
SOCS2	3.02E-26	-0.1903722	0.441	0.559	5.34E-22
H3F3A	3.27E-26	-0.08571168	1	1	5.78E-22
YWHAB	3.39E-26	-0.08090958	1	1	5.99E-22
SRSF5	4.36E-26	-0.12042668	0.994	0.998	7.71E-22
GLRX	4.49E-26	-0.15528276	0.957	0.988	7.94E-22
COMTD1	1.19E-25	-0.14914531	0.878	0.935	2.11E-21
RABAC1	1.36E-25	-0.1511182	0.955	0.976	2.41E-21
HMG2	1.84E-25	-0.10541797	1	1	3.26E-21
APBB1IP	2.60E-25	-0.17084846	0.853	0.921	4.59E-21
HAPLN3	3.46E-25	-0.19595224	0.342	0.482	6.11E-21
ATP5IF1	4.68E-25	-0.08887354	1	1	8.26E-21
SLC25A1	1.16E-24	-0.15858065	0.716	0.8	2.04E-20
CBX5	1.77E-24	-0.15913654	0.918	0.97	3.12E-20
CALM1	2.06E-24	-0.11587794	1	1	3.64E-20
RNF166	2.57E-24	-0.1670275	0.66	0.766	4.54E-20
SLC16A3	2.70E-24	-0.20161242	0.459	0.548	4.78E-20
PXN	2.98E-24	-0.1925203	0.396	0.517	5.27E-20
GIMAP7	3.07E-24	-0.22596604	0.758	0.844	5.42E-20
TMPO	3.11E-24	-0.13748329	0.993	0.998	5.49E-20
GYPC	3.58E-24	-0.12442471	0.996	1	6.33E-20
TFDP1	4.09E-24	-0.12922924	0.969	0.984	7.22E-20
NDUFA11	4.46E-24	-0.09552832	0.999	1	7.89E-20
INSIG1	5.61E-24	-0.19316099	0.773	0.867	9.91E-20
HIST1H2BN	8.71E-24	-0.18568474	0.298	0.412	1.54E-19
STX10	1.16E-23	-0.12442249	0.954	0.979	2.04E-19
TUBB	1.17E-23	-0.12258106	0.999	1	2.07E-19
PARVG	1.20E-23	-0.15990495	0.733	0.801	2.13E-19
PPIA	1.25E-23	-0.06948812	1	1	2.20E-19
ABHD17A	1.50E-23	-0.12433722	0.982	0.99	2.65E-19
HIGD2A	2.05E-23	-0.10407524	0.996	1	3.62E-19
C9orf16	2.26E-23	-0.10893459	0.998	0.999	3.99E-19
RHOF	2.41E-23	-0.13887825	0.918	0.958	4.26E-19
ADA	2.44E-23	-0.17233567	0.825	0.908	4.31E-19
ARHGEF1	2.51E-23	-0.15160307	0.877	0.934	4.44E-19
MRPS15	4.52E-23	-0.09211563	1	1	7.98E-19
VCL	6.16E-23	-0.18131704	0.367	0.483	1.09E-18
ATP5MG	7.38E-23	-0.0670138	1	1	1.30E-18
ID2	1.53E-22	-0.21903471	0.888	0.938	2.70E-18
MINOS1	2.13E-22	-0.11347261	0.994	0.999	3.76E-18
IFITM2	2.70E-22	-0.2260659	0.889	0.935	4.77E-18
CARHSP1	3.15E-22	-0.13851666	0.988	0.994	5.56E-18
TMC8	5.03E-22	-0.15131782	0.644	0.734	8.90E-18
CDC42SE1	5.45E-22	-0.1584265	0.888	0.933	9.64E-18
NUCB1	6.30E-22	-0.13068834	0.946	0.967	1.11E-17
NT5C	6.77E-22	-0.12696856	0.956	0.978	1.20E-17
DNPH1	8.76E-22	-0.13557284	0.927	0.961	1.55E-17

DDX5	9.31E-22	-0.09502255	0.999	0.999	1.64E-17
UBALD2	1.05E-21	-0.16215509	0.978	0.986	1.86E-17
PAXX	1.23E-21	-0.13622001	0.926	0.958	2.17E-17
SRSF3	1.36E-21	-0.09050942	0.998	1	2.41E-17
CHMP2A	3.08E-21	-0.12540202	0.966	0.987	5.44E-17
B2M	3.09E-21	-0.09270258	1	1	5.46E-17
SEC61G	3.64E-21	-0.09381713	1	1	6.44E-17
TMEM223	4.32E-21	-0.14161849	0.764	0.836	7.64E-17
SRSF7	5.21E-21	-0.10547404	1	1	9.21E-17
SAMHD1	8.78E-21	-0.15068388	0.898	0.932	1.55E-16
IL16	8.83E-21	-0.1779222	0.627	0.714	1.56E-16
SH3GLB2	1.26E-20	-0.14178101	0.744	0.807	2.23E-16
MZT2B	1.30E-20	-0.07994926	1	1	2.29E-16
ACSL3	1.45E-20	-0.15388788	0.564	0.636	2.57E-16
AQP3	1.49E-20	-0.34578937	0.367	0.512	2.63E-16
PREX1	1.58E-20	-0.15988081	0.67	0.758	2.79E-16
ANP32E	2.05E-20	-0.10945503	0.999	1	3.63E-16
GAPDH	2.43E-20	-0.05972575	1	1	4.29E-16
DNAJC8	2.46E-20	-0.09621873	0.998	1	4.35E-16
PSMA2	3.03E-20	-0.10238076	0.992	0.998	5.36E-16
NDUFA2	4.47E-20	-0.09633361	0.998	0.999	7.90E-16
FBXW5	6.11E-20	-0.12430857	0.922	0.954	1.08E-15
NDUFA1	6.82E-20	-0.07926339	1	1	1.21E-15
KLF13	7.47E-20	-0.15260209	0.88	0.92	1.32E-15
MGST3	9.84E-20	-0.16549126	0.853	0.902	1.74E-15
LAT2	1.11E-19	-0.15177064	0.188	0.292	1.96E-15
TSPO	1.15E-19	-0.14373321	0.967	0.982	2.04E-15
TMEM258	1.36E-19	-0.08956343	1	1	2.41E-15
ARPC5L	1.45E-19	-0.09548884	0.998	1	2.56E-15
AKR1A1	1.84E-19	-0.11822479	0.957	0.975	3.25E-15
RASGRP2	3.56E-19	-0.15899854	0.857	0.928	6.29E-15
MEI1	4.88E-19	-0.15228447	0.488	0.56	8.63E-15
RDH11	5.50E-19	-0.13783767	0.764	0.825	9.71E-15
FASN	5.65E-19	-0.1515964	0.655	0.712	9.98E-15
HNRNPF	5.77E-19	-0.08732521	0.998	1	1.02E-14
USP1	6.09E-19	-0.12227324	0.965	0.984	1.08E-14
STN1	7.20E-19	-0.14455184	0.614	0.694	1.27E-14
FKBP8	7.29E-19	-0.10077045	0.996	0.996	1.29E-14
1-Sep	7.91E-19	-0.11454308	0.975	0.987	1.40E-14
CUTA	1.05E-18	-0.09929475	0.994	0.998	1.85E-14
TPST2	1.06E-18	-0.17945734	0.66	0.733	1.87E-14
LAMTOR1	1.44E-18	-0.09406827	0.992	0.998	2.55E-14
HOPX	1.64E-18	-0.25053982	0.825	0.906	2.89E-14
H2AFX	2.13E-18	-0.13623757	0.97	0.989	3.76E-14
CENPK	2.34E-18	-0.12140862	0.943	0.968	4.14E-14
DCK	2.39E-18	-0.13442508	0.811	0.876	4.23E-14
TMEM256	2.81E-18	-0.12039084	0.926	0.956	4.97E-14
MAD2L2	3.12E-18	-0.12354428	0.914	0.945	5.52E-14
GLUL	3.56E-18	-0.18990953	0.287	0.406	6.30E-14
RNASEH2C	3.80E-18	-0.09531501	0.997	0.998	6.71E-14
SLC25A5	3.91E-18	-0.07037464	1	1	6.92E-14
RGS19	4.45E-18	-0.13449278	0.931	0.959	7.86E-14
EIF3K	4.91E-18	-0.06909379	1	1	8.68E-14
SEC61B	5.25E-18	-0.08299895	1	1	9.28E-14
MAL	8.27E-18	-0.37781629	0.179	0.346	1.46E-13
ITGB7	9.52E-18	-0.13961229	0.962	0.97	1.68E-13

ARL4C	9.62E-18	-0.15238918	0.974	0.987	1.70E-13
GSDMD	1.18E-17	-0.11797774	0.951	0.975	2.08E-13
GNAI2	1.66E-17	-0.08438436	1	1	2.93E-13
NAA38	2.08E-17	-0.0831918	1	0.999	3.67E-13
PFKL	2.09E-17	-0.12108738	0.896	0.929	3.69E-13
RPL36AL	2.36E-17	-0.05825689	0.999	1	4.17E-13
DOCK8	2.55E-17	-0.12375283	0.96	0.98	4.51E-13
MIR4435-2HG	2.91E-17	-0.16314383	0.675	0.768	5.15E-13
FEN1	2.96E-17	-0.1170821	0.97	0.981	5.23E-13
SPCS2	3.86E-17	-0.08659474	0.999	1	6.82E-13
TMC6	4.23E-17	-0.13091071	0.806	0.858	7.48E-13
OPTN	4.25E-17	-0.16015353	0.865	0.891	7.51E-13
MVD	4.28E-17	-0.13748811	0.746	0.8	7.57E-13
SF3B5	4.31E-17	-0.07833	0.999	1	7.62E-13
CLTA	4.63E-17	-0.07136199	0.998	1	8.18E-13
PSMB8-AS1	5.04E-17	-0.13501403	0.71	0.776	8.91E-13
IL10RA	5.12E-17	-0.16176861	0.657	0.738	9.04E-13
UXT	5.48E-17	-0.09386564	0.994	0.998	9.68E-13
RPL3	6.04E-17	-0.05053046	1	1	1.07E-12
E2F2	6.35E-17	-0.16564324	0.427	0.518	1.12E-12
UBE2F	6.73E-17	-0.15271347	0.738	0.774	1.19E-12
C4orf3	7.65E-17	-0.11553814	0.961	0.976	1.35E-12
CHCHD5	1.06E-16	-0.10627128	0.955	0.97	1.88E-12
TC2N	1.07E-16	-0.1568503	0.381	0.478	1.90E-12
SDF2L1	1.20E-16	-0.11816316	0.989	0.997	2.12E-12
MYO1F	1.28E-16	-0.1528321	0.816	0.906	2.26E-12
APRT	1.60E-16	-0.07618145	1	1	2.83E-12
TRAF3IP3	1.95E-16	-0.10218105	0.994	0.998	3.45E-12
ADD3	2.00E-16	-0.13431088	0.902	0.948	3.53E-12
WAS	2.04E-16	-0.10168041	0.973	0.984	3.60E-12
CYB561D2	2.23E-16	-0.11886235	0.837	0.893	3.94E-12
SIGIRR	2.31E-16	-0.1372769	0.718	0.795	4.08E-12
ZSCAN16-AS1	2.98E-16	-0.13917437	0.443	0.518	5.27E-12
TGFBR1	3.87E-16	-0.1395098	0.36	0.421	6.84E-12
CD8B	4.56E-16	-0.12592313	0.967	0.984	8.06E-12
HIST2H2AC	5.07E-16	-0.19785874	0.702	0.777	8.97E-12
ELOVL6	6.09E-16	-0.13765338	0.295	0.381	1.08E-11
HLA-A	6.24E-16	-0.08300142	1	1	1.10E-11
LCP1	6.56E-16	-0.08567922	1	1	1.16E-11
H1FX	9.95E-16	-0.13370436	0.985	0.996	1.76E-11
TRPV2	1.37E-15	-0.12840794	0.755	0.816	2.42E-11
EMC9	1.54E-15	-0.11727322	0.816	0.856	2.72E-11
SCAND1	1.55E-15	-0.11044995	0.968	0.987	2.75E-11
MIF4GD	1.56E-15	-0.11921719	0.756	0.8	2.76E-11
ARHGAP4	1.58E-15	-0.12527397	0.746	0.799	2.79E-11
NKG7	1.60E-15	-0.18611479	0.96	0.973	2.82E-11
EIF1	1.70E-15	-0.06763537	1	1	3.01E-11
GRK6	1.83E-15	-0.11199018	0.967	0.986	3.23E-11
ORAI1	1.89E-15	-0.12037573	0.866	0.918	3.34E-11
CTDSP1	1.97E-15	-0.12347567	0.758	0.819	3.48E-11
CD53	2.24E-15	-0.09459235	0.994	0.999	3.95E-11
HMGB1	2.25E-15	-0.07099259	1	1	3.98E-11
MFNG	2.29E-15	-0.09954724	0.966	0.988	4.05E-11
CARD19	2.49E-15	-0.1282814	0.833	0.899	4.40E-11
VPS29	3.26E-15	-0.08801884	0.995	0.997	5.75E-11
MPG	3.31E-15	-0.09026566	0.99	0.995	5.85E-11

UQCR11	4.27E-15	-0.0647271	1	1	7.54E-11
PCBP1	4.43E-15	-0.08245716	0.999	1	7.83E-11
CDKN2A	4.50E-15	-0.17844487	0.412	0.478	7.96E-11
HIST1H1E	5.01E-15	-0.22240199	0.767	0.824	8.85E-11
IFI16	6.16E-15	-0.09854664	0.99	0.996	1.09E-10
ZNF22	6.34E-15	-0.13052753	0.809	0.866	1.12E-10
ARL6IP4	6.89E-15	-0.06500581	1	1	1.22E-10
CNPY3	7.73E-15	-0.11630533	0.78	0.835	1.37E-10
TCEA2	9.31E-15	-0.12143122	0.678	0.736	1.65E-10
RNF167	9.79E-15	-0.11096	0.955	0.97	1.73E-10
RPS10	1.20E-14	-0.06053368	1	1	2.12E-10
WDR54	1.20E-14	-0.11062707	0.867	0.912	2.13E-10
SERPINB1	1.24E-14	-0.11144689	0.975	0.99	2.20E-10
EIF4A1	1.44E-14	-0.11105368	0.954	0.977	2.54E-10
FKBP2	1.47E-14	-0.10100725	0.983	0.992	2.60E-10
NDUFB4	1.55E-14	-0.07152416	1	1	2.74E-10
SNRPB2	2.05E-14	-0.07862634	1	1	3.63E-10
REX1BD	2.09E-14	-0.09557142	0.973	0.989	3.69E-10
COPE	2.37E-14	-0.07172357	1	1	4.19E-10
FBXO6	2.42E-14	-0.13248918	0.716	0.773	4.28E-10
NDUFA6	2.43E-14	-0.07458579	0.998	1	4.30E-10
GALK1	2.82E-14	-0.11693811	0.774	0.816	4.99E-10
CCDC69	2.92E-14	-0.12668851	0.756	0.806	5.16E-10
ANP32B	3.96E-14	-0.06402457	1	1	7.00E-10
PRR5	4.53E-14	-0.15057286	0.331	0.409	8.01E-10
SLFN5	5.31E-14	-0.15597097	0.818	0.878	9.39E-10
IDI1	7.42E-14	-0.11713145	0.95	0.971	1.31E-09
MIEN1	7.52E-14	-0.09660248	0.946	0.97	1.33E-09
CXCR3	9.14E-14	-0.18455299	0.738	0.798	1.61E-09
RPS6KB2	9.33E-14	-0.09853066	0.914	0.942	1.65E-09
ACAP1	9.66E-14	-0.09349715	0.99	0.995	1.71E-09
UBXN4	9.77E-14	-0.09109913	0.988	0.995	1.73E-09
MT-CO1	1.08E-13	-0.08109601	1	1	1.92E-09
CLEC2B	1.16E-13	-0.18485507	0.676	0.782	2.05E-09
HMOX2	1.20E-13	-0.09004001	0.974	0.987	2.13E-09
GZMM	1.31E-13	-0.13832808	0.816	0.866	2.31E-09
ANXA6	1.40E-13	-0.09143796	0.987	0.994	2.48E-09
TMX4	2.12E-13	-0.12643924	0.689	0.76	3.74E-09
SUSD3	2.66E-13	-0.12121153	0.732	0.81	4.69E-09
CHCHD1	2.99E-13	-0.07638497	0.993	0.999	5.29E-09
SNRPF	3.08E-13	-0.06233125	1	1	5.44E-09
MYL12B	3.19E-13	-0.06178389	1	1	5.64E-09
CISD3	3.33E-13	-0.0950023	0.956	0.973	5.89E-09
OSTC	3.37E-13	-0.0861077	0.989	0.996	5.96E-09
MSN	3.47E-13	-0.09429136	0.998	0.998	6.14E-09
LFNG	3.52E-13	-0.11741427	0.229	0.313	6.23E-09
SNRPN	3.57E-13	-0.11509071	0.608	0.655	6.30E-09
FAM173A	4.01E-13	-0.12047559	0.723	0.76	7.09E-09
DMAC1	4.51E-13	-0.09823973	0.915	0.944	7.98E-09
ARRB2	4.62E-13	-0.08061411	0.99	0.998	8.17E-09
HIST1H3B	5.28E-13	-0.16473517	0.383	0.448	9.34E-09
BRK1	5.68E-13	-0.07057296	0.999	1	1.00E-08
CD99	9.98E-13	-0.07888611	0.999	1	1.76E-08
IRF9	1.05E-12	-0.13093736	0.374	0.457	1.86E-08
DNMT1	1.16E-12	-0.08313172	0.996	0.999	2.04E-08
TAF10	1.19E-12	-0.08611145	0.985	0.99	2.10E-08

BIN1	1.23E-12	-0.11595187	0.888	0.94	2.17E-08
NASP	1.24E-12	-0.08080607	0.998	1	2.18E-08
ARGLU1	1.54E-12	-0.09426363	0.98	0.994	2.73E-08
CALM3	1.56E-12	-0.06445374	1	1	2.76E-08
TRABD	1.59E-12	-0.09128208	0.988	0.99	2.82E-08
GADD45B	1.61E-12	-0.13566923	0.427	0.529	2.84E-08
GNG5	1.62E-12	-0.06401157	1	1	2.86E-08
TES	1.76E-12	-0.10448601	0.894	0.945	3.11E-08
ATP5MC1	1.91E-12	-0.08222616	0.997	0.999	3.38E-08
MFGE8	2.02E-12	-0.10596293	0.252	0.318	3.58E-08
TSTD1	2.03E-12	-0.08720732	0.987	0.997	3.59E-08
SNHG9	2.28E-12	-0.11287046	0.675	0.717	4.04E-08
PRF1	2.46E-12	-0.1736857	0.769	0.844	4.35E-08
CSK	2.67E-12	-0.08268366	0.988	0.995	4.73E-08
PTPN18	2.80E-12	-0.10912427	0.784	0.834	4.94E-08
PCED1B	2.89E-12	-0.12446492	0.372	0.442	5.11E-08
CYTOR	3.19E-12	-0.11559893	0.927	0.956	5.64E-08
RANGRF	3.51E-12	-0.09353772	0.924	0.953	6.20E-08
PTTG1	3.55E-12	-0.09381287	0.994	0.999	6.28E-08
HACD4	3.65E-12	-0.11971812	0.564	0.628	6.45E-08
ILK	3.73E-12	-0.10501788	0.892	0.919	6.60E-08
CDKN2D	4.02E-12	-0.15962848	0.801	0.853	7.11E-08
CYBC1	4.45E-12	-0.09764624	0.908	0.936	7.87E-08
DUSP2	4.47E-12	-0.15225044	0.352	0.442	7.90E-08
SRP9	5.31E-12	-0.06873964	0.999	1	9.38E-08
CCNDBP1	5.85E-12	-0.09923901	0.872	0.909	1.03E-07
DNAJC9	5.99E-12	-0.08646862	0.984	0.992	1.06E-07
CCDC12	6.61E-12	-0.08371856	0.97	0.991	1.17E-07
MED11	6.64E-12	-0.10038281	0.75	0.794	1.17E-07
MDFIC	6.93E-12	-0.10395673	0.835	0.873	1.23E-07
MXD3	7.92E-12	-0.14349641	0.466	0.51	1.40E-07
MRPL16	8.01E-12	-0.0790902	0.989	0.996	1.42E-07
NDUFS7	8.03E-12	-0.06882682	0.998	1	1.42E-07
SRSF2	8.13E-12	-0.07612956	0.998	1	1.44E-07
CBR1	8.22E-12	-0.09438734	0.908	0.944	1.45E-07
FUBP1	8.86E-12	-0.09838879	0.902	0.938	1.57E-07
TLNRD1	9.32E-12	-0.10888757	0.72	0.762	1.65E-07
FAAP20	1.01E-11	-0.0919136	0.908	0.94	1.78E-07
TIMM8B	1.11E-11	-0.0756321	0.996	0.997	1.96E-07
RAMP1	1.11E-11	-0.17641082	0.121	0.208	1.97E-07
PRKCB	1.14E-11	-0.10631419	0.844	0.89	2.01E-07
SPCS3	1.20E-11	-0.08397608	0.991	0.996	2.13E-07
C15orf39	1.23E-11	-0.11233373	0.431	0.492	2.17E-07
CASP4	1.26E-11	-0.11029755	0.776	0.825	2.22E-07
NUDT1	1.40E-11	-0.08182753	0.996	0.996	2.48E-07
HIST1H1D	1.44E-11	-0.21261576	0.781	0.858	2.55E-07
POLR1D	1.59E-11	-0.07275378	0.998	0.999	2.80E-07
VAMP2	1.76E-11	-0.10398496	0.838	0.881	3.11E-07
APEH	1.90E-11	-0.09703004	0.831	0.877	3.35E-07
PCYT2	2.17E-11	-0.10679791	0.609	0.638	3.84E-07
SLC39A10	2.18E-11	-0.11713011	0.479	0.52	3.86E-07
ATP5PB	2.22E-11	-0.06558909	0.998	1	3.93E-07
ACSL6	2.28E-11	-0.10025881	0.142	0.206	4.02E-07
RNF126	2.32E-11	-0.08227871	0.976	0.991	4.09E-07
MCUB	2.32E-11	-0.09421494	0.931	0.961	4.10E-07
TCEAL8	3.04E-11	-0.10398558	0.703	0.759	5.37E-07

PGM1	3.10E-11	-0.10437554	0.437	0.484	5.48E-07
ERG28	3.30E-11	-0.09775218	0.814	0.848	5.83E-07
FAM111A	4.14E-11	-0.11409459	0.848	0.886	7.32E-07
GBP5	4.42E-11	-0.1493651	0.548	0.612	7.81E-07
WDR82	4.46E-11	-0.09698866	0.82	0.842	7.88E-07
MZT2A	4.52E-11	-0.06155999	1	1	7.98E-07
TSPOAP1	4.84E-11	-0.09681073	0.198	0.264	8.56E-07
PXMP2	5.30E-11	-0.10372623	0.643	0.69	9.36E-07
TRBC2	5.60E-11	-0.1366767	0.932	0.964	9.90E-07
G6PD	5.66E-11	-0.09817178	0.829	0.848	1.00E-06
GPKOW	6.01E-11	-0.11276546	0.49	0.529	1.06E-06
HIST1H1C	6.16E-11	-0.17438851	0.814	0.866	1.09E-06
ARHGAP30	6.50E-11	-0.09942042	0.952	0.976	1.15E-06
SLC25A29	6.83E-11	-0.10699079	0.524	0.577	1.21E-06
MAPKAPK5-AS1	7.12E-11	-0.10254539	0.617	0.664	1.26E-06
PSIP1	7.16E-11	-0.07815332	0.994	0.998	1.26E-06
LGALS3	7.86E-11	-0.15236613	0.893	0.931	1.39E-06
HNRNPDL	8.65E-11	-0.0770147	0.995	1	1.53E-06
C19orf70	9.13E-11	-0.07413521	0.991	0.998	1.61E-06
ARPC5	9.98E-11	-0.0638764	1	1	1.76E-06
TECR	1.03E-10	-0.07155751	0.993	0.996	1.82E-06
UBE2E3	1.06E-10	-0.09431345	0.83	0.866	1.87E-06
MYLIP	1.17E-10	-0.08865598	0.202	0.278	2.06E-06
CHCHD2	1.32E-10	-0.04011236	1	1	2.33E-06
PYM1	1.35E-10	-0.09884398	0.743	0.8	2.39E-06
SMIM7	1.37E-10	-0.08666881	0.909	0.93	2.42E-06
ATF4	1.52E-10	-0.09880502	0.98	0.996	2.68E-06
ATP6V1G1	1.52E-10	-0.07758958	0.989	0.994	2.68E-06
AL031777.3	1.52E-10	-0.09336044	0.188	0.26	2.69E-06
TRIB2	1.52E-10	-0.08892651	0.171	0.234	2.69E-06
UPF3A	1.70E-10	-0.08545359	0.946	0.958	3.00E-06
AC007952.4	1.74E-10	-0.13720112	0.429	0.516	3.07E-06
SYPL1	1.74E-10	-0.11308697	0.652	0.677	3.08E-06
DAXX	1.86E-10	-0.08886636	0.893	0.919	3.28E-06
KIF21B	2.40E-10	-0.10690383	0.358	0.414	4.24E-06
RNF168	2.44E-10	-0.1080914	0.548	0.592	4.31E-06
BANF1	2.86E-10	-0.06357051	0.999	1	5.05E-06
PSMG4	2.93E-10	-0.09343401	0.875	0.913	5.17E-06
WDR45	2.95E-10	-0.10334311	0.551	0.6	5.22E-06
TBCA	3.16E-10	-0.06127766	0.999	1	5.59E-06
ATP5MC2	3.62E-10	-0.05820228	1	1	6.39E-06
HPRT1	3.79E-10	-0.07340308	0.985	0.99	6.70E-06
ATP5PD	3.99E-10	-0.07531984	0.992	0.995	7.05E-06
CLDND1	4.33E-10	-0.10022397	0.957	0.989	7.65E-06
FAM126A	4.33E-10	-0.10073738	0.873	0.916	7.65E-06
MRPS21	4.33E-10	-0.0685331	0.996	0.999	7.66E-06
SLC38A2	5.17E-10	-0.10019114	0.762	0.803	9.13E-06
MMP25	5.22E-10	-0.12322983	0.535	0.574	9.23E-06
CKLF	5.34E-10	-0.07448556	0.995	1	9.43E-06
C19orf48	5.53E-10	-0.09654622	0.936	0.956	9.78E-06
HDDC2	5.58E-10	-0.08413596	0.915	0.941	9.86E-06
RNF157	5.61E-10	-0.12299946	0.496	0.576	9.92E-06
NPDC1	6.20E-10	-0.12914625	0.453	0.478	1.10E-05
DAZAP2	6.92E-10	-0.08562719	0.938	0.958	1.22E-05
CCR5	7.70E-10	-0.10927503	0.182	0.234	1.36E-05
NCKAP1L	7.91E-10	-0.09463447	0.804	0.843	1.40E-05

TRABD2A	8.12E-10	-0.10432964	0.614	0.657	1.43E-05
IL32	8.34E-10	-0.09300109	1	1	1.47E-05
SSR2	8.40E-10	-0.05859289	1	1	1.48E-05
SLC50A1	1.06E-09	-0.0955505	0.598	0.623	1.87E-05
RAN	1.07E-09	-0.05827206	1	1	1.89E-05
TPT1	1.11E-09	-0.0376061	1	1	1.96E-05
SPN	1.14E-09	-0.08995886	0.957	0.971	2.02E-05
ZNF652	1.20E-09	-0.10063212	0.334	0.399	2.12E-05
RAC2	1.25E-09	-0.06083866	1	1	2.21E-05
MT-CO2	1.35E-09	-0.07161446	1	1	2.39E-05
ACTN4	1.47E-09	-0.08114184	0.99	0.989	2.60E-05
HEMK1	1.48E-09	-0.09541957	0.447	0.5	2.62E-05
RASGRP1	1.49E-09	-0.1164763	0.772	0.81	2.63E-05
CORO7	1.53E-09	-0.10283416	0.659	0.703	2.71E-05
RASA3	1.56E-09	-0.10828801	0.235	0.316	2.76E-05
ALKBH7	1.75E-09	-0.08266558	0.919	0.944	3.09E-05
CENPM	1.81E-09	-0.07651616	0.981	0.993	3.21E-05
SREBF2	1.92E-09	-0.09494243	0.408	0.458	3.39E-05
PAG1	1.99E-09	-0.11947916	0.494	0.548	3.52E-05
SH3BP5	2.10E-09	-0.10503777	0.818	0.872	3.70E-05
CAPN2	2.10E-09	-0.09697172	0.9	0.944	3.71E-05
HBEGF	2.19E-09	-0.14457021	0.196	0.26	3.87E-05
CTSH	2.36E-09	-0.1628951	0.52	0.572	4.17E-05
SNX20	2.50E-09	-0.09616225	0.318	0.377	4.42E-05
DEAF1	2.62E-09	-0.0948887	0.431	0.486	4.62E-05
CD247	2.64E-09	-0.09001576	0.912	0.943	4.66E-05
RPP25L	2.91E-09	-0.09312185	0.589	0.626	5.14E-05
DPM2	3.02E-09	-0.0809535	0.881	0.902	5.35E-05
PIN4	3.19E-09	-0.08055807	0.876	0.914	5.65E-05
UBE2L6	3.24E-09	-0.08476738	0.933	0.953	5.72E-05
JAKMIP1	3.54E-09	-0.1039115	0.46	0.513	6.25E-05
MANF	4.06E-09	-0.08110445	0.989	0.995	7.18E-05
CST7	4.32E-09	-0.12459166	0.846	0.915	7.64E-05
TESC	5.29E-09	-0.0971063	0.917	0.951	9.35E-05
BTF3L4	5.68E-09	-0.08031726	0.868	0.912	0.0001
MAD1L1	6.51E-09	-0.10500677	0.706	0.764	0.000115
RHOG	6.54E-09	-0.06733312	0.991	0.993	0.000116
ZWINT	6.67E-09	-0.07765343	0.97	0.987	0.000118
SSNA1	6.98E-09	-0.05809361	0.997	1	0.000123
NDUFB7	7.65E-09	-0.05298747	0.999	1	0.000135
CAPNS1	7.75E-09	-0.07184379	0.982	0.987	0.000137
IL17RA	7.93E-09	-0.09261602	0.288	0.345	0.00014
ANXA2	8.45E-09	-0.07553308	0.995	0.999	0.000149
IMPDH1	8.64E-09	-0.08672	0.78	0.813	0.000153
CALHM2	1.09E-08	-0.10613084	0.437	0.497	0.000192
RDM1	1.23E-08	-0.07791388	0.214	0.26	0.000218
TMEM71	1.38E-08	-0.09850289	0.382	0.433	0.000244
NCF4	1.58E-08	-0.10087371	0.831	0.873	0.000279
SH3BP1	1.85E-08	-0.08650363	0.898	0.937	0.000328
KIAA0040	1.89E-08	-0.09460312	0.625	0.663	0.000334
PPM1M	2.04E-08	-0.08446833	0.336	0.397	0.000361
HIST1H2AG	2.17E-08	-0.11553205	0.46	0.507	0.000384
RRBP1	2.21E-08	-0.10050712	0.883	0.918	0.00039
IL2RG	2.25E-08	-0.08836732	0.943	0.954	0.000398
GGNBP2	2.32E-08	-0.08045698	0.924	0.955	0.000411
ZNF207	2.34E-08	-0.06876915	0.988	0.994	0.000414

C16orf54	2.43E-08	-0.10013168	0.354	0.426	0.000429
MAPKAPK3	2.46E-08	-0.06808436	0.976	0.985	0.000434
SLC27A5	2.52E-08	-0.0966783	0.581	0.604	0.000446
SH2D3A	2.65E-08	-0.07704443	0.194	0.245	0.000468
APOL4	2.68E-08	-0.10433899	0.23	0.288	0.000474
CRELD2	3.00E-08	-0.08854069	0.834	0.882	0.00053
ARL6IP1	3.07E-08	-0.10798292	0.884	0.928	0.000543
METTL23	3.30E-08	-0.08750123	0.75	0.779	0.000583
CD37	3.34E-08	-0.07939703	0.95	0.964	0.000591
PTPRC	3.36E-08	-0.07670313	0.998	1	0.000593
CENPX	3.38E-08	-0.0688688	0.99	0.994	0.000598
TBCB	3.41E-08	-0.06609722	0.982	0.992	0.000602
ATM	3.57E-08	-0.10164219	0.569	0.622	0.000632
RALY	3.67E-08	-0.06167015	0.993	0.998	0.000648
TMEM238	3.70E-08	-0.07835331	0.867	0.898	0.000654
TSEN15	3.70E-08	-0.08214273	0.779	0.828	0.000654
GMPPB	3.71E-08	-0.08233268	0.788	0.819	0.000655
CKS1B	3.77E-08	-0.08053226	0.985	0.996	0.000666
RNASEH2B	3.83E-08	-0.06928269	0.984	0.992	0.000678
RPL39L	3.87E-08	-0.05620015	0.998	0.998	0.000684
ARHGAP45	3.95E-08	-0.08379433	0.901	0.921	0.000699
LDLR	4.24E-08	-0.10355056	0.519	0.568	0.00075
GPR108	4.44E-08	-0.08657943	0.713	0.746	0.000785
SLC2A3	4.50E-08	-0.09921585	0.599	0.64	0.000795
CDKN2C	4.61E-08	-0.09431068	0.234	0.286	0.000814
SGO1	4.73E-08	-0.08819595	0.832	0.88	0.000835
MYC	4.75E-08	-0.13431149	0.569	0.634	0.00084
CD55	4.84E-08	-0.09512655	0.828	0.863	0.000856
DEK	4.86E-08	-0.05966877	0.997	1	0.000859
RBMX	5.11E-08	-0.06173723	0.994	1	0.000903
MT-ND5	5.14E-08	-0.06350984	0.999	1	0.000909
SLC27A3	5.24E-08	-0.07631831	0.229	0.284	0.000926
B3GAT3	5.28E-08	-0.07688642	0.85	0.873	0.000933
FLNA	5.43E-08	-0.08731426	0.987	0.991	0.000959
LRRC45	5.43E-08	-0.0873571	0.437	0.475	0.000961
HIST1H1B	5.81E-08	-0.17621993	0.768	0.842	0.001027
ATP8B2	5.84E-08	-0.07092055	0.19	0.24	0.001033
TCIRG1	5.93E-08	-0.0871519	0.686	0.74	0.001048
GRHPR	5.96E-08	-0.07813332	0.797	0.829	0.001054
XAF1	6.37E-08	-0.10226048	0.299	0.378	0.001126
SAR1A	6.40E-08	-0.07590307	0.922	0.947	0.001132
HJURP	6.41E-08	-0.11129486	0.617	0.654	0.001134
THEMIS	6.70E-08	-0.1006627	0.685	0.746	0.001185
POLR2G	7.24E-08	-0.07090966	0.916	0.938	0.00128
LMNB1	7.34E-08	-0.08151408	0.955	0.978	0.001298
SIPA1	7.53E-08	-0.08646944	0.674	0.705	0.001331
ICAM2	8.59E-08	-0.08462268	0.855	0.886	0.001518
NSMCE1	8.95E-08	-0.0897716	0.879	0.897	0.001582
PTRHD1	9.00E-08	-0.07222478	0.914	0.934	0.001591
EIF4E3	9.91E-08	-0.09119476	0.573	0.614	0.001752
H2AFJ	1.02E-07	-0.08246555	0.94	0.962	0.00181
SMC1A	1.03E-07	-0.07998001	0.965	0.98	0.001814
SRSF10	1.04E-07	-0.05695519	0.998	0.999	0.00184
KRT10	1.07E-07	-0.05962889	0.991	0.999	0.00189
NOSIP	1.07E-07	-0.08872345	0.967	0.976	0.001898
ACTR6	1.24E-07	-0.08265639	0.746	0.776	0.002192



LBR	1.34E-07	-0.0759037	0.978	0.989	0.002376
CDCA4	1.56E-07	-0.08348048	0.794	0.838	0.00276
ATP2A1-AS1	1.69E-07	-0.0812847	0.32	0.365	0.002989
PRDX2	1.74E-07	-0.04484951	1	1	0.003083
VPS28	2.02E-07	-0.06439849	0.972	0.986	0.003572
VKORC1	2.03E-07	-0.06960783	0.918	0.931	0.003596
B3GALT4	2.10E-07	-0.07953862	0.25	0.307	0.003716
DPM1	2.18E-07	-0.06886724	0.93	0.952	0.003861
TAZ	2.29E-07	-0.08286752	0.5	0.557	0.004054
SCAMP1-AS1	2.32E-07	-0.07592869	0.28	0.328	0.004096
SUN2	2.41E-07	-0.09228946	0.78	0.819	0.00426
RPS15	2.42E-07	-0.02915475	1	1	0.004276
GMPS	2.45E-07	-0.06740948	0.973	0.98	0.004323
MIAT	2.57E-07	-0.08679478	0.258	0.318	0.004546
THUMP3-AS1	2.70E-07	-0.07973968	0.784	0.83	0.004769
SLC44A2	2.79E-07	-0.07774448	0.344	0.4	0.004933
TPGS2	2.81E-07	-0.06431845	0.962	0.974	0.004967
LRP8	3.08E-07	-0.08208353	0.396	0.432	0.005441
TROAP	3.14E-07	-0.08287569	0.764	0.794	0.005546
NCBP2-AS2	3.21E-07	-0.07490007	0.872	0.906	0.005676
LGALS1	3.35E-07	-0.07963954	0.997	0.998	0.005928
NDUFB9	3.42E-07	-0.05047769	1	1	0.006052
BNIP3	3.43E-07	-0.10782636	0.538	0.493	0.006066
MRPL9	3.46E-07	-0.06316389	0.962	0.977	0.006112
RASAL3	3.46E-07	-0.0761333	0.912	0.928	0.006114
OCIAD2	3.59E-07	-0.06812551	0.965	0.974	0.006353
HIST1H2AL	3.63E-07	-0.09832475	0.306	0.362	0.006415
LRCH4	3.68E-07	-0.08269465	0.642	0.668	0.006499
HDCC3	3.79E-07	-0.07493141	0.796	0.839	0.006707
ARHGAP15	3.81E-07	-0.08059461	0.843	0.876	0.006735
TRBC1	3.83E-07	-0.17563767	0.711	0.782	0.006773
RCAN3	3.87E-07	-0.08713829	0.673	0.701	0.006844
PAQR4	4.01E-07	-0.08658503	0.457	0.488	0.007094
MPI	4.25E-07	-0.07583651	0.333	0.372	0.007517
HNRNPD	4.28E-07	-0.0524703	0.999	1	0.00756
SMPD1	4.41E-07	-0.08059244	0.36	0.398	0.00779
LAIR1	4.43E-07	-0.10232864	0.479	0.55	0.007837
S100P	4.87E-07	-0.1469269	0.163	0.221	0.008612
KIFC1	5.01E-07	-0.08824829	0.792	0.843	0.008851
BID	5.18E-07	-0.08541856	0.764	0.814	0.009158
RPL26	5.40E-07	-0.03290551	1	1	0.009539
ARHGDIB	5.55E-07	-0.03937431	1	1	0.009816
CD79B	5.59E-07	-0.10456147	0.495	0.542	0.009873
TMEM106B	5.82E-07	-0.08173496	0.437	0.469	0.010278
NBEAL2	5.88E-07	-0.08043994	0.508	0.528	0.010387
MPLKIP	6.07E-07	-0.06840906	0.921	0.94	0.010732
HPF1	6.15E-07	-0.07085594	0.83	0.864	0.010865
AP006621.3	6.19E-07	-0.05982491	0.181	0.224	0.01094
CBFB	6.64E-07	-0.07820427	0.744	0.777	0.011736
NCAPH	6.87E-07	-0.08089799	0.785	0.826	0.012139
MLX	6.95E-07	-0.07095358	0.848	0.873	0.01229
RAB5IF	7.42E-07	-0.05921377	0.986	0.994	0.013123
COASY	7.70E-07	-0.07302514	0.695	0.72	0.013602
STXBP2	7.71E-07	-0.07415152	0.778	0.803	0.01362
FYB1	8.26E-07	-0.09045392	0.936	0.965	0.014605
SYNRG	8.51E-07	-0.08210563	0.814	0.839	0.015036

RPL10A	8.73E-07	-0.02837942	1	1	0.015425
ASF1B	9.03E-07	-0.06892423	0.921	0.954	0.015965
EXOSC9	9.05E-07	-0.06897769	0.901	0.938	0.01599
GCLM	9.24E-07	-0.07280683	0.866	0.894	0.016324
NDC80	9.57E-07	-0.09032593	0.878	0.918	0.016912
SUB1	9.79E-07	-0.04245845	1	1	0.017301
TINF2	9.82E-07	-0.07694739	0.663	0.683	0.017364
OCEL1	1.00E-06	-0.07006756	0.303	0.349	0.017679
PSMA3	1.01E-06	-0.04859536	0.998	1	0.017914
JAGN1	1.04E-06	-0.06609681	0.881	0.898	0.018395
DBF4	1.05E-06	-0.06848998	0.964	0.976	0.018552
COMMD7	1.07E-06	-0.06374907	0.961	0.972	0.018847
AIF1	1.13E-06	-0.11682472	0.785	0.85	0.019946
CD47	1.15E-06	-0.05573132	0.99	0.999	0.020358
TKT	1.16E-06	-0.05065553	1	1	0.020447
ADAM8	1.18E-06	-0.0930291	0.418	0.459	0.020769
GMNN	1.23E-06	-0.06378172	0.98	0.992	0.021764
HMBS	1.28E-06	-0.0676827	0.848	0.881	0.022579
KRAS	1.28E-06	-0.08059714	0.892	0.94	0.02266
MAT2A	1.28E-06	-0.07413522	0.926	0.946	0.022701
P4HB	1.30E-06	-0.04865267	1	1	0.022985
TPGS1	1.34E-06	-0.0774476	0.712	0.724	0.023754
PCSK7	1.36E-06	-0.07769348	0.824	0.862	0.024009
NIPSNAP3A	1.41E-06	-0.07252535	0.376	0.404	0.024965
PKN1	1.46E-06	-0.06114651	0.955	0.972	0.025839
SNRNP35	1.46E-06	-0.07298018	0.687	0.716	0.025891
SRSF6	1.47E-06	-0.07087044	0.789	0.833	0.025907
MCRS1	1.50E-06	-0.06935669	0.815	0.849	0.026435
EGR1	1.61E-06	-0.10336466	0.144	0.229	0.028513
DBNL	1.65E-06	-0.05900233	0.978	0.986	0.029123
AC007240.1	1.68E-06	-0.06518598	0.186	0.234	0.029686
NEDD8	1.74E-06	-0.04000654	1	1	0.030733
RAB29	1.80E-06	-0.09128009	0.626	0.669	0.031889
TRIR	1.88E-06	-0.0460617	0.995	1	0.033212
HAGHL	1.95E-06	-0.08344607	0.318	0.37	0.03446
TMSB4X	1.96E-06	-0.04814077	1	1	0.034666
LBH	2.02E-06	-0.09276888	0.337	0.386	0.035652
GTPBP6	2.05E-06	-0.06782466	0.865	0.896	0.036253
UBQLN2	2.24E-06	-0.07326508	0.385	0.415	0.039611
NDUFB10	2.49E-06	-0.0416275	1	1	0.044076
METTL21A	2.53E-06	-0.07526797	0.529	0.539	0.044782
SSU72	2.59E-06	-0.04970203	0.998	0.998	0.045863
SRP19	2.72E-06	-0.05569288	0.983	0.99	0.048041
TMEM126B	2.78E-06	-0.06060577	0.939	0.955	0.049104
DPP7	2.78E-06	-0.05942491	0.97	0.982	0.049155
STARD4	2.98E-06	-0.07801273	0.375	0.419	0.052625
MED4	3.03E-06	-0.06371581	0.92	0.944	0.053547
UBL4A	3.12E-06	-0.07239675	0.697	0.724	0.055097
HNRNPA3	3.13E-06	-0.05222881	0.999	1	0.055241
ACAA2	3.22E-06	-0.05801928	0.986	0.989	0.056944
SKA2	3.23E-06	-0.05724825	0.983	0.989	0.05707
CSNK1G2	3.57E-06	-0.06497104	0.857	0.893	0.063056
NPC2	3.79E-06	-0.07664164	0.56	0.588	0.066948
FLNB	3.79E-06	-0.07724885	0.363	0.409	0.067025
HLA-E	3.87E-06	-0.05871251	0.997	0.998	0.068395
MMAB	3.88E-06	-0.0738125	0.667	0.683	0.068615

DHFR	3.97E-06	-0.0612985	0.974	0.986	0.070121
PLGRKT	4.08E-06	-0.07358934	0.785	0.807	0.072185
CD27	4.13E-06	-0.14058737	0.441	0.5	0.073039
DBP	4.15E-06	-0.05940503	0.216	0.254	0.073325
SF1	4.15E-06	-0.05570164	0.989	0.993	0.073383
SERP1	4.39E-06	-0.04404771	1	1	0.077546
HIST1H2AH	4.56E-06	-0.10335158	0.368	0.406	0.08065
STK4	4.56E-06	-0.06336244	0.975	0.984	0.08065
FKBP5	4.56E-06	-0.07529142	0.732	0.769	0.080663
SSR4	4.61E-06	-0.04653494	1	1	0.081455
UGP2	4.68E-06	-0.06503676	0.974	0.982	0.082741
SAMD9L	4.72E-06	-0.08812974	0.562	0.605	0.083487
FAM49B	4.89E-06	-0.05347068	0.988	0.996	0.086497
RPA3	5.14E-06	-0.04826814	0.998	0.999	0.090886
TOE1	5.27E-06	-0.07231604	0.601	0.613	0.093121
TUBB4B	5.30E-06	-0.07141151	0.999	1	0.093685
TXNDC17	5.31E-06	-0.04581466	0.999	1	0.093904
ACP1	5.34E-06	-0.04805388	0.998	1	0.094403
SLC43A1	5.48E-06	-0.06230797	0.253	0.294	0.09686
MKI67	5.48E-06	-0.08554081	0.986	0.996	0.096905
C1orf131	5.51E-06	-0.06615196	0.86	0.894	0.097422
PDCD6	5.59E-06	-0.05169463	0.985	0.994	0.098788
FKBP3	5.59E-06	-0.05048797	0.993	0.995	0.098859

### A1.5 – Top genes in in vitro gels from cNMF analysis

1	2	3	4	5	6	7	8
GZMB	C1QBP	THBS1	CENPF	DUSP8	FDXR	TMIGD2	HIST1H1B
C12orf75	TOMM40	ITGA2B	HMGB2	JUN	PHLDA3	KLRD1	HIST1H1E
SRGN	SRM	NFE2	ASPM	RSRC2	TP53I3	CCL5	HIST1H4C
SIRPG	HSPE1	RGS18	NUSAP1	BTG1	CMBL	HLA.DRB1	HIST1H1C
DHRS3	HMGA1	C2orf88	UBE2C	IL1A	RPS27L	CTSC	HIST1H1D
CAPG	MRTO4	MMRN1	TOP2A	ATF3	MDM2	HLA.DPB1	ATAD2
EVL	HSPD1	MEST	DLGAP5	PMAIP1	PHPT1	HLA.DRB5	FBXO5
LRRN3	ODC1	KALRN	TPX2	IER5	GADD45A	AC103702.2	HIST2H2AC
CD82	DKC1	HBD	CENPE	PPP1R15A	RPS19	GYG1	HIST1H2AH
CD7	NPM1	GUCY1B1	CDCA8	KLF6	TRIM22	TRGC1	SMC3
PGGHG	PRMT1	P2RX1	CKS1B	BIRC3	CDKN1A	HLA.DPA1	HIST1H3B
MYO1E	TIMM13	PLEK	CENPA	NFKBIA	XPC	GSTP1	ESCO2
CD3D	NME1	LTC4S	HMMR	ZNF267	PYHIN1	CST7	HIST1H2AG
GZMA	NOP16	LTBP1	CDKN3	DDIT3	FBXO22	RARRES3	TYMS
NKD2	MRPL12	LMO2	AURKA	IL23A	TRIAP1	CD244	CLSPN
HRH2	CYCS	MYLK	KPNA2	B3GNT5	PLAC8	RNF213	HIST1H2BC
ASB2	FKBP4	GUCY1A1	KIF20B	RGS1	TM7SF3	HLA.DRA	RRM2
SELENOH	MRPL4	BTK	CCNB1	TNFAIP3	UNC5B.AS1	LAG3	FAM111A
SHC4	NPM3	PRKAR2B	KIF23	BBC3	TIGAR	CD74	PCNA
AC020571.1	SERBP1	GSN	AURKB	PNRC1	BAX	HLA.DQA1	HIST1H2AL
DBN1	PPP1R14B	PBX1	GTSE1	TNFRSF12A	PADI4	GLIPR1	TMPO
CAMK1	RSL1D1	SNCA	TUBB4B	EIF4A2	HES2	GZMA	USP1
NDFIP2	RANBP1	BEX1	SMC4	ARID5B	BLOC1S2	HOPX	DNAJC9
RGS10	IFRD2	GNG8	PLK1	PIM3	ZMAT3	IKZF3	HIST1H3G

TNFSF10	DDX21	HGD	CCNB2	DUSP4	ISCU	HLA.DMA	HELLS
FGFR1	PA2G4	PTGS1	CALM2	GADD45A	TP53TG1	CCR9	FEN1
CD27	TUFM	CXCL8	TUBA1C	ZFP36L2	MIR34AHG	STOM	EZH2
STAP1	CD320	IGSF10	KIF2C	RHOB	CCDC90B	CD81	MKI67
LEF1	MCRIP2	GATA2	CDK1	BTG2	ZNF385A	FYB1	DNMT1
FUT8	SNU13	GP1BA	CKAP2	TAF1D	VWCE	COTL1	HIST1H2BF
IFITM2	CDK4	EGR3	CDCA3	CLK1	ACTA2	TRGC2	MCM7
GRK3	ZNF593	SPARC	SGO2	SQSTM1	LINC01759	F2R	SRSF4
IL2RB	TOMM22	IGF2BP2	CKS2	TRIB1	FUCA1	RCAN2	SRSF10
C20orf204	CCT3	NRGN	CCNA2	DUSP5	DDB2	LINC01871	E2F8
CYP1B1	DCTPP1	TBXAS1	NUF2	PHLDA1	MUC5AC	CLU	MCM3
CD38	NOP56	CTTN	BIRC5	AEN	SESN1	LINC02446	BRCA1
UBASH3B	PAICS	SLC22A17	TUBA1B	THAP9.AS1	LCE1E	KLRC2	FAM111B
CD96	EIF5A	PTGIR	CDC20	DUSP1	DRAM1	OSTF1	CDCA4
PLPP1	PPID	EMILIN1	UBE2S	REL	CCNG1	CD2	SMC1A
HIC1	GNL3	AC004130.1	NDC80	SAT1	FAM198B.AS1	HLA.DMB	HIST1H4E
PECAM1	WDR43	ANXA3	STMN1	SERTAD1	BBC3	ASB2	PRKDC
SEMA4D	SLC43A3	C3orf80	TUBB	PLK3	SDC1	ITGA1	SUPT16H
SLC12A8	EBNA1BP2	TNNC2	NCAPG	MCL1	AL138781.1	AOAH	RRM1
SUPT4H1	VDAC1	SRC	MKI67	ZFP36L1	ID3	RORA	CDKN2D
ACTN1	MRPS34	KCNE3	CDCA2	SNHG12	PGF	NKG7	ATAD5
CTSD	BOP1	GMPR	NEK2	STX1A	PLXNB2	CD48	DUT
ATP8B4	NOLC1	CST3	HJURP	CD80	PAR6G	FYN	PCLAF
GPAT3	RPL22L1	SPX	SPC25	UBE2Z	NDUFAF8	CLEC2B	CDCA5
MT.CO1	PPA1	CAVIN1	KIF14	FRMD4B	RRM2B	PLA2G16	MCM4
RHOC	CCDC85B	SMIM6	KNL1	BTG3	PIDD1	FASLG	KIF11
IER3	C20orf27	PTAFR	KNSTRN	BHLHE40	CYP4F3	GRAP2	FUS
LDLRAD4	NDUFAB1	TNS1	BUB1	ZFAND5	CD70	XCL2	CEP152
MICAL2	EEF1E1	FUT1	TACC3	CCNL1	TNFRSF10B	ALOX5AP	TK1
HEG1	HSP90AA1	SMIM1	KIFC1	NR1D2	RPS15A	NUGGC	CENPU
IL16	RAN	CTDSPL	MXD3	PLCG2	GPR87	RAB27A	ASF1B
NPTX1	PRELID1	TCEAL9	PIF1	JUND	RRAD	ST3GAL5	STMN1
JARID2	TRAP1	RASGRP3	RACGAP1	WEE1	ASTN2	RNF157	NASP
MT.ND2	RPL7L1	GP6	ARL6IP1	NR3C1	TCEA3	GZMM	PKMYT1
CKLF	CCR7	ESAM	KIF20A	CYTIP	PVT1	BCAS4	WDR76
PHOX	GRPEL1	CATSPER1	CKAP2L	CFL2	YPEL3	FES	HIST1H2BH
PHLDA1	FABP5	BANK1	BUB3	TSC22D3	LAPTM5	GBP5	CTCF
LPXN	CCT5	LGALS	CEP55	ZBTB43	PRKAB1	ARL6IP5	ANP32B
MT.ND3	NIFK	LTBR	H2AFX	HIVEP1	SULF2	LCP2	TUBA1B
SLAMF7	IMP4	AP003068.2	KIF22	ZEB2	AL109976.1	ITGA2	LMNB1
REG4	RRP9	SYK	KIF11	TNFRSF10B	GLS2	HLA.DQB1	CDC45
DUSP6	CCT2	ELOVL7	TMPO	CXCR4	FAS	EOMES	SAC3D1
STK17B	GCSH	TYROBP	PBK	TNFSF4	CYSRT1	CFH	C21orf58
CDK6	GPATCH4	LHFPL2	UBALD2	RYBP	AC007342.4	AC090152.1	SRSF3
FDX1	CCT6A	LRRN4CL	JPT1	INPP5F	ASCC3	CD160	HNRNPU
JAML	CCT8	TOMM20L	NUCKS1	FAM53C	FHL2	EVL	HIST1H4D
PTK2B	MRPL3	ADAMTSL4	KIF15	RELB	ORAI3	FAM3C	BAZ1B
SEPHS2	RRP1	FNBP1L	KIF4A	JUNB	GDF15	LIMS1	HIST1H3F
SRGAP3	PHB	CD9	CKAP5	RBM39	SP110	CD99	MND1
MT.ND4	RPS26	GATA2.AS1	HMG2	NFKB2	AL133485.1	TNIP3	TAF15
FCER1G	ATP5MC1	DLC1	INCENP	CLK4	ANKRA2	ZBTB38	TUBB
MBOAT7	PUM3	RGS6	HP1BP3	KMT2E	EDA2R	HIPK2	DEK
TESC	SLIRP	RSPH1	DEPDC1	TRAF4	PDLIM1	ABI3	MCM6
IL2RA	PGAM1	ZGLP1	PRR11	SNHG15	RNF19B	SRGN	MYBL2
MT2A	NCL	WASF1	HMGB1	FOXO3	DQX1	TRPS1	POLQ
FAM3C	PPIF	MPP7	TTK	ZBTB10	KRT17	TRAT1	KIFC1

ITGA1	POLR3G	TNFSF13B	PRC1	MDM2	MYH10	PITPNC1	MELK
SPART	LYAR	NFIX	ECT2	PRPF38B	RPS27	KLRB1	RFC4
ORAI2	EIF1AX	SEPT7.AS1	PSRC1	GATA3	TNFSF4	ARHGAP18	MCM5
CABLES1	TSR1	KIFC3	SMC2	NFE2L2	NDUFS5	IFNG	LIG1
RFLNB	SNRPD1	NR4A2	SPAG5	SIAH2	F5	IQGAP2	H1FX
NUCB2	HSP90AB1	SPTB	DBF4	CD69	ACBD6	GAB3	RAD51AP1
ALOX5AP	PHB2	PSTPIP2	BORA	TRAF1	RPL11	REEP5	HIST1H2AE
RASGRF2	PDCD5	RAB31	BUB1B	CDKN1A	PRPH	SMCO4	CHAF1A
HDGFL3	PRDX4	ARHGEF10	G2E3	DDIT4	OTP	STK17A	HNRNPAB
CTSW	CCT7	CHRNE	HMGB3	RUNX3	AC025423.1	CCR6	NCAPD3
TSPAN4	POLR3H	SLC6A4	ANLN	YPEL5	FAM198B	FSD1	NCAPG
MT.CO2	DCUN1D5	ITGB5	CCNF	FOSB	PLXNA2	PRKACB	HMG2
MUC20.OT1	NUDC	SPTBN5	SGO1	MAFG	RGS12	APBB1IP	HIST2H2AB
PDLIM7	PPAN	CIART	ARHGAP11A	NFAT5	AC007342.5	GPR35	H2AFX
CD63	MRPL36	LMTK3	UBE2T	NAMPT	KANK3	GPR171	KNL1
KIT	POLR3K	MGAT3	SPDL1	TNFRSF10D	RHOC	CD8A	POLA1
FLOT1	NDUFAF4	CLU	KIF18A	KCNN4	NEAT1	ARHGAP25	NDC80
LAYN	RPL23	SLC18A2	ANP32E	CTLA4	RPS4X	MAF	THRAP3
ADAM19	ATAD3B	EGR1	MAD2L1	AREG	DENND2D	PDCD4	GMEB1
SEPT11	SLC29A1	GLIS3	PTTG1	RORA	PLK2	MXD4	UHRF1

9	10	11	12	13	14	15
PHGDH	HNRNPU	FANK1	KLF2	CD52	MEF2C	RPL27A
PSAT1	HNRNPA3	IL17RB	RASGRP2	S100A4	MS4A1	RPS16
CTH	HNRNPA2B1	LMNA	CCND2	SH3BGRL3	CD19	RPL35
EIF4EBP1	SFPQ	CHDH	S100A11	B2M	LY86	RPL22
GARS	ACTR3	PTGDR2	S100A10	ITGB2	SPI1	RPL15
RACK1	SMARCA5	SEC11C	S1PR4	LTB	TNFRSF13B	RPL10A
ASNS	TAF15	IL2RA	CD59	HCST	IGHM	RPL21
RPL12	EIF3A	CREM	PRSS57	S100A6	CD79A	CHCHD2
TRIB3	NCL	TNFRSF4	AQP3	IL32	IGHD	RPL13A
ATF4	LMNB1	TNFSF10	CCNA1	UCP2	PAX5	RPS25
RPL3	HNRNPD	TYMP	ANXA2	CTSW	SPIB	RPL24
SHMT2	ACTR2	IL9R	SELPLG	TIMP1	AICDA	RPL23A
RPS18	MYH9	LIMA1	TAGLN2	NKG7	SYK	RPL32
SLC3A2	CAPRIN1	PHLDA2	EMP3	CYBA	POU2AF1	RPS18
RPS3A	SET	GATA3	TXN	LIMD2	CD40	RPS15
RPL32	NORAD	CRLF2	CDC25B	ICAM3	CD180	RPLP2
RPL10	RAD21	SRGN	FLNB	TPT1	BANK1	RPS6
ZFAS1	CANX	ITGB1	CTSH	PRF1	IGHA1	PTTG1
RPS12	BDP1	CCDC86	ICAM2	DOK2	PNOC	RPL41
RPS8	MACF1	PXDC1	GLRX	FXYD5	BASP1	RPL11
RPLP1	EIF4G2	GATA3.AS1	E2F2	SERF2	NEIL1	RPS27
RPS3	GOLGB1	MAN1C1	MT.CO3	AES	AFF3	RPS29
SARS	YWHAZ	ETFB	MOSPD3	BIN2	CD22	RPL18A
RPL13	TPM3	CD74	GRK6	LAT	NCF1	RPL37
RSL24D1	SPTBN1	BHLHE40.AS1	USP46	LY6E	IGHG3	FAU
HAX1	GOLGA4	GPR183	PRDX1	EMP3	BX547991.1	GAPDH
RPLP0	PAK2	EGLN3	MT.ND4	PYCARD	TSPAN33	RPS9
RPL10A	PRRC2C	TMEM173	BAK1	GIMAP4	IGKC	RPL37A
RPS4X	DDX3X	CSGALNACT1	LGALS1	ISG20	1-Mar	GNG5
RPS6	LCP1	PPARG	SPN	MAL	RALGPS2	RPLP1
MTHFD2	TPM4	IL3RA	S100A6	GPSM3	FAM129C	RPS3A
RPL26	BAZ1B	GK	TMSB10	RIPOR2	TCF4	RPL8
RPS2	LBR	PPFIBP1	MT.CO2	LST1	CCL17	RPS27A
PCK2	ARCN1	ACSL4	GNAI2	VSIR	FCER2	H2AFZ

EEF1B2	NOP14	TSP0	CES1	CCL5	SCIMP	TMA7
RPL14	TPR	NTRK2	TTYH2	TGFB1	RAB31	RPS24
RPL34	SAFB	SLC35D2	ADD3	S1PR4	JCHAIN	RPL14
RPS14	CLINT1	SCPEP1	LRRC8A	IL10RA	SNX22	RPL18
RPL11	ETS1	TGFBR3	APOL4	SIT1	IGHG1	UBA52
RPL30	HNRNPM	CCR4	SH3BP5	GIMAP7	GNG11	RPL28
RPS5	NRDC	AH1	GLUL	TSPAN32	CNR2	RPS23
RPS23	RANBP2	CRNDE	CCND3	HLA.A	SCARF1	RPS21
RPL18A	PCM1	IL13	MAP1A	GLIPR2	IL13RA1	RPS5
RPL8	TOP2B	MIIP	MT.CYB	AGTRAP	LINC00926	RPL27
RPL39	SYNCRIP	ZC2HC1A	NDUFB9	MALAT1	SIGLEC14	RPS14
PSPH	RIF1	HLA.B	PRR5	ITM2B	HDAC9	RPS7
RPL41	EIF4B	CD82	BIN1	APOBEC3G	MARCKS	ATP5MG
CEBPB	XPO1	CTNNA1	MT.CO1	RAMP1	SH2B2	RPL30
EIF1	AHCTF1	10-Sep	ZBTB32	ID2	DENND5B	RPL38
RPL28	HSPA4	LMCD1	MT.ATP6	HOPX	KREMEN2	MRPL51
SESN2	TM9SF3	AC099552.1	TSTA3	RASGRP1	CLNK	NACA
RPS15A	MSH6	TNFRSF11A	PLEC	SLFN5	LINC02245	PSMA7
RPL35A	NIN	SPOCK2	TRABD2A	OPTN	GNG7	RPL19
CHAC1	PHF3	RBPJ	RAP1GAP2	TPST2	CXXC5	RPSA
RPL19	ITGA4	KCNK1	PXN	PLP2	FAM30A	RPS3
SLC7A11	HNRNPH1	ETV7	NQO1	ITGB7	PPP1R14A	RPL13
STC2	DDX6	IL5	CARD19	LGALS3	BTK	RPL39
RPL9	NONO	TIGIT	A4GALT	CD3E	CD79B	RPL35A
RPLP2	ACIN1	LINC02195	RGS19	UBE2F	SLC43A2	ARPC3
MARS	HSPH1	TNFRSF18	NCF2	PDLIM2	VPREB3	COX7B
PYCR1	ROCK1	ALOX5AP	F2RL3	CD37	HOMER2	ATP5MD
RPL13A	HNRNPA1	RNF19A	SPSB1	CD7	SMIM14	SNRPB
SPNS3	SPEN	RHBDD2	MYO1F	ATP5F1E	HHEX	UBL5
BCAT1	CHD4	KRT7	CNN2	BLOC1S1	HLA.DRA	RPA3
GPT2	PTPN11	ADAM12	AIRE	IL2RG	RAB6B	RPS4X
RPL37	HSP90B1	MYL9	SLC9A3R1	SSR4	CHI3L2	RPL36
RPS16	DDX5	SMKR1	F12	RABAC1	FGD2	NDUFB3
RPS9	SNRNP200	MFSD10	DOK2	CD44	IFNGR2	OAZ1
RPL37A	TFRC	IKZF2	MT.ND3	VAMP5	GRN	RPL7A
TPT1	EZR	STAT1	PLEKHG3	HLA.E	ZNF730	HMG2
RPL18	ZNHIT6	JAML	ZFP36	NCR3	EPHB1	PFN1
RPL7A	KTN1	LPCAT2	ADAM8	TMSB4X	FGR	RPL29
RPL29	DIAPH1	HLA.DPB1	CALHM2	TEX264	PKIG	RPL26
JDP2	PNN	NDFIP2	FTL	CHMP2A	BFSP2	RPL9
RPSA	PTBP3	CCNI	MYD88	GZMB	HLA.DMB	COX6B1
RPL36	TRIP12	CCNG2	TMBIM1	MGST3	MYCL	GINS2
RPS27A	DNAJA1	ACADVL	RAB29	MYL12A	AC012557.1	UQCRH
TM6SF1	SMC1A	TESPA1	CCR3	SCAND1	ALOX5	ACTG1
EIF2S2	HNRNPK	MB21D2	TRABD	CD3D	CD74	PSMB3
RPL7	MBNL1	ITPR1	SYNJ2	STK17B	NME5	SRP14
TCEA1	EIF4G1	GSTK1	TMEM173	RNPEPL1	UBE2L5	RPS28
EEF1A1	API5	AL606807.1	AHNAK	RHOF	POU2F2	SNRPD2
CAMTA2	SUPT16H	CD63	TPST2	RFLNB	LILRB1	RPL10
WARS	CSDE1	HLA.C	ANXA6	SLAMF1	PIK3AP1	SLBP
RPS28	LARP1	TSPAN13	CORO7	DOCK8	CXCL10	RPS15A
RPS27	SPTAN1	TIAM1	IL3RA	CLEC2B	CXCR5	BTF3
RPS24	ARHGEF6	MYL6	TUBA4A	CD27	AC009950.1	SEM1
SLC1A5	ANP32E	BCAR3	CCDC112	DPP4	CYSLTR1	LSM5
TMBIM6	NUFIP2	HLA.DQA1	LDLRAP1	SAMD3	NBEA	SNRPF
HERPUD1	CNTRL	DUSP4	UBE2F	NOSIP	ARHGAP42	PSME2

RPL15	SRSF1	DMD	TRIM58	CLIC3	ALPK1	PTMA
DNAJC12	DYNC1H1	PLIN2	TRIB2	NSMCE1	ARL11	ACTB
GOT1	SLK	AL031280.1	CALM1	UPP1	ENPP1	RPS12
VLDLR.AS1	SMC5	ATP6V0E1	ANXA5	ARL4C	DNAJC5B	TMSB4X
ADM2	HNRNPAB	NEK6	HPCAL1	CCDC107	HVCN1	LSM3
VLDLR	BCLAF1	CCDC71L	CAPN2	CTSD	HLA.DQA1	RPL3
RPL27A	TCEA1	HLA.DRB1	NDRG1	CALM1	MZB1	RAN
RPS29	CEP350	SPINT2	QPRT	TMC6	TNFRSF13C	CLIC1
COX7A2L	SMARCC1	RALB	MFGE8	ZNF683	ACP5	ATP5F1E
SLC6A9	CHD1	NDFIP1	DSTN	ORAI1	AC010226.1	RPL12

### A1.6 – Top genes in liver fibrosis from cNMF analysis

1	2	3	4	5	6	7	8
FGFBP2	PLAT	RPS12	KCNN3	CYR61	CYP3A5	HP	LRRC25
GZMB	FABP4	RPS3A	MZB1	CTGF	CD24	TF	LILRB2
GNLY	TCN2	RPL13A	DERL3	TACSTD2	SPP1	FABP1	PTGS2
SPON2	CDC42EP2	RPS23	CCR10	CHST4	SDC4	ORM2	FCGR1A
PRF1	LMO2	EEF1A1	IGLL1	SERINC2	ATP1B1	HPX	APOBEC3A
NKG7	MAFB	RPS4X	RP11.16E12.2	DEFB1	ANXA4	FGG	CD300LF
CX3CR1	VWF	RPS8	TNFRSF17	ITIH2	EGR1	ORM1	TTYH3
AKR1C3	RNASE1	RPL13	P2RX1	SOD3	ATF3	APOC3	MT1M
FCGR3A	FABP5	CCR7	COBL1	SORBS2	PMEPA1	APOA1	LINC01272
PLAC8	DNASE1L3	RPS6	SPAG4	RBPMS	HNMT	APOA2	MT1G
PRSS23	CLEC14A	RPL9	DUSP26	PLK2	ITGAV	AHSG	IGSF6
ADGRG1	C4orf32	RPL30	TXNDC5	CLDN10	TPM1	FGB	DAPK1
CLIC3	HSPG2	TPT1	IGLV1.40	HES1	ERRF1	APOC1	HBEGF
HOPX	PDK4	RPS18	RP11.96H19.1	TM4SF4	TNFRSF12A	RBP4	NCF2
MYOM2	ZNF503	RPL19	IGLC7	ANXA4	MTRNR2L1	FGA	MT1X
S1PR5	IFI27	RPL11	IGLL5	SFRP5	PHGDH	ALB	RBM47
KLF2	ENG	RPS13	RP11.290F5.1	KRT18	H1FO	GSTA1	FCN1
C1orf21	CDKN1C	RPLP2	SDC1	CA2	SESTD1	HAMP	AIF1
EFHD2	LDB2	RPS16	XBP1	RBP1	MAP4K3	TTR	GNA12
CD247	NPDC1	RPL32	RP11.492E3.2	FXDY2	RP11.14N7.2	ALDOB	DRAM1
CST7	IGFBP4	RPL34	DOK3	KRT8	ALDH6A1	APOH	SLC7A7
CEP78	AHDC1	RPL3	IGLC5	OCLN	TRAK1	FGL1	RAB20
LITAF	LINC01560	RPL5	PRDX4	WWTR1	NR5A2	AMBIP	S100A9
CHST2	WFS1	RPS14	LMTK3	ADGRG6	RHOB	APOE	LST1
PLEK	ACTN1	RPS25	FCRL5	DMKN	GCNT4	SERPINC1	CSTA
TTC38	CTNND1	RPS15A	PNOC	ERRF1	HLA.DOA	IGFBP1	AQP9
PTGDS	HILPDA	RPL37	C2orf88	RCAN1	CRIPAK	PLA2G2A	HCK
RHOBTB3	CRIP2	RPS20	SMPDL3B	TRIP6	NET1	C3	LILRB1
ASCL2	NUPR1	RPL7	SSR4	AKR1C1	HEATR3	APOB	CD68
KLRF1	AC091729.9	RPS28	AC104699.1	DCDC2	SLC12A2	AZGP1	S100A8
ZEB2	GNG11	RPS3	IGLV1.51	ELF3	CLU	AGXT	CSF3R
PTPN12	ZNF169	RPL39	EAF2	CLDN1	GMNN	SERPINA1	SPI1
FCER1G	SRP14.AS1	RPL18A	NT5DC2	PBX1	PKD2	C1S	LILRB4

GZMH	MARCKS	RPL21	ITM2C	PAH	XYLT2	HRG	IFITM3
TBX21	FAM198B	RPSA	AC093818.1	CLDN7	ULK1	MGST1	SULT1A1
LAIR1	TSHZ2	RPL18	CHST15	FGGY	RIC3	CYP2C9	RNF19B
UCP2	ITGAX	RPL38	IGLC6	KRT19	BIVM	CES1	TNFAIP2
TXNIP	CD93	RPS2	SEC11C	ALDH1A1	VMP1	CYP2E1	OTOA
RP11.81H14.2	SEPN1	RPL14	IGHGP	CDC42EP1	MGAT4B	GC	CYBB
HAVCR2	MRC1	EEF1B2	PYCR1	APP	RAB3IP	VTN	LAMC1
KLRD1	PPP1R13B	SELL	SLC2A5	CNN3	SH3YL1	HPD	WFS1
CTSW	ID1	RPL31	DPEP1	SOX4	MLLT1	IGFBP2	CAMKK2
CYBA	HID1	RPS27A	IGF1	ZNF700	LEPROT	APCS	CSF1R
EMP3	FLNB	RPL4	E2F5	MTMR2	ID1	NNMT	MS4A4A
B2M	NR2F6	RPL23A	IGHG1	FGFR2	SCRN3	CFI	LILRB3
MTSS1	CD36	RPS5	IGHG3	WDR34	METTL7A	RARRES2	FAM26F
KIR2DL3	AC009404.2	RPL26	POU2AF1	ENPP2	SPINT2	ASS1	LILRA2
ITGB2	KLF4	RPL27	CTA.293F17.1	KRT7	SCARB2	APOM	CPVL
SPN	RNASEH1.AS1	RPS9	JCHAIN	GMNN	NCKAP5L	C1R	ASPHD2
C12orf75	SLC7A1	RPL10A	CPNE5	SERPING1	SLX4IP	FBP1	MS4A7
TRDC	IGFBP7	RPL35A	TCN2	WBP5	CRIM1	ASGR2	RP6.159A1.4
TYROBP	SMTN	LEF1	KIF19	PARVA	DAAM1	CYP2C8	CEBPA
AES	LDOC1	RPL37A	FAM27C	ANPEP	MT.CO3	AGT	RRAGD
UPP1	CAV2	RPS17	IGLC4	HNMT	CTNNA1	GATM	MGLL
SLC15A4	ZSCAN9	RPL27A	KLK1	PPIC	PLAGL1	ANG	IFI30
PDE6G	BRSK1	RPL7A	IGKC	HES4	ABCC1	ASGR1	FTH1
FGR	TRPM4	RPL36	DHRS9	IGLV1.44	LDOC1L	RGN	OSCAR
RAMP1	FCHO2	RPS21	CNKS1R	CLU	MT1E	CYP27A1	CTSS
CCND3	TM4SF1	GNB2L1	IGLV6.57	STAP2	ARHGAP24	ADH1B	ADAP2
HLA.C	CRYBG3	RPL28	SMIM1	DOK4	KANSL3	TMEM176B	CD14
UBE2F	HSF4	RPLP1	SCNN1B	FRMD4A	TTN	CFH	C5AR1
MYO1F	ZBTB5	RPL10	CD79A	CNKS3R	IFNGR2	UGT2B15	CFD
PFN1	EPAS1	RPL29	SLC1A4	CD24	STX7	TMEM176A	ZNF467
GNPTAB	SERPINH1	RPL22	PIP5K1B	NGFRAP1	PER2	CPB2	SCIMP
IFITM2	TAF9B	RPL12	CTHRC1	AQP1	PPP1R12B	TST	RAB32
FAM65B	IFITM3	RPS27	JSRP1	ZNF665	RRNAD1	C4BPA	MAP3K1
TPST2	MANSC1	LDHB	TBC1D9	SLPI	PHLDA2	SERPING1	FTL
HLA.B	ZDHHC8	RPS11	RAB30	ALDH7A1	CSPP1	EPHX1	PSAP
CLEC16A	ADRBK2	RP11.664D1.1	PLA2G2D	RCOR1	SPATS2L	SERPINA6	FCGR2A
SH3BP5	ZNF775	RPS15	IGLC2	SH3YL1	C1orf27	SLC27A2	LMO2
SYNE1	GPR160	RPL23	B9D1	SOX9	APP	A1BG	DENND1A
PYHIN1	RAB13	LINC00402	FKBP11	LIMS2	HS2ST1	PGLYRP2	S100A11
TFDP2	NFIA	GLTSCR2	ABC9	ARHGAP29	ZKSCAN1	FN1	TFE3
CTBP2	SPARC	MAL	IGKV4.1	RIN2	TELO2	FXYD1	SAT1
PLEKHG3	TCF4	RPS7	AP001058.3	EXTL2	PRKCD	KHK	P2RY13
CD300A	RGPD5	RPL6	RP5.887A10.1	TFPI	ARNT	HRSP12	CLEC12A
LAIR2	ID3	IL7R	TXNDC11	WFDC2	GAS6	PRAP1	CASP9
SSBP3	BEND5	RPL15	MIXL1	EPCAM	TM9SF1	PAH	MT2A
CALM1	AC074289.1	NOSIP	FKBP7	SPP1	CD59	LEAP2	FPR1
ABHD17A	FAM89A	RPS10	ICAM4	VTN	VPS41	HSD17B2	CFP
LILRB1	LCMT2	NACA	IGHM	NFIB	VTN	AKR1C1	
BIN2	LAMA5	EIF3E	HID1	TINAGL1	LDLR	PTGR1	CLEC7A
MBP	ZNF467	LDOC1	GPR160	GNPNAT1	IFT88	ITIH2	MAFB
HLA.E	STAB1	RPL8	IGHV6.1	CKB	GOLGB1	A2M	HLX



TSPAN32	RP11.635N1 9.1	KLF2	AMPD1	CPLX1	ECHDC2	ALDH2	IPMK
UBB	FXYD6	FXYD7	LAMP5	HSPA1A	BACH1	CYP4A11	SMPDL3B
RASGRP2	CYFIP1	RPLP0	NAGLU	C4BPA	MGST2	SERPINA4	RETN
MT.CO2	QSER1	NPM1	IGKV1.12	CD302	SRGAP2B	GPX3	IL1B
ACOX3	ADAMTS6	RPL24	IGLV3.1	GGT7	NFIC	CYP4F3	LYL1
KLF3	RP11.500C1 1.3	LAPTM4B	SLC17A9	PTBP2	TOR1AIP2	CLU	CDKN1C
MLC1	TAF5L	GORASP1	IGLC3	SERPINA5	PERP	ACSL1	SLC11A1
PXN	SETD7	TSHZ2	C19orf38	TPBG	MTA1	KRT18	CD36
JAZF1	HSPB1	C6orf48	BLNK	SNCG	FLVCR1	CYB5A	RP11.634H2 2.1
SH3BGR3	ZNF674.AS1	TKTL1	FKBP2	VWA1	SERPINA1	GOT1	CTD.2035E1 1.5
GLRX	WDR24	UBA52	RP11.446N1 9.1	SLC16A11	RUFY3	COL18A1	TIMP1
KCTD10	TBC1D9	ZNF565	LINC01358	VPS50	ZNF12	GAMT	NAT1
RASSF4	ZNF628	BORA	ITGAX	MFSD7	GNG7	TIMP1	NAMPT
ARPC2	ZNF785	PPRC1	FAM92B	MYO10	ARHGAP5	FAH	CEBPB
TES	FAM20B	SH3PXD2A	CHAC1	UGT2B15	TMEM245	SLC27A5	RXRA
KIR3DL1	LAPTM4B	RPS19	QPRT	PTGR1	MUM1	FAAH	ZMYND19

9	10	11	12	13	14	15
GZMA	IFIT1	STMN1	CD34	NBEAL1	ZNF683	JUNB
HCST	IFIT2	TOP2A	PLVAP	AC090498.1	S100A4	DUSP1
TMSB4X	IFIT3	RRM2	NOSTRIN	TIPIN	SH3BGR3	CXCR4
HLA.A	MX1	TUBA1B	CALCRL	RPL17	S100A6	CD69
ATP5E	ISG15	ZWINT	EMCN	ZNF90	CD52	ZFP36
RPS27	IFI44L	ASF1B	RBP7	MTRNR2L8	ACTB	ZFP36L2
IL32	RSAD2	SHCBP1	SPARC	RPS4Y1	LGALS1	JUN
GZMK	CMPK2	HMGB2	PLPP3	HNRNPA1L2	VIM	BTG2
ARHGDIB	TNFSF10	HMG2	RAMP2	RELB	CXCR3	FOS
CORO1A	OAS1	NUF2	PLPP1	HLA.G	PLP2	MALAT1
CCL5	NT5C3A	TUBB	C8orf4	NACA2	PTMS	TSC22D3
RPS29	IFI6	NUSAP1	IFI27	PZP	TMSB4X	NR4A2
PFN1	SAMD9	CENPE	MGP	ATXN8OS	CRIP1	CCL4
HLA.B	EPST11	PRC1	CNN3	RP11.255M2.3	S100A11	BTG1
GZMH	NEXN	KIAA0101	VWA1	AC004556.1	CD101	CTD.3252C9.4
HLA.C	IFI35	HIST1H4C	PCAT19	CXCL8	CTLA4	CCL4L2
CD3D	HERC5	CENPF	CLEC14A	FYN	NCF1	DUSP2
MT.CYB	C5orf51	CLSPN	EGFL7	C1orf56	S100A10	MT.ND2
CD8B	MX2	CENPN	ESAM	AC116366.6	ANXA2	CITED2
CFL1	EIF2AK2	GGH	ID1	HNRNPH1	ANTXR2	FOSB
B2M	UTP14C	H2AFZ	SLC9A3R2	REL	CAPG	KLF6
MYL12A	ISG20	EZH2	DLC1	CDC42SE2	STX3	NFKBID
CD2	ABCD1	MCM7	CCND1	RP11.415F23.2	TPM4	IER2
MT.CO2	USP18	MCM2	GSN	CAPZA1	TMSB10	H3F3B
TRAC	PARP11	CDT1	SPARCL1	PPP1CB	LGALS3	PNRC1
MT.ND1	IRF7	KNSTRN	GNG11	PRDM1	GLIPR2	BRD2
MYL6	GBP7	TUBA1C	RNASE1	PABPC3	PHOSPHO2	NR4A1
RPL23A	STAT2	PAQR4	TIMP2	S100A12	ZYX	DDX5
MYL12B	LIMS2	CKS1B	AQP1	EML4	LCP1	MT.ND3
CST7	PNPT1	PTTG1	TSPAN18	KCNN1	EMP3	RSRP1
APOBEC3G	DDX60	UBE2T	ENPP2	NFKB2	ARHGFE39	RGCC
MT.ATP6	IFI44	MKI67	FXYD6	CREM	ACTR3	IFNG
RPS4X	C5orf42	ORC6	PTRF	STK17B	ALAD	PPP1R10

ACTB	RPAP3	RACGAP1	NFIB	FAM177A1	CD9	MT.CO1
TMA7	PIGA	ITGAV	MLLT4	NHSL2	SIT1	MYADM
RPS26	TRIM21	TUBB4B	TINAGL1	ANKRD9	ZNF853	GADD45B
RPL27A	IFI16	PCNA	SERPINH1	CHRM3.AS2	CFL1	NFKBIA
GZMM	LY6E	HMGB3	C10orf11	RP11.138A9.1	ADIRF	CCL5
TRBC1	FAM188A	DTYMK	ENG	PABPC1	MYO1G	XCL2
RPL38	NUP155	HMGB1	ROBO4	RPL10L	SLC43A1	BIRC3
PSMB9	C4orf33	CKS2	KANK3	GS1.124K5.11	LDHA	TUBA1A
CLIC1	C4BPA	FEN1	HYAL2	RP11.138A9.2	HMGCR	ANXA1
NKG7	URB1.AS1	EPT1	EHD2	RP11.701H24.9	FLT3LG	SARAF
PSME1	PIK3R4	LIG1	MESP1	B4GALT1	ITGB1	MT.CO3
RPS21	TMEM123	SMC4	TSPAN13	ZFAND4	CD2	ID2
SH3BGR13	CH507.9B2.5	TUBG1	PPIC	CDC42	IL2	MT.ATP6
TRBC2	RP5.1042K10.10	DUT	CTNNAL1	LTB	SNRNP2	CDKN1B
CTSW	C1RL	GAPDH	LATS2	FAM132B	PSMA7	ZNF331
GIMAP7	PARP3	CENPK	TCF4	S100A8	IGLV3.19	EGR2
RPS15A	PLCG2	MED9	HSPG2	LTK	ZNF133	MT.ND1
HIST1H1D	SAMD9L	HIST1H2BH	FSCN1	BEX1	TFF3	HSPA8
MALAT1	BST2	MICB	CCL14	RP11.302B13.5	BEND7	UBN2
RPS24	CHMP5	CENPU	ARHGAP29	ZNF843	RNPEPL1	TNF
COTL1	ZNF846	KIF22	APP	HSPA1B	PTTG1	ZFP36L1
RPS7	CYB561D2.1	MAD2L1	CRHBP	DDX6	44450	SRSF7
RARRES3	TMEM135	KIF11	RGCC	GPR85	SEC24B	TNFAIP3
PSMB10	USP30.AS1	TOPBP1	CD9	THBD	TIAM2	TAGAP
RPL37	OASL	CKAP5	WWTR1	ACSL1	PDIA5	HSP90AA1
TMEM8A	NMI	ATAD3A	DNASE1L3	IL7R	IL32	XCL1
RPL30	NUDT19	DHFR	SOX4	TTI1	CISH	KLRC2
HLA.DRB1	PLSCR1	CENPW	PRKCDBP	S100A9	TOB1	TGIF1
RPS3	TAP1	IFI27L1	IGFBP4	SLC4A10	PLPP2	CCL3L3
RPL28	RTP4	AURKA	TSC22D1	P2RY14	EIF4G2	FAM46C
XIST	VAR52	H2AFX	DAB2	PFKFB3	FKBP1A	DNAJA1
FCRL6	XAF1	MTHFSD	S100A16	RP4.671O14.7	CAP1	SOCS3
ARPC3	RETSAT	AACS	RAB13	SEMA6B	TRIM62	PTGER4
ACTG1	CASP1	PTMA	CFI	INTS6	SYCP2	ZNF773
RPL31	UBE2L6	HS2ST1	C7orf31	RPL41	CKLF	MT.ND4
RPS20	FAM65C	MASTL	RAMP3	NUP62	CD3E	UBC
SRP14	WDR7	C9orf40	HES1	CDC42SE1	WDR1	ISG20L2
CD99	SERPINA6	ACTB	CALD1	CSDE1	CTSA	RP11.473M20.16
STK17A	SHPK	BARD1	ZNF468	VCAN	CD164	PPP1R15A
CD3E	SERINC2	COTL1	ATP6VOA1	ZNF234	AP4E1	TSPYL2
SIT1	TTC9	DEK	MCF2L	MCL1	CRAT	YPEL5
RPL41	TMX1	SGCB	AFAP1L1	ARRDC3	CPA5	PRKCE
PPP1CA	CBWD1	DNAJC9	ACKR1	A2M.AS1	KRT86	IRF1
CCL4	RP11.305L7.3	RRM1	SCFD2	BHLHE40	EMC1	KDM6B
MT.ND3	CNP	ANP32E	IGFBP7	TNRC6B	IGHV3.7	BMPR1A
OTUD3	SPATS2L	PPIA	PLK2	SLC51A	RBPJ	ABCC5
CYBA	C18orf25	ZNF714	RBPMS	MAN2B1	PRR11	RGS1
CMC1	IFIH1	CORO1A	A2M	SYTL3	VAMP8	GPR157
RPS25	DDX58	LRR1	RGN	TNFAIP3	CDK1	SERTAD1
RPL37A	GBP1	SND1.IT1	PROS1	PIK3R1	PIM1	DDIT4
RPS16	LY6G5C	PRKCD	ARL15	RPL21	HMHA1	CYTIP
TRGV10	APOL6	CDKN2D	HTRA1	AP1S3	ITM2C	CTD.2515O10.5
MT.CO3	PDE12	UBL7.AS1	PRCP	SERPINB9	CENPF	SLC2A3
RAC2	NFKBIL1	CENPM	ICA1	CYLD	SMPD3	SYNM
RPLP2	PHRF1	GMNN	SGK1	SMG1	CORO1A	CEP70
LCK	PYGB	KNTC1	NGFRAP1	RPL34	COX8A	EIF1

RPL7A	LAG3	ANP32B	EPHX1	MTRNR2L6	ANXA1	LYAR
RPL27	TRIM62	TRAV8.2	ITGA6	NFKB1	PCOLCE	LUC7L3
ARPC2	TAF1C	ACTR5	LIMK2	RP11.706O15.3	C12orf75	SPRYD3
HN1	ISYNA1	HELLS	PTBP2	NME2	TBC1D10C	PLCD1
TRG.AS1	PARP9	SMC2	MARCKS	NAIF1	AC092580.4	SCML4
RPS28	CHCHD6	GCNT1	LDB2	NAMPT	CCR5	EGR1
MSC	NCOA3	RLN2	PIP4K2B	GOS2	PTGER4	MT.ND5
CD3G	GIMAP7	H2AFV	ABL1	SMAP2	CXCL1	PARP8
MTRNR2L12	RAB34	DAG1	VWF	ETS1	ALOX5AP	N4BP2L2
PSMB1	VPS45	CENPH	ZNF827	FEZ1	CTD.3252C9.4	GZMK
UBA52	CUL2	TMPO	EMP2	DDX3Y	RP11.347P5.1	NYAP2

16	17	18	19	20	21	22
TNFRSF9	PAOX	KLRB1	FCER1G	CLEC10A	FOLR2	CXCL2
CXCL13	C19orf38	NCR3	TYROBP	ST3GAL6	GPNMB	UACA
MIR155HG	CHAC1	LTB	KLRF1	HLA.DRA	TLR1	GLIS3
GEM	POU2AF1	NFKBIA	IL2RB	SMOX	CLIC4	CALD1
GAPDH	JSRP1	TPT1	TOX2	LYZ	CYFIP1	IGFBP7
DUSP4	B9D1	IL4I1	CD7	HLA.DPA1	ADAP2	CCL2
PKM	WFS1	EEF1A1	TRDC	CD74	FCGR2A	MYL9
TNFRSF18	IGF1	IL23R	CMC1	NCF2	ST14	WBP5
AC133644.2	RP11.446N19.1	CD40LG	LAT2	HLA.DRB5	IGLV1.51	ACTA2
LINC00158	IGHG2	CH17.373J 23.1	TXK	CD1D	OSCAR	FHL2
TIGIT	SLC2A5	CCL20	NCR1	CHKA	MRC1	NGFRAP1
ITM2A	TBL2	SLC4A10	CD160	PILRA	MS4A4A	ADM
CD200	RP11.1070N10.3	TSPAN15	GSTP1	FES	IFNGR2	RP11.119B16.2
CD27	HSP90B1	S100A4	CCL3	GPX1	OTOA	RARRS2
ZBED2	CCDC50	AC092580. 4	IFITM2	ALOX5	TRPM4	CAV1
TNFSF4	SSR3	RPLP1	CLIC3	HLA.DRB1	CD14	CCND1
WHSC1	SEC11C	RORC	FGR	RP6.159A1.4	TIMP2	LAMB1
ZNF80	BASP1	TMIGD2	XCL1	HLA.DQA1	ZNF503	FBXL19.AS1
ENTPD1	FAM27C	RP4.539M 6.22	CD247	HLA.DPB1	CRYBG3	ITIH5
VCAM1	GPR160	KLRG1	CEBPD	MS4A6A	GPX1	IFITM3
SEMA4A	CADM1	RPLP0	BCO2	P2RY13	RBM47	TAGLN
FAM118A	CASP9	RP11.160E 2.6	SH2D1B	RP5.1065J22.8	MYO1E	MEGF8
IL2RA	AC104699.1	TNF	P2RY11	BTK	C15orf48	EPAS1
CRTAM	CLIC4	RNU11	CD63	HLA.DQB1	CD68	S100A13
LAYN	VIMP	RPS4X	SRGN	HLA.DQA2	NADK2	ZNF155
MTRNR2L1	PHGDH	SPOCK2	XCL2	PLBD1	USP6NL	RGS16
RP11.14N7. 2	CLPB	IL26	MATK	RAB32	SH2B2	ANKS3
ADAT2	MYO1E	RAB6B	TMIGD2	AIF1	CTSB	RWDD2B
TBC1D4	HERPUD1	CD160	SPRY2	CST3	ADRBK2	KRT18
FABP5	DERL3	CACNA2D4	CLPTM1	FCN1	GM2A	DLG3
TOX	ZNF503	GTF3C1	NKG7	MRC1	FTH1	ERLIN1
PLAGL1	PARM1	C21orf33	RHOC	CD180	CSF3R	EVA1C
CCDC141	RP11.161M6.2	ZFP36	STK17A	PLAUR	MARCKS	GNG11
TNFRSF4	USP6NL	TNFRSF25	EOMES	SLC1A4	C5AR1	MT1E
C3orf14	CARM1	RPS26	KLRC1	ASTN2	KCTD12	HES1
CAMK1	CD33	SLAMF1	STARD3NL	MNDA	STAB1	ENG
GBP2	CAMKK2	S100A6	IRF8	IL1B	LMO2	TSPAN4
RGS1	RP11.73E17.2	CEBPD	KLRD1	FCGR2B	RALGPS1	TM4SF1

LAIR2	CD19	MCAM	BST2	RP11.147L13.2	RIC1	ARHGEF19
GK	PRMT3	CCR6	CXXC5	MEF2C	FCGR1A	CLDN5
C17orf96	DESI1	PRSS35	GZMM	RP11.11N9.4	POMGNT2	CRIP2
PCAT29	RRAGD	JAML	FAM49B	IFI30	MPZL1	IFT43
GPR137B	DNAJC25	RPL5	PLAC8	HBEGF	ALCAM	APP
HLA.DRB5	ZXDC	LST1	FAM43A	CCDC106	CACTIN	LGALS4
FKBP1A	EAF2	TMEM117	PDLIM1	PTGS2	VSIG4	SLC39A11
LMCD1	RAB30	GPR171	B3GNT7	PLD4	ZNF823	TIMP1
SLC35F2	IPMK	SLFN12	CD38	PGBD4	MGLL	CYSTM1
SARDH	AC022182.3	IL17RE	AOAH	HLA.DMA	SMURF1	TM4SF4
LINC01480	RAPGEF2	AE000662.92	KSR1	ZNF503	WTIP	LMNTD1
TNFRSF1B	FER	PROCR	GADD45B	BASP1	SOD2	LXN
ZC2HC1A	TRAF3IP1	AQP3	CHST12	RGS2	FTL	MYBBP1A
COTL1	WARS	COLQ	SERPINE2	RNASE6	TNFAIP2	NOTCH4
MSC	METTL20	RP11.403A21.1	CCL4	SPAG8	CHKA	RRBP1
HAVCR2	ADAP2	ARL3	C12orf73	SLC27A4	NACC2	SLC9A3R2
SNX9	SLC3A2	JUNB	FASLG	C19orf38	PLXNB2	TPSAB1
NDFIP2	THAP7.AS1	ZBTB16	GFOD1	CSF1R	CTNND1	QSOX1
PDCD1	FBXL16	RP11.401F2.3	MCTP2	LGALS2	RETN	CD81
DNP1	ALCAM	GLB1L	TTC38	CD33	FES	NUDT8
SIRPG	BLNK	ENO1	APMAP	DUSP3	CD36	SELM
CHN1	TRIB3	RARG	CTBP2	FCER1A	CEBPA	NNMT
BTLA	BHLHE41	NR4A1	LDB2	ASPHD2	C1QB	ARHGAP10
RILPL2	FAAH2	IL2RG	ICAM1	SCIMP	ZNF347	RAMP1
C9orf64	RP1.197B17.3	UTS2	IFITM1	FZD3	ATP6V0A1	DOPEY2
TSPAN17	MPZL1	HBA1	MAPK1	GPR160	CTSL	ID1
AH1	SERP1	YWHAH	CCL3L3	1-Mar	LY86	MAST4
SEMA7A	ATF5	DPP4	NFKBIA	ADAM28	STK3	NEIL1
JAKMIP1	ZNF837	IER3	MIR181A1HG	CYFIP1	BHLHE41	ADGRE2
RYR1	SDF2L1	RPS13	CD300A	LILRA2	C1QA	RBFA
TMEM260	RAB20	RPSA	ARPC5L	RRAGD	SULT1A1	BCAM
PARK7	WIPI1	PKM	ARRB1	CSTA	PSAP	CEP41
CLNK	PPM1D	KIF5C	ABCB1	HLA.DQB2	CTSD	H2AFY2
MOSPD2	RNASEH1.AS1	BLK	SOCS2	NBPF1	RP5.1065J22.8	TPSB2
C17orf58	CTU2	EIF5AL1	PILRB	HARBI1	TTYH3	ISYNA1
ANKS1B	CENPN	PPP1R15A	HEG1	ARL11	LGALS3	FXD2
HLA.A	UBE2J1	CTD.2026K11.4	SLFN13	FAM20C	C1QC	ZC3H14
UCP2	NCOA5	FEZ1	PTGDR	C1QB	MS4A7	CCDC146
TNFRSF13B	TRIM32	DUSP1	LINC00996	RAB11B.AS1	AC079767.4	CEP44
MIR3142HG	MS4A4A	SNHG8	CTSW	THBD	NPC2	SKI
AFAP1L2	ZNF593	B3GALT2	SYNGR1	SPI1	LILRB4	ARHGEF12
ICOS	GMPPB	EIF5A	PTPN12	AC022182.3	ALDH2	GSN
TRAC	PLPP5	SNTA1	CAPN12	RHOBTB2	DRAM1	NFIC
STK11IP	MANF	RP11.290D2.6	QSER1	NPC2	MS4A6A	RP3.402G11.26
SLC27A2	SLC35B1	CISD3	MIR181A2HG	IGSF6	AIF1	IL6ST
PSME2	PHLDB1	HNRNPA1	AGTRAP	VMO1	SPI1	SLC22A18
MYL6B	PKHD1L1	LTA	PIK3R3	GRN	DOK3	TFEB
EPHX2	ATF4	CDHR1	SKAP1	GAPT	GRINA	CRIM1
LYST	MZB1	THAP8	LPAR6	PAXIP1	HLA.DMA	HYAL2

CALR	GNG7	IKZF2	GSN	HLA.DMB	TYMP	ORC6
PHLDA1	IFI27L1	CTSA	FAM41C	S100A9	CPVL	CLU
MS4A6A	IGKC	TLE1	NEDD9	CENPW	LINC01272	CLCN3
DAB2IP	PDXK	RPL36A	LYN	SPIB	RAB31	SAA1
BIRC3	PLBD2	IER2	OSTF1	CD40	PLBD2	CFH
GFOD1	SRM	BTG2	EIF3G	IMPA2	MT1H	ATAD3C
RP11.1399P 15.1	SLC1A5	RORA	MAP3K8	C1orf162	VEGFB	DNAL4
TTN	SSR4	CD69	PFN1	PPM1D	FPR3	GSTM4
LINC00152	NOP9	ADAM12	NUDT8	CLEC4A	SLC43A2	SLC25A16
CD79B	IGKV3.11	TNFSF14	THEMIS2	CTNND1	KLF4	B3GALT6
SLC4A2	NUDT18	CAPG	KLRB1	PHACTR1	ALOX5	TRRAP
TNIP3	PDIA6	DUSP2	DHRS3	FAM26F	LRRC25	S100A16
SOD1	TXNDC11	SNHG25	SYK	CD79A	CD9	MALAT1

### A1.7 – Top genes in idiopathic pulmonary fibrosis from cNMF analysis (dataset 1)

1	2	3	4	5	6	7	8
LIMD2	MS4A6A	KRT17	KHDRBS3	MALAT1	ADAMTS9	TYMS	SFTPB
NKG7	FCER1A	TACSTD2	SNTN	PTPRC	PCDH17	RRM2	SLPI
RARRES3	HLA.DRA	KRT7	TPPP3	MBNL1	ACKR1	TK1	MUC1
GZMH	HLA.DPA1	KRT18	FAM183A	SYNE2	GJA1	DUT	SLC34A2
ISG20	CD74	GDF15	DNAI1	MACF1	CLDN5	KIAA0101	NAPSA
GZMA	HLA.DPB1	KRT8	ADGB	SYNE1	EMP1	PCNA	SFTPC
CORO1A	PKIB	CXCL1	TEKT1	UTRN	ADGRL4	GINS2	C16orf89
PFN1	CPVL	CST6	C20orf85	RNF213	TM4SF1	CENPU	MACROD2
IL32	HLA.DQB1	SFN	RGS22	DIP2A	THBD	DHFR	CYB5A
PSME2	CD1C	TUBB3	FAM92B	STAT4	CTGF	CLSPN	SFTA3
GZMB	CD207	MDK	AGR3	SRSF11	IL6	MCM7	S100A14
HLA.A	HLA.DQB2	COL1A1	DNAH12	XIST	SOX18	FEN1	RNASE1
PSMB10	CST3	ANXA8L1	RSPH9	SLFN12L	MYCT1	UHRF1	SFTPD
CD52	CD1E	IGFBP7	TMEM45B	LNPEP	AQP1	ASF1B	SCGB3A2
PSME1	CSF2RA	TPM1	CAPS	DDX17	SOCS3	PKMYT1	SFTPA2
CCL5	CD1A	LRRN1	PPP1R32	PTBP3	TCF4	STMN1	SFTA2
SH2D2A	SIGLEC10	EPCAM	RSPH1	NEAT1	GNG11	MCM5	NKX2.1
CD3D	C15orf48	CD24	CFAP126	SMCHD1	CD34	FAM111B	SELENBP1
UBE2L6	HLA.DQA1	CXCL2	TSPAN1	ZEB2	ADIRF	CDT1	SUSD2
GYPC	RNASE6	DSG2	C11orf88	ANKRD44	BCAR1	H2AFZ	CEACAM6
CASP4	CSF1R	F3	C5orf49	CELF2	LIFR	ZWINT	KLK10
ARHGDIB	HLA.DRB1	ITGB6	FXD3	SSH2	SPARCL1	MCM2	SFTPA1
IFITM1	PLD4	TNFRSF21	CAPSL	KIAA1551	TUSC1	CDC6	ELF3
CD38	FAM26F	CTSE	C9orf24	RSRP1	SPRY1	CENPM	CXCL17
PSMB8	AIF1	PLAU	FAM166B	HNRNPA2B1	ANGPT2	MCM3	SEPP1
PPP1CA	IL18	C8orf4	ZMYND10	ATM	TSPAN7	RAD51	CRTAC1
PSMB9	MNDA	TNFRSF12A	DNAH10	VPS13C	IFI27	CDC45	S100A13
STAT1	PLEK2	CLDN4	FAM216B	RBM39	ID3	CDC45	MGST1
SUB1	CD14	PTGS2	C6orf229	AIM1	VWF	TUBA1B	EMP2
TNFRSF14	LST1	MMP7	DNALI1	LCP1	PALMD	RANBP1	WFDC2
GIMAP4	CLEC4A	PON2	TUSC3	MTRNR2L12	POSTN	GAPDH	C1orf116
LY6E	CD86	MUC4	PIFO	DDX3X	A2M	MCM10	AGR2

CST7	CLEC7A	CH17.360D5.2	DYNLRB2	CASP8	ROBO4	MND1	C19orf33
GBP1	KCNMB1	CLDN7	SMIM6	FAM65B	MSRB3	RAD51AP1	KCNJ15
COTL1	KCTD12	SERINC2	CASC2	PRKCH	TIMP3	MCM4	CLDN18
RPS24	BASP1	RIPK4	DRC3	THEMIS	SNCG	PAICS	ACOXL
ATP5G2	GPX1	TMEM98	DNAH6	NKTR	C6orf141	TUBB	SLC22A31
S1PR4	CACNA2D3	KRT19	FAM229B	CLEC2D	SDPR	GMNN	PRR15L
GBP4	EREG	ITGA2	RP11.295M3.4	CCNL1	INHBB	UBE2T	FOLR1
CLIC1	TRPM4	FHL2	CFAP157	PRRC2C	SHB	CDCA7	MALL
TAP1	THBS1	NRG1	CLDN3	PRMT2	WNT2B	PTMA	EHF
TMSB10	RAB32	CCND1	C11orf70	EML4	FGD5	DTL	MET
RPS15A	FCGR2A	LAD1	CFAP221	DDX5	HSPG2	HMG2	PLA2G10
AES	IL13RA1	LAMC2	EFCAB1	CHD2	PCAT19	RRM1	MECOM
PRKCB	IFNGR2	WNT7A	SRGAP3.AS2	GPRIN3	YBX3	HELLS	SFTA1P
CD8B	CXCL10	ALDH1A3	NME5	ARGLU1	KLF4	SMC2	EFNA1
IRF1	TMEM176B	CDH1	OSCP1	KDM6A	DLC1	BRCA1	IRX3
UCP2	IL1R2	EPB41L4B	PACRG	ITK	SPARC	RAN	TSPAN12
HIGD2A	TMEM176A	GAS6	C1orf194	SLC20A1	EGFL7	WDR34	NPC2
RAC2	CLEC5A	TINAGL1	C9orf135	DOCK10	NNMT	RFC4	AQP5
HAVCR2	CLEC4E	CYR61	CKB	KLRG1	IGFBP4	CENPH	CTSH
VAMP5	FPR1	FN1	MAATS1	LUC7L3	RCAN1	CHEK1	BCAM
LITAF	TNFAIP2	ITGB8	PLPP2	PARP8	CYYR1	SLBP	MTUS1
ARPC2	ADORA3	LAMB3	SPAG17	MBP	ENPP2	CENPW	CNKS1R
HCST	IDO1	LINC00511	C7orf57	RNF19A	MYC	ESCO2	GOLT1A
MIR4435.2HG	LY96	CLDN1	FAM81B	IQGAP1	EGLN3	HMGB1	PIGR
ARPC3	ADAP2	TAGLN	LRRIQ1	STK17B	AIF1L	TCF19	AC026471.6
MYL6B	LPAR3	TGFBI	HYDIN	ADAM10	PDK4	PPIA	PGC
LDHB	RTN1	TSPAN6	MORN2	MDM4	EPHB4	TMEM106C	LIPH
CAPZB	LILRB2	RHOD	TMEM190	CBLB	RNF217	NASP	TACC2
BIN1	FCGBP	S100A16	C6orf118	DDX6	APOD	HMGA1	H1FO
CFL1	CD163	KDR	SPATA18	STK4	CYTL1	LMNB1	FAM3B
HLA.C	HLA.DRB5	EPHB2	ROPN1L	RORA	CAV1	MCM6	CDKL2
CARD16	TCN2	CXCL8	ENKUR	FNBP4	MGP	ORC6	CAV1
PSMA4	S100A8	TM4SF1	CALML4	IL10RA	ESAM	FANCI	MAL2
C5orf56	TIGD3	TPBG	CFAP43	AKAP13	TDRP	HNRNPAB	LIMCH1
CNN2	S100B	TMEM92	TSPAN6	MKLN1	EMCN	CCNE2	SCGB3A1
CD8A	HLA.DMB	CDH3	DPCD	RABGAP1L	MGST2	RNASEH2A	RAB25
BTF3	BTK	TP53I3	CYP4B1	FUS	ARHGAP23	C19orf48	AK1
SH3BGR13	DFNA5	ANXA3	ZBBX	IKZF3	C4orf32	CHAF1A	DUOX1
ADA	VCAN	SPINT2	WDR38	TGFBR3	PREX2	HIST1H4C	GPRC5A
ATP5F1	PLAUR	C19orf33	CFAP45	DGKD	PDE2A	DNAJC9	CGN
GMFG	SPI1	GPRC5A	CCDC39	PPP1R10	GIPC2	SPC25	CLDN4
GBP2	SERPINF1	CTXN1	FOXJ1	SF3B1	PTRF	EZH2	CAV2
LIME1	S100A9	IER3	ABO	ITGA4	CLIC4	RPA3	EPHX1
PTRHD1	RNASE2	NOTCH3	MUC15	ANKRD36B	NFIB	MYBL2	NEDD4L
CD27	CCL17	CD9	C9orf116	CD46	MEOX1	HIST1H1B	PVRL4
TRAV13.2	IGSF6	SLC4A11	TNFRSF19	STAT3	HRH1	RFC2	C4BPA
MRPL10	HCK	PTGFRN	LINC00511	PAK2	OLFM1	SAC3D1	PON3
RTP4	MEF2C	SPINT1	SLC44A4	CYTH1	CDC42EP5	SLC25A5	GSTA4
ATP5L	LYZ	SOX4	UBXN10	ATF7IP	CCL14	TPI1	GPRC5C
ARPC1B	IFITM3	PRKAA2	CCDC113	TSPYL2	CXorf36	DTYMK	LAD1

LSP1	SAT1	MISP	ERICH3	SON	ETS2	SNRPD1	OLFM1
IDH2	CSF3R	GRB7	DYNC2H1	ANKRD36C	BCAM	NME1	NGFRAP1
ACTG1	PARM1	SERPINA1	MAP1A	7-Mar	MID1	LIG1	LRP6
SLC25A6	ADAM28	IGFBP3	WDR78	BIRC6	KANK3	C1QBP	SCNN1B
PRF1	SERPINF2	IGFBP4	MAPK15	EIF4G2	ASAP2	ENO1	RAI14
LAG3	TMIGD3	PHLDA2	PRR29	MYCBP2	MGLL	CENPP	PTPRU
NDUFB9	EGOT	ANKRD65	LDLRAD1	PNISR	CNKSR3	HIST1H2AJ	SERPINF2
SLC1A4	HPGDS	PDLIM4	MYH14	SMG1	VWA1	ANP32E	LMO3
LAT	PAPSS2	EPHB4	MISP	DOCK8	ARMCX1	ATAD2	GRAMD2
EIF3F	CXCL9	KCNK1	CCDC148	KDM5A	EPHA2	HMGB2	ANKRD65
KLF3	MARCKS	PTPRU	NPHP1	DYNC1H1	PLS3	ANP32B	AC007405.6
BRK1	PVRL2	PPIC	RP11.53M11.3	MYH9	PLSCR4	NUDT1	ARHGEF17
GPSM3	CD1D	IFI27	CATSPERD	SP100	IGF2	SNRNP25	SMIM22
DECR1	MAFB	SORBS2	TMEM231	RANBP2	SH3BP4	DEK	SPINT2
TWF2	GK	APBB2	CCDC40	PCM1	LAMA5	H2AFX	PDPN
ATP5C1	AC009506.1	DSP	DZIP1L	TMEM2	EFNB2	HSPD1	AJUBA
GBP5	GAPT	ST14	EFCAB10	SYTL3	LAMB2	DSCC1	PEG10
LINC00152	LILRA2	SIK1	ST5	RP11.488L18.8	CDKN1A	RAD54L	TMEM125

9	10	11	12	13	14	15
CD68	UBE2C	RPS12	ALOX5AP	NR4A1	RGL1	GNLY
C1QA	CDC20	RPL32	ZNF683	HSP90AA1	JARID2.AS1	FCGR3A
APOC1	PLK1	RPS14	TMSB4X	JUNB	AC093627.9	KLRF1
C1QB	CCNB1	RPL13	CKLF	HSPA1B	KDELR3	IFITM2
FBP1	HMMR	RPL30	CRIP1	HSPA8	ACVR1C	SH2D1B
MCEMP1	TOP2A	RPS3	RGS1	NR4A2	NRN1L	FGFBP2
C1QC	CCNB2	EEF1A1	S100A4	DUSP1	RP11.1212A22.4	CTSW
MARCO	CENPF	RPS27A	SH3BGRL3	BTG2	PRRT2	TYROBP
CYP27A1	ASPM	RPS23	PTPRCAP	DNAJA1	TMEM86A	NKG7
MS4A7	TPX2	RPS25	PLP2	DNAJB1	C2	MYOM2
TREM1	CENPE	RPS18	VIM	FOS	RP11.63L7.5	PRF1
TNFSF13	CDCA8	RPL34	CAPG	HSPA1A	CACNA1I	CD247
MRC1	ARL6IP1	RPS5	ITM2C	HSP90AB1	AP001046.5	CST7
CXCL16	NEK2	RPS13	CD82	TNFAIP3	RP11.856F16.2	SPON2
ACP5	DLGAP5	RPL9	AC092580.4	FOSB	AP000304.12	CMC1
SLC11A1	CENPA	RPL10	IL32	NFKBIA	CTD.2105E13.16	TTC38
GRN	KIF14	RPL11	S100A6	CD69	RP11.705O1.8	FGR
FTL	MKI67	RPL19	CD2	PPP1R15A	LHFP	TRDC
LGALS3	KIF23	RPS8	APOBEC3G	CSRNP1	ADAMTS17	KLRD1
RP11.598F7.3	FAM64A	RPLP2	LGALS1	ZNF331	RALGPS2	EFHD2
VSIG4	BIRC5	RPL18A	CXCR6	RGCC	MAMLD1	ITGB2
GPNMB	DEPDC1	RPS21	CXCR3	SLC2A3	HDAC11.AS1	CD300A
APOE	AURKB	RPS28	ITGAE	ATF3	SPSB1	KLRC3
LINC01272	KPNA2	RPL18	CD52	HSPH1	RP11.141B14.1	KIR3DL2
SLC7A7	CDCA3	RPS6	MYL6	ZFP36	RP11.91G21.1	PRSS23
ALDH2	NUSAP1	RPL5	CD63	UBC	AMPD3	FCER1G
OLR1	AURKA	RPL21	ATP5E	NR4A3	LINC01220	TRBC1
CTSD	NUF2	RPS3A	BATF	TNFSF9	RAMP3	PLAC8
CTSL	KIF20A	RPS27	ZYX	JUN	CCNI2	PTPRCAP
SPI1	CCNA2	RPS10	ACTB	GADD45B	HIST1H2BI	LITAF
FTH1	CEP55	TPT1	RPS4Y1	CTD.3252C9.4	COL6A1	FCRL6
CTSB	CKAP2L	AC090498.1	MT.ATP8	DDX3Y	TTC12	CCL3

CSTB	TTK	RPL14	RBPJ	NFKBID	SH3BP5.AS1	PLEK
IL3RA	CDK1	IL7R	HLA.B	MYADM	SBF2	RPL17
FABP4	GTSE1	RPS4X	PHLDA1	NFKBIZ	C6orf120	ADGRG1
INHBA	CDKN3	RPL35A	ITGA1	FAM46C	FBXO45	RHOC
ALOX5	SGOL2	RPL3	DUSP4	RGS2	RP11.486I11.2	KLF2
CCL18	KIF2C	EEF1B2	RPS29	KLF6	FLVCR1.AS1	S1PR5
MS4A4A	TROAP	RPL39	ITM2A	NFKB1	PGBD4	OSBPL5
PLXDC2	HMGB2	RPL23A	PTMS	ANXA1	PSMG3.AS1	PTGDR
TREM2	CKS1B	RPL7A	CPNE7	BRD2	ZNF124	TBX21
CSTA	KIF11	RPLP0	CLIC1	MCL1	AC062029.1	LAT2
ASAH1	TUBB	RPL36	TAGLN2	PNRC1	OBSCN	IFITM1
DAB2	CDCA2	RPLP1	AC002331.1	LMNA	DCLRE1B	CX3CR1
LYZ	TUBA1C	RPS16	LAG3	REL	DHODH	APMAP
CD9	PRC1	RPL29	NDPIP2	RASGEF1B	ZNF558	RAP1B
PLBD1	CKS2	RPL28	PPDPF	ZFP36L1	LATS2	CHST2
LPL	APOBEC3B	RPL26	RGS18	TNF	ZNF624	CYBA
RETN	PTTG1	RPS26	B2M	BIRC3	C21orf91	HOPX
PCOLCE2	KIF20B	RPS19	S100A11	H3F3B	C11orf63	B2M
GLDN	TUBA1B	RPL8	LCP2	HSPE1	DPY19L3	ZEB2
CTSZ	BUB1	RPL10A	PGK1	CDKN1A	RP1.178F15.4	LYN
SERPINA1	CASC5	RPS15A	CISH	PHLDA1	TAPT1	AKR1C3
FCGR1A	KIFC1	RPL12	SLC1A5	SLC38A2	PEX5	CLIC3
GRINA	TUBB4B	RPL37	CTLA4	DUSP2	ZNRD1.AS1	NCR1
FCGRT	ECT2	RPSA	ENTPD1	YPEL5	SAMD10	GZMM
FCER1G	MXD3	EEF1G	ACTG1	IER2	GS1.124K5.3	GSAP
TIMP2	ANLN	FAU	GLIPR2	BHLHE40	STARD9	PLEKHG3
MSR1	SMC4	RPS9	COTL1	IFNG	FER	RHOB
TYROBP	RACGAP1	RPS2	LDLRAD4	SQSTM1	CNTROB	SYNGR1
NCF2	HJURP	RPS15	TRBV27	ZC3H12A	KLHDC10	GZMH
LTA4H	STMN1	RPL22	IL2RG	TUBB2A	POC1B.GALNT4	CTBP2
HCAR3	NCAPH	RPL13A	CBFB	HSPD1	DAG1	TPST2
S100A11	CCNF	RPS7	MINOS1	UTY	ARF4.AS1	NMUR1
IFI30	PSRC1	RPL27	MYL12B	RALGAPA1	GATC	LILRB1
CXCL3	KIF15	RPL15	HCST	RSRP1	CERS4	MIR181A2HG
HMOX1	IGHV1.69	MT.ND4L	CD40LG	TIPARP	PFKL	KIR2DL1
GCHFR	PRR11	GNB2L1	CD3D	RHOH	DGKA	TMSB10
CD163	TMPO	RPL6	SIT1	NABP1	AC002117.1	CD244
LRP1	ARHGAP11A	MT.CO2	HLA.DRB1	CD83	FUT8	CALM1
CD302	HMGNT2	RPL35	XCL1	CORO1B	SEC24D	CCND3
PPARG	PBK	RPL24	RPL17	KDM6B	SIK3	CXCR2
HLA.DRB5	KIF4A	RPL27A	USMG5	SRSF7	CNOT3	SIGLEC7
CPM	NDC80	UBA52	CD96	IFRD1	RASSF2	KLRC2
GPD1	SGOL1	RPL38	CTSA	ICOS	OXNAD1	RP11.81H14.2
RAB13	IGLV1.51	NACA	AGTRAP	PTGER4	HUWE1	UCP2
GPX1	HN1	GLTSCR2	KLF6	SERTAD1	INTS6	LAIR2
GSN	GPIHBP1	RPL4	IL9R	TRAF1	MAP4	MT.CO3
BRI3	KIF18B	RPL7	EGR1	EML4	OSBPL3	RP11.277P12.6
TGM2	H2AFX	RPL37A	SMPD3	CREM	MYO19	CD160
PSAP	SHCBP1	RPS29	TRBV20.1	GATA3	NBAS	PFN1
IGSF6	KIF22	TOMM7	CFL1	CCR8	HAUS5	CXXC5
MITF	MAD2L1	RPL31	S100A10	PDE4B	POLR3E	GPR141
HBEGF	DEPDC1B	MT.ATP6	ZFP36	SGK1	RRN3	LGALS1
SLC1A3	NCAPG	PFDN5	DAD1	CITED2	IRF2BP2	KIR3DX1
COLEC12	UBE2S	RPS20	APOBEC3C	EIF5	B3GNT2	SLC1A7
HNMT	SPC25	RPS11	SRGAP3	RELB	GPATCH8	PTPN12
RP5.839B4.8	CDKN2C	SESN1	CALR	DNAJB4	ZNF91	GZMB



FFAR4	H2AFV	PCBP2	HLA.DQA1	CHMP1B	CDR2	C1orf21
PILRA	KNSTRN	EEF1D	ID2	ANKRD37	ZNF362	IL2RB
CD300LF	GPSM2	BTG1	UBC	RBKS	RPUSD4	SH3BGR13
MMP19	HIST1H4C	MT.ND4	UQCR11	NEU1	TPK1	SERF2
HLA.DRA	KIF18A	SARAF	PTPN7	ARL4D	KIAA1328	MTSS1
RAB31	POLQ	KLRC1	MYL12A	TUBA1A	ZBED4	BIN2
AGRP	CENPW	EEF2	CD99	LTB	AP5M1	MLC1
SLC31A2	CKAP5	CCNI	TMEM200A	SOCS3	FCRL5	PRMT2
MAFB	FAM83D	RPL36A	KRT86	HMGCS1	CEP164	FCRL3
DCSTAMP	HMGB3	BTF3	LSP1	LINC.PINT	ZDHHC13	GSTP1
DEFB1	SPAG5	RPL23	LINC00152	TAGAP	PTPN9	IFITM3
RAB20	C21orf58	RPS24	CCDC167	NELL2	TRMT2B	TXK

### A1.8 – Top genes in idiopathic pulmonary fibrosis from cNMF analysis (dataset 2)

1	2	3	4	5	6	7
RPL41	CTSL	MICA	CDK6	C8orf4	HLA.DPB1	AC004832.6
RPS27	OLR1	RANBP9	PTPN4	KRT8	HLA.DPA1	MYC
RPL39	C1QB	IGHGP	KLRF1	SFTPA1	CD74	RRM2B
RPS4Y1	MIR3945HG	GRK6	KIF21B	KRT18	HLA.DQA1	AL160400.1
HSP90AB1	C1QA	WHAMM	P2RX5	AQP1	HLA.DRB1	AL662844.4
RPL36	IGSF6	NUMA1	SH2D1B	SFTA2	HLA.DQB1	BIRC3
RPL34	TCEAL9	SDE2	GTF3C1	EDN1	HLA.DRA	DCP2
RPL13A	GCHFR	FAM53C	IL2RA	MGST1	HLA.DRB5	FAM43A
DNAJB1	CCL18	USP47	S1PR5	ADIRF	WFDC21P	PIM1
RPL21	HPGD	SUCO	SLC15A4	NAPSA	S100B	MBD1
RPS29	FABP4	MARK2	GNLY	AGR2	CST3	ACVR1
RPL12	C1QC	PGGHG	OSGIN2	KRT19	HLA.DQA2	IFNG
RPL36A	CD109	TRIM27	NBN	FOLR1	TXN	PFKFB3
RPL11	MS4A7	LETM1	BCL2L1	PGC	RNASE6	APPBP2
RPL17	TNFAIP2	SEC24B	IL18RAP	SLC6A14	U62317.5	NFKBIA
RPS28	FPR2	DNAJC4	TMEM125	CLDN7	CXCL16	RALGAPA1
RPL9P9	ACP2	FZR1	TMEM41B	SFTPA2	CSF2RA	SOCS3
RPS15A	CD163	NDUFS2	SPON2	FXYD3	CPVL	OSM
RPS27A	CTSD	RING1	MCTP2	WFDC2	AXL	TMEM263
RPS25	FBP1	N4BP1	PLAC8	CTSH	IL1R2	ADD3
RPL32	VAT1	EIF1AY	TRAF1	NNMT	LDLRAD4	AC087239.1
SNHG5	LAIR1	GADD45G	MLST8	SFTPB	LY86	RAB29
RPL10	MRC1	RBM14	KIAA1191	AQP3	NAAA	MAPKAP1
HSPE1	TLR2	PREX1	HAVCR2	FGFBP1	PPT1	MAST4
HSP90AA1	ANXA5	MAP1LC3A	STX3	SDR16C5	LGALS2	BTG2
RPS15	VCAN	AIDA	RRAS2	C19orf33	PPA1	SLC25A32
RPS8	SDCBP	UBE2H	STAM	CXCL2	TCN2	ARHGEF2
RPL13	BACH1	PRPS1	SLA2	KLF5	NQO2	CDK8
RPL10A	S100A11	FAM162A	ATF2	CLDN4	NLRP3	HDHD3
SOD1	CTSB	OFD1	GBP2	CXCL17	UROD	SNHG19
DDX3Y	FCER1G	TRAF4	KMT2B	KRT7	CEBPD	NFE2L2
RPL26	AVP11	LPIN2	APOL3	MAL2.1	TIMP1	AL121839.2
PABPC1	LGALS1	MFSD1	INPP5D	CYB5A	HLA.DRB6	IL18R1
RPS26	MMP19	MIAT	RPP25L	MSMO1	SAT1	ZFP91
RPL35A	ASAH1	EXOSC8	CHST2	PEBP4	HLA.DMA	ZFP36L2

RPLP2	CTSZ	TNFRSF9	GSKIP	SFTPC	TUBGCP2	SLC2A3
RPS14	ACSL1	BCL2	BPGM	ABCA3	CLEC7A	CRK
RPS12	RPF2	AC022431.1	TNFRSF4	SFTPD	C1orf162	TUFT1
RPL18A	SDSL	GPRIN3	CAV2	KRT16P1	RIPK2	STAB1
HSPA1A	PMP22	RASSF7	LAT2	TM4SF1	AIF1	DUSP22
TSC22D3	ALDH2	GTF2F1	KIF3A	SELENOP	RAMP1	SLC25A4
RPS23	S100A6	BTN3A2	DCLRE1C	CXCL8	RPL8	RASD1
TOMM7	MT2A	TMEM219	SLC50A1	NPC2	GNA15	CSRNP2
HSPA8	ALG8	TMEM170A	CST7	CCND1	FCGR2B	CDK2
RPS3A	UBE2E2	MT1F	YBEY	SDC4	NR4A3	KLHL21
RPL30	FN1	BEST1	ST6GALNAC4	TACSTD2	YIF1B	MINDY2
RPS7	TYMP	DCTN3	FAM3C	PIGR	RALA	HES6
UBB	SNX2	PRPF6	VIM.AS1	MUC1	RAB31	SPAG9
RPS19	MCEMP1	ABI3	TRGC1	EMP2	PGLS	EIF5A2
IGLC3	BLVRB	CWC25	PES1	LAMB3	CD86	TRIB2
RPS3	MARCO	MAFB	TMEM115	RND1	CD302	ZFR
RPL22	TPMT	TAOK3	GSAP	HSD17B4	TRMT6	AL049840.4
HSPA1B	CREG1	PCNA	STAR10	SOLE	ERGIC1	GAK
HSPH1	ALOX5AP	SFT2D1	RN7SL2	AGPAT2	CPM	AL365361.1
RPS6	AC015912.3	DPM3	CLPB	GPRC5A	TRIM28	UFL1
RPL7	JPT2	SDC4	KLRD1	SLC9A3R2	MGST2	UTP23
RPL23A	MGST3	NT5C	MMD	MPZL2	AL022311.1	ALAS1
RPL6	GK	ADGRE5	C19orf66	EPCAM	RAB11FIP1	UNC13D
MS4A1	GLRX	PTBP1	KRT16P1	MFSD2A	HBEGF	KATNBL1
RPL15	CD9	TNIP1	RAB29	PAR6B	AP1S2	DNAJC2
RPL3	IFI6	TAF1D	DNTTIP1	SERPINA1	ATP1B3	AL118516.1
UBC	LGMIN	TAF15	FAM160A2	GJA1	SLC16A3	LAPTM4B
UBA52	SERPINA1	TMEM134	GBP5	ASPH	SYNGR2	CD69
EIF1	GSTO1	WNK1	KDM5C	ISOC2	PPP4R2	KIAA1191
RPL38	BCAT1	NR1H2	TRIM44	DHCR24	COTL1	UCK1
EP400	CAPG	GRAP2	FAM91A1	LAMP3	NEAT1	ZNF317
RPS21	SMIM25	GADD45A	BTN3A1	ALCAM	B3GNT5	ABHD17B
ADAM28	VSIG4	SNRPN	DLST	RGS16	GPX1	ABHD13
RPL31	SNX3	EBP	TIMM50	TNFRSF12A	TREM1	STK38
AC058791.1	SH3BGRL3	ISCA1	SMARCD2	UTP3	BIN1	PMEP1
FAU	C19orf25	ZYX	ADRB2	SFN	MAP7D1	SLC38A10
DONSON	MS4A4A	NSMCE3	FGFBP2	DHCR7	PTPRE	ZBTB4
SELENOK	ATP6V1C1	SSNA1	CAMK1D	TACC2	LAT2	NPC1
SNHG8	TSPO	UPF2	AC093010.2	MAST4	TMSB10	SGTB
METTL8	RRAD	TES	DFFA	SLC34A2	SERPINB1	LACTB
RPS13	PAPSS1	ZNF267	FAM126B	EPS8	GPR137B	C21orf59
RPLP1	LST1	TLE3	NFX1	CNN3	GOS2	TRAF4
COQ8A	PSAP	ECH1	DPF2	CD274	AMPD2	NUPL2
C1orf228	MRPL15	SLBP	AGAP3	TSPAN4	CD83	UBR3
RPL27A	GLUL	DDX27	DPP8	SLPI	FOXN2	SEC31A
FCMR	ETS2	KMT2E.AS1	GK5	LGALS3BP	SPI1	RLF
DNAJB6	MS4A6A	PSMB6	HDAC5	F3	IDH3G	DYM
KLF6	RAB13	TMED9	PIGV	CLDN1	MXD1	MTRF1L
BCAS4	CNDP2	KHDRBS1	CTNNA1	RAB34	TUBA1B	STT3A
ZC3HAV1	FABP5	SMS	CHPF2	PRSS8	GSN	TPP2
CACYBP	SEMA6B	JUND	DRAM1	IFT57	MAPKAPK3	AC113398.1
RGCC	TYROBP	ITGAE	PIK3R5	NCOA7	COPS2	RYK
ATN1	FKBP1A	TAX1BP1	ZNFX1	CAVIN1	FNIP2	ACBD5
CNOT9	GRN	HIST1H2BG	FAM122A	PON2	HLA.DMB	MYCBP
ZNF831	OGFRL1	HIPK1	RNF19B	FPGS	SLC25A6	BTN3A1
CCR7	MCOLN1	PSMB10	HSD17B4	NEDD4L	MS4A6A	STIM2

RGS2	TMBIM4	RNF7	NCOR1	C11orf96	B4GALT5	TNPO1
EEF1D	THBD	LSM8	TAF11	ITPR3	SNX8	NARF
RPL28	ACP5	CDC42EP3	SCAF1	EID3	STAR4	TUG1
METTL12	FCGRT	TXNIP	CISD1	CISD1	THBD	ICOS
SNHG12	NOP10	AKAP9	BHLHE40	ELF3	RAC1	HMGB3
COL18A1	TMEM50A	MOB1A	TM2D2	CSF3	RNF2	GPR137
NUDCD3	VAPA	SF1	DGKZ	CTNNA1	FLII	CHD8
MT.TV	LGALS3	ARID4B	HTRA2	CAV1	LYZ	KLF6
PFDN5	CORO1C	ARID5B	ADIPOR2	CADM1	GCA	TMEM30B

<b>8</b>	<b>9</b>	<b>10</b>	<b>11</b>	<b>12</b>	<b>13</b>	<b>14</b>
CUX1	DENND1C	BCL9L	NUSAP1	PGK1	IGHG1	PI3
S100A9	CD3D	PAPD5	CKAP2	CXCR6	SPAG4	SGMS2
IL1B	TMSB4X	KDM3A	PTPN18	CD7	IGHG3	TMC5
S100A8	RAC2	POLR1E	STMN1	MT.ND2	WARS	PEG10
SERPINB2	TMEM107	PBRM1	SAC3D1	GZMB	PRDX4	CYP2B7P
NBPF14	ACTB	HNRNPL	LIMA1	SRP54	BASP1	MGLL
TNFAIP6	CCL5	CPQ	PCLAF	LAG3	COBLL1	S100A14
ATP13A3	CKLF	LINC00623	KIF22	FAM129A	CHST2	GPRC5A
CD93	FOSB	VEGFB	AP1S1	PRF1	SSR4	ERRFI1
PTGS2	TRAC	CEBPZOS	PRKY	PTMS	Z93930.2	LRRC8A
AQP9	KLRK1	DICER1	NCF4	PTMA	RSU1	SFTPC
THBS1	CD52	RNPEPL1	SPNS3	CLDND1	FAM89B	C11orf96
NAMPT	MPV17	ARID1A	ACAA2	MT.CYB	IGHM	SFN
VEGFA	FKBP3	RIPK2	CRNKL1	SARAF	TNFRSF18	F3
CYFIP1	AC245014.3	SDHB	DES1	D2HGDH	COMMD1	SLPI
SERPINB8	JUN	ZNF24	HMGB2	COMMD5	MIR4435.2HG	DUSP7
PPIF	GIMAP1	PPM1D	ECI1	FURIN	JCHAIN	CAV1
NDUFA4	ERICH1	UNC93B1	RGL4	LINC01871	SCYL1	BBC3
CCDC93	TFPT	AKAP17A	ZSCAN16.AS1	MRPL32	CYTOR	SYNE1
MED13L	MLLT10	SPN	TPGS1	P2RY10	CAV2	LMO7
MLST8	IER2	DHX15	DUT	NKAP	VOPP1	MFSD2A
G0S2	MALAT1	ELP2	TMEM33	THUMPD3.AS1	ITPR3	C19orf33
CXCL8	RBL2	SZRD1	TFDP2	GPR171	CSNK1E	ELF3
PHC2	PRAF2	PMVK	ZNF688	SURF4	SEC11C	TACSTD2
ANPEP	SCCPDH	FAS	NMRAL1	TPT1	FNDC3A	MAL2.1
SOD2	SPRY1	PQLC1	FHOD1	POLR3E	IGHA1	THOC2
PRPF8	NAA38	TGIF2	MIS18BP1	COA4	NCR3	SLC34A2
SNX27	TMEM42	RANGAP1	SP110	SEC61B	TSPAN13	RRAD
FOPNL	CHMP4A	KAT6B	HIST1H4C	SC5D	RAB31P	BEX3
TNIP3	U3.42	ITSN2	DCTN3	POM121	EDEM2	FAM129B
SLC15A3	S100A4	WAC	CENPX	TUBA1B	SEL1L	CAVIN1
CDC42EP2	POM121C	ITGAL	CALCOCO2	NR2C2AP	VIM.AS1	TNFRSF12A
RNF44	CBX5	CAMK4	CENPH	NOLC1	IGKC	TM4SF1
PLAUR	CCDC18	TSEN54	AC008443.5	MT.ND3	CHPF	PHLDA2
PIGK	PLEKHF1	CMIP	FLYWCH2	MT.ND1	TSPAN31	IL1R1
INHBA	AC103591.3	SERINC3	CKS1B	SLC35A4	INSIG1	LIF
SLC9A8	PIK3IP1	FMNL1	CCNK	LGALS8	ELK3	RAB13
GK	EVL	SMC4	TMEM120B	CREM	RBM48	TXNRD1
NCOA6	MOSPD3	LIMS1	CNTRL	SNAI3	CUL1	MYO6
MRPS18A	UCHL5	JMY	HMG2	NEU4	KRTCAP2	MPZL2
PDHX	CD3G	RBM7	DDX50	CSTF2T	XBP1	SFTPB
EREGL	RECQL	C6orf89	PPM1M	SRGN	BCL2L1	GJA1
TADA2B	AC005921.2	CRBN	DDX23	GRAMD1B	FKBP11	EPCAM
BNIP3L	NUDT14	ANKRD44	MALT1	DDX56	AC011446.2	EMP2
RAB31	MCM5	MYH9	MCM3	PIGC	HENMT1	WFDC2

SRF	ARRDC3	SAT2	SUGP2	TMEM173	TNFAIP2	PIGR
USP21	CD2	PPM1B	HMGXB4	BTG1	DGAT1	PEBP4
PLEKHG2	THEM4	APOL2	APOBEC3C	AL390719.1	LARP1B	LAMB3
ZNF350	TSTD1	BRD4	TOR3A	SRSF2	TOR2A	STEAP4
RASA3	MT.RNR1	TMUB1	RPS27L	IL7R	SPSB1	NEDD4L
B9D2	LCP1	AC073861.1	DTYMK	MMGT1	MFNG	S100A16
RNPC3	HCST	ETV3	NUP205	EML2.AS1	ERGIC3	TMEM125
PGRMC1	BABAM1	MRPS23	CENPM	EMD	H1FX	NRP2
HAPLN3	FAM207A	AZIN1	RNASEH2B	TGFB1	EPHX1	MBIP
FTH1	FOS	ANKRD11	SLC35A3	BIK	AC018926.2	CSF3
S100A2	MRPS21	SPAG7	TUBB	LDHA	UBE2G2	CCND1
ZNF92	AC087190.2	SEMA4D	ZNF800	CTU2	TRIM4	SFTPD
GK5	RNF113A	MAGED2	PDCL3	IL32	NCSTN	SFTPA2
VAMP7	NADK	LBH	IDH2	RNU6ATAC39P	PELI1	C2
CEPT1	MSRA	IGLC3	H2AFX	POLE3	GUSB	CLDN1
SEC24C	GIMAP7	6-Mar	OXSRI	DCTN1	AQP3	ICAM1
OGDH	ZNF480	SMARCA2	H2AFZ	RPS16	ALYREF	SMCO4
KAT7	CD27	DIP2A	KIF20B	MCRS1	MPST	PRSS8
ELK1	CDK5RAP3	DDOST	IPCEF1	SNX9	TAP2	CAPN1
TRMT6	APOBEC3G	RHBDD2	EMC3.AS1	EIF3B	TSPAN3	EPHA2
NF1	ATRAID	USE1	SLC2A4RG	FAM118A	TESK1	UBALD1
AGPAT1	GFER	TCIRG1	TMX2	DEXI	TMEM19	DOT1L
TOMM34	PDRG1	MAP7D1	TUBA1B	PRPF4	TAOK1	PARD6B
PAPD7	EGR1	AP1G2	ZFAND2B	C4orf32	HIST2H2BE	IER3
ATP11A	ZBTB20	LRPAP1	HACD4	ST3GAL1	HSP90B1	CXCL17
HMOX1	CWF19L2	MTCH1	CTDSP1	GOLGA2P7	AP001324.1	MYO1B
TNFRSF1B	JUNB	MEPCE	LSM2	ITGB1BP1	ELOVL1	TSPAN3
USP33	STK17B	CHD4	RFC1	CDK16	WDR46	NRIP1
KIF3A	SLC25A1	RTN4	PLA2G16	LINC.PINT	TPD52L2	SLC6A14
HSDL1	IFI27L2	CNN2	TPI1	POLR2M	MYDGF	DUOX1
CXCL1	COP9	CCT2	COTL1	TRIP13	INHBA	CAV2
RAB34	PPDPF	PRDX2	KLHDC4	PERP	AC004556.1	ANXA2
DMXL1	ZNF683	PBXIP1	TRIB1	LSR	IGHG2	QSOX1
IRAK2	DBNL	CLECL1	ST3GAL5	MED8	TIMM50	TACC2
PWWP2A	LINC00963	C16orf54	AC108693.1	LINC00239	NFKBID	MYO1C
METTL23	ANKRD13D	MAGOH	IDH3G	ARFGAP2	RAB3GAP2	VEZT
CEP135	AC243960.1	1-Sep	UBA6	HSPBP1	MIR155HG	EVI5
CKAP4	PRCC	PLEKHB2	GABPB1	BAG5	SRM	RUNX1
IKKBK	NEMF	TMEM259	TCEAL3	ATL3	DUSP11	GEM
TCOF1	AC109326.1	TLE3	SNF8	NF2	PANK2	SLC35B2
RHBDF2	SNRNP40	PPIG	DMAC1	ABCF3	LY96	SNX25
C15orf48	RANBP3	SPI1	CNPY3	SEC14L2	RUNX1	TOMM34
EAF1	TBCD	CYB561A3	ANAPC11	IL2RB	HSD17B12	LUCAT1
LINC00674	ISG20L2	ADGRE5	PEF1	GTPBP4	UBE2J2	HDHD5
MARCKS	GRAP2	NAP1L4	UBXN11	RTP5	PGP	PSTPIP2
DOT1L	POLR2C	GRB2	SYTL2	MTCH2	PIK3CD	MGST1
TRIM24	LRBA	ARRB2	CLK3	BOP1	ZBTB44	CYFIP1
ZBTB21	DUSP1	SP100	UBA2	MOGS	TMEM258	UTP11
BDH2	MRPL48	TUBA1C	THUMPD1	DUSP16	TRIB1	NDUFAF4
NAP1L4P1	COX17	RNH1	CMTM3	TFB2M	TSR2	SGMS1
DGKD	GIMAP4	CANX	RPA3	GRK5	PNP	MBD2
RDX	DCAF11	SMCHD1	TRIM33	RRP8	LLGL2	ITPR3
TIGAR	AL390728.6	PTGES3	STK24	BTF3	CUEDC2	INPP1
AC079331.1	SNW1	PEBP1	ARHGEF3	TUBB4B	ITM2C	TOP1
TMEM167A	ZNHIT6	PPP1R15B	SMG6	COPS7B	ISY1	ASPH

15	16	17	18
CBWD5	CEP78	GPNMB	SLAMF7
PHACTR4	RAB1B	APOC1	HIST1H2BK
CLIC4	MTHFS	CTSS	MRPS9
SDR42E2	APBA3	FTL	CCDC91
FAM102A	C8orf76	CD68	DOK4
EIF3J.AS1	ATP2C1	CYP27A1	LEMD3
PRDM2	CTBP2	SPP1	SLC11A2
TNKS2	VAMP4	LYZ	PARD6B
MRPS18C	SAMD4B	CSTB	ZFAND3
FAM110A	OAZ2	CD14	IP6K1
SLK	KLHL36	ACP5	ZNF106
SUPT16H	DCP1B	PSAP	DDX49
EPM2AIP1	PRKD2	GSN	CANT1
C20orf27	PLAC8	CYBB	TNRC6C
DNAJA4	AC130469.2	CTSK	THAP11
STRN3	LRRC8C	CD63	ADAR
COPB2	FEZ1	GRN	EFTUD2
CTNBNB1	CADM1	CTSB	GIGYF2
PDXDC1	CEP135	APOE	ACO2
KIF21A	LINC00944	LILRB4	CCAR1
PUM3	LYSMD2	CHI3L1	S1PR1
CCNL2	CASZ1	GM2A	GTF2H1
KAT6B	ITGA5	SDC2	MRPL19
GRHPR	AGPS	EMP1	GAPVD1
SLC25A37	CCDC9	LILRB3	PEX11B
MRPL12	TMEM199	MMP9	GSAP
RBBP7	VRK2	BRI3	RLF
ARFRP1	LRWD1	LIPA	MFSD3
SYNRG	KLF3	DAB2	BLVRA
CTBP1	KLF2	CFD	ZNF639
WDR33	PPIE	TYROBP	TRNT1
PPP1R35	ZDHHC6	NPL	PIEZO1
RSBN1L	GSE1	LGALS3	LYRM4
IDH3B	PEPD	CHIT1	CD274
ZBTB7A	BCL7C	MSR1	TNFRSF10B
PRKCH	RNF169	CAPG	INTS14
MRPS33	VRK3	TIMP2	GALNT1
PDIA4	STAT6	MARCO	ZC3H12D
PYCARD	MRPS35	TFRC	EID3
MRPL53	ISOC2	CD9	AP3B1
TMEM57	CLUH	LEPROT	TMEM199
RHOT2	WSB2	CSF1	HTT
CLTB	MFN2	LGALS1	PON2
PYHIN1	AP3B1	S100A11	CRTC2
BEST1	SEC24C	PLD3	KIF3A
HDDC2	DCTPP1	GPX1	RBM12B
GZMK	LYST	DPYSL2	NF1
SEC22B	PRRC2A	ATOX1	SOCS4
ACOT9	PUM2	PLA2G7	TMEM30B
TLN1	DHRS13	TREM2	SLC7A6OS
SLC11A1	CRCP	CTSD	FAM199X
SPTY2D1	EOMES	HTATSF1	BEX2
SREK1IP1	IARS2	FCGR2A	SLC38A5
NUDT4	ADGRG1	OXR1	PWWP2A
UBXN6	OTUD5	FAM96A	SPTBN1

ANXA2R	JADE2	MATK	NUP62
SSR1	ZNF524	LY96	LINC02001
HAX1	RDH14	MFSD1	KIF21B
FOXN3	PINK1	CCDC88A	PLEKHA1
NENF	S1PR1	SLC16A10	SENP2
TMEM258	GBA2	RHOB	IKBKB
JAML	LINC00861	CCL18	CHKB
N4BP2L2	UBR5	APLP2	FAM210A
POLR2I	WDR45	CTSA	TRIP4
PAN3	FAM193A	TWSG1	THOC6
SLBP	ZNF701	NPC2	AC005261.2
ZNF331	PHRF1	TSPO	VRK3
TES	PTS	ASAH1	DENND4B
PLSCR1	TJAP1	ANXA2	TRAF3IP2
SELENOF	DCAF10	LAMP1	LYSMD2
GMFG	CHKB	PANK3	CD93
THRAP3	NIPSNAP3A	ATP6VOB	SOS2
STUB1	NKG7	AC020656.1	MEF2A
ICAM3	BAP1	PLEK	CSNK1G2
AC074033.1	STAG3L2	OPN3	ASB1
LRPAP1	SLC39A1	UCHL3	TNIK
GIMAP4	KIFAP3	VSIG4	KHNYN
CHD1	RPP25L	FBP1	FRYL
EIF4B	TMEM71	SGK1	GALC
RNF213	MRPL27	SPI1	COL4A3BP
FYN	MFHAS1	EMP3	FAM104A
DDX18	LRRFIP2	KLF4	PMPCA
GTF3A	GFOD2	C15orf48	DNPEP
SMIM26	PCNT	ATP6V1B2	CIC
SP100	C1orf21	LAPTM5	SYVN1
CASP4	IL12RB1	ACTN1	EEFSEC
GABARAPL2	CIAO1	SLC38A6	PSMD5.AS1
COPE	ZNF397	LTA4H	MCTP2
GSPT1	AGPAT3	KCNN4	RBM18
AAK1	PCSK7	MEF2C	HEIH
HLA.A	UNC50	ATP6V1F	SNHG10
DANCR	SH2B3	GUSB	EXOC7
DDIT3	ZNF148	CTSZ	CTU2
ARHGAP4	ARMC1	CRTAP	JAK3
C19orf53	BATF3	ATP6AP1	EVA1C
ATP5J2	RBM12B	DBI	NOL10
SKIL	GTF2F2	ATP6AP2	FAM168B
STOM	ZNF451	MS4A4A	PYGO2
APOLD1	CCDC58	GLUL	ESCO1
TAF7	AP1AR	BASP1	P2RY8

## A1.9 – List of antibodies

Human Antibody	Channel	Catalog Number	Vendor
CD62L	BV510	304844	Biolegend
LAG3	APC/Fire 750	369214	Biolegend

CD45RA	PE/Cy7	304126	Biolegend
CCR7	FITC	353216	Biolegend
Trail	PE	308206	Biolegend
CD25	BV711	356138	Biolegend
Fas/CD95	PE/Dazzle	305634	Biolegend
Annexin V	BV421	640924	Biolegend
Trail-R2	APC	307408	Biolegend
CD8	PerCP/Cy5.5	344710	Biolegend
CD3	PerCP/Cy5.5	300328	Biolegend
CD4	BV510	344634	Biolegend
CD8	APC/Cy7	344714	Biolegend
CAR	BV711	352920	Biolegend
IL17A	PE/Dazzle	512336	Biolegend
IFNG	APC	502512	Biolegend
GZMB	BV421	515408	Biolegend
TNF	PE	502909	Biolegend
IL2	PE/Cy7	500326	Biolegend
CD4	BV711	563033	BD Biosciences
CD62L	BV510	304844	Biolegend
CD103 (ITGAE)	APC	350216	Biolegend
CD27	PE/Dazzle	356422	Biolegend
CD127 (IL7R)	PE	351304	Biolegend
PD1	BV421	621608	Biolegend
CD25	PE/Dazzle	356126	Biolegend
TIM3	BV510	345030	Biolegend
OX40	PE	350004	Biolegend
CD39 (ENTPD1)	PE/Cy7	328212	Biolegend
TIGIT	APC	372706	Biolegend
CTLA4	BV421	369606	Biolegend
LAG3	FITC	369210	Biolegend
OX40	PE/Dazzle	350020	Biolegend
CD62L	APC	304810	Biolegend
pAKT1 (Thr308)	PE	13842S	Cell Signaling
Jun	AF647	sc-74543 AF647	Santa Cruz
pJun (Ser73)	AF488	12714S	Cell Signaling
pERK1/2 (Thr202/Tyr204)	Pac Blue	14196S	Cell Signaling
pMAPK14 (Thr180/Tyr182)	AF594	8632S	Cell Signaling
pMAPK8 (Thr183/Tyr185)	PE	5755S	Cell Signaling
pAKT1 (Ser473)	PE/Cy7	88106S	Cell Signaling
pPLCG2 (Tyr759)	APC	17-9866-42	ThermoFisher
pPLCG1 ((Tyr783))	AF488	25678S	Cell Signaling
pCD3z (Y142)	PE	558448	BD Biosciences
pZAP70 (Y319)/Syk (Y352)	AF488	557818	BD Biosciences
pPyk2	PE	560255	BD Biosciences
Anti-rabbit IgG (H+L), F(ab') <sub>2</sub> Fragment	PE	79408S	Cell Signaling
JunB	Unconjugated	3753S	Cell Signaling
c-Jun	Unconjugated	9165S	Cell Signaling
BATF	Unconjugated	8638S	Cell Signaling
c-Fos	Unconjugated	2250S	Cell Signaling
FosB	Unconjugated	2251S	Cell Signaling
CD45 (Intracellular Domain)	Unconjugated	13917S	Cell Signaling
Anti-rabbit IgG	HRP-linked	7074S	Cell Signaling
CD4 (SK3)	BUV 805	612887	BD Biosciences
CD127 (IL7R)	AF 700	351344	Biolegend
CD25	APC	302610	Biolegend

TIM3	APC Cy7	345026	Biolegend
CD39	BV 711	328228	Biolegend
TIGIT	BV 605	372712	Biolegend
LAG3	BV 785	369322	Biolegend
CD45RO	BUV 563	748369	BD Biosciences



## Appendix 2 – Detailed protocols

### A2.1 – Synthesis of G400 sugar polymer

1. Dissolve 20 mmol of  $\text{CH}_2\text{BrCOOH}$  (bromoacetic acid) and 40 mmol of  $\text{NaN}_3$  (sodium azide) in deionized water, stir at room temperature for 16-24 hours
2. Use  $\text{HCl}$  (hydrochloric acid) to adjust the pH of the resulting solution to  $\text{pH} = 1$
3. Use  $(\text{C}_2\text{H}_5)_2\text{O}$  (ether) to extract the resulting solution with a separating funnel. Collect the organic phase on the top. Extract three times
4. Add surplus anhydrous  $\text{NaSO}_4$  (sodium sulfate) to dry the solution, filter the resulting solution with a filter paper
5. Dry the resulting anhydrous solution with Rotovap to yield  $\text{CH}_2\text{N}_3\text{COOH}$  (2-azidoacetic acid) (product 1) as a colorless oil
6. Dissolve 10 mmol of  $\text{N,N}'$ -dicyclohexylcarbodiimide (DCC), and 10 mmol of 2-azidoacetic acid (product 1) in anhydrous  $\text{N,N}'$ -dimethylformamide (DMF)
7. Add 10 mmol of  $\text{N}$ -hydroxysuccinimide (NHS). Stir the mixture at room temperature for 24 hours
8. Filter all the precipitate, and collect the liquid phase. Use rotovap to remove all the solvent to yield a yellow solid (crude product)
9. Dissolve the crude product in a small amount of dichloromethane (DCM). Gently add hexane to the top of the solution to precipitate out a white solid (product 2)
10. Dissolve 2.5 mmol of  $\text{D}$ -mannosamine and 2.5 mmol of triethylamine in methanol, and add 2.75 mmol of product 2 into it. Stir the mixture at room temperature for 24 hours
11. Remove the solvent with rotovap, dry, and redissolve the resulting solid in pyridine

12. Add surplus acetic anhydride to the reaction mixture, and stir at room temperature for 24 hours
13. Remove the solvent of the resulting reaction with rotovap
14. Purify the resulting crude product with silica gel column chromatography
  - a. Fill the bottom 1/3 of the column with silica gel, flush with hexane/ethyl acetate (3:1, v/v), let silica sit, avoid shaking to obtain a flat surface
  - b. Dissolve product from step 13 with as little MeOH as possible
  - c. Carefully and evenly load the sample onto the top of the silica column, open the bottom of the column, let the sample load into the column
  - d. Add pure hexane to try to elude the by-product, then switch to hexane/ethyl acetate (3:1, v/v) after ~50 ml
  - e. Use thin layer chromatography to identify whether product has come through.  $\text{NH}_3\text{-OAc}$  is visible as a black spot under 254 nm of UV, while our product is visible as a black spot under 365 nm of UV
  - f. Once seeing a black spot under 365 nm of UV, switch the washing solution to hexane/ethyl acetate (1/1, v/v), and collect flow through
  - g. Gradually switch to only ethyl acetate as washing solution to elude the product. Collect flow through until nothing could be seen under 365 nm of UV
15. Combine all the flowthroughs collected, and remove solvent with rotovap to yield a white solid product  $\text{Ac}_4\text{ManAz}$ . It is also normal if the resulting product looks a bit yellow
16. Dissolve 1 mmol of  $\text{Ac}_4\text{ManAz}$  in methanol/anhydrous tetrahydrofuran (1/2, v/v)
17. Add 1.2 mmol of ammonium carbonate into the dissolved mixture. Stir at room temperature for 24 hours

18. Remove solvent with Rotovap. Redissolve crude product with dry dichloromethane, add 3.0 mmol acryloyl chloride and 1 mmol triethylamine. Stir at room temperature for 24 hours
19. Remove solvent with rotovap. Redissolve crude product with DCM, and wash with deionized water for three times with a separation funnel.
20. Purify the crude product with silica gel chromatography according to step 14. Remove solvent to yield Ac<sub>4</sub>ManAzAL
21. Wash Ac<sub>4</sub>ManAzAL with deionized water for three times, use rotovap and lyophilizer to dry the product
22. Dissolve 1.0 mmol Ac<sub>4</sub>ManAzAL, 0.05 mmol azobisisobutyronitrile (AIBN), and 0.0025 mmol poly(ethylene glycol) methyl ether 2-(dodecylthiocarbonothioylthio)-2-methylpropionate (PEG DDMAT) in anhydrous DMF
23. Freeze mixture with liquid nitrogen, vacuum, and thaw to remove oxygen. Repeat for 3 times
24. Put the mixture in oil bath at 65°C for 48 hours
25. Prepare 4 tubes of cold ether. Stop the polymerization reaction by putting the reaction container into liquid nitrogen
26. Quickly inject the reaction into cold diethyl ether and shake violently.
27. Centrifuge at 3,000g for 5 minutes. Discard upper layer liquid, and wash with diethyl ether for 2 more times
28. Dry resulting solid in vacuum to obtain G400 polymers

## **A2.2 – Preparation of G400 sugar nanoparticles and metabolic labelling of T cells**

1. Dissolve desired amount of G400 sugar polymer with DMF at 100 µg/ml concentration
2. Prepare milliQ water in a glass vial at a volume that is 20x to 40x of the volume of G400 sugar DMF solution
3. Put stir bar in a glass vial. Stir very vigorously until the vortex almost touches the bottom of the vial
4. Add in G400 sugar DMF solution drop by drop directly into the vortex. Keep stirring at room temperature for 2 hours
5. Transfer the solution to a 1K dialysis tube. Dialyze against deionized water for 2 days, and change water everyday
6. Pass the resulting solution through a 70 µm strainer
7. Use an Amicon 3K filter to concentrate. Centrifuge in the filter at 5,000g room temperature for 20 minutes. Repeat if necessary

## **A2.3 – Synthesis of DBCO-cytokine and cytokine conjugation onto T cells**

1. Dibenzocyclooctyne-sulfo-N-hydroxysuccinimidyl ester (DBCO-sulfo-NHS) are taken out of the freezer and equilibrated to room temperature. This step is critical in preventing DBCO-sulfo-NHS from being hydrolyzed by water in the air
2. DBCO-sulfo-NHS was dissolved in PBS to 1 mg/ml
3. DBCO-sulfo-NHS and the cytokine to be modified was added into the same low-bind Eppendorf tube at a molar ratio of 8:1. The reaction was filled up with PBS if the volume is < 200 µl

4. The Eppendorf tube with the reaction mixture is placed on a rocker at 4°C for 2 days
5. After the reaction is completed, the reaction is washed for 3 times with PBS by centrifuging through a 3k Amicon column at 4°C
6. The modified cytokine is then aliquoted and stored at -80°C for future use
7. To conjugate DBCO-cytokines onto metabolically labeled T cells, activated T cells are first treated with 200 µM sugar nanoparticles for three days
8. Metabolically labeled T cells are washed 4 times with PBS by centrifuging at 4°C, 300g for 7 minutes
9. Washed T cells are resuspended in PBS, DBCO-cytokine are then added to the T cell culture and mixed well. The resulting mixture is left at 4°C for 30 minutes for click reaction to happen
10. T cells are then washed for 4 times with PBS by centrifuging at 4°C, 300g, for 7 minutes
11. T cells are counted and are ready for downstream use

#### **A2.4 – Manufacturing of CAR viruses and CAR-T cells**

1. Low passage (< P10) HEK 293T cells are cultured in Complete 293T media (DMEM, low glucose w/ Glutamax supplement and HEPES, 10% FBS, 1x non-essential amino acid solution, 1mM Sodium Pyruvate). Using DMEM with high glucose could help HEK 293T cells grow faster, but it reduces transfection efficiency
2. Passage HEK 293T cells in T-75 or T-150 flasks. Allow HEK 293T cells to grow for 4-5 days. Do not let cells become confluent, and always keep the confluency below 90%

3. The day before transfection, in late afternoon, harvest 293T cells and count. Seed 1 million HEK 293 T cells per well in a 6-well plate. Shake the plate gently to evenly distribute the cells. The cells should attach and become ~95% confluent on the morning of the transfection day
4. On the morning of the transfection day, allow Lipofectamine 2000 and Opti-MEM reduced serum medium to equilibrate to room temperature
5. Re-measure the concentration of all plasmids with nanodrop
6. To transfect a single well of a 6-well plate, dilute the following plasmids in 250  $\mu$ l Opti-MEM:
  - a. 0.2  $\mu$ g pFMC63(CAR vector)
  - b. 1.9  $\mu$ g psPAX2
  - c. 0.9  $\mu$ g pMD2.G
7. Mix well with 10 ml strippet. Allow diluted DNA solution to sit at room temperature for 5 minutes
8. Mix Lipofectamine 2000. Add 10  $\mu$ l of Lipofectamine 2000 to 250  $\mu$ l of Opti-MEM, mix well with 10 ml strippet. Let the mixture sit undisturbed at room temperature for 5 minutes. The mixture should turn more milky
9. Combined diluted Lipofectamine and diluted plasmid DNA solution into one tube, let the mixture sit undisturbed for 20-30 minutes at room temperature
10. Lift the 6 well plate on one side to create a deep pool of media in the walls. Add the lipofectamine-plasmid-Opti-MEM solution dropwise to the pool of media without disturbing the attached HEK 293Ts. Make sure the Opti-MEM is not settled directly onto the cells

11. Wait for 48 to 60 hours to harvest lentivirus
12. Collect all lentivirus supernatant. Filter supernatant through a 0.22  $\mu\text{m}$  syringe filter, aliquot and freeze the lentivirus at  $-80^{\circ}\text{C}$  for future use
13. To transduce T cells. T cells are first activated with dynabead at 1:1 ratio for 2 days in a 96-well plate in 100  $\mu\text{l}$  T cell media
14. Thaw virus supernatant on ice. Add 100-200  $\mu\text{l}$  virus supernatant to each well of activated T cells in the 96 well plate. Pipette up and down gently to mix
15. Allow T cells and virus to sit for 2 days before passaging and expanding the culture.
16. Transduced T cells could be expanded, frozen, and thawed for immediate use. There is no need to reactivate these T cells

#### **A2.5 – Collagen modification, crosslinking, cell embedding, and fabrication of Matrigel-Collagen-Nb interpenetrating networks**

Please refer to Appendix 4.1-4.5 of Dr. Kwasi Adu-Berchie's PhD thesis, *Modulating T cell Therapies with Biomaterials*, for detailed protocols.

#### **A2.6 – Rheology on Col-Nb gels**

1. Rheology on Col-Nb gels were conducted with AR-G2 magnetic bearing rheometer and Rheology Advantage software from TA instruments
2. Turn on rheometer, allow rheometer to initialize
3. Open Rheology Advantage software, allow rheometer to connect to computer

4. Load 40 mm cone geometry, perform precision mapping for two iterations
5. Zero-gap the geometry. After machine is zero-gapped, do not raise the geometry, and use a pencil to gently circle out the area the geometry is covering on the loading plate
6. Cool the rheometer to 4°C, wait until temperature is equilibrated
7. While waiting for Step 6, make 880 µl of Col-Nb solution according to methods described in A2.5. Keep the Col-Nb on ice to avoid crosslinking
8. Raise the geometry up. Gently wipe the geometry plate with kimwipe to get rid of any moisture
9. Add 800 µl of Col-Nb gel to the middle of the loading plate. Spread the gel with a P1000 pipette tip so that the gel covers the entire area marked in Step 5
10. Cover the Col-Nb gel with moisture chamber, and use wet kimwipes to seal all the edges and the top
11. Raise the temperature of the loading plate with a Temperature Ramp step to 37°C. Ramp rate: 4.7°C/minute
12. Allow Col-Nb to continue gelling at 37°C for 23 minutes.
13. While waiting for Step 12, prepare 4 mL of methyltetrazine-(PEG)<sub>5</sub>-methyltetrazine crosslinker solution according to methods described in A2.5
14. After Step 12 has completed, adjust the temperature of the loading plate to 25°C and allow gel to equilibrate, put a small moisture chamber with seal at the bottom around the collagen gel, and drop-by-drop add 4 mL of crosslinker solution into the chamber. Make sure the gel is entirely covered with crosslinker solution
  - a. Moisture chamber with sealing could be constructed by laser cutting the bottom of a petri dish of appropriate size to create window for crosslinker addition, and use



window/door sealant from home improvement stores to create sealing needed at the bottom of the moisture chamber

15. Allow the crosslinker solution to diffuse for 20 minutes at 25°C
16. Remove crosslinker solution by pipetting. Cover Col-Nb gel with moisture chamber, seal all windows and edges with wet kimwipes, and allow click crosslinking reaction to carry out at 37°C for 1 hour
17. Remove moisture chamber, gently lower the geometry until the geometry is in full contact with Col-Nb gel. Reinstall moisture chamber and seal all edges with wet kimwipe. Proceed to any downstream analysis
18. Storage and loss modulus, and tan delta: perform time sweep step at 37°C, 1 Hz frequency, 1% strain
19. Frequency sweep: 1% strain, 0.01 Hz – 25 Hz, at 37°C
20. Shear stress relaxation: 20% shear strain were applied within 1 s, shear stress is monitored at 37°C for 0.5-12 hours. It is critical to keep the gel moisturized by ensuring kimwipes used to seal the moisture chamber is wet at all times

## **Appendix 3 – Manufacture and expansion of CIML NK cells with mesoporous silica rod system**

### **A3.1 – Introduction**

Natural killer (NK) cells are innate lymphoid cells that have demonstrated a key role in the defense against viral infections and tumors<sup>265</sup>. These cells express a variety of activating and inhibitory receptors, and the signals they transmit determine the outcomes of NK cell activation. Shortly after their discovery, NK cells were found to be effective at killing different types of tumor cells, indicating their important role in tumor immunosurveillance<sup>266</sup>. Therefore, NK cells have become a promising candidate for adoptive cell therapy against tumors in recent years. In comparison to T cells, which can only be used as autologous cells, NK cell therapies can use both autologous and allogeneic NK cells, enabling the production of off-the-shelf NK cell therapies, which significantly reduces the time patients need to wait to receive the therapy<sup>267</sup>. Moreover, the use of healthy donor-derived NK cells offers the advantage of not being primed by previous anti-tumor treatments and not being educated in an immunosuppressive tumor environment, resulting in fully functional cells<sup>268</sup>. The effector functions of NK cells can be substantially enhanced through the expression of a chimeric antigen receptor (CAR).

NK cells are traditionally considered as innate immune cells, since unlike T cells and B cells, they do not rearrange antigen-specific receptors. However, recent research observed a pool of NK cells that exhibit memory-like features. These cytokine-induced memory-like (CIML) NK cells display enhanced proliferation and effector functions after resting periods, and could persist in the body for months after contraction<sup>269</sup>. Additionally, these CIML NK cells demonstrate potent anti-leukemia activity both preclinically and clinically, with minimal toxicity or

neurotoxicity<sup>270</sup>. These features make CIML NK cells a promising candidate for adoptive cell transfers against tumors to achieve long-term tumor control, and the expansion and manufacturing of CIML NK cells have been widely pursued.

Despite being an attractive candidate for adoptive cell transfer, NK cells have limited ex vivo expansion capabilities. Their ex vivo expansion constantly involves the use of multiple cytokines, including IL-12, IL-15, and IL-18, as well as feeder cells, making large-scale manufacturing difficult<sup>271,272</sup>. Here, we have developed a novel mesoporous silica rod (MSR)-based biomimetic scaffold for the expansion of NK cells, CIML NK cells, and CAR-NK cells. The MSR scaffold enables the controlled release of necessary cytokines to the NK cells, and is also coated with a functionalized lipid bilayer that mimics the presentation of membrane-bound signals provided by feeder cells. This chapter provides a detailed protocol for the manufacturing of these MSR scaffolds for NK cell expansion.

*This is a collaboration project with the Romee group at Dana Farber Cancer Institute.*

## **A3.2 – Methods**

### *A3.2.1 – Manufacture of MSR scaffold with membrane bound IL-21 and 4-1BB*

1. This protocol is for the manufacturing of 500 µg of MSRs. Please scale accordingly.
2. Use glass syringes to transfer chloroform-dissolved lipids into a glass vial to achieve the desired lipid composition. For 0.1 mol% biotin binding, use 100 µl of 25 mg/ml POPC, and 3.6 µl of 1 mg/ml biotinyl cap PE. For 1 mol% biotin binding, use 100 µl of 25 mg/ml POPC, and 3.6 µl of 10 mg/ml biotinyl cap PE.

3. Evaporate most chloroform out under a gentle stream of nitrogen gas under the fume hood. The glass vial should have a translucent film at the bottom
4. Use a vacuum chamber to get rid of any residual chloroform overnight
5. Resuspend the lipid with 1x PBS to 2.5 mg/ml. Mix the lipid suspension vigorously with vortex until no visible lipid film could be observed at the bottom of the glass vial
6. Assemble the extrusion apparatus according to manufacturer's protocol. Use a 0.1  $\mu\text{m}$  polycarbonate membrane. Pre-wet the glass extruder syringe with 1 ml of PBS, and dispense the PBS
7. Aspirate the lipid suspension into the pre-wet extruder. Pass the lipid suspension through the extruder for 21 times. The lipid suspension should become transparent compared with the start
8. Carefully remove the syringe from the extruder, and transfer the suspension to a low-bind Eppendorf tube
9. Weight out appropriate amount of MSR into a 1.5 ml low-bind Eppendorf tube. The amount should be slightly larger than the amount that is used for the experiment. At least 10 mg is recommended for this step.
10. Resuspend the MSR in milli-q water to 50 mg/ml. Mix with a P1000 pipette, and cut the tip when mixing. Gently mix the MSR suspension until it is fully and evenly dissolved. Never vortex the MSRs.
11. Add 40  $\mu\text{l}$  of milli-q water to a 1.5 ml, low-bind Eppendorf tube. Transfer 10  $\mu\text{l}$  of 50 mg/ml MSR suspension into the assembly tube, and gently mix with a P1000 pipette with the tip cut

12. Add 100  $\mu$ l of liposomes from Step 8 to the assemble tube. Gently mix until it's mixed throughout. Leave the tube at 4°C overnight to allow lipid coating
  - a. If short on time, could also leave the tube at room temperature, and gently mix every 10 minutes for a total of 7 mixes.
13. Add 850  $\mu$ l of PBS to the tube, mix gently, and centrifuge at 700 g for 5 minutes at room temperature
14. Carefully aspirate the supernatant out with a P1000 pipette. Wash the pellet with 1,000  $\mu$ l of PBS for 2 times, and resuspend the pellet in 200  $\mu$ l 0.25% BSA in PBS. Block the MSR for 10 minutes at room temperature
15. Thaw streptavidin on ice. Add 6  $\mu$ l of 1 mg/ml streptavidin to the tube. Mix every 2 minutes for 10 minutes to allow the streptavidin to bind to the MSR
16. In the meanwhile, make cocktail for biotinylated 4-1BBL and biotinylated IL-21. Leave the mixture on ice
  - a. For 0.1 mol% (Material E), mix 2.6  $\mu$ l of 4-1BBL at 0.4 mg/ml concentration, and 4.6  $\mu$ l of IL-21 at 0.2 mg/ml concentration
  - b. For 1 mol% (Material E), mix 26  $\mu$ l of 4-1BBL at 0.4 mg/ml concentration, and 46  $\mu$ l of IL-21 at 0.2 mg/ml concentration
17. Add surface ligand mixture from Step 16 to tube from Step 15. Allow surface ligands to bind to streptavidin for 40 minutes at room temperature, with gentle mixing every 10 minutes
18. Add 800  $\mu$ l of 0.25% BSA in PBS, mix gently, and centrifuge at 700g for 5 minutes at room temperature

19. Carefully aspirate the supernatant out with a P1000 pipette. Wash the pellet with 1,000  $\mu$ l of PBS for 2 times, and resuspend in 62.5  $\mu$ l of PBS. The material is ready for downstream use

#### *A3.2.2 – Manufacture of MSR with loaded IL-18 and IL-21 for sustained release*

1. Weight out appropriate amount of MSR into a 1.5 ml low-bind Eppendorf tube. The amount should be slightly larger than the amount that is used for the experiment. At least 10 mg is recommended for this step.
2. Resuspend the MSR in milli-q water to 50 mg/ml. Mix with a P1000 pipette, and cut the tip when mixing. Gently mix the MSR suspension until it is fully and evenly dissolved. Never vortex the MSRs.
3. Add 40  $\mu$ l of milli-q water to a 1.5 ml, low-bind Eppendorf tube. Transfer 10  $\mu$ l of 50 mg/ml MSR suspension into the assembly tube, and gently mix with a P1000 pipette with the tip cut
4. Thaw IL-12 and IL-18 on ice. Make cytokine mix
  - a. For C1 (12.5 ng IL-18 and 2.5 ng IL-12): Add 6.3  $\mu$ l of 1:5 diluted, 0.05 mg/ml IL-18, and 2.5  $\mu$ l of 1:10 diluted, 0.05 mg/ml IL-12
  - b. For C2 (25 ng IL-18 and 5 ng IL-12): Add 12.6  $\mu$ l of 1:5 diluted, 0.05 mg/ml IL-18, and 5  $\mu$ l of 1:10 diluted, 0.05 mg/ml IL-12
5. Add cytokine mix to assembly tube from Step 3. Mix gently and thoroughly. Leave the tube at 4°C overnight to allow cytokines to absorb
  - a. If short in time, could also leave the assemble tube at room temperature, and mix every 10 minutes for 1 hour

6. Add 100  $\mu$ l of liposomes (0.1 mol% or 1 mol%) to the assemble tube. Gently mix until it's mixed throughout. Leave the tube at 4°C overnight to allow lipid coating
  - a. If short on time, could also leave the tube at room temperature, and gently mix every 10 minutes for a total of 7 mixes.
7. Add 850  $\mu$ l of PBS to the tube, mix gently, and centrifuge at 700 g for 5 minutes at room temperature
8. Carefully aspirate the supernatant out with a P1000 pipette. Wash the pellet with 1,000  $\mu$ l of PBS for 2 times. The material is ready for downstream use

## Appendix 4 – Effects of ECM mechanical properties on NK cells

### A4.1 – Introduction

Human peripheral blood contains ~10% NK cells, the majority of which belong to the CD56<sup>dim</sup>CD16<sup>+</sup> cytolytic subset. Compared with CD56<sup>bright</sup> subsets that produce only negligible amounts of cytokines, these NK cells produce significantly greater levels of IFN- $\gamma$ , TNF- $\beta$ , GM-CSF, and other cytokines upon stimulation, and play a key role in NK cells' response against tumors<sup>273,274</sup>.

Solid tumors generate a suppressive microenvironment which dampens the immune cell function and tumor infiltration. Particularly, the CD56<sup>bright</sup>CD16<sup>-</sup> NK cell subset (non-cytokine secreting) is highly enriched in human non-small cell lung cancer (NSCLC), but not the CD56<sup>dim</sup>CD16<sup>+</sup> subset<sup>275</sup>. Additionally, NK cells isolated from human NSCLC demonstrate significantly reduced cytolytic potential as compared to those isolated from peripheral blood or normal lung tissues<sup>275</sup>. Dissecting the mechanisms behind this observation is critical to eliciting potent immune response against NSCLC.

The tumor microenvironment significantly remodels the mechanical properties of the surrounding extracellular matrix. This not only includes increased deposition of ECMs such as collagen I, III, and IV, but also increased collagen crosslinking predominantly catalyzed by enzymes such as lysyl oxidase (LOX). These structural changes not only increase the stiffness of the tumor, but also makes the tumor ECM more elastic, and these changes in mechanical properties may play a significant role in modeling NK cell phenotype and migration. Here, we use the Col-Nb system developed in Chapter 4 to understand whether the mechanical property of



the tumor microenvironment affects NK phenotype and consequently resulted in the absence of the cytotoxic NK subset.

*This is a collaboration project with the Ingber group at the Wyss Institute.*

#### **A4.2 – Methods for embedding NK cells into Col-NB gels**

1. This protocol is for the manufacture of 200  $\mu$ l Col-Nb gels with NK cells. Please scale accordingly.
2. Dissolve lyophilized Co-Nb to 6mg/ml in 0.025M acetic acid at 4°C 2-3 days before the experiment. Vortex collagen when acetic acid is initially added, in next day, and on day before experiment. Do not vortex on the experiment day as this will create many bubbles.
3. Prepare NK cells. Centrifuge and wash NK cells from their media. Wash with PBS for 3 times. Count the cells and resuspend the cells at 25 million/ml
4. Make 20  $\mu$ l aliquots of cells into Eppendorf tubes. Cool the tubes down at 4°C
5. Cool MatTek dishes down at 4°C
6. Add 20  $\mu$ l of ice cold 10x PBS to a 1.5 ml low-bind Eppendorf tube. Keep the tube on ice for all times
7. Add 0.022x – 0.026x of 1M NaOH. The exact value needs to be determined empirically to obtain a final Col-Nb pH of 7
8. Add milli-q water to the tube. Water volume = 200  $\mu$ l – NaOH – 20  $\mu$ l 10xPBS – Col-Nb
9. Vortex the mixture to ensure even mixing

10. Cut the tip of a P1000, and slowly pipette the required volume of collagen to the tube from Step 8. Make sure there is no collagen dangling outside the pipette tip, and no collagen remaining in the tip afterwards
11. Vortex solution vigorously for 5-10 seconds (go longer if the concentration is high), spin down briefly in a cold centrifuge
12. Test the pH of the solution, make sure it is around 7.0-7.5
13. Take the MatTek plate out from the fridge. Place the plate on ice in the tissue culture hood. Take one tube of aliquoted NK cells from Step 3 and put it on ice
14. Cut the tip of P1000, and slowly add 180  $\mu$ l of neutralized collagen from Step 12 into the tube containing NK cells. Gently but thoroughly mix to make sure cells are evenly distributed throughout the gel without creating bubbles
15. Pipette all solution out from the tube and pipette it into the glass well in the middle of the MatTek dish, make sure the Col-Nb-cell mixture covers the entire glass slide
16. Place the MatTek dish into a 37°C cell incubator for 30 minutes
17. After collagen gelling, take the MatTek dish out and leave the plate at room temperature for 7 minutes to cool down
18. Meanwhile, prepare methyltetrazine-(PEG)<sub>5</sub>-methyltetrazine crosslinker by dissolving it in ultrapure DMSO to 50 mg/ml
19. Dilute dissolved crosslinker solution by adding 8.9  $\mu$ l to 4 ml 1x NK cell media for 158  $\mu$ M crosslinking, and 4.45  $\mu$ l for 79  $\mu$ M crosslinking
20. Add diluted crosslinkers to the Col-Nb gel once it's cooled down. For control group, use DMSO instead of crosslinker

21. To enhance crosslinker diffusion, gently lift the gel by using a 10  $\mu$ l tip. Insert the tip between the gel and the well wall, carefully go around the entire circumference of the wall, and use a p200 tip to gently lift the gel up by pushing the tip slightly into the bottom of the gel. Go around the gel in similar fashion until gel lifts up
22. Allow crosslinkers to diffuse for 20 minutes at room temperature, and remove crosslinker solution, and place gel in 37°C incubator for 1 hour for click crosslinking reaction
23. After crosslinking, wash gels 4 times (15 minute/wash with media, 37°C)